DEVELOPMENT OF SURFACE MECHANICAL ATTRITION TREATMENT (SMAT) AND ELECTRODEPOSITION PROCESS FOR GENERATING NANOSTRUCTURED MATERIALS AND STUDY OF THEIR TENSILE PROPERTIES

CHAN, HOI LAM

Ph.D

The Hong Kong Polytechnic University

2010

THE HONG KONG POLYTECHNIC UNIVERSITY

DEPARTMENT OF MECHANICAL ENGINEERING

DEVELOPMENT OF SURFACE MECHANICAL ATTRITION TREATMENT (SMAT) AND ELECTRODEPOSITION PROCESS FOR GENERATING NANOSTRUCTURED MATERIALS AND STUDY OF THEIR TENSILE PROPERTIES

CHAN, HOI LAM

A thesis submitted in partial fulfilment of the requirements for the Degree of Doctor of Philosophy

August 2009

CERTIFICATE OF ORIGINALITY

I hereby declare that this thesis is my own work and that, to the best of my knowledge and belief, it reproduces no material previously published or written, nor material that has been accepted for the award of any other degree or diploma, except where due acknowledgement has been made in the text.

______________________ (Signed)

CHAN, Hoi Lam
AUGUST, 2009

ABSTRACT

This work systematically investigates two of the most promising synthesis methods for producing nanostructured (NS) materials: surface mechanical attrition treatment (SMAT) and the electrodeposition (ED) process, and obtains the proper conditions for fabricating NS materials in bulk form and studies the properties of these materials.

The development of the fabrication process for NS materials begins with the discovery of the superior mechanical properties of the materials with nano-sized grains on the laboratory scale. The unique properties of NS materials and the ways to produce them have drawn much attention from materials researchers. Recently, one of the research directions for nanotechnology has been extended to the development of the fabrication methods for generating NS materials in bulk form.

The SMAT process is one of the promising synthesis methods to fabricate bulk NS materials. Exploiting the actuation of spheres at high velocity which results in high strain-rate, SMAT facilitates the formation of nano-twins which render high strength as well as high ductility. This project first examined the key parameters that influence the effect of SMAT.

The effects of sizes, materials and numbers of balls on the ball velocity were evaluated using a high-speed camera. The factors affecting the ball velocity were examined by using images taken by the high-speed camera. The kinetic energy transmitted from the balls to the treated specimens was computed and hence correlated with the tensile properties of the SMATed samples treated by different numbers of balls; eventually, the relationship between the treatment efficiency and the number of balls was determined. Transmission Electron Microscopy (TEM) was adopted to examine the microstructures at different depths from the surface of the treated samples. Using the measured velocity, a theoretical model was then established to predict the strain-rate reached by a ball at different depths of the treated materials. Simulation using a finite element method (FEM) was also performed to reveal the plastic strain history of a ball on the treated materials. By associating the strain-rate obtained from calculation and plastic strains from simulation with the microstructures from TEM observations, the least requirement of the strain-rate for the formation of twins with nanoscale spacing was evaluated.

Materials subjected to SMAT have a gradient structure with layers composed of nano-grains having a thickness of about ~30 - 100 μm. To obtain NS materials with favorable strength as well as desirable ductility, the selection of base materials is crucial. One promising method for producing matrix materials in bulk form is the ED process. It has the great potential to be applied to many different materials, and can tailor the metallurgical structure and hence the properties of the electrodeposits when the proper process conditions are chosen.

In this study, electrodeposits of thickness ranging from ~160 μm to 1 mm were examined. In the general conditions for small-mass production scale, the effect of process parameters, including the current type, the current density and the deposition duration was studied. Tensile property tests were carried out, both *in situ* and *in vitro*, to reveal the microstructure-property relationship. Scanning Electron Microscopy (SEM) was used to observe the fracture mechanism and the morphology of the electrodeposits. Focus ion beam (FIB) and electron backscattered diffraction

(EBSD) techniques were employed to exhibit the structures and grain orientations, respectively. TEM observations were carried out to statistically summarize the grain size and twins thickness distribution of the electrodeposits obtained in various durations. The relationship between the ED duration, electrodeposits thickness, and grain size and twins thickness was revealed. Texture characterization was performed by X-ray diffraction (XRD), which showed the strong relation of texture of the electrodeposits and the process duration. EBSD was further used to demonstrate the relation of the texture and the structure of the electrodeposits. An analysis from the point of view of Hall-Petch relation and strain hardening exponent showing the comparable properties of this study with the other literatures, is presented. The process conditions used in this study were applicable to produce NS materials with desirable strength, ductility and sufficient thickness.

The effect of SMAT on the electrodeposits was studied. Tensile properties, microstructures and textures of the SMATed electrodeposits were examined. The results demonstrated that the NS matrix obtained by the ED process with sufficient thickness retained desirable ductility after employing SMAT technology, and the SMAT process further enhanced the strength of the electrodeposits.

LIST OF PUBLICATIONS: ALREADY PUBLISHED, ACCEPTED OR SUBMITTED

1. **CHAN, H. L.**, RUAN, H. H., CHEN, A. Y., LU, J., *Optimization of Strain-rate to Achieve Exceptional Mechanical Properties of 304 Stainless Steel Using High Speed Ultrasonic SMAT.* Acta Materialia. 2010, In Press.

2. BLONDE, R., **CHAN, H. L.**, ALLAIN-BONASSO, N., BOLLE, B., GROSDIDIER, T., LU, J., *Evolution of texture and microstructure in electro-deposited Cu treated by SMAT.* Journal of Alloys and Compounds. 2010, In press.

3. RUAN, H. H., CHEN, A. Y., **CHAN, H. L.**, LU, J., *Characterization of Plastically Graded Linear Hardening Material: Part II the Experimental Validation of Nanostructured Material with Microstructure Gradient*. Mechanics of Material. 2010, In press.

4. **CHAN, H. L.** and LU, J., *Comparison of Surface Nanostructured Electrodeposited Cu produced from Different Power Types: Microstructure and Tensile Properties.* Material Science Forum, 2009. 614: p. 189-196.

5. **CHAN, H. L.**, LU, J. and SCHOBERTH, A., *Study of the Mechanical Properties of Nanostructured Aluminum Obtained by SMAT.* Proceedings of the ASME International Mechanical Engineering Congress And Exposition 2007, Vol. 13 - Processing And Engineering Applications of Novel Materials. 11 -15 November, 2007. Seattle, Washington, 2008, p. 39-43. (HB: ISBN 0-7918-4307-6; E-book: ISBN 0-7918-3812-9).

6. **CHAN, H. L.** and LU, J., *Study of the Tensile Strength of Nanostructured Copper Obtained by Electrodeposition and SMAT.* Proceedings of the ASME International Mechanical Engineering Congress And Exposition 2007, Vol. 10, Pts A And B - Mechanics of Solids And Structures, 11- 15 November, 2007. Seattle, Washington, 2008, p.455-462. (HB: ISBN 0-7918-4304-1; E-book: ISBN 0-7918-3812-9).

7. **CHAN, H. L.** and LU, J., *Tensile Strength of Surface Nanostructured Copper. Experimental Analysis of Nano and Engineering Materials and Structures.* Proceedings of the International Conference on Experimental Mechanics- 13th, 1 – 6 July, 2007. Alexandroupolis, Greece. (HB: ISBN 978-1-4020-6238-4; E-book: ISBN 978-1-4020-6239-1).

Honors:

1. **Coordinating Ambassador**, The Sixth International Forum on Advanced Material Science and Technology, IFAMST 6, Hong Kong, 12-14 June 2008.

2. **Session Chair**, The First International Conference on Multi-functional Materials and Structures, MEMS-2008, Hong Kong, 28-31 July 2008.

ACKNOWLEDGEMENT

The author would like to express her most sincere gratitude to her PhD project supervisor, Prof. Jian Lu, for all the supports, guidance and patience throughout her study. The author also wishes to express her appreciation to Dr. Y. Yang, Dr. H. H. Ruan, Dr. C. S. Wen, Dr. A. Y. Chen and Dr. X. F. Yang for their helpful discussions and suggestions as well as assistance in drafting papers and conducting experiments.

Heartfelt thanks to Prof. Thierry Grosdidier, Dr. N. Allain-Bonasso, Dr. B. Bolle and Mr. R. Blonde for their collaborations on the EBSD experiments in France.

Special thanks to all the people who have been actively involved in carrying out this thesis, especially, the scientific officer in Materials Resources Center, Mr. Jeremy Yeung, technician in Product Testing and Analysis Center, Mr. C.N. Tang, research assistant in Mechanical Engineering Department, Mr. Vic Li, other technicians in the Project Lab and other staffs in Industrial Center for their kind supports.

Finally, the author is grateful to her family and friends for their care, love and supports.

TABLE OF CONTENTS

LIST OF TABLES

LIST OF FIGURES

NOMENCLATURE

Symbol	**Description**
a	core radius (m)
b	geometric factor
c	boundary radius of plastically deformed region (m)
d	grain size (m^2) lattice spacing in TEM (m) spacing between the planes in the atomic lattice (m)
D	average grain size (m^2)
e	charge of electron
E	Young's Modulus (Pa)
E^*	reduced Young's Modulus (Pa)
h	penetration depth (m)
i	current density (A/dm^2)
I_p	peak current (A/dm^2)
J	two-dimensional nucleation rate
k	Boltzmann constant in electrodeposition
K	constant in Scherrer Formula
K_1	rate constant
L	camera length (m)

m	strain-rate sensitivity mass of ball (g)
n	integer in XRD
P	load (N)
r	radius (m)
R	radius of ball (m) distance between two neighbouring patterns in electron diffraction pattern (m)
s	area occupied by one atom on the surface of the cluster (m^2)
t	time (s)
T	temperature (°C)
$u(r)$	radial displacement (m)
$v(h)$	velocity of ball (m/s)
v_0	initial impact velocity (m/s)
V	activation volume (m^3)
w_{hkl}	width of peak of special phase (*hkl*) (m)
Y_R	representative stress (Pa)
z	electronic charge of ion

β	angle of the ball indented at the edge of the treated sample during the ball's penetration (°)
ε	strain (%) specific edge energy in electrodeposition (J)
ε_R	representative strain (%)
$\dot{\varepsilon}$	Strain-rate (s^{-1})
$\bar{\dot{\varepsilon}}$	average plastic strain-rate (s^{-1})

$\dot{\varepsilon}_e$	equivalent plastic strain-rate (s^{-1})
$\dot{\varepsilon}_r$	radial plastic strain-rate (s^{-1})
$\dot{\varepsilon}_\theta$	longitude plastic strain-rate (s^{-1})
$\dot{\varepsilon}_\phi$	latitude plastic strain-rate (s^{-1})
η	overpotential (V)
θ	angle between the incident ray and the scattering planes (°)
θ_{hkl}	angle of center of peak (°)
λ	twin lamellar spacing (m) electron wavelength in TEM (m) wavelength of incident X-rays (m)
ν	Poisson ratios
σ	flow stress (Pa)
σ_0	friction stress (Pa)
σ_y	yield strength (Pa)

Chapter 1: INTRODUCTION

1.1 Research Background and Significance

Nanostructured (NS) materials, which were firstly introduced as nanocrystalline (NC) materials, have unprecedented mechanical properties over the conventional coarse-grained counterparts owing to the composition of grains with sizes in the nano-scale regime. The extraordinary characteristics have directed significant worldwide attention to this research area during the past two decades.

In 1959, Physicist R. Feynman delivered a significant talk entitled ‘There’s plenty of room at the bottom’[1], raising the concept of nanomaterials, which not only named him as the father of nanotechnology, but also led to the designing of structure starting from the atomic scale. However, not until 1983, did the prominent possibility on producing ‘microcrystalline materials’ [2] specified by H. Gleiter and his co-workers once again raise the research interest in this area. After his landmark paper published in 1989 [3] which further resulted in a tremendous response from researchers in materials science, thousands of papers on this topic then appeared.

Targeting at revealing the potential ultra-high strength underlying structures and the structure-property relationships of NS materials, materials scientists have extended their interest in developing processes in producing materials with minimum grain size on the nano scale. The bottom-up and top-down approaches for obtaining NS materials correspondingly by consolidating small clusters and breaking down the polycrystalline bulk materials into crystalline units with dimensions of nanometers were used. The early developed fabrication methods, such as inert gas condensation (IGC), chemical vapor deposition (CVD) and pulse electron deposition (PED), were successful in obtaining NS materials with a grain size of a few nanometers. Nevertheless, these techniques are quite costly and are limited on the laboratory scale. The materials obtained by them easily suffer contamination and porosity.

Owing to the extraordinary physical, chemical and mechanical properties of NS materials, there is a consistent quest to process these materials in bulk form for technological application. Therefore, researchers, on one hand, persist in exploring the structure-property relationship of NS materials, while on the other hand, they have directed their focus to the development of the synthesis methods. Some technologies, such as severe plastic deformation (SPD), mechanical attrition (MA), surface mechanical attrition treatment (SMAT) and electrodeposition (ED), have shown their potential availability. Using these synthesis methods, however, the theoretical ultra-high strengths of the materials are not yet achieved and the ductility is still too low. The proper parameters used in the synthesis process have not been acknowledged. The capability of these methods in producing higher strength and high ductility of bulk NS materials has not been fully uncovered. To implement the incentive of producing such materials in bulk form, studies on the control of parameters in the synthesis process are essential for further developments.

1.2 Aim and Objectives

A thorough understanding of the fabrication process is essential for its further development and for tailor-making the advanced materials with desirable properties.

Surface Mechanical Attrition Treatment (SMAT), an efficient way to create nanostructured surface/subsurface layers, has been widely exploited in the last decade [4]. Extensive research efforts have focused on the evolution of microstructures of the materials subjected to this treatment. When the SMAT process is adopted alone, rather low ductility is always the price needed to pay for obtaining high strength. Nevertheless, owing to the simple implementation and low cost in fabrication, it is still one of the most promising synthesis methods to produce NS materials in bulk form for industrial applications. SMAT has been successfully applied to many materials, yet in-depth investigation on the measurement and effect of the parameters in the treatment and henceforth their relationship with the resultant mechanical properties and associated microstructures is still very limited.

Electrodeposition (ED) has been developed since the early 17th century and has recently been applied to the creation of nanostructures. It is also one of the most practical and low cost processes to synthesize NS materials with few shape and size limitations. Limited experimental studies have been performed beyond the laboratory scale. The properties and structure of NS materials were found to be quite sensitive to the dimensions and operating conditions. It is noticed that finished materials with tailoring properties according to applications can be obtained by modifying the process conditions.

This project aims at studying the feasibility of combining SMAT and electrodeposition technologies to produce nanostructured materials in bulk form, which possess relatively better strength with desirable ductility as compared with their pristine form. The objectives of the project are:

- To study different parameters that affect the mechanical properties of materials through experimental, theoretical and numerical analyses (FEM) in the SMAT process;
- To experimentally study the micro-structural properties, in relation to the mechanical performance of the materials produced by conventional direct current (**dc**) electrodeposition and;
- To explore the feasibility of combining SMAT and electrodeposition to produce bulk nanostructured materials for evaluating the potential extension to industrial applications.

1.3 Outline

A comprehensive literature review is presented in Chapter 2 which provides an overview of the background of NS materials and the fundamentals of recent approaches for their synthesis methods. A brief introduction and the pros and cons of the most widely used fabrication technologies are presented with a highlight on electrodeposition (ED) and surface mechanical attrition treatment (SMAT).

Chapter 3 introduces the investigation methodology and equipment used in this work, which includes scanning electron microscopy (SEM), transmission electron microscopy (TEM), X-ray diffraction (XRD), electron backscattered diffraction (EBSD), focused ion beam (FIB), tensile property test, In-situ tensile property test, SMAT machine and electrodeposition equipment.

An experimental study of the SMAT process with theoretical and numerical analysis (FEM) is presented in Chapter 4. The impact ball velocity and its effect on the resultant mechanical properties and the microstructures are investigated. By employing a high-speed camera, the ceiling impact velocity of a ball is quantified, and henceforth the factors affecting this velocity are exhibited. Furthermore, the optimum number of balls which is related to the treatment efficiency for improving their tensile properties is identified. Based on the detailed knowledge of the ball velocity obtained, the strain-rates at different depths of the treated materials are estimated using a theoretical model and the strain distribution was simulated using finite element method (FEM). The correlation between the resultant microstructures and the strain/strain-rate history of the material are then explored.

A detailed study of the ED process is performed in Chapter 5. The effect of the parameters, such as the power type, the current density and the duration, is addressed. Experimental investigations on the microstructures of electrodeposits of different thicknesses by means of TEM are focused on. The relationship between the samples with different grain sizes obtained by varying process durations and their tensile properties is discussed in accordance with the corresponding fracture behaviors. The textures of samples of different thicknesses obtained by XRD are also demonstrated. Hence, the optimized conditions for further development are identified.

On the basis of the optimum conditions obtained in the above two chapters, a potential novel material is produced by combining SMAT and ED technologies and the feasibility of this method is investigated in Chapter 6. The electrodeposits with desirable microstructures and thickness are first produced by ED technology, which are then subjected to SMAT. The microstructures at different depths of the SMATed samples are evolved. The tensile properties are then examined. The optimized conditions of the SMAT process for the electrodeposits are elucidated.

Finally, main conclusions of this project are drawn in Chapter 7. Some thoughts on possible areas for future research will also be proposed.

The flow chart of this work is illustrated as follows:

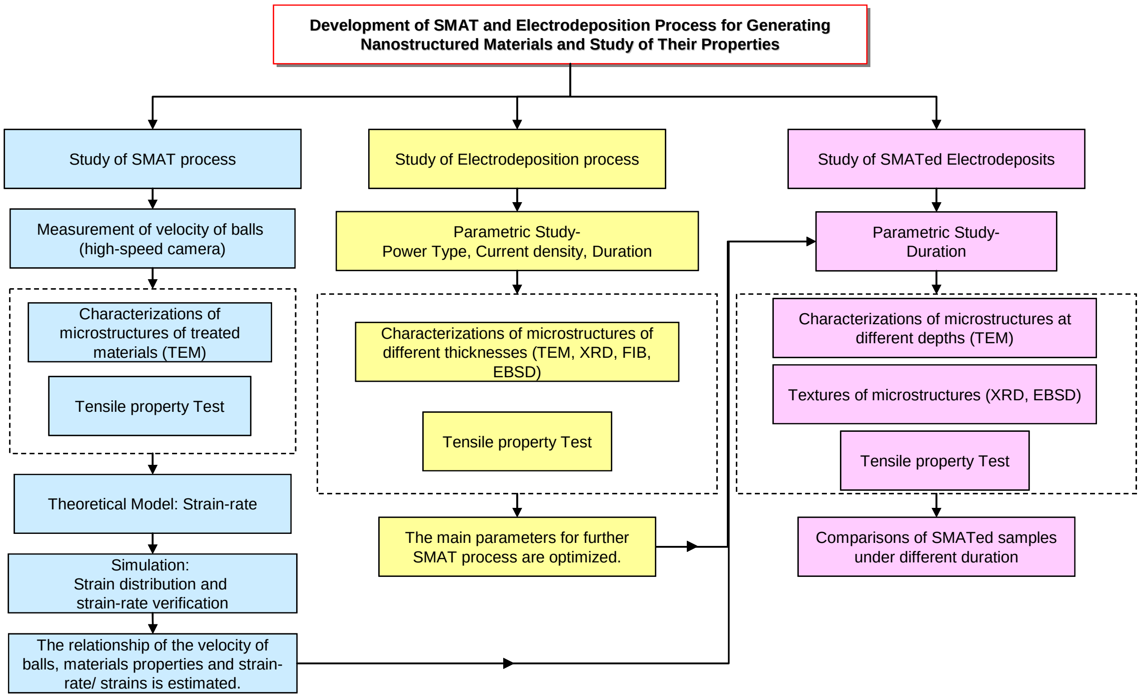

Chapter 2: LITERATURE REVIEW

Nanostructured (NS) materials have outstanding properties compared with their conventional coarse-grained pristine form, for example, high yield strength and high hardness, etc. Such advantages have prompted many researchers to manipulate and optimize the microstructures of NS materials and to achieve their theoretical strengths in the past two decades [3, 5-9]. In this review, a brief introduction of the definition and the background of NS materials are presented. Mechanical properties of NS materials, especially face center cubic (fcc) metals are focused on. The recent approaches adopted to produce NS fcc metals are presented. Then the most widely used synthesis methods are introduced, while electrodeposition (ED) and surface mechanical attrition treatment (SMAT) are highlighted.

2.1 Definition and Background

In the early stage, according to Gleiter, NS materials were solids composed of structural elements - mostly crystallites - with a characteristic size (in at least in one direction) of a few nanometers [6]. Recently, they are usually defined as polycrystalline solids with average grain size of no larger than 100 nm [7], while sometimes loosely ranging from 1 – 250 nm [10]. A grain size that falls into the regime between the upper limit of the NS materials and micrometer is termed 'ultra-fine grain'. When the NS materials are applied in bulk form, they are termed 'bulk NS materials', which are defined as bulk solids with nanoscale or partly nanoscale microstructures [11].

Before the significant talk delivered by Feynman [1] and remarkable paper by Gleiter [3], NS materials had already stemmed from the discovery of the too-small-microstructures of aluminium alloys to be resolved by optical microscopy by Wilm [12] since 1906. The phenomenon of property enhancement owing to microstructural refinement was explained by Merica, Waltenberg and Scott in 1919 [12], and was first inferred by the X-ray studies by Guinier and Preston in 1938 [12]. With the development of the sophisticated methods, such as TEM and XRD, the speculation of the relationship between optimized properties and refined microstructures was then proved. In the 1980s, Gleiter and his coworkers [2, 3] successfully synthesized ultra-fine-grained materials by *in-situ* consolidation of nanoscale atomic clusters and henceforth peaked the research interest of this area in modern material science in the past two decades.

NS materials can be classified in many ways. Some may classify them simply based on the grain size. Seigel [13] classified them into four categories according to their dimensionality: 0D-nanoclusters; 1D-multilayers; 2D-nano-grained layers; 3D-equiaxed bulk solids. Gleiter [6] further classified the NS materials according to composition, morphology and distribution of nanocrystalline component, which is widely adopted, as shown in Fig. 2.1. According to the shape of the crystallites, three categories of nanomaterials may be distinguished: layer-shaped crystallites, rod-shaped crystallites (with a layer thickness or rod diameter in the order of a few nanometers), and nanostructures composed of equiaxed nanometer-sized crystallites. On the basis of the chemical composition of the crystallites, the three categories of nanomaterials may be grouped into four families: (1) all crystallites and interfacial regions with the same chemical composition; (2) the crystallites with different chemical compositions (multiple phases); (3) the NS materials with compositional variations primarily occurring between the crystallites and the interfacial regions; and (4) the nanometer-sized crystallites dispersed in a matrix of different chemical composition. The NS materials consist mostly of crystallites. This classification broadly presents the possible permutations of NS materials.

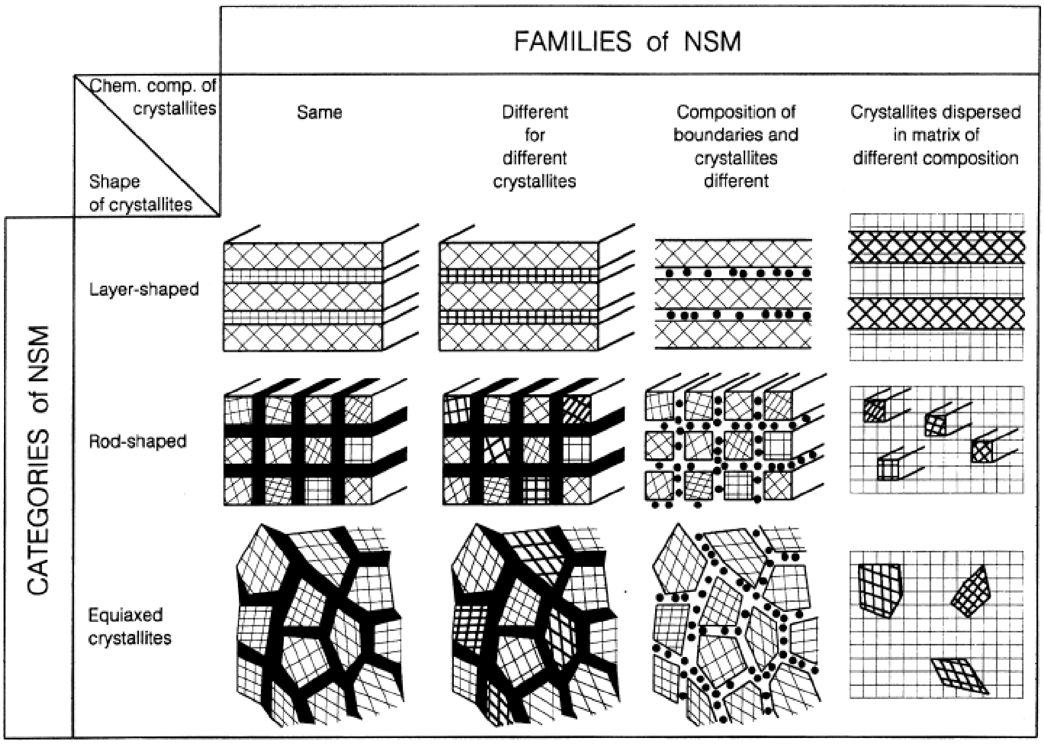

FIG. 2.1. Classification scheme for nanostructured materials according to their chemical composition and their dimensionality (shape) of the crystallites (structural elements) forming the nanostructure. The boundary regions of the first and second family are indicated in black to emphasize the different atomic arrangements in the crystallites and in the boundaries [14].

2.2 Mechanical Behavior of Structural NS Metals

As it is known, properties of materials can be dramatically improved by reducing the grain size while keeping the composition unchanged. The unique mechanical responses owing to the materials with nano-grains inspired most of the recent research works. In this project, mechanical performance of NS metals is the main concern. Therefore, some of the state of the art mechanical responses of structural NS metals, such as Hall-Petch effect, yield strength and hardness, ductility and strain-rate sensitivity are focused on in this section, which are detailed in the following.

2.2.1 Hall-Petch effect

The theory of the relationship between grain size and strength was firstly introduced by Hall [15] and Petch [16] independently in the 1950s. They began with the study of different behaviors. Hall studied the factors that influence the mechanical properties of mild steels, and proposed the relationship between the yield stress of a single crystal and the maximum length of the slip band (which is related to the grain size). Meanwhile, Petch focused on the brittle failure of steels and suggested the relationship between cleavage strength and mean intercept length (which is proportional to grain size). The similarity between the behaviors of cleavage and yield strength was attributed to the fact that yield strength involves shear stresses while cleavage involves normal stresses. Therefore, they drew the same conclusion which is now known as the Hall-Petch relation suggesting that yield stress increases with the inverse of the square root of the grain size:

$$\sigma_y = \sigma_0 + kd^{-1/2}, \tag{2.1}$$

where σ_y is the yield strength for materials with grain size *d*; σ_0 the friction stress; and *k* a constant. It should be noted that the materials that Hall and Petch studied were of the conventional coarse-grained pristine form, and the deformation mechanism of such materials was induced by dislocation pileups and motions. Hence, the extrapolation of the materials with smaller grain sizes of the Hall-Petch trend needs to be verified.

Recently, there have been a number of papers which reported the breakdown in the Hall-Petch trend [17-21] when the grain size falls to a few tens of nanometers. Koch [22] suggested that this breakdown was attributed to the different deformation mechanisms becoming dominant once the grain size was reduced to below a critical value. Chokshi et al. [18] were the first to report the negative Hall-Petch effect on Cu and Pd samples produced by IGC. They concluded that the reason for causing this effect was the existence of diffusional creep in NS samples at room temperature which was similar to the grain-boundary sliding in conventional coarse-grained samples at high temperature. Meanwhile, Weertman [23] suggested that the negative effect should be attributed to the presence of flaws in the materials and the repeat annealing of the single crystal to obtain different grain sizes in Chokshi's experiments.

Meyers et al. summarized the Hall-Petch trends for a range of grain sizes from the micro to the nanocrystalline from different sources for four different metals: Cu, Fe, Ni and Ti, which is shown in Fig. 2.2 [10]. The significant decrease in the slope for small grain size and diverse data points at grain sizes below ~10-15 nm were observed. While there is insufficient information to reach agreement at this stage, debate on the existence of a Hall-Petch negative effect is still ongoing.

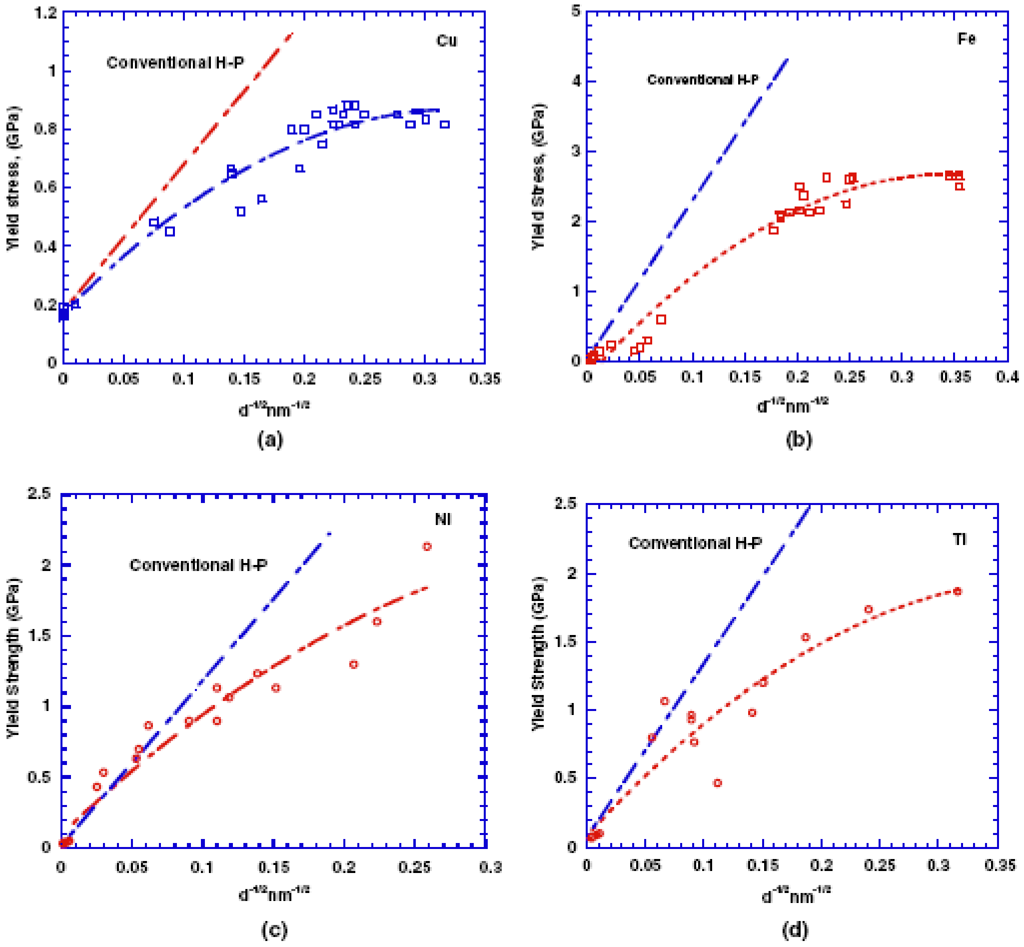

FIG. 2.2. The trend of yield stress with grain size for different metals as compared to the conventional Hall-Petch response: (a) copper; (b) iron; (c) nickel; (d) titanium [10].

2.2.2 Yield strength and hardness

Experimental data accumulated so far indicates that ultra-high strength which is several times that of the coarse-grained counterparts, is almost a given property of NS materials [3, 10, 11, 13, 18, 19, 22, 24-35]. This is true for both yield strength and hardness, which also obeys the Hall-Petch relation by replacing the yield stress (σ) in Eq. 2.1 by hardness (H) [27].

However, the Hall-Petch extrapolation and the theoretical strength of a crystalline lattice are still scarcely achieved. Taking Cu as an example, the recent experimental data showed quite a large degree of deviation from the conventional Hall-Petch relation as shown in Fig. 2.2 (a). The deformation mechanism, as suggested by Koch [22] and addressed in the previous section, may be one of the main factors causing this difference. Schiøtz et al. [36] proved this saying by using molecular dynamics simulations (MDS) with system sizes up to 100 million atoms to simulate plastic deformation of NS Cu. The simulation result showed that the deformation mechanism changes from dislocation-mediated plasticity in the coarse-grain regime to grain boundary sliding in the NS region. However, the theoretical maximum strength obtained from simulations was still as high as 2.5 GPa as the Hall-Petch relation proposed. Beyond the critical grain size, like 10 nm, the softening effect was observed. In practice, except produced in whiskers form, which is extremely small in size and dislocation-free, the theoretical yield strength has not been reached so far [37]. Hence, processing bulk form NS materials to achieve the theoretical yield strength and studying the corresponding deformation mechanism are still the worldwide challenges.

2.2.3 Ductility

Low ductility is always a trade-off for ultrahigh strength for materials with grain sizes of a few tens of nanometers [4, 38, 39]. Several reports showed virtually no strain hardening after an initial stage of rapid strain hardening over a small plastic strain regime (~1- 3%) which is different from the response of conventional coarse-grained metals [29, 37, 40, 41]. In the conventional grain size regime, the reduction of grain size results in increasing ductility by impeding the dislocation motion. However, the limitation of the intra-granular dislocation activity resulting from further reduction on grain size in nanoscale region lowers the ductility. It is believed that the mechanisms of plastic deformation not only enhance the strength as mentioned in the previous subsection, but also significantly affect the ductility.

Since it is still difficult to produce artifact-free NS materials to reveal their inherent mechanical properties, MDS were hence widely used in exploring the underlying deformation mechanisms [36, 42-47]. It seems that an agreement has been reached for the existence of three regimes conforming to the relationship between the plastic deformation mechanisms and the grain size, *d*, by several atomistic simulations [42-48] and a few experimental studies [49, 50], as illustrated in Fig. 2.3. However, it is possible that these mechanisms may vary to a certain degree with different materials, particularly in regime II (10 nm < *d* <1000 nm).

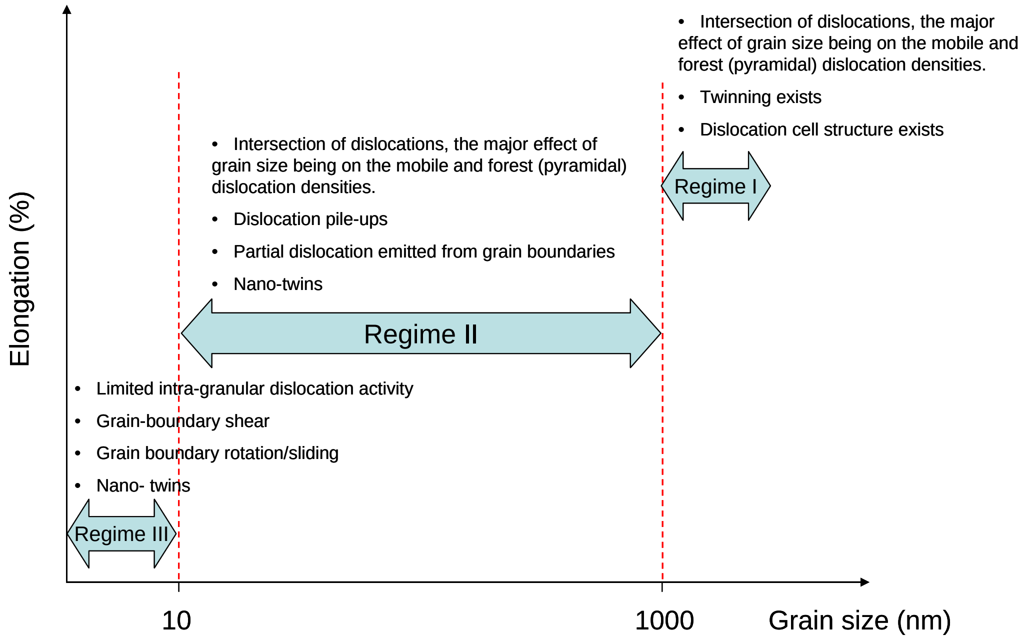

FIG. 2.3. Schematic illustration of three regimes suggesting the relationship of the plastic deformation mechanisms by molecular dynamics simulation.

According to Conrad [42] in his study of Cu, in regime I (*d* >1000 nm), the intersection of pyramidal forest dislocations controlled the rate of plasticity. The major effect of grain size in this regime was on the mobile and forest dislocation densities. In regime II (10 nm < *d* <1000 nm), grain boundary shear promoted by dislocation pile-ups was the dominant mechanism and the main effect of grain size was on the number of dislocations and on the number of grain boundary atom sites. In regime III (d < 10 nm), grain boundary shear and sliding governed the plastic mechanism, and the intra-granular dislocation activity was limited. The effect of grain size in this domain was on the number of grain boundary atom sites. The results from other studies [42-50] agreed with the different mechanisms proposed by Conrad well for regime I and III. However, with the later discovery of special structures, such as nano-twins [51] and partial dislocations emitted from grain boundaries [49], the knowledge of plastic deformation mechanism for regime II is updated from time to time and is still not yet fully understood.

Processing NS materials with desirable ductility is a long-term challenge, as low (or absence of) strain hardening behavior, which causes localized deformation leading to low ductility, has always been observed for samples obtained by equal angular channel pressing (ECAP) [41], powder consolidation [29] and SMAT [40]. Recently, several routes, such as annealing [52], developing bimodal model [53] and inducing twinning [51], have been employed to reduce the loss of ductility. By relieving the stress between the grain boundaries, annealing regains the ductility while sacrificing a certain amount of strength. By creating the nano- micro- scale structure, materials with bimodal structure may have a large gain in work hardening and are able to achieve the uniform strain with only a small loss of strength. Twinning with nano-scale spacing saves room for dislocation storage and helps strengthen the materials further upon tensile straining. It is possible that some approaches can be applied together to supplement individual disadvantages if the conditions are carefully chosen [52]. This is a global challenge for synthesizing NS materials with desirable ductility for industrial applications without giving up too much strength. Furthermore, contributions of experimental data for testifying the results of MDS and for completing the story of the intermediate region (10 nm < *d* < 1000 nm) are essential for the development of NS materials.

2.2.4 Strain-rate sensitivity

There are quite a number of studies reporting extraordinary strain-rate sensitivity when the grain size in metals is decreased [54-65]. Results on decrease in strain-rate sensitivity at the critical grain size for body center cubic (bcc) NS metals [66] and opposite effect for fcc NS metals were reported [55]. In this chapter, a review of fcc NS metals is the focus.

The engineering parameter measuring strain-rate sensitivity, m, is commonly defined as

$$m = \left.\frac{\partial \log \sigma}{\partial \log \dot{\varepsilon}}\right|_{\varepsilon,T}, \tag{2.2}$$

where σ is the flow stress and $\dot{\varepsilon}$ the corresponding strain-rate; *m*, is one of the key engineering parameters for controlling and understanding the deformation in metals. For example, a highly strain-rate sensitive material, such as Cu, is expected to resist localized deformation and hence to be ductile. With decreasing grain size, an increase in *m* – value is recorded.

Fig. 2.4 summarizes the variation of *m* as a function of grain size *d* and twin lamellar spacing λ for Cu samples from some of the recent important literatures [33, 54, 56, 57, 67, 68]. The trend clearly showed that as the grain size and twin lamellar spacing decreased, *m* increased significantly, especially for grain sizes under 100 nm. The reading *m* for the grain size of 10 nm was 0.06, which is much larger than that of conventional coarse-grained Cu (about ~0.002). The little variance shown in the figure is attributed to the different sample synthesis methods and different testing methods. An exceptional one was obtained by ECAP with 16 passes [33]. The reason for such an extraordinary high *m* is not discussed in the paper; however, some researchers believe that it was due to the switch of mechanism to thermally-activated dislocation annihilation at the grain boundaries [10].

Since *m* is also inversely proportional to the activation volume *V*, the increase in *m* indicates that the activation volume for grain-boundary diffusion processes decreases. Hence, the dominant mechanism is changed from cutting of forest dislocations to inducing large numbers of grain boundaries and/or sub-grain boundaries that serve as obstacles to dislocation motion. A sufficiently large *m* (0.5-1) may help resist inhomogeneous deformation and delay the onset of necking according to the Hart's criterion [69] for a rate-sensitive material, and results in the improvement of tensile ductility. If *m* is indeed elevated, it may be made good use of to prolong nearly uniform elongation which is always the global challenge for researchers.

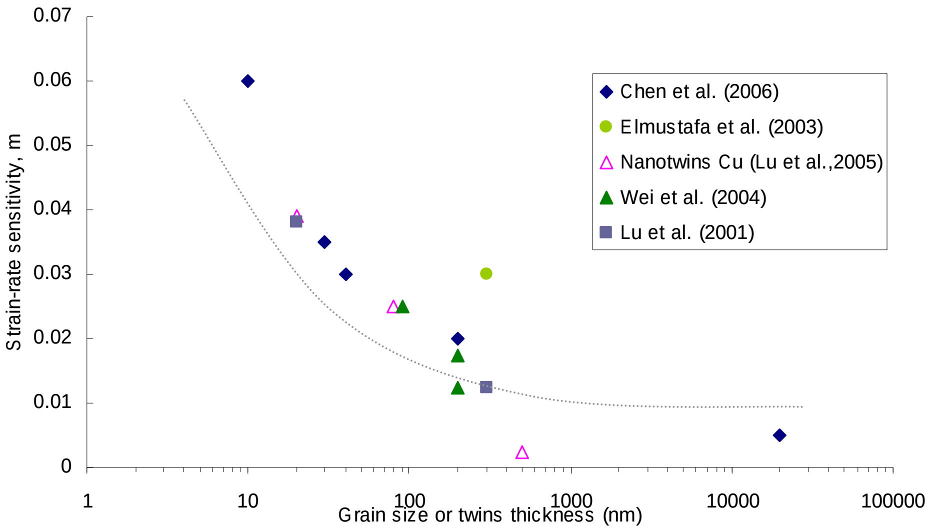

FIG. 2.4. The variation of *m* as a function of grain size *d* and twin lamellar spacing λ for Cu samples from some of the important literatures [54, 56, 57, 67, 68].

2.3 Approaches

NS materials can be prepared by a variety of methods based on the 'top-down' and 'bottom-up' approaches. By introducing a sufficiently large total area of grain boundaries into the material, the former transforms a coarse crystalline bulk material into a nanocrystalline state. Meanwhile, the latter attempts to prepare bulk nanocrystalline samples from nanometer-sized particles formed in the gas phase or in a liquid reaction solution. Some of the widely used measures are described as follows:

2.3.1 Dislocation induced grain boundary

For the synthesis methods employing a top-down approach, dislocation induced grain boundary is one of the most common ways to produce nanostructures. By creating a large number of dislocations by work hardening like ECAP and high-energy compressive impact forces (e.g. ball mills and attrition mills), materials with sufficiently high volume fraction of grain boundaries are produced. Hence, the grain size can be reduced to an ultra-fine or nano-scale level depending on the operation conditions of the synthesis methods. The typical synthesis methods using this measure are severe plastic deformation (SPD) [9, 33, 41], mechanical attrition (MA) [70-75] and SMAT [4, 31, 32, 39, 40, 76-85].

It is capable of producing grains with sizes down to a few nanometers. However, materials produced by this approach are always rather brittle. Subsequent treatment for enhancing ductility is usually needed.

2.3.2 High strain-rate/-low temperature

As NS materials always suffer from brittle behavior, recent results show that the introduction of nano-twins lamella to materials may strengthen them while retaining desirable ductility [7, 51, 57, 86, 87]. However, it is not easy for materials with medium to high stacking-fault energy (fcc metals) to produce twinning. One of the ways to significantly induce nano-twins into these materials is to employ sufficiently high strain-rate (10^4 – 10^8 s^{-1}) treatment and / or at cryogenic temperatures (~77K) [58]. These methods are usually adopted by the synthesis methods with a top-down approach, such as SPD and SMAT. It should be noted that the combination of operation parameters should be carefully chosen; otherwise, too high a strain-rate may result in the over-deforming of the materials; on the contrary, insufficient strain-rate may not enable the potential properties to be reached.

Some recent results show that NS copper treated with SPD with low strain-rate and room temperature also produce a nano-twins structure [88, 89] via a grain boundary mediated twinning mechanism [88]. Nevertheless, this observation is rather new; henceforth more experiments are necessary to verify this.

2.3.3 Twinning

Heavy twinning whose boundaries serve as barricades restricts the motion of dislocations and thus enhances the strength of the materials. On the other hand, when a dislocation encounters a twin boundary, partial dislocation can be generated and hence increases the ductility [49, 90, 91]. There are two types of twins which are commonly considered: mechanical and growth twins. Mechanical twins [40, 86, 90, 92] are the twin structures obtained from extreme deformation regimes as mentioned in the section 2.3.2. Meanwhile, growth twins [51, 53, 57, 87, 93, 94] are usually obtained from annealing, recrystallization and electrodeposition. Both mechanical and growth twins play significant roles in NS materials.

Mechanical twins are induced in materials by those synthesis methods adopting the top-down approach, such as SPD, MA and SMAT. As aforementioned, it is hard for fcc metals to produce mechanical twins as the twinning stress is directly related to the stacking fault energy which is always medium to high for this kind of metal. It appears that mechanical twinning and slip compete with each other in playing roles in NS materials. When the grain size reduces to a few tens of nanometers, even higher shock pressures have no further effect on generating twinning [95]. In this grain size range, the dislocation activity has become difficult, and hence grain rotation and grain boundary sliding take places instead [91].

Growth twins can be induced in materials via annealing, recrystallization and electrodeposition. The former two means are top-down approaches which can produce microstructures consisting of a combination of nanoscale/-ultra-fine grains (80-200 nm) in the coarse grain matrix resulting in optimizing strength and ductility [53]. The grain size distribution contributes to provide room for significant strain hardening which prevents localized deformation and premature fracture.

Another kind of growth twins obtained by the bottom-up approach, electrodeposition, has drawn the enormous attention of researchers since Lu et al. [93] demonstrated the availability of electrodeposited nano-twins Cu with tensile strengths about ten times higher than that of the conventional coarse-grained pristine form. This nano-twins Cu has ultra-high strength and desirable ductility (~14%) which is also much higher than that of NS Cu (~1%). This kind of twins grows in particular conditions: pulse power type, relatively high current density and in well-controlled oxygen and hydrogen contents. This strengthening ability is believed to have originated from the coherent nano-scale twin boundaries interacting with dislocations [96]. By reducing the thickness of twins via increasing the deposition rate by 10 nm/s in the electrodeposition process, different combinations of strength and ductility can be obtained. However, it is noted that the thickness of test samples are in the thin film range (150 - 200 μm) and the sample size is rather small.

2.3.4 Surface nanocrystallization (SNC)

Most material failures such as fatigue fracture, fretting fatigue, wear and corrosion, etc., are very sensitive to the structure and properties of the material surface and hence occur on the surface in most cases. Optimizing the surface structure and properties may effectively enhance the global behavior of materials. By employing NS surface layer, it is possible that the overall properties of materials can be improved without changing the chemical composition. This was the incentive for Lu et al. to develop the concept of surface nanocrystallization (SNC) of bulk metallic materials in 1999 [79].

Based on the basic concept of NS materials and their formation mechanism, three types of SNC approaches are proposed, as shown in Fig. 2.5:

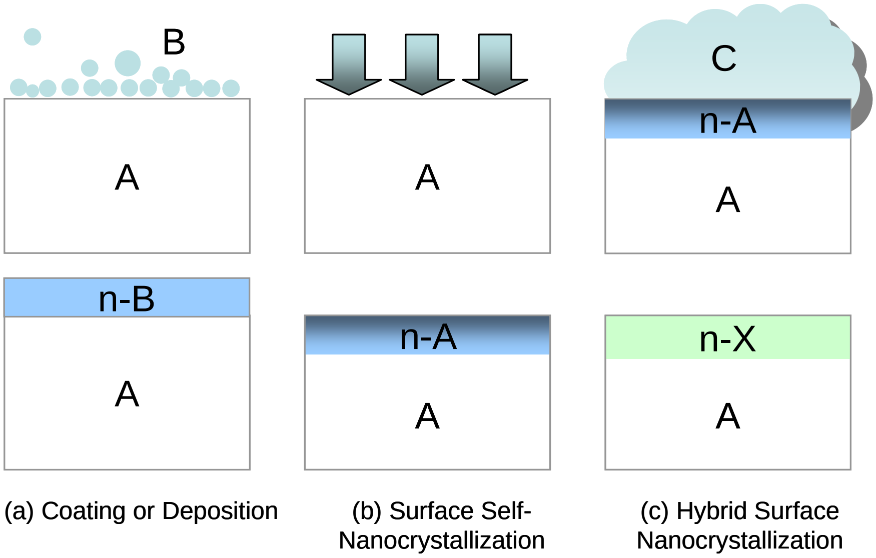

(a) Coating or Deposition (b) Surface Self-Nanocrystallization (c) Hybrid Surface Nanocrystallization

FIG. 2.5. Schematic illustration of three types of SNC approaches: (a) coating or deposition; (b) surface self-nanocrystallization; (c) hybrid surface nanocrystallization [79].

a. *<u>Surface coating or deposition</u>*

The first type of SNC approach is surface coating or deposition as shown in Fig. 2.5(a). A nanocrystalline (NC) surface, denoted as n-B in Fig. 2.5(a), is deposited or coated with either nanometer-sized isolated particles or polycrystalline powders with nano-sized grains by technologies such as physical vapor deposition (PVD), chemical vapor deposition (CVD), plasma processing, sputtering, IGC and electrodeposition (ED). The NC surface layer and the matrix can be made of different or the same kind of materials. The main factors in this process are the bonding of the NC layer with the matrix and the bonding between particles while maintaining the nanostructure.

b. Surface self-nanocrystallization

The second type of SNC approach is surface self-nanocrystallization as shown in Fig. 2.5 (b). Transforming the surface layers of the materials into nanoscrystalline states while keeping the overall composition and-/or phases unchanged, this type of SNC can be achieved by means of mechanical or thermal activation. Materials with gradient microstructure from nano-scale at the top surface to coarse-grained matrix can be obtained.

Mechanically induced surface self-nanocrystallization (MISS-NC) creates an NS surface layer by contact loading with repeated multidirectional severe plastic deformation. With such loading, shear bands consisting of arrays of high-density dislocations are formed at the first stage. Continuous loading results in grain refinement with small angle grain boundaries created by dislocation annihilation and recombination. Further treatment changes the orientation of the grains, which results in the formation of a random-oriented NS surface layer. This approach can be achieved by techniques such as rolling and SMAT, which will be further discussed in the next section. Temperature control during MISS-NC is usually employed to optimize the mechanical behaviors. The optimization results are found to depend on the operation conditions.

c. Hybrid surface nanocrystallization

Specific properties can be obtained by the combination of the pre-treated NS surface layer with a chemical, thermal or metallurgical process, as shown in Fig. 2.5 (c). This approach is Hybrid surface nanocrystallization which facilitates chemical processes, like catalysis, diffusion and surface chemical combination, on the NS surface layer. The composition and phases in this layer are consequently modified to enhance its reactivity. It is one of the widely used approaches to produce a platform for growing high-density lengthy nanowires.

2.4 Synthesis Methods

As aforementioned, the fabricating history plays a crucial role on the mechanical behaviors of NS metals. For example, the early discovery of reduction of Young's Modulus in NS metals obtained by IGC [29, 97], was believed to be one of the extraordinary properties of NS metals. Later, the subsequent work on the porosity-free materials produced by the improved fabricating methods showed that the intrinsic elastic moduli of NS materials are essentially the same as those for their conventional coarse-grained counterparts [98] until the grain size becomes extremely small (e.g. <5 nm) [11]. It seemed that the early misleading results were due to the flaws like porosity and incomplete bonding among the grains obtained in the fabrication process [29, 97]. Therefore, the effect of the synthesis methods should be carefully considered when studying the mechanical behaviors of materials. Since the discovery of the superior properties of the NS materials, a number of principal synthesis methods for production of NS materials have been developed. In this section, five of the most common ones, i.e. inert gas condensation (IGC), mechanical attrition (MA), severe plastic deformation (SPD), electrodeposition (ED) and Surface Mechanical Attrition Treatment (SMAT), are discussed.

2.4.1 Inert gas condensation (IGC)

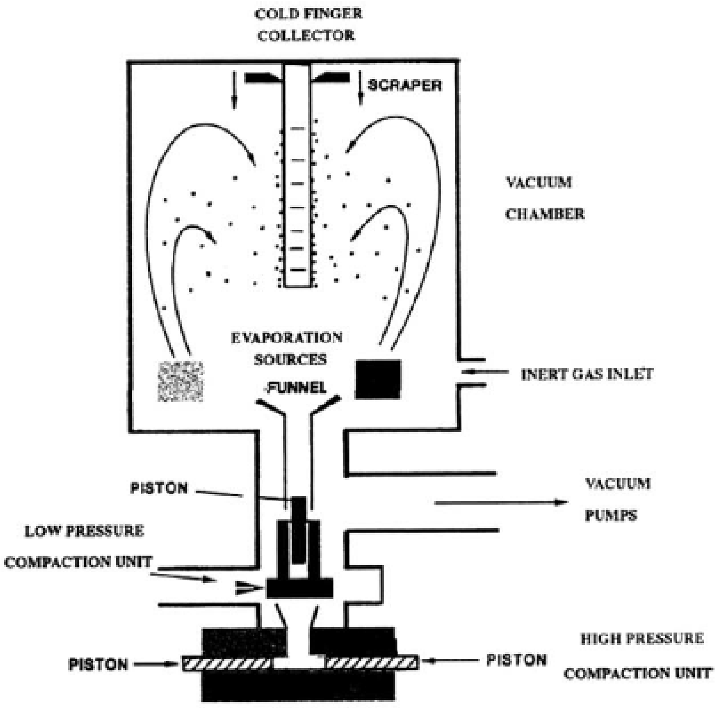

FIG. 2.6. Inert gas condensation (IGC) technique [10].

The inert gas condensation (IGC) technique [99, 100], a bottom-up approach, was the first successful approach to produce NS materials and has set a platform for the early important studies of their mechanical properties [23, 29, 101]. The schematic drawing of this technique is shown in Fig. 2.6. In IGC processing, an evaporative source is used to generate the powder particles, which are convectively transported to and collected on a cold substrate by means of interactions between the hot vapor species and the much colder inert gas atoms in the chamber. This process has to be carried out under ultra-high vacuum conditions to guarantee the cleanliness of the particle surfaces and a minimum amount of trapped gases. *In-situ* consolidation is almost a necessary follow-up process to improve the density of the NS metal obtained by IGC.

IGC is one of the most common synthesis methods for producing NS materials in experimental quantities. This process has the advantage of production of equiaxed crystallites which have sizes of a few nanometers with a narrow size distribution. Many kinds of NS materials can be obtained by this method. However, there exists the possibility of contamination of powders and porosity due to insufficient consolidation. Also, there is the possibility of imperfect bonding between particles. These greatly affect the behavior of NS materials.

2.4.2 Mechanical attrition (MA)

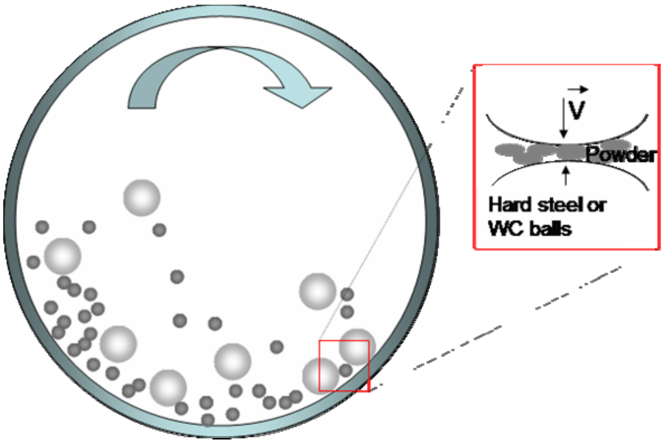

FIG. 2.7. Mechanical attrition (MA) as a means of synthesis of NS materials.

Mechanical attrition (MA) is a convenient top-down approach by exerting strain-rate and dislocations onto the materials to reduce the grain sizes [70-75, 102-104]. This process can be achieved through ball milling, repeatedly fracturing and cold welding [70-75, 102-104]. It is also called mechanical alloying. The setup is shown in Fig. 2.7. The grain size decreases with the increase of milling time [75]. When the time is sufficient, the shear bands and mechanical twins are also formed [75].

MA is a simple and convenient synthesis method which results in high materials yield and is capable of being applied to a wide variety of materials. It also has potential for large quantity production. However, it is difficult to avoid the introduction of impurities into the powder in the form of wear debris arising from the milling chamber and balls, and the introduction of a significant amount of microstrains into the nanocrystals which may result in undesirable mechanical properties.

2.4.3 Severe plastic deformation (SPD)

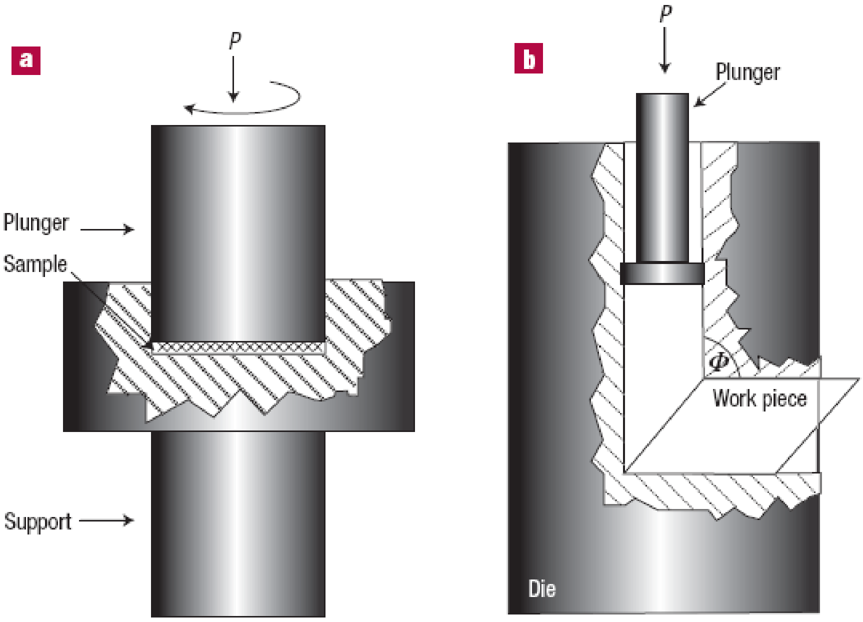

FIG. 2.8. Principles of SPD methods: (a) torsion under high pressure; (b) ECA pressing [105].

Severe Plastic Deformation (SPD), a top-down approach, refines the microstructure in bulk billets by means of heavy straining under high imposed pressure [9, 33, 105-114]. It is one of the most widely used processes for producing bulk ultra-fine grained materials. There are several available SPD methods, and the most commonly used ones are high pressure torsion (HPT) [113] and equal channel angular pressing (ECAP) [106]. A schematic illustration of these two methods is shown in Fig. 2.8.

Fig. 2.8 (a) shows the principle of HPT. A disk-formed sample with a diameter of 10-20 mm and a thickness of about 1 mm is held under high pressure and then subjected to straining in torsion under the applied pressure of several GPa. The lower anvil turns and friction forces result in shear straining of the sample. Materials obtained by HPT have the advantage of producing exceptionally small grain sizes, often in the nanometer range (<100 nm). HPT also has the ability to process brittle materials such as intermetallics and semiconductors. Nevertheless, specimens processed by HPT are confined to be a small size.

ECAP is a process to obtain bulk ultra-fine grained materials by means of pressing the sample through a special die via pure shear. The principle of ECAP is shown in Fig. 2.8 (b). The die consists of two channels, which are equal in cross-section and intersect at an angle, ϕ. The angle is generally 90°. The sample is first machined to fit the channel. It is then pressed down by a plunger and is forced round the sharp corner. In ECAP, the strain imposed on the sample greatly depends on the channel angle between the two channels, as well as the angle defining the outer arc of curvature where the two channels intersect. An ultra-fine grained structure with rather wide distribution is then obtained with desirable elongation.

SPD methods have been successfully developed to produce NS materials in bulk form. They also show their applicability to various metals. Nevertheless, the problems of fabricating NS materials with larger dimension and sufficient homogenous structure still exist.

2.4.4 Electrodeposition (ED)

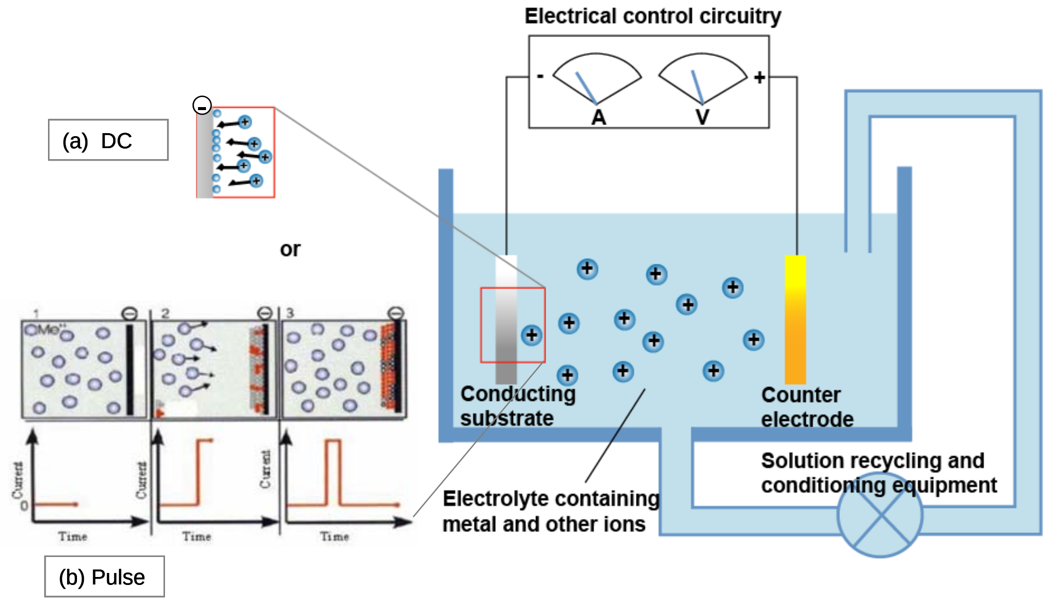

FIG. 2.9. Electrodeposition setup: (a) direct current; (b) pulse electrodeposition.

Electrodeposition (ED) is a bottom-up approach, and has been developed for more than two centuries. Recently, it is widely applied in the creation of nanostructures [8, 93, 115-126]. The basic components for the ED process setup include an anode, a cathode, electrolyte and a power source. The whole process of ED is shown in Fig. 2.9. When an electric field is applied, precursor ions are drawn towards the surface of the conducting substrate. After the ions reach the surface, it chemically bonds with certain bonding sites and stays there to form electrodeposits.

2.4.4.1 Historical background

The ED process was first invented by Brugnatelli and was applied to electroplate gold with dry batteries in 1800 [126]. However, not until 1840 did it draw great attention when it was used to electroplate Cu for printing press plates, and silver and gold for decoration purposes. In the 1850s, it was widely employed to plate many metals, such as bright nickel, brass, tin and zinc, for engineering and special commercial purposes. In the 1940s, its application was extended to electronics and telecommunication industries. At that time, direct current power supplies, whose mechanism is illustrated in Fig. 2.9 (a), were used instead of dry batteries [126]. Since then, the more sophisticated and comparatively safer electroplating bath formulae have been developed for different applications. In 1994, Erb et al. [119, 120] appeared to be the first to successfully utilize the ED process to produce bulk NS Ni with grain sizes of 11 nm by means of pulse current power supplies, whose mechanism is illustrated in Fig. 2.9 (b). After that, the ED process became one of the most important synthesis methods for producing bulk NS materials. When Lu et al. [93] demonstrated that nano-twins structures obtained from the ED process in particular conditions have mechanical strengths 10 times higher than that of their conventional coarse-grained counterparts with desirable ductility, the foci of many researchers in the NS field were further directed to this promising process.

2.4.4.2 Principles

The basic principle of the ED process for ordinary usages was addressed at the beginning of this section. To create NS metals using the ED process, there are two major modes of grain evolution, i.e. nucleation and growth. Nucleation is the forming of new grains from ions, and growth is the outward spreading of the nucleated regions. The former one should be promoted while the latter one should be limited.

Nucleation and growth are two competitive processes and can be influenced by different factors. The two key mechanisms are deposition rate (rate of transfer of charge at the surface of substrate) and the surface diffusion of the ad-atoms. High deposition rate and low diffusion rate favour grain nucleation, while low deposition rate and high diffusion rate promote grain growth [115]. It is believed that utilizing pulsed current encourages grain nucleation by allowing ED only in short bursts. Other ED variables, such as the basic composition of the electrolyte, addition of grain nucleators, stress relievers and grain-growth inhibitors, the pH value, the deposition temperature and the current density, are chosen based on the rule that the nucleation of new grains is favored rather than growth of existing grains [8, 119]. Recently, Lu et al. [51] demonstrated that different thicknesses of nano-twins structures can be tailor-made by the ED process under well-controlled conditions as aforementioned in Section 2.1.3.3. It is important to note that the adjustment of any one of the ED variables may result in electrodeposits with different structures and hence properties.

2.4.4.3 Parametric reviews

The properties of materials are determined by their structures. There are four typical structures encountered with electrodeposited metals [117], which are: (1) *Columnar*: Deposits of this structure are obtained from a bath at elevated temperature and with low current density, which exhibits lower strength and hardness than other types but high ductility [117]; (2) *Fine-grained*: Deposits of this structure are obtained from a bath with additional agents, high current density and high pH value, and exhibits relatively hard and strong properties [117]; (3) *Fibrous*: Deposits of this structure obtained from a bath with additional agents, high current density and at low temperature have properties which are intermediate between the *columnar* and *fine-grained* type [117]; and (4) *Banded*: Deposits of this structure obtained from a bath with special additional agents and pulsed current have high strength and hardness but low ductility [117]. With high current density, a twin structure can be obtained with improved resultant ductility.

In order to promote desirable structures while inhibiting unwanted ones, the ED process allows a precise control of composition, crystallographic texture and grain size of the materials by varying the process parameters. Fig. 2.10 schematically illustrates the relation between the process parameters and grain size of the electrodeposits [117].

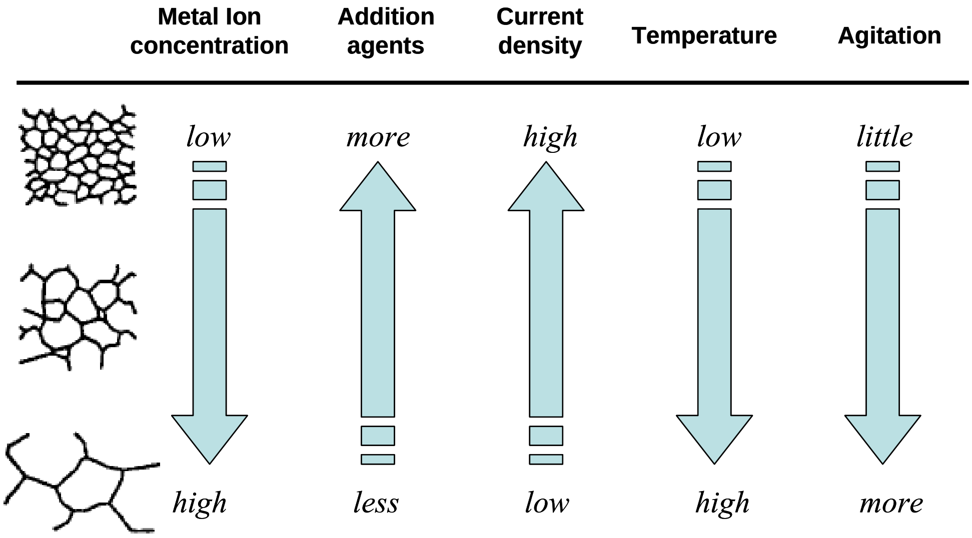

FIG. 2.10. Relation between the structure of electrodeposits and operating conditions of solutions, modified from [117].

The most important parameters in the ED process are summarized below:

Basic composition of the electrolyte: an electrolyte solution contains metal ions, support chemicals and addictives. By varying the concentration of the chemicals and the amount of addictives, one may obtain materials with different structures and properties. Meanwhile, addictives may serve as grain nucleators, stress relievers and grain-growth inhibitors, which may significantly decrease the grain size and result in better mechanical properties. A cyanide bath is another kind of bath commonly used in the industry, but this will not be discussed in detail in this work.

pH value: pH is a measure of the hydrogen ion concentration in solution. The pH value of a metal deposition electrolyte is critical, because it influences the ED process in many aspects, especially the deposition rate. For producing NS materials, a bath with a pH value equal to 1 is usually adopted [51, 93].

Deposition temperature: maintaining close temperature control of the deposition bath is one of the most important criteria in operating ED processes. It determines deposition rate and bath stability [122]. To obtain materials with nano-scale grain size and nano-twins structure, the operation temperature is usually well-controlled to be 20°C ± 1 [51, 93].

Solution agitation: good solution agitation results in rapid solution exchange and adequate uniform solution movement at the cathode surface. This allows electrodeposits with uniform properties over a wide range of current densities. Without agitation, severe surface irregularities may be obtained. Meanwhile, too speedy agitation results in a rough surface and coarse-grains [123].

Influence of substrate: there are a number of studies reporting the influence of substrate [116, 117, 123-125] on the structure of the electrodeposits. The crystallographic texture and topography of the deposited layer are greatly affected by that of the substrate materials, since the grains of the electrodeposits usually grow with the orientation of the substrate materials [125]. Some studies have reported that amorphous Ni-P substrates facilitate the growth of ideal fiber textures and twins structures of the electrodeposits owing to its unbiased growth [124, 125]. Some reported that substrate with fine structure and well-defined texture, such as MP35N alloy, may increase the opportunity for forming textured electrodeposited film to grow high density twins [116]. An agreement on how to choose substrate materials which are beneficial in obtaining NS materials with desirable structures has not yet been reached. However, it is known that combining the effect with other operation parameters, such as current density, the effect of substrate on enhancing texture or the density of twins structure are remarkable [116].

Types of current: there are different types of current that can be adopted in the ED process, such as direct current (**dc**), triangular pulse current (**tpc**), rectangular pulse current (**rpc**), etc. [121]. Properties and grain size of the electrodeposits vary with the type of current employed in the ED process. Among them, **rpc** is widely used in obtaining NS materials [119, 120] or ultra-fine grained materials with nano-twins [51, 86, 93] owing to its facilitation for grain nucleation rather than growth. Usually, the combination of short on-time, such as 0.02s and long off-time, such as 2.0s is adopted to produce the nano-twins structure [51, 86, 93]. However, for rather thin films of a few micrometers, the effects of **dc** and **rpc** have very little difference [121].

Current density: there are many studies reporting that microstructure and surface topography of the Cu layers are influenced by the current density [116, 121, 124]. Based on the classical theories on electrochemical phase formation and growth, the two dimensional (2D) nucleation rate, J is given by [127]:

$$J = K_1 \exp[\frac{-bs\varepsilon^2}{zekT\eta}], \tag{2.3}$$

where K_1 is the rate constant; b the geometric factor depending on the shape of the 2D cluster; s the area occupied by one atom on the surface of the cluster; ε the specific edge energy; z the electronic charge of ion; e the charge of the electron; k the

Boltzmann constant; T the temperature; and η the overpotential. The overpotential is established by Tafel as follows [127]:

$$\eta = a + b\log i, \tag{2.4}$$

where a and b are constants and i is current density. According to Eq. (2.4), the larger the current density, the higher the overpotential. Therefore, the increase of the nucleation rate (Eq. (2.3)) might lead to more homogeneous structures and finer crystal grains.

It is important to note that these parameters cannot be considered independently, since synergetic effects need to be taken into account [124].

2.4.4.4 Pros and cons

The ED technique has significant advantages over other methods for synthesizing NS materials: (1) potential of synthesizing a large variety of nano-grain materials, such as pure metals, alloys and composite systems with grain sizes as small as 20nm; (2) low investment; (3) high production rates; (4) few limitations on size and shape; (5) high probability of transferring this technology to existing electroplating and electroforming industries [10, 119]; and (6) probability in tailoring the properties of the materials for different applications. Since the structure and properties of the deposits are very sensitive to the operation conditions, the parameters, such as current power, current density and temperature, etc., have to be monitored and controlled well. Otherwise, low ductility may result from the existence of porosity and contamination. Furthermore, when the thickness of electrodeposits increases to a certain extent, the peeling of the deposits due to stress build-up may happen [8]. Hence, the scale-up production and re-productivity of sufficient thickness and size with the same structure and mechanical properties for bulk application are still challenging.

2.4.5 Surface mechanical attrition treatment (SMAT)

On the basis of strain-induced grain refinement, SMAT, employing the surface self-nanocrystallization approach, has been developed to synthesize a nanocrystalline surface layer on bulk metallic materials [4, 79] and has been successfully applied to a number of materials [79, 128-133].

2.4.5.1 Principles

The basic principle of SMAT is to introduce a large amount of defects and / or grain boundaries into the surface layer in order to transform the microstructure into nanocrystalline. Fig. 2.11 schematically illustrates the experimental setup of SMAT. Spherical balls with smooth surfaces are placed in a reflecting chamber and are actuated by the vibration generator. In the treatment process, the surface of the sample is impacted by a large number of flying balls over a short period of time. The impact directions of the balls onto the sample surface are rather random owing to the random flying directions of the balls. Each impact induces plastic deformation with a high strain-rate in the surface layer of the sample. As a consequence, the repeated multidirectional impacts at high strain-rates onto the sample surface result in severe plastic deformation and a nanostructured layer is formed in the surface of the sample [4].

Comparing the SMAT with other conventional surface treatment such as shot peening, one may find obvious differences in several aspects which stated as follows [4]:

1) Much larger balls (a few mm) are used in the SMAT than in the shot peening (0.2 – 1 mm);
2) Spherical balls with smooth surface are necessary for obtaining a nanostructured surface layer in the SMAT. However, there is no specific requirement for the surface roughness of the balls in shot peening process. These rough-surfaced balls usually result in wearing and damaging the nanostructured surface layer during the conventional treatment;
3) The velocity of the balls in the SMAT is much lower (1 – 20 m/s) than that of the balls in the conventional shot peening (typically about 100 m/s);
4) The balls impact at 90° to the sample surface in conventional shot peening treatment, while the impact directions of the balls at the sample surface are rather random in the SMAT in order to facilitate the grain refinement process.

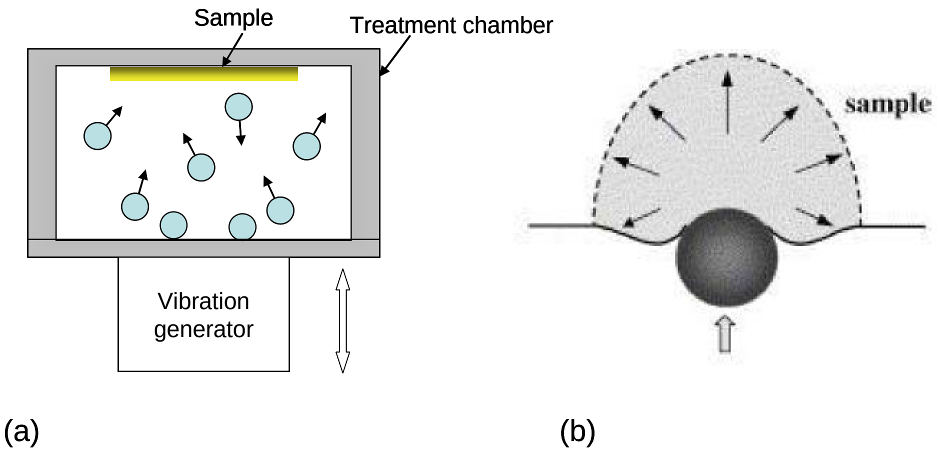

FIG. 2.11. Principle of SMAT: (a) experimental setup; (b) the localized plastic deformation in the surface layer induced by the impact of the ball [4].

2.4.5.2 The surface nanocrystallization mechanism of different materials

The samples treated by the SMAT process always have a specific gradient structure. A gradient grain size distribution from a few nanometers at the top surface layer to several micrometers in the near deep matrix is developed in the SMATed sample. This originates from the gradient variation of the strain and strain-rate from the treated top surface (which are very high) to the deep matrix (essentially zero), as schematically shown in Fig. 2.12.

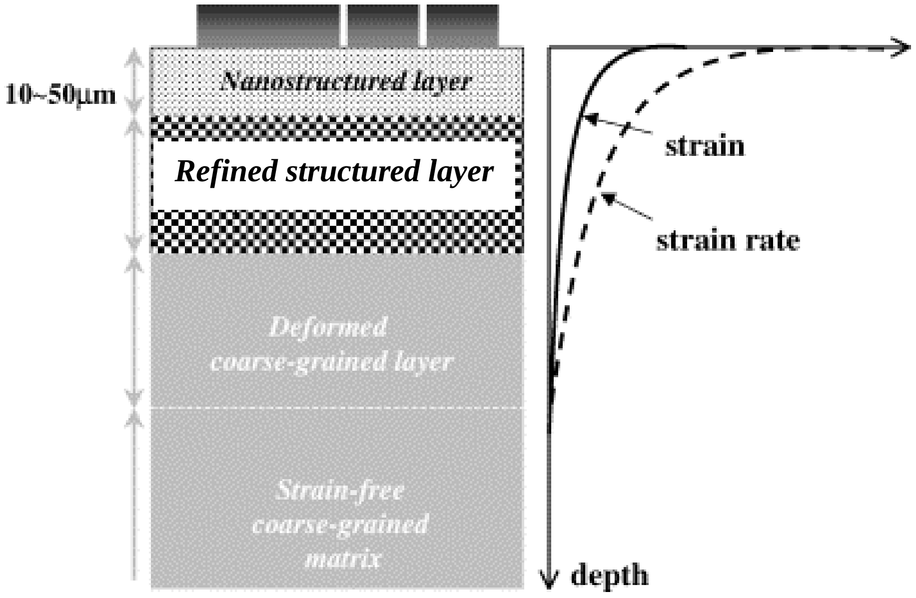

FIG. 2.12. Microstructure characteristics and distributions of strain and strain-rate along depth in the surface layer subjected to SMAT [4].

The formation mechanisms of nanostructured materials have been systematically investigated in [31, 39, 60, 78, 80, 83-85, 134]. Since plastic deformation behavior and dislocation activities in metals depend strongly on the lattice structure and stacking fault energy (SFE), different grain refinement approaches and nanocrystalline formation mechanisms can be identified in these deformed materials owing to different material natures. For materials with high SFE, such as Fe (about 200 mJ/m^2), the grain refinement and microstructure development during SMAT can be summarized as follows [80] as shown in Fig. 2.13:

1) Development of dense dislocation walls (DDWs) and dislocations tangle (DTs) in original grains and in the refined cells (under further straining);
2) Transformation of DDWs and DTs into sub-boundaries with small misorientations separating individual cells or sub-grains;
3) Evolution of sub-boundaries into highly misoriented grain boundaries;
4) Formation of nanostructures in the top layer (~60 μm thick).

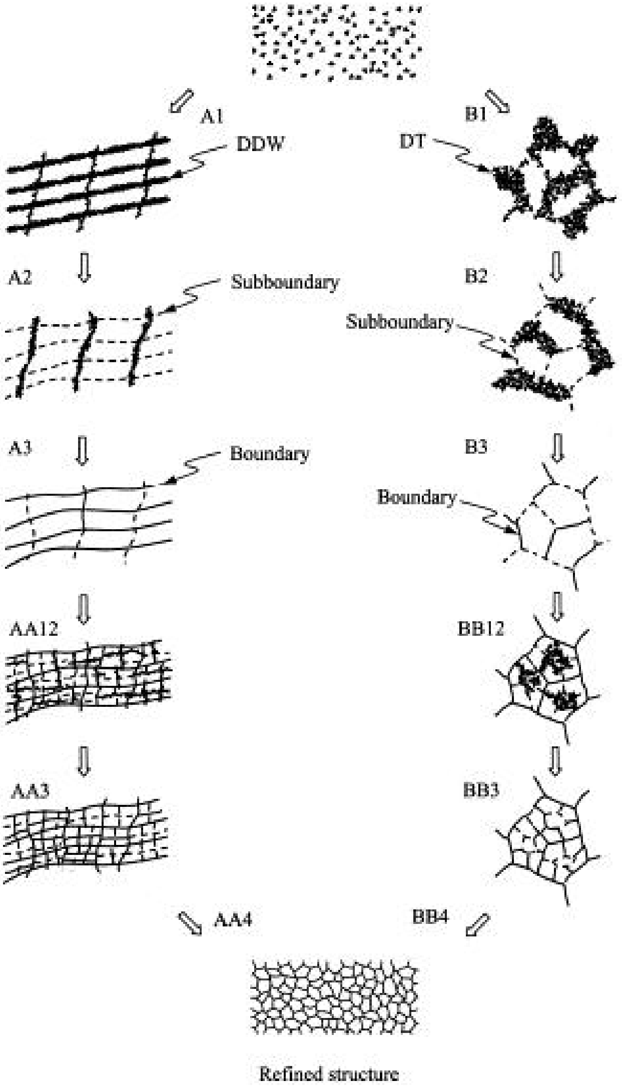

FIG. 2.13. Grain refinement mechanism of Fe [80].

For materials with low SFE, such as AISI 304 stainless steel (about 17 mJ/m^2), the grain refinement mechanism during SMAT can be summarized as follows [82] as shown in Fig. 2.14:

1) Formation of planar dislocation arrays and mechanical twins;
2) Grain subdivision by twins and martensitic transformation;
3) Formation of randomly oriented nanocrystallites.

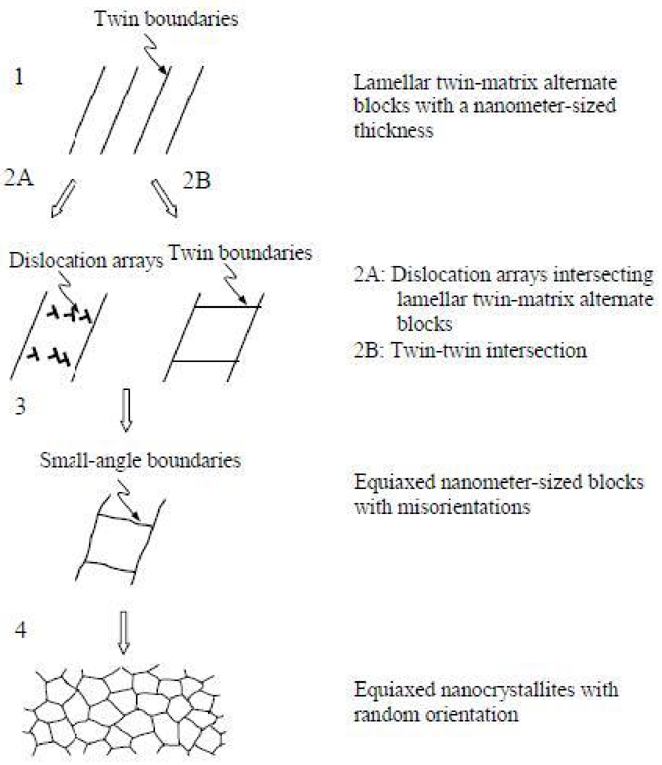

FIG. 2.14. Grain refinement mechanism during SMAT for AISI 304 stainless steel [82].

For materials with medium SFE, such as Cu (about 78 mJ/m^2), the grain refinement mechanism during SMAT can be summarized as follows [60]:

I. At the subsurface layer (thickness > 25 μm):

1) Formation of dislocation cells (DCs) in original grains;
2) Transformation of DC walls into sub-boundaries with small misorientations

separating the initial grains into individual sub-grains;

3) Evolution of sub-boundaries into highly misoriented grain boundaries.

II. At top surface layer (thickness < 25 μm):

1) Formation of high-density, nanometer-thick twins dividing the original coarse grains into T–M lamellae;
2) Development of dislocation walls that further subdivide the T–M lamellae into equiaxed nanosized blocks;
3) Evolution of these preferentially oriented blocks into randomly oriented nanosized grains;
4) Formation of nanostructures in the top layer (~35 μm thick).

It is noted that the materials were treated with stainless steel balls having 8 mm in diameter and the operating frequency of the system was 50 Hz in all the above examples. It should be noted that different operation parameters possibly result in different levels of strain-rate which may cause different mechanisms of strain-induced grain refinement. Therefore, a full understanding of the relation of operation parameters and the resulting strain-rate is necessary, which is still limited.

2.4.5.3 Parametric reviews

The SMAT technique, on the basis of the two types of SNC approaches: surface self-nanocrystallization and hybrid surface nanocrystallization, has been developed since 1999. The design of the equipment and the adoption of the operation parameters are attributed to the needs of the applications [135].

There are mainly two types of SMAT machine which are widely used. One type of the machine is operated at a rather low frequency (50 Hz) and in a vacuum;

the ball size for the process varies from a few millimetres to 10 mm. The strain-rate at the top surface is relatively low.

The other type of machine is operated under high powered ultrasound, firstly named ultrasonic shot peening (USSP); hence the reflecting chamber is vibrated under high frequency, usually 20 kHz. The balls with sizes ranging from 1 mm to a few millimetres fly at high speed in the treatment chamber at the surface of the sample. This results in a higher strain-rate at the top surface than that achieved by the first type of machine.

The parameters in the SMAT process are in need of great concern, since they greatly affect the properties of the treated samples. It is known that the materials and size of the balls, operating temperature and duration play important roles in the refinement - degree of the grains and the thickness of the nanocrystalline layer. Some studies have already shown the relation between the process duration and the microstructures of the SMATed samples [60, 78, 80]. However, systematic studies on the relation between the characteristics of balls and the microstructures of the treated materials have not been fully investigated and are worth performed.

2.4.5.4 Properties of treated materials

The mechanical and chemical properties are greatly enhanced for the SMATed materials. Some of the most important properties are addressed in the following:

Hardness [32, 54, 136]: the hardness of the top surface layer of the SMATed samples can be enhanced up to 2 – 3 times that of the coarse-grained matrix for SMATed Fe samples owing to the nano-grains formed on it [32]. The hard surface also allows the improvement of the friction and wear properties [32, 136, 137].

Tensile Strength [34, 138]: the tensile strength of the SMATed samples is also a promising property. Both yield strength and tensile strength can be enhanced 6 times that of the coarse-grained pristine form for the SMATed stainless steel sample [138] and in different degrees for other materials [34]. However, the low ductility is always the trade-off.

Fatigue [139]: with the formation of high compressive residual stress and grain refinement of the microstructure resulting from the localized plastic deformation, the SMATed surface layer is capable of resisting fatigue ignition and propagation and hence of enhancing the fatigue strength. Taking SMATed stainless steel as an example, if the right size of balls is chosen, the fatigue endurance limit can be improved by 21 % when compared with the coarse- grained counterpart.

Diffusion properties [140, 141]: as grain boundaries can act as the quick-diffusion channels, the atomic diffusivity in the nanostructured surface layer will be considerably enhanced in comparison with the conventional polycrystalline materials. This behavior can be utilized to upgrade traditional surface chemical treatment techniques, such as the nitriding process of steel, by improving the diffusion kinetics and/or reducing the diffusion temperature. SMAT has achieved great progress in this aspect [140, 141].

2.4.5.5 Pros and cons

SMAT is a rather simple and low cost technique to obtain a nanostructured surface layer on bulk materials. Besides the superior surface and mechanical properties as aforementioned, the SMAT technique provides a unique opportunity to examine the microstructure characteristics at different levels of strain and strain-rate. It is plausible that the optimum operating conditions vary with different materials.

However, a thorough and quantitative understanding of the relation between the process parameters and microstructure characteristics is still lacking.

2.5 The State of Art Tensile Properties of NS Cu (Obtained from Different Synthesis Methods)

The synthesis methods have great effect on the tensile properties of the NS materials obtained as addressed in the above sections. As the enhanced yield strength is the promising property for NS materials and together with the ductility are the main concerns in this study, a summary of the recent tensile property results of the NS Cu obtained from these state of the art synthesis methods is presented, as shown in Fig. 2.15.

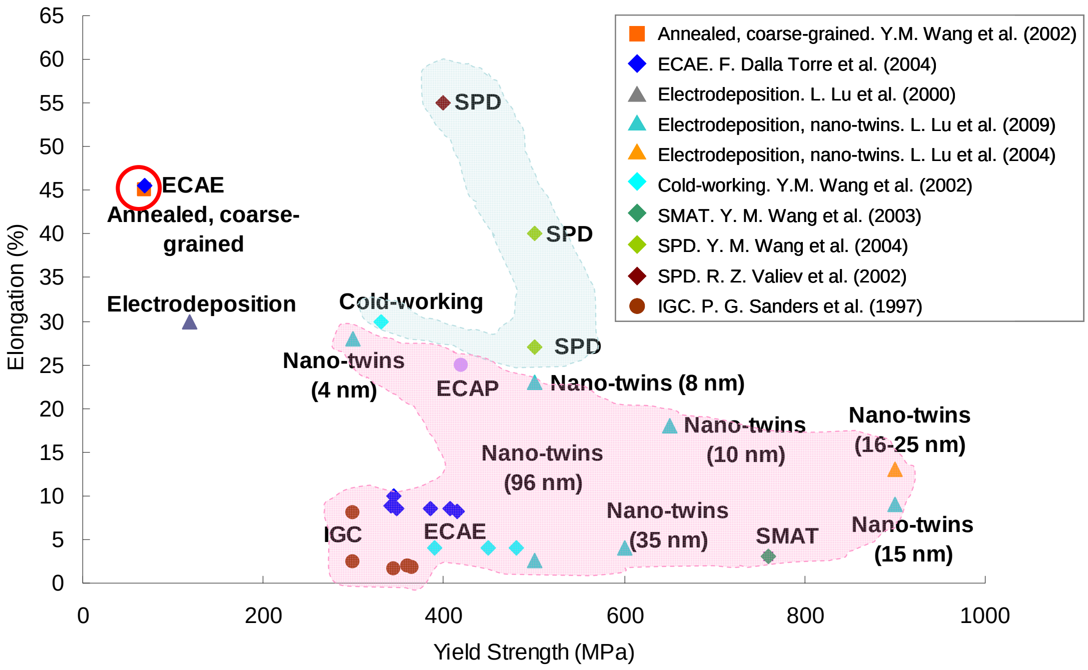

FIG. 2.15. The overview of the tensile properties of NS Cu obtained by different synthesis methods from the recent literatures [29, 33, 34, 51, 53, 65, 93, 142, 143].

It is noted that the tensile properties of the NS Cu obtained from different synthesis methods are widely distributed. Some have ultrahigh yield strength but low ductility as expected for most of the NS materials, while some have rather high ductility but lose certain amount of yield strength as trade-off. It is obvious that the tensile properties of NS Cu are strongly related to the synthesizing history of the materials experienced. However, special attention has also to be paid to the sizes of the experiment samples. The data can then be basically grouped into two categories, which denoted by pink and blue color, respectively, according to the sample sizes.

The data in the red circle is the tensile properties of coarse-grained Cu for comparison and those in pink area represent the tensile properties of Cu either with nano-grains or nano-twins which have the promising yield strength. The sample sizes for these nano-grained or nano-twinned Cu are usually small. These samples usually have the thickness of less than 0.2 mm, except for those produced by ECAP having the thickness of 1 mm. However, this ECAP-produced Cu still has the limitation on the sample diameter of less than 10 mm.

On the other hand, the NS Cu produced by SPD and cold working which have rather high ductility, denoted in the blue area, have less limitation on size. The samples can be produced in a relatively large dimension and usually have relatively high ductility. However, the NS Cu produced by these methods has the limitation on geometry which is restricted by the dies used during the fabricating process.

In general, developing a synthesis method to produce NS materials in bulk form to overcome these sizes and shape limitations is still a global challenge to the researchers and engineers.

2.6 Concluding Remarks

NS materials have drawn enormous attention of researchers owing to their outstanding mechanical properties and unique characteristics. This review summarized the centers of the attention, such as superior yield strength and hardness, Hall-Petch relation, response to plastic deformation and abnormal strain-rate sensitivity. Some of the recent discrepancies in knowledge were also pointed out. Furthermore, the widely adopted approaches in fabricating NS materials, such as dislocation induced grain boundary, high strain-rate and cryogenic temperature, twinning and SNC were discussed. The recent synthesis methods, including IGC, MA, SPD, ED and SMAT were introduced with the pros and cons addressed. Below are some of the research directions where new opportunities abound.

As the grain size decreases, the yield strength and hardness increase. This is similar to the prediction from the conventional Hall-Petch relation and MDS. However, some experimental results showed that a reverse Hall-Petch effect or materials softening happens at the critical grain size. Some researchers explained this by the distinct deformation mechanisms in the particular range of grain size, while some blamed this on the flaw or porosity resulting from the synthesis methods. The argument continues. It is worth noting that synthesis methods play significant roles not only in producing NS materials, but also in affecting how the researchers understand them.

NS materials have ultra-high strength, but low ductility. Researchers suggest that a large number of grain boundaries from the small grains inhibit the movements of dislocations and hence result in a lack of room for plasticity. Hence, approaches like annealing and bimodal structure are adopted to gain the ductility, but losing some of the strength is the drawback. Recently, a nano-twins structure is found to be able to significantly retain certain ductility and to maintain the ultra-high strength. This structure can be obtained by electrodeposition in the strictly-controlled conditions or by high strain-rate and / at cryogenic temperature. This is probably one of the favorable routes for developing bulk NS materials for industrial applications. Moreover, most of the recent studies are on the laboratory scale. It is worth extending the work to a larger scale to verify the practicality of these approaches. Therefore, developing bulk engineering materials for industrial application with desirable plasticity is still an intended objective.

Chapter 3: EXPERIMENTAL STUDY

3.1 Experimental Equipment

3.1.1 SMAT equipment

The SMAT machine that was used to produce an NS surface layer in this project is the ultrasonic type mentioned in Section 2.4.5.3. Fig. 3.1 and Fig. 3.2 show the sketch and photograph of the experimental setup, respectively. The operation frequency of this machine was 20 kHz. The power amplitude of the electronic signal was adjusted by the generator. The ultrasonic converter then transformed electrical energy to mechanical vibrations. The amplitude of the vibration was amplified by the booster and the vibration was applied to the horn, and resulted in the actuation of the balls in the reflecting chamber and hitting the sample.

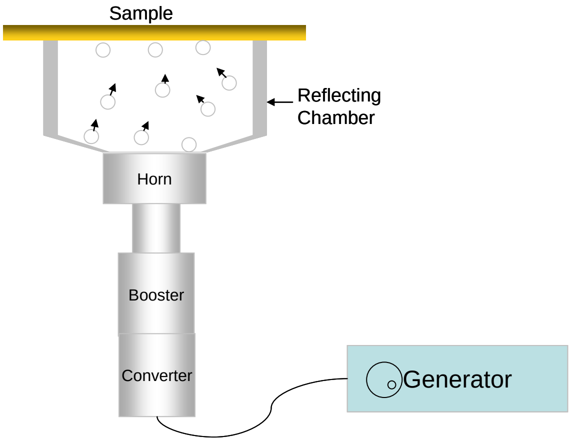

FIG. 3.1. Sketch of the experimental setup of the SMAT machine.

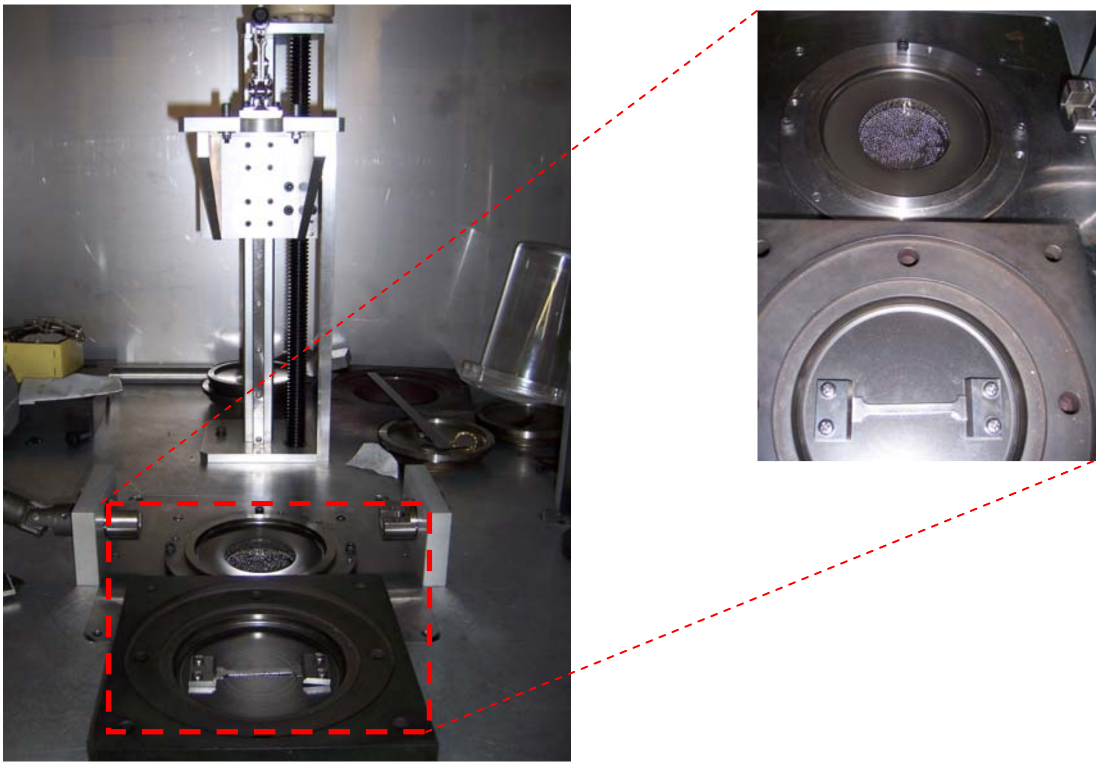

FIG. 3.2. Photograph of the experimental setup of the SMAT machine.

3.1.2 Electrodeposition (ED) equipment

The ED equipment used for this project was designed for small-mass production, as shown in Fig. 3.3. Fig. 3.3 (a) shows the electronics part of the equipment controlling the power type, the current density, the on-off time settings for the pulsed current (**pc**) and the mechanical agitation of the electrolyte. Fig. 3.3 (b) schematically illustrates the size and the arrangement of the bath for the ED process. The cathode bar allowed the substrate to be placed. There was also a filtering system inside the bath for solution recycling and conditioning. The composition of the acidic electrolyte is listed in Table 3.1.

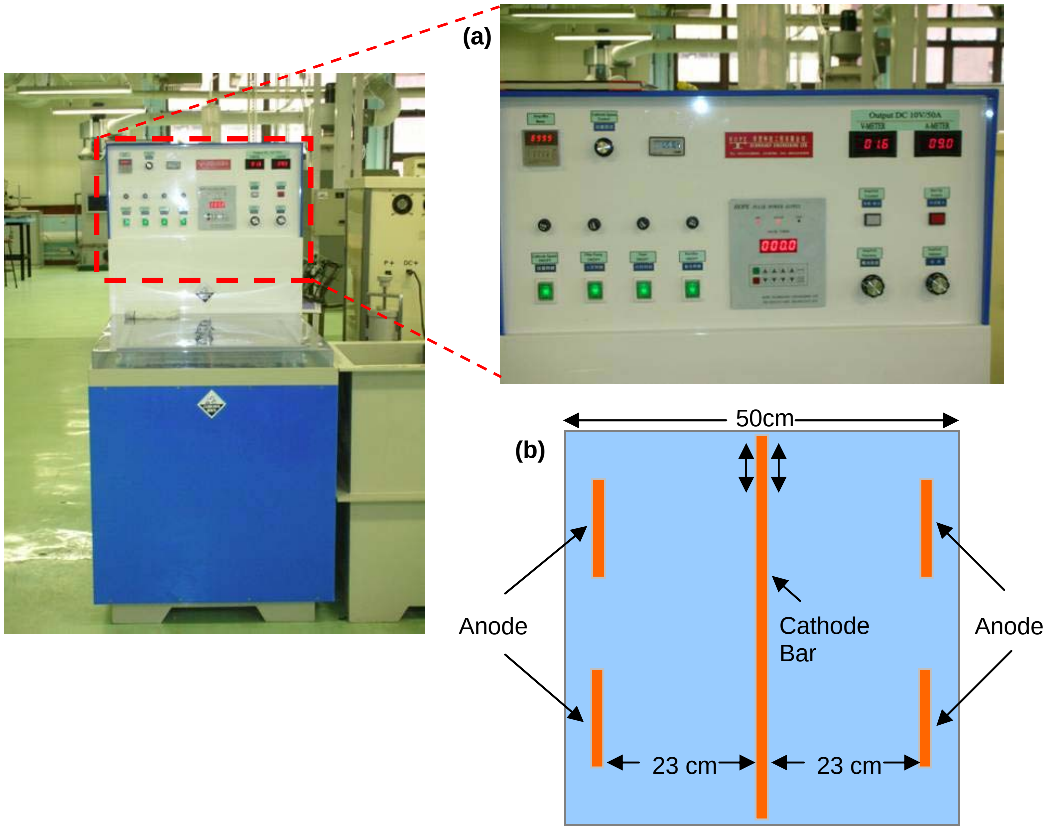

FIG. 3.3. Experimental setup of the ED equipment: (a) electronics part of the equipment; (b) size and arrangement of the bath for the ED process.

Table 3.1. The composition of the acidic copper bath.

Composition of the solution	**Volume**
$CuSO_4 \cdot 5H_2O$	100 g/L
H_2SO_4	150 g/L
HCl	25 mL

3.2 Materials

3.2.1 SMAT process study

The sample used for studying the relation between the parameters and resultant microstructures in the SMAT process was AISI stainless steel plate with 1 mm thickness. As-received extruded Copper plate with 1 mm thickness was also subjected to the SMAT process for parametric study.

3.2.2 ED process study

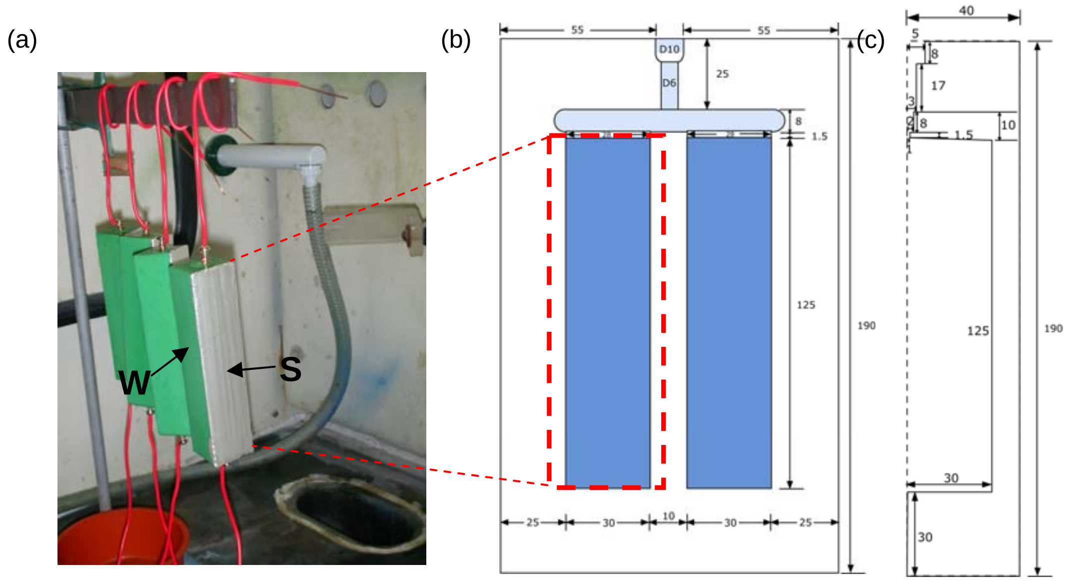

FIG. 3.4. Wax substrate for the ED process: (a) rectangular block of wax substrate with one side, denoted by S, covered by silver conducting paint. 'W' denotes the original wax; (b) top view; (c) side view of the mold tool of the wax substrate.

The materials used as the substrate of ED process was wax (No. 16181 TUFFYTM Green Injection Wax from KerrLab). It is molded in a rectangular block (30 (W) × 30 (L) × 120 (H)) mm^3), as shown in Fig. 3.4. Since wax allows the model of complicated shapes and can be easily removed afterwards, it was adopted as substrates. This method is also common in investment casting and other industrial applications.

The rectangular wax block was first milled to obtain level surfaces. Each surface was cleaned with ethanol and was sprayed with silver conducting paint. They were then ready for the ED process. Cu was the material to be electrodeposited in this project. The ED process was carried out at the ambient temperature of 24°C and in the electrolyte solution with a pH value of 1. The anodes were Cu bars with a purity of 99.99%.

After the ED process, the Cu coated wax block was de-waxed in an ultrasonic bath heated to 70°C. The free-standing electrodeposited Cu was then cut into dog-bone shapes by Electrical Discharge Machining (EDM). Eventually, they were ready for the mechanical property tests or to be further treated with SMAT.

3.3 Experimental Processes

As discussed above, there are two major processes in experiments for the current project:

1) Formation of base materials from ED

As expected, when the parameters in the ED process change, different structures are formed in the electrodeposited Cu, resulting in different mechanical properties. The key parameters of this process include the composition and conditions of the bath, the substrate, the power current type, the current density and the duration. The former three parameters were kept constant in this project. The power current type, the current density and the duration were varied in the production of electrodeposited Cu to obtain different structures. In experiments, applicable power current types had direct current (**dc**) and pulsed current (**pc**). For the latter type, the effect of the on-off time was also examined. The current density was varied from 1 to 12 A/dm^2. The deposition duration ranged from 3 to 78 hrs.

A series of experiments were carried out to study the effect of the above parameters, including materials characterization and tensile property tests. The details will be discussed in Chapter 5.

2) Formation of surface nanocrystalline layer by SMAT

The electrodeposited Cu was subjected to SMAT for surface modifications on both the strength and texture enhancement. The optimal conditions of the SMAT process and electrodeposited Cu obtained from Chapters 4 and 5 respectively were employed. The details will be discussed in Chapter 6.

3.4 Materials Characterization Techniques

The morphology and structure of the electrodeposited Cu were investigated by scanning electron microscopy (SEM), transmission electron microscopy (TEM), X-ray diffraction (XRD), electron backscattered diffraction (EBSD) and focused ion beam (FIB). The tensile properties of samples were then in-situ and ex-situ examined. For the samples subjected to SMAT, the microstructure was also explored by means of SEM, TEM, XRD and EBSD. The tensile properties of the SMATed samples were also examined. The details of the characterizations are described as follows.

3.4.1 Scanning Electron Microscopy (SEM)

The SEM uses a beam of electrons to scan the surface of a sample to build a three-dimensional image of the specimen. When the electron beam hits the sample, a variety of signals, such as secondary electrons (SE), backscattered electrons (BSE) and characteristics X-rays, are generated by the interaction of the beam electrons from the filament and the sample atoms.

- SE are the electrons emitted from the sample surface due to the irradiation of the coming electron beam. They usually take the responsibility to image the sample surface.
- BSE are the electrons that are greatly scattered by the atoms in the material and reflected back from the sample surface. Since heavy atoms can scatter more electrons than light ones, the image collecting the backscattered electrons contains the information of elements in the material.
- Characteristic X-rays are emitted by the atoms in the material because of the irradiation of high-energy electrons. The analysis of the dispersed energy of the characteristic X-rays, EDXA, can be used to identify the elements contained in the materials.

In this project, SEM was performed using JEOL Model JSM-6490 or Leica Stereoscan 440, as shown in Fig. 3.5 (a) and (b), respectively.

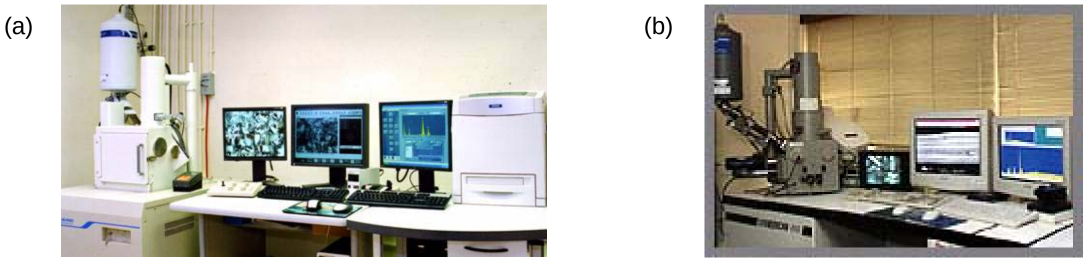

FIG. 3.5. SEM machines used in this project: (a) JEOL Model JSM-6490; (b) Leica Stereoscan 440.

3.4.2 Transmission Electron Microscopy (TEM)

TEM is analogous to optical microscopy except for the light source. TEM uses electrons instead of light. Since the resolution of microscopy is determined by the wavelength of the light source and electrons have much lower wavelength than light, TEM consequently has a much higher resolution than optical microscopy.

The electron source at the top of the microscope emits electrons that pass through the vacuum column of the microscope. The electromagnetic lens focuses the electrons into a thin beam which then passes through the sample. The unscattered electrons then form the image on the fluorescent screen with its different parts displayed in varied darkness according to the density of the materials. The bright field, dark field and diffraction pattern of the sample can be obtained to give its information on morphology and structure.

A formula describing the relation between the lattice spacing of the materials and the camera length reads:

$$Rd = L\lambda\,, \tag{3.1}$$

where R is the distance between two neighboring patterns; d the lattice spacing of the materials; L camera length; and λ the electron wavelength. In the current case, $L\lambda$ is 10.4 Å cm. This formula is widely used to interpret the electron diffraction pattern.

In this project, TEM was performed utilizing JEOL JEM 2010 with a nominal resolution of 0.14 nm and 200 kV accelerating voltage. TEM micrographs were recorded on a CCD camera using Digital Micrograph software.

3.4.3 X-ray Diffraction Spectroscopy (XRD)

XRD is a widely adopted method in materials research. It is an analytical technique for revealing the crystalline structure and materials composition. It can be applied to all kinds of materials.

XRD makes good use of the fact that an electron in an alternating electromagnetic field oscillates with the same frequency as the field. When an X-ray beam hits an atom, the electrons around the atom start to oscillate with the same frequency as the incoming beam. A few directions allow the constructive interference owing to the regular pattern of the arrangement of the atoms in a crystal. Then the well-defined x-ray beams leave the sample at various directions rendering the information of orientation and interplanar spacings of the planes in the crystal. This relation can be expressed by Bragg's Law:

$$n\lambda = 2d\sin\theta \,, \tag{3.2}$$

where n is an integer determined by the order given; λ the wavelength of the incident X-rays; d the spacing between the planes in the atomic lattice; and θ the angle between the incident ray and the scattering planes.

Information obtained by XRD can be presented in different forms, such as pole figures, and powder diffraction diffractogram etc. Pole figures render the texture information while powder diffraction diffractogram shows crystalline structure and sizes.

As the grain size decreases, the peaks of the powder diffraction diffractogram are broadened. The crystallite size can be calculated according to the Scherrer formula:

$$D = \frac{K\lambda}{w_{hkl}\cos\theta_{hkl}} \,, \tag{3.3}$$

where D is averaged grain size; K a constant that varies with the method of taking the width ($0.89<K<1$); λ the wavelength of the incident X-rays; w_{hkl} the width of the peak of a special phase (hkl); and θ the angle of the center of the peak. In this project, XRD was performed with Bruker D8 Discover as shown in Fig. 3.6.

FIG. 3.6. Photograph of XRD equipment used in this project.

3.4.4 Electron Backscattered Diffraction (EBSD)

EBSD is a technique which allows crystallographic information to be obtained from samples in the SEM. In EBSD, a tilted crystalline sample is struck by a stationary electron beam and henceforth the diffracted electrons form a pattern on a fluorescent screen. This pattern reveals the crystal structure and the orientation of the particular region of the sample. A map of the crystal orientation of the sample can then be formed rendering the information of grain morphology, orientations and boundaries. Hence, the preferred crystal orientations (texture) present in the material are shown. EBSD has the advantage of quantitatively showing the crystal orientation with the microstructures of the materials.

Sample preparation

Electrodeposited Cu obtained by **dc** and **pc** with 0.2 ms on time and 2.0 ms off time were examined by EBSD respectively. SMATed electrodeposited Cu was also examined.

Before being subjected to EBSD, the samples were cut by EDM and polished with silicon carbide paper with numbers from 800 - 4000. Then they were further polished with diamond polishing cloth of 3 to 1 μm. To reveal the microstructure, electro-chemical etching was carried out. The conditions of the etching process are listed in Table 3.2. In this project, EBSD was performed using a JEOL 6500F type field emission gun scanning electron microscope (FEG-SEM) and was carried out in France by Prof. T. Grosdidier's research team.

Table 3.2. The conditions of etching process for EBSD.

Composition of etching solution	
Nitric Acid	300 mL
Methanol	600 mL
Parameters	
Voltage	14 – 15 V
Time	3 s
Temperature	16 - 19°C

3.4.5 Focused Ion Beam (FIB)

The Focused Ion Beam (FIB) system utilizes a Ga^+ ion beam to raster over the surface of the sample as SEM does. The generated SE are collected to form images of the sample. This method is widely adopted owing to the availability of picturing the cross-sectional images of the structure and modifying the structure by means of milling small holes in the sample at well localized sites by the ion beam. Besides the cross-sectional imaging and the modification of the structure, FIB can also be applied to prepare samples for TEM. In this project, observations from FIB performed with FEI Quanta 200 3D were focused on the cross-sectional imaging of the structure of electrodeposited Cu and SMATed ones.

3.4.6 Tensile Property Test

The tensile experiments were, then, conducted under the ambient conditions with a temperature of 22°C and humidity of 45% on a MTS RT-50 (50 kN) Axial Static Testing Machine which is shown in Fig. 3.7(a). The crosshead speed was kept at a constant of 0.05 mm/s, which corresponded to the nominal strain-rate of 0.002 s^{-1}. The MTS 632 24F-50 extensometer shown in Fig. 3.7 (b) was employed to measure the displacement of the specimen during the tensile experiments.

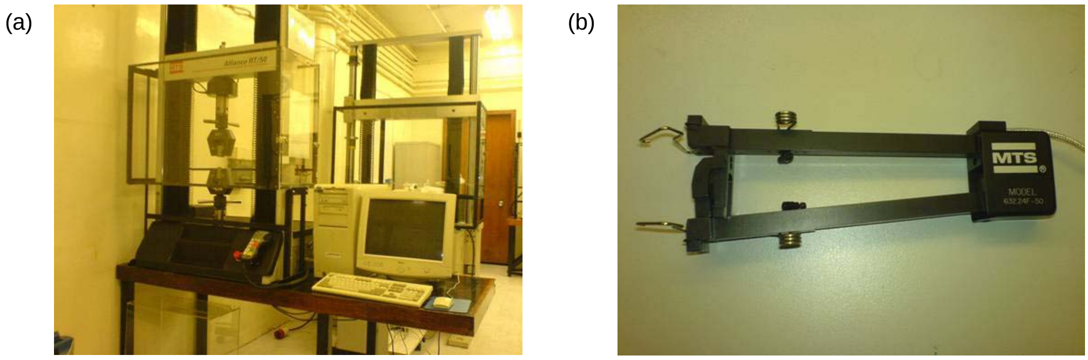

FIG. 3.7. Tensile property test equipment: (a) tensile property test machine, MTS RT-50; (b) extensometer, MTS 632 24F-50.

Sample preparation

Some of electrodeposited Cu and the SMAT samples were cut into dog-bone shapes according to the ASTM E8M-04 standard with the EDM technique. For the conventional tensile testing, the EDMed dog-bone specimens had a gauge length of 25 ± 0. 1 mm and a gauge width of 6.0 ± 0.1 mm. Samples with this size were subjected to SMAT processes. Specimens with different ED history had an average in-plane gauge dimension of 3 × 1 mm^2, and thicknesses in the range of 0.16 - 1.1 mm to study the effect of different parameters in the ED process.

3.4.7 In-situ Tensile Property Test

In order to reveal the deformation and failure mechanisms at a high magnification, *in-situ* scanning-electron-microscopy (SEM) tensile experiments were conducted. In contrast, the dog-bone specimens were EDMed from the same batch of Cu layers for the in-situ SEM tensile experiments, and had an average in-plane gauge dimension of 3 × 1 mm^2. This dimension allows the specimens to be installed into the testing frame in the Leica Stereoscan 440 SEM, as shown in Fig. 3.5(b). The thicknesses of the specimens were varied in accordance with those in the conventional tensile experiments. During the in-situ SEM tensile experiments, the deformation and failure sequences were imaged.

Chapter 4: THEORY AND MODELING OF THE SMAT PROCESS

As aforementioned, nanocrystalline (NC) materials, exhibiting superior strength over their coarse-grained counterparts [3], have attracted significant scientific interest in the past two decades. SMAT [79] was one of the recently developed processes to form nano-crystallized surface layer and refine grains in the subsurface layers, by actuating a number of spherical projectiles to impact the sample surface [4, 79]. This technology has been employed by material scientists for a number of materials, such as pure iron [128], pure titanium [129], pure copper [130], pure cobalt [131], aluminum alloy [132] and stainless steel [133], for producing NC materials. The detailed concept and the results of the quasi-static tensile tests achieved so far have been introduced in Chapter 2.

As a matter of fact, the NC materials suffer from low ductility which hinders their applications. Alternatively the nano-twinned (NT) materials, inside which the twin boundaries are spaced several or tens of nanometers, are considered another promising microstructure for contributing superior mechanical properties [51, 87]. In particular, recent experimental results on NT copper seem to suggest that denser twins could render higher strength as well as higher ductility [51, 87]. Recently, a promising amount of NT was obtained in AISI 304 stainless steel via SMAT. It has been well documented in the literatures that the twinning dominant plastic deformation could be achieved under the conditions of sufficient high strain-rate [58]. Multiplication of grain boundaries due to aggregation of dislocations or twins could also be enhanced by elevated strain-rate [144]. Strain-rate thereby is a very significant factor in the deformation induced nano-crystallization process.

The early work on SMAT highlighted the importance of strain-rate [4, 80]. As a matter of fact, the original attempts of SMAT were the study of the microstructure evolution in a particular treated material after it was dynamically and plastically deformed in SMAT process [31, 83]. It was noted that since the sample taken out from different depths experienced different intensity of strain and strain-rate, it could be possible to correlate the microstructures to the straining history of the material. However, in the subsequent papers, detailed measurement of ball impinging velocity and the resulted strain-rate were not presented. Consequently the relation between plastic strain history and the observed microstructures was not established. This large discrepancy between the knowledge of dynamic elastoplastic response of material subjected to SMAT and knowledge of post-SMAT microstructures and mechanical properties triggered our attempt in this work to look further into the detailed process of SMAT.

In the present work, the focus is dedicated to the process of the treatment of 1 mm thick AISI 304 stainless steel sheet. A bearing steel ball of 3 mm diameter was used, as adopted by Tao [31, 81, 82], Liu [78], Guo [76, 77] and Roland [28]. In order to observe the motion of the balls, a high-speed camera was adopted, which is capable of taking pictures at the rate of over 10000 frames per second. The behavior of a ball is firstly observed. The strain-rate henceforth can be estimated and the plastic strain/strain-rate distribution is simulated. The SMAT process with different numbers of balls is explored to manifest that an optimum number of balls exists for the highest efficiency. The corresponding final tensile properties of the treated AISI 304 stainless steel sample are presented. The treated sample was also characterized by the TEM observation to reveal its post-treatment submicron-sized structure.

4.1 Experiment

4.1.1 Setup

The ultrasonic SMAT setup was firstly introduced by Lu et al. [135] and built recently in our SMAT lab in the Hong Kong Polytechnic University, which has been introduced previously. A 20 kHz ultrasonic transducer was exploited as the impulse source to excite a number of hard steel or ceramic balls (typically 100 ~ 400 balls) to impact the sample surface. The SMAT process is essentially the dynamic plastic deformation process in which the projectiles must be perfect spheres to avoid any significant stress concentrations. Fig. 4.1 sketches the process and setup. The similar setup has been used in many articles (e.g. [28, 31, 76-79, 81, 82]).

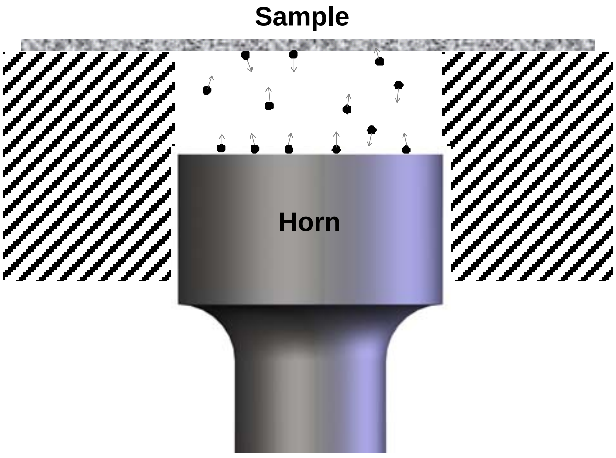

FIG. 4.1. Sketch of the ultrasonic SMAT system.

Fig. 4.2 schematically describes the experiment setup of the present work. The velocity of the ultrasonic horn surface was measured by the non-contact laser Doppler Vibrometer (Polytec OFV3001 Vibrometer Controller, Polytec OFV512 Fiber Interferometer). Fig. 4.3 shows the relation between the frequency and velocity of different positions of a 70 mm-diameter horn surface, in which the maximum vibration velocities are all about ~20 mm/s at the frequency of 20 kHz. This high frequency vibration source renders the extra high sound pressure close to the horn surface, which will be the main driving force to jet the balls to a desired velocity.

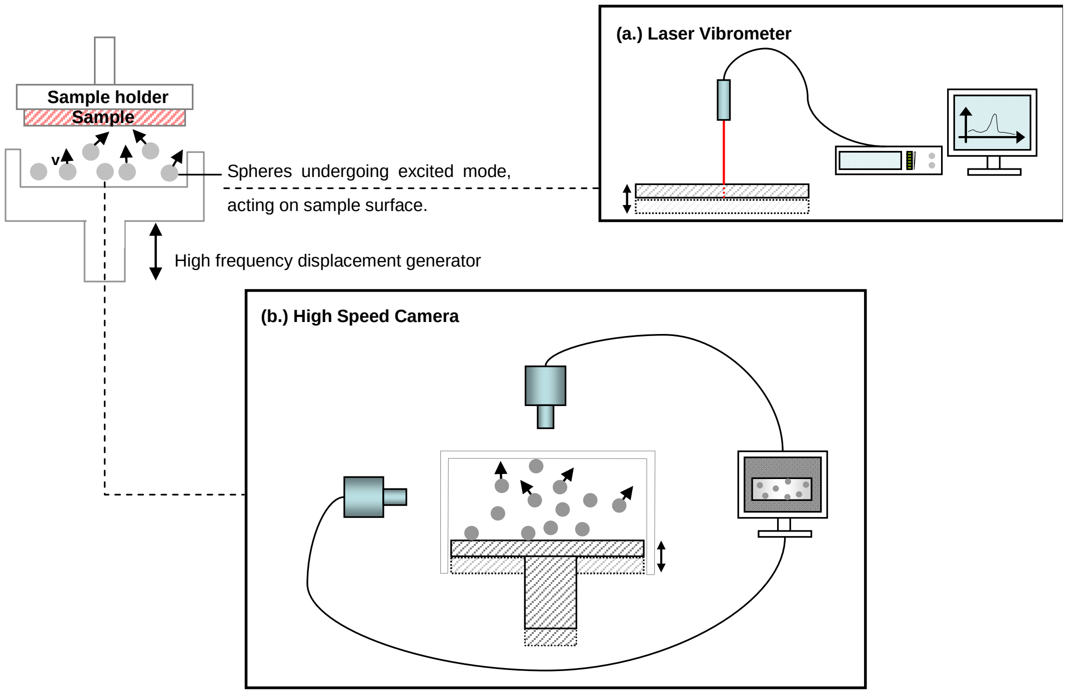

FIG. 4.2. Experiment setup of this work: (a) laser vibrometer; (b) high speed camera.

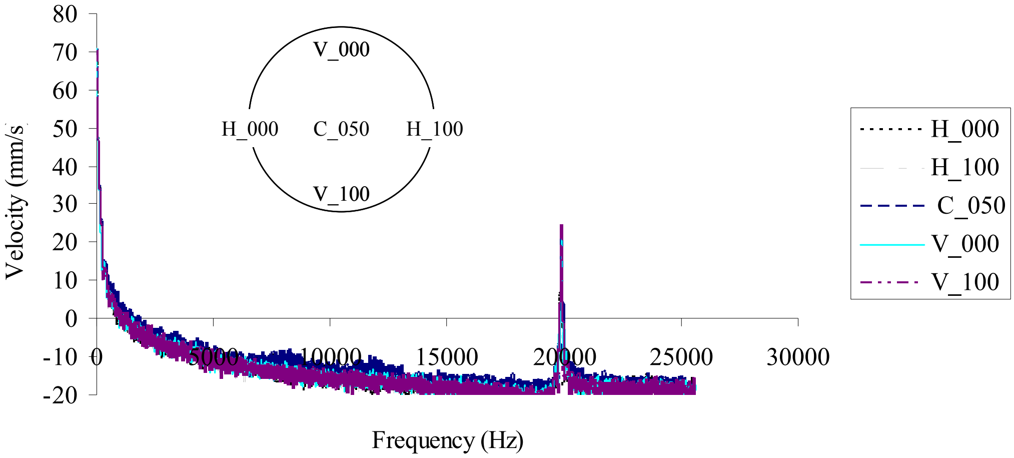

FIG. 4.3. The velocity profile of different positions of the horn surface at the system frequency: 20 kHz.

The velocities of the balls were measured by taking high-speed photographs. The high-speed camera (Phantom VR706) is capable of taking pictures at rates as high as 15000 frames per second (fps) with reduced frame size. The rate of 8000 fps was employed to capture the motion of the balls and the impact velocity was then measured by counting the number of frames a ball took to travel from bottom (transducer surface) to the top (sample surface). The treatment was performed on the 1 mm 304 Stainless Steel sheet by using the 3 mm bearing steel ball. The kinematics of a single ball and multiple balls (50 ~ 400) are all discussed.

4.1.2 The kinematics of balls

The velocity of the balls in the SMAT process is significant in determining the strain-rate and localized straining of the material, which plays a crucial role in the plastic strain-induced grain refinement processes [60]. However, the velocity was not actually measured in the SMAT-related papers except leaving behind an estimated value. In the following subsections, a single ball's motion is first reported followed by the study of multiple balls; the data will then be used in calculating the strain-rate in the later section.

4.1.2.1 The motion of one ball

In the treatment chamber, if a 3 mm bearing steel ball was placed on the ultrasonic horn as sketched in Fig. 4.4(a), it is noted that the ball was not excited after the ultrasonic power was turned on. Alternatively, the ball was floating on the surface of the ultrasonic horn as shown in Fig. 4.4(b). In such a state, the gravity of the ball was balanced by the ultrahigh sound pressure underneath.

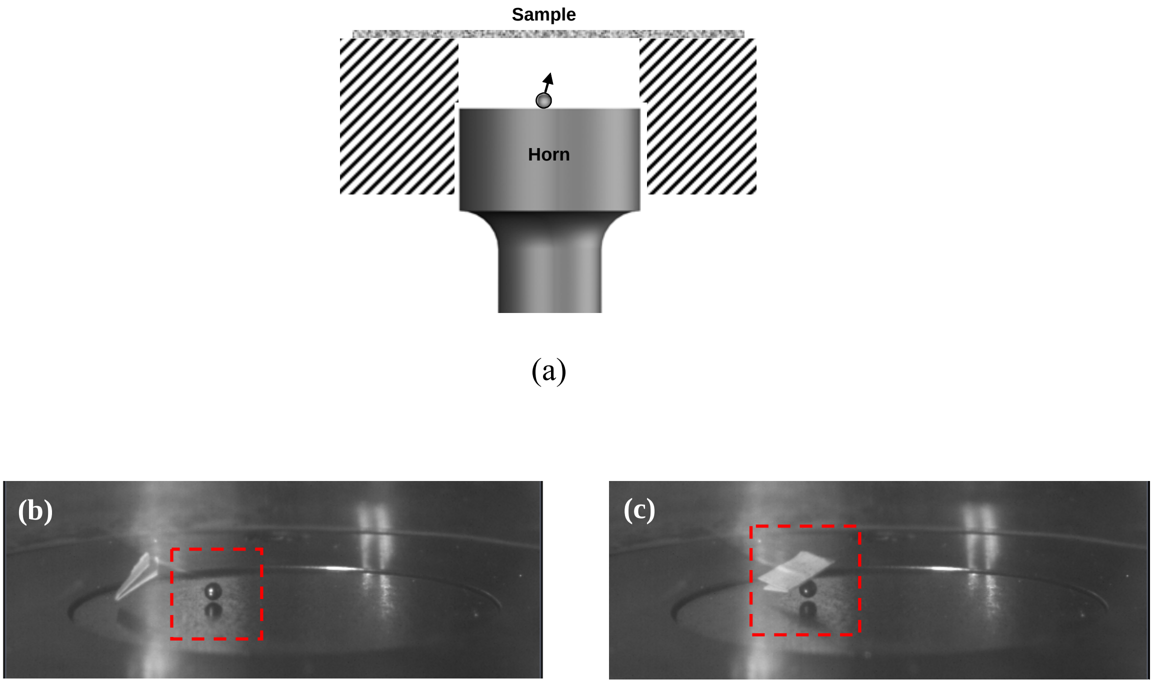

(a)

FIG. 4.4. The motion of a single ball. (a) the sketch of the a ball in an ultrasonic SMAT chamber; (b) The floating of a ball in the stationary state; (c) The drops of the piece of paper initiate the jumping motion of the ball.

The motion of the ball was finally triggered by a small piece of paper close to the ball. Through the high-speed video, one can observe the upward swim of the paper due to the high sound pressure level and large windward area. The flying attitude of the paper finally lost and the paper tilted and dropped onto the ball accidentally. This moment is displayed in Fig. 4.4(c). It is interesting to note that such a small disturbance was then able to make the ball jump from the stationary state. It is believed that this small disturbance broke the equilibrium state of the sound pressure between the horn surface and the ball and consequently, the ball was moved by this unbalanced force. The triggered ball then dropped from a certain height due to gravity and was moved to a higher position. After several bounces inside the chamber, the ball can attain a velocity as high as 10 m/s.

The velocity of the ball was measured from the consecutive pictures of a ball flying to the sample surface in a given height (15 mm) recorded by the high speed camera at 8000 fps. Fig. 4.5 shows the consecutive frames of a 3 mm bearing steel ball hitting the surface of hardened steel (60 HRC) at its maximum velocity. Nine frames passed as the ball moved from bottom to top, which indicate the ball took 1 ms (which is obtained by $\frac{8}{8000}$ (frames/fps)) to move 12 mm. (The traveling distance is the height of the chamber (15 mm) minus the diameter of the ball (3 mm).) The average velocity is then evaluated as ~12 m/s. This value is higher than the maximum velocity in the subsequent case of a 304 stainless steel sample, since the hardened steel absorbs less kinetic energy.

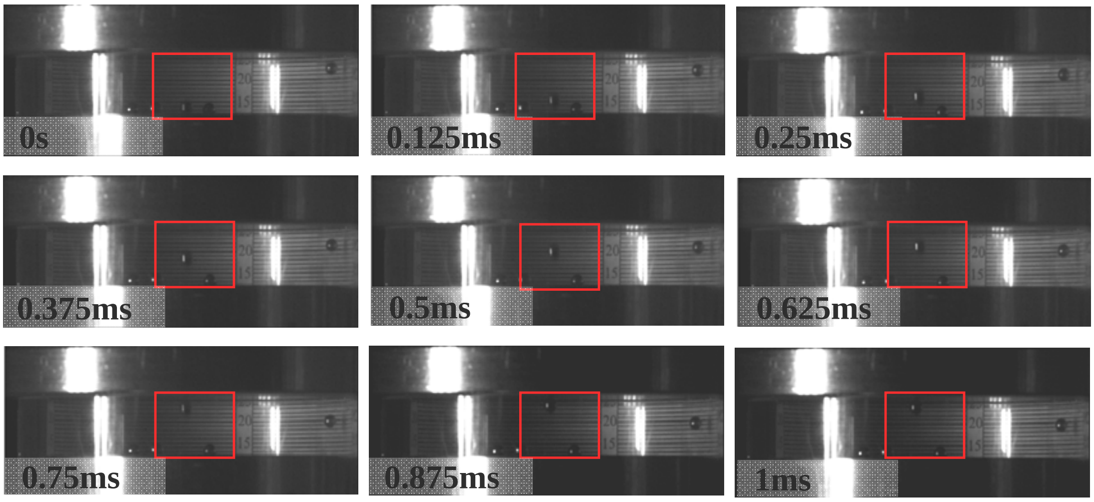

FIG. 4.5. The consecutive frames of the 3 mm stainless steel ball hitting the hard steel surface at its maximum velocity: 12 m/s in 1 ms, taken by high speed camera at the recording frame rate: 8000 frames/s.

Fig. 4.6(a) illustrates the velocity distribution of a single ball in multiple impacts, in which the as-received 304 stainless steel was used as the top surface. 20 successive impacts were observed and the corresponding velocities are shown in Fig. 4.6(a). It is noted that the impact velocities were rather random with a ceiling of 10 m/s. In the 20 impacts, the ball attained this velocity 5 times. On the other hand, the rebounding velocities were always low indicating that a very large proportion of energy was absorbed by the sample surface.

It is important to keep an eye on the ceiling velocity a ball can attain. As mentioned before, the higher velocity results in higher strain-rate and consequently enhances the formation of nanostructures. A number of researchers have shown the responsibility of high strain-rate for the increment of saturated dislocation/twins densities, which are the main contributor to the strength enhancement [25, 144-146]. The high velocity, which accounts for the high strain-rate and the subsequent microstructure, is thus of great concern.

Every time the ball returned to the horn surface, it received extra kinetic energy from the near field sound pressure, as well as the collision between ball and horn surface, and it rebounded at a higher velocity. The difference of the incident and rebound kinetic energy is the energy obtained (EO) by the ball from the transducer surface. Consecutively, while the ball hit the sample, a portion of kinetic energy was lost (EL) due to the elastoplastic deformation of the sample.

Fig. 4.6(b) illustrates the corresponding energy distribution in the 20 impacts. It shows that all the corresponding EO and EL points are very close to each other, which reveals that the ball delivers almost all the obtained ultrasonic energy to the sample. The little remaining energy and the existence of gravity return the ball to the horn surface at a rather low speed.

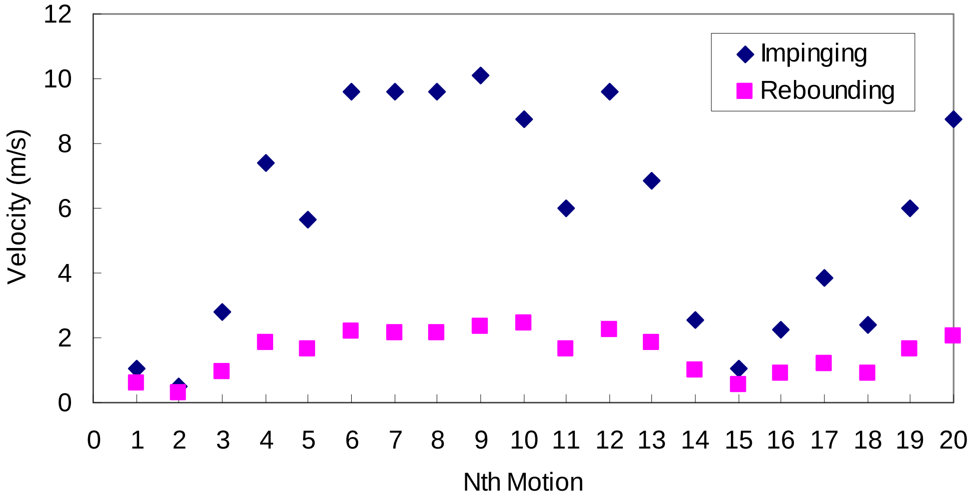

(a)

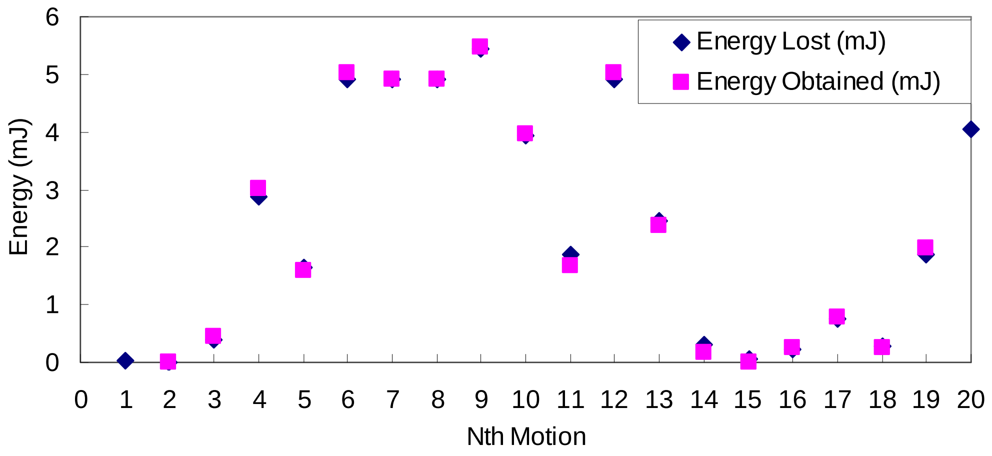

(b)

FIG. 4.6. (a) Velocity distribution of the 3 mm bearing steel ball hitting the AISI 304 stainless steel plate; (b) corresponding profile of energy lost (EL) to the sample and obtained (EO) from the horn by the 3 mm bearing steel ball.

Fig. 4.7(a) plots EO and EL against their incident velocity. It demonstrates that the kinetic energy obtained from the horn is quite random in every collision and has no relation to the velocity of the dropping ball. A plausible reason is that the extra high sound pressure near the horn surface fluctuating at the frequency of 20 kHz provides different amounts of energy to the ball according to its particular state at that moment. In sharp contrast, there is a strong correlation between the kinetic energy absorbed by the sample surface and the impact velocity. The ball with high impinging velocity is able to transfer larger amounts of energy to the sample. Conforming to this relation, the energy dissipated by the top sample surface is linearly related to the impact energy as shown in Fig. 4.7(b). The dissipation ratio, which is the ratio between energy lost to the sample surface and incident kinetic energy, i.e. the slope in Fig. 4.7(b), is about 0.95.

Fig. 4.7(c) illustrates the EL/EO ratio of the corresponding impact. It shows that all the impacts transferred over 90% EO from the transducer surface to the sample surface. It implies that the variation of the source energy would proportionally affect the energy absorbed by the sample. The extreme high ratios of EL/EO were noted when the velocity is very low, which occasionally happened when the EO is small while the dissipation energy remains high. This extra dissipation can be explained by the effect of sound pressure discussed above; however, its effect on the sample surface is rather small.

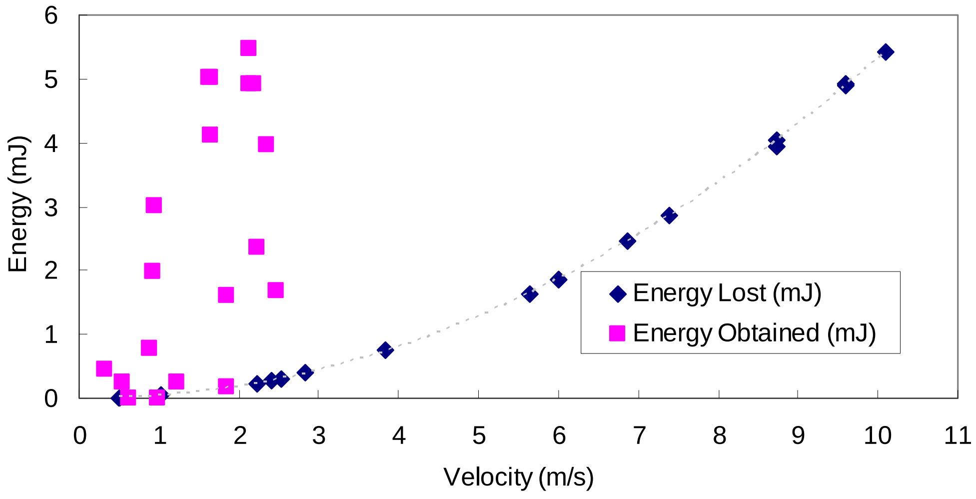

(a)

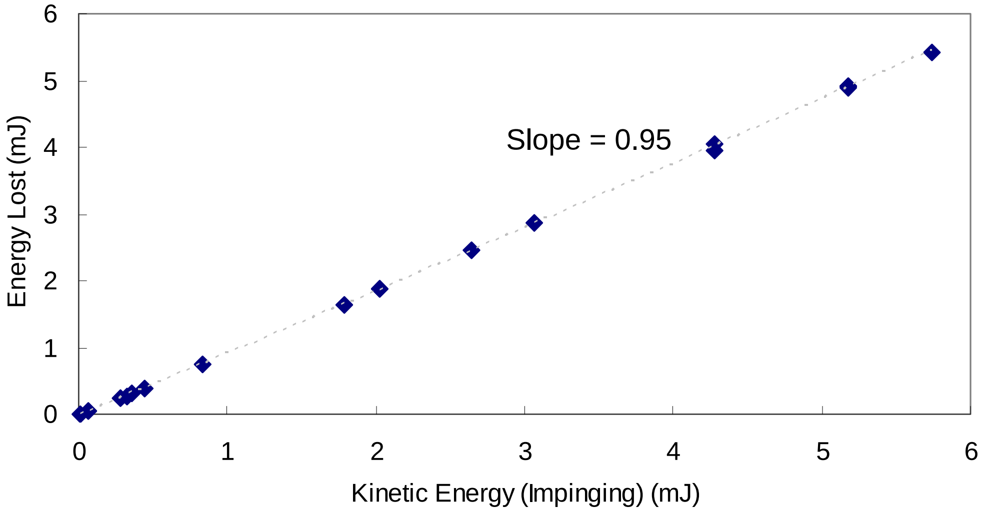

(b)

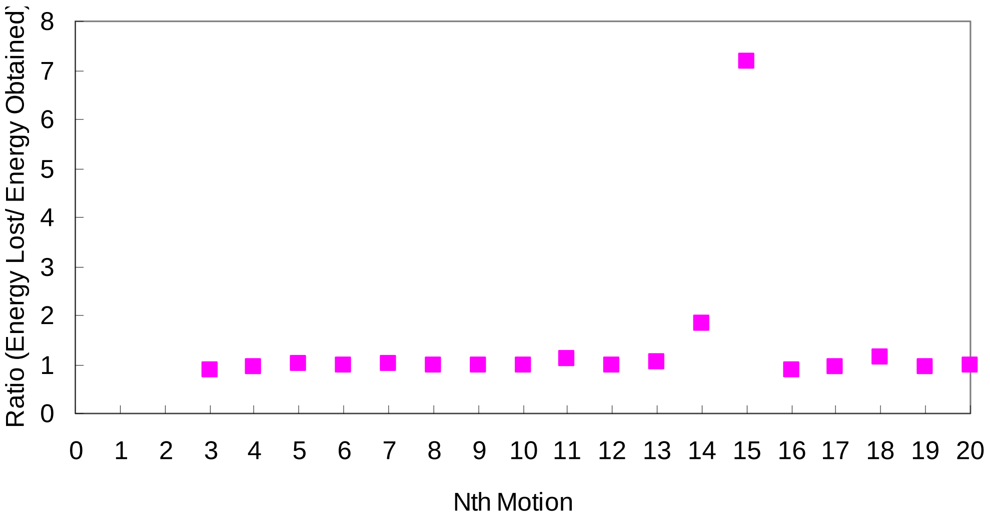

(c)

FIG. 4.7. (a) Energy obtained (EO) from the surface of the horn and lost (EL) when hitting the sample by a 3 mm bearing steel ball against their velocity; (b) linear relationship of the energy dissipation by the sample surface and the impinging kinetic energy of the ball; (c) dissipation ratio of Energy Lost (EL) to the treated surface to the Energy Obtained (EO) from the horn surface is always more than 90%, except in the exceptional low energy cases like the 13th and 14th motion.

There are other parameters that may affect the ball velocity in SMAT treatment, such as the mass (in terms of size) and materials of the ball, the power of the ultrasonic generator, as well as the mechanical properties (mainly hardness) of the sample. The effect of the above factors is summarized in Table 4.1. A general trend can be concluded.

i). Lighter balls can attain higher ceiling impact velocity; however, the amount of energy transmitted by a light ball is comparatively less than a ball with larger mass. If the ball is too large (i.e. 4 mm), the maximum velocity drops and the impact energy reduces severely. A 3 mm ball seems to be the optimum choice in terms of the energy transmission efficiency as well as the level of strain-rate.

ii). A ceramic ball (ZrO_2) has a smaller density than the steel ball does. It can attain higher velocity, and its sufficient weight enables it to have higher impinging energy carried to the sample surface. Therefore, it could be more efficient.

iii). There is a linear relationship between the power amplitude of the ultrasonic generator system and the maximum velocity that a ball can attain, as shown in Fig. 4.8. The higher the power, the higher the velocity of a ball. This is a fascinating feature of ultrasonic SMAT as the velocity of the ball can then be well controlled in the SMAT process.

Table 4.1. The effect of the parameters on ball velocity (Treated materials: AISI 304 stainless steel, Power amplitude: 80%).

Parameters	Maximum Velocity (m/s)	Maximum Kinetic Energy (mJ)
- Bearing Steel (2 mm dia)	12	2.41
- Bearing Steel (3 mm dia)	10	5.62
- Bearing Steel (4 mm dia)	4	2.10
- Ceramic (ZrO_2) (3 mm dia)	11.5	6.73

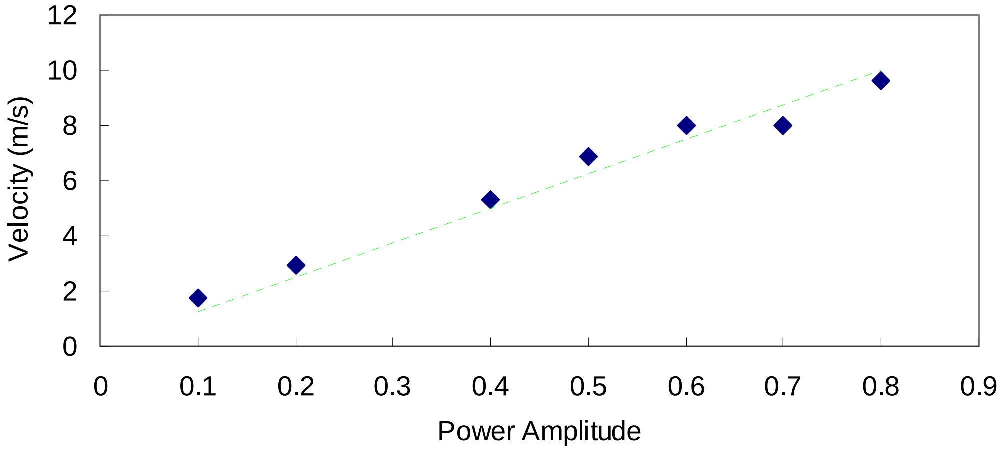

FIG. 4.8. The relationship of the power amplitude of the SMAT system and the maximum velocity attained by a 3 mm bearing steel ball.

Compared with the other parameters, the effect of the material properties of the sample is comparatively small. The difference of the ceiling velocity a ball can attain with different sample materials is around ~1 – 2 m/s. Softer materials, such as copper, allow the ball to penetrate deeper and dissipate more energy. Henceforth the ceiling impinging velocity is comparatively lower (~9 m/s). For harder materials, such as AISI 304 stainless steel plate and hardened steel, the ceiling velocity could be ~10 – 12 m/s.

In the real SMAT process, it is unrealistic to treat the sample using a single ball, since the efficiency will be too low. The behavior of different numbers of balls was then recorded by the high-speed camera, and reported in the following sections.

4.1.2.2 The motion of multiple balls

The impinging velocity of a ball can be affected by the number of balls in the limited space of the chamber in the real treatment. Due to the ball-ball collision, the maximum vertical velocity of a ball could be lower than that of the single ball case. In the following sections, the cases of 50, 100, 200 and 400 balls are studied. Attention is paid to the corresponding maximum vertical velocity that most of the balls can reach. To distinguish this velocity from the ceiling velocity of a single ball, we call it the nominal velocity of the multiple balls.

The velocities of balls were also measured in the same way as the single ball case. However, due to the limited depth of view, it is not possible to count all the balls in a video frame. Therefore, the nominal velocity of multiple balls is estimated based on the observable balls. For the purpose of demonstration in this work, we take high-speed photos from an angle to the top surface. The photos were taken at the frame rate of 1000 fps such that the trace of the balls can be visualized. As shown in

Figs. 4.9(a - d), which are respectively for the cases of 50, 100, 200 and 400 balls, the different lengths of white lines represent the different velocities that the balls traveled in 0.001 s. The longer is the white line, the higher is the velocity.

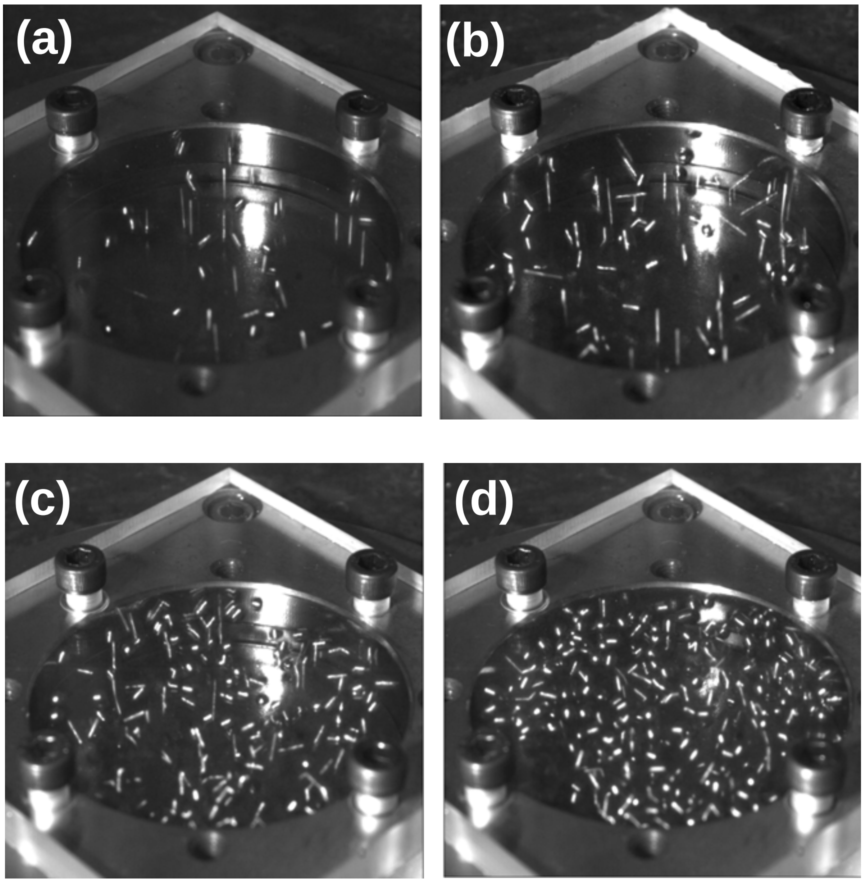

FIG. 4.9. The motion of (a) 50, (b) 100, (c) 200 and (d) 400 balls captured by high speed camera at the frame rate 1000 frame/s.

For the case of 50 balls, ball-ball collision seldom occurs. Almost all the balls behave similarly to a single ball with the nominal velocity of 10 m/s, which is shown in Fig. 4.9(a). Assuming all the balls fly at the ceiling velocity, the approximate total energy transferred by all the balls to the sample surface is about ~260 mJ.

In the case of 100 balls, fewer balls can attain the velocity of ~10 m/s than the 50-ball case. On the other hand, we observed that almost all the balls could attain a velocity as high as ~7 m/s, which is shown in Fig. 4.9(b). The nominal velocity attained by the balls in this case is not as high as the previous one, but the total amount of energy carried by the balls to the sample surface is higher. The cause of lower nominal velocity is attributed to the fact that the possibility of collision among balls is higher than in the 50-ball case and the energy lost in the horizontal motion is increased. Assuming all the balls fly at the nominal vertical velocity of ~7 m/s, the total energy transferred by all the balls to the sample surface for one shot is approximately ~275 mJ.

In the case of 200 balls, there are very few balls that can fly at the velocity of ~7 - 10 m/s, which is shown in Fig. 4.9(c). Despite a few rare balls with extremely high velocity (~7 - 10 m/s), the actual nominal velocity for this case by tracing the balls' motion in a large number of video frames, is around ~3 m/s. Most of the balls collide with each other with the consequence of energy dissipation and horizontal motion. The vertical velocity hence largely decreases. Assuming all the balls fly at the nominal velocity (~3 m/s), the total energy transferred by all the balls to the sample surface for one shot is around ~100 mJ.

In the case of 400 balls, it is quite similar to that of the 200-ball case in terms of nominal velocity, as shown in Fig. 4.9(d). The nominal velocity attained is also about ~3 m/s, while some extremes can achieve a higher value (~7 – 10 m/s). However, due to the larger number of balls, the total energy absorbed by the sample surface in a unit period of time is accordingly more. The same as for the 200-ball case, the cause of such low nominal velocity is ball-ball collision. Assuming all the balls fly at the nominal velocity (~3 m/s), the total energy transferred by all the balls to the sample surface for one shot is roughly ~200 mJ.

Smaller numbers of balls result in higher nominal velocity in the treatment process. This is due to fewer collisions between the balls. However, it seemed that the nominal impact velocity reduces to a steady value as the amount of balls increases. On the other hand, as the number of balls increases, the total energy transferred by the balls and henceforth absorbed by the sample surface increases for a constant nominal velocity. These two contradictory factors indicate the existence of an optimum number of balls in terms of the efficiency in transmitting energy from ultrasonic transducer to the sample. For the present case, using 3 mm bearing steel balls to treat AISI 304 stainless steel plate, the optimum number of balls should be close to 100, as the overall kinetic energy of the 100-ball case, evaluated from the product of the ball number and each ball's kinetic energy at the nominal velocity, is the maximum in the four cases.

The plastic deformation of the treated sample - AISI 304 stainless steel - is proportional to the energy transmitted by the balls. Therefore, with the same treatment time, different numbers of balls will certainly affect the mechanical properties of the treated sample as well as the resulting microstructures, which is demonstrated in the next section.

4.2 Mechanical Properties and Microscopic Characterization

AISI 304 stainless steel sheets of 1 mm thickness were subjected to SMAT with different amounts (50, 100, 200 and 400 pc) of bearing steel balls of diameter 3 mm for the same duration respectively. Each surface of the samples was treated for 10 minutes. After that, they were cut into dog-bone samples by Electrical Discharge Machining (EDM) for the tensile property test (carried out by MTS RT-50 (50 kN) tensile testing machine). Samples treated with 100 and 400 balls, respectively, were grinded and ion-thinned for TEM observations.

4.2.1 The mechanical properties

The tensile property test was most often adopted to examine the efficiency of the SMAT in the sense of enhancement of yielding strength. Fig. 4.10(a) shows our tensile results of the double-side treated samples. Apparently, the treatment efficiency (eff) in terms of yield or ultimate strength, can be sorted in the sequence as $\text{eff}_{100} > \text{eff}_{50} > \text{eff}_{400} > \text{eff}_{200}$, where the subscripts pertain to the number of the balls in the treatment. This sequence is identical to the sequence of total kinetic energy in one shot sorted from maximum to minimum for the cases of different numbers of balls, as shown in Fig. 4.10(b).

Ductility, on the other hand, is generally inversely related to the yield strength, except that the sample treated with 50 balls has the lowest ductility. The ball velocity seems to be more relevant. Highest velocity (~10 m/s) treatment (50-ball case) results in lowest ductility. For the relatively low velocity (~3 m/s) treatment (200-ball and 400-ball case), the ductility of the treated samples is comparatively higher. This result may on the other hand be attributed to the small quantity of balls in the 50-ball case. As a result, the treatment intensity may be unevenly distributed on the sample surface. Therefore, necking could be triggered more easily with the consequence of lowest ductility.

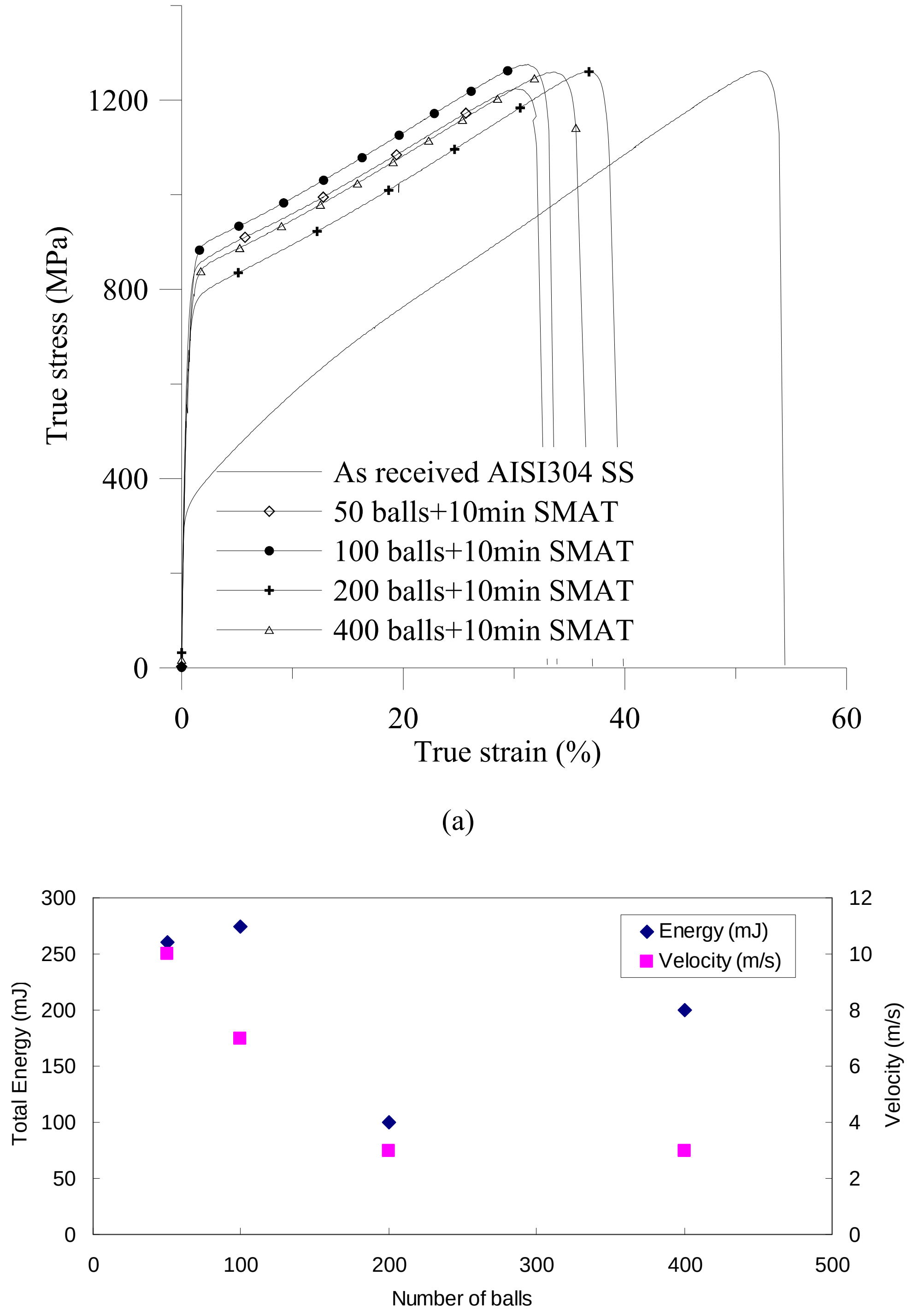

(a)

(b)

FIG. 4.10. (a) The true stress-strain curve of the as received 304 stainless steel and those after SMAT treatment by 50, 100, 200 and 400 balls for 10 minutes; (b) The relationship of the maximum velocity attained and the total energy absorbed by the sample surface in the cases with different numbers of balls.

The treatment efficiency, intuitively speaking, can be increased by increasing the impact velocity and the number of balls. However, these two are contradictive parameters. For our recent case, treatment with 100 balls is apparently the optimum choice. It renders the highest tensile strength (~850 MPa yield strength and ~950 MPa ultimate tensile strength) and desirable ductility (~40%) after the same treatment duration.

4.2.2 The microstructures of the treated steel

Transmission Electron Microscopy (JEOL JEM 2010) was adopted to reveal the microstructures of the treated samples. The plane-view TEM foils of the layers from different depths were obtained first by mechanical polishing until the sample reaches about 30 μm thickness and then ion-thinned at low temperature. Figs. 4.11 (a-j) show the microstructures of the surface and subsurface (depth ≈ 50, 200 and 400 μm) layers of the 100-ball treated sample. Herein, the surface layer refers to the layer very close to the surface, whose depth is within 10 μm. At this layer, the grains were intensively refined to the nanoscale and the size was tens of nanometers, as shown in Figs. 4.11 (a, b), while at the subsurface layer of depth around ~50 μm, nano-twins with minimum spacings less than 10 nm were found everywhere under the microscope, as shown in Fig. 4.11 (c, d). Nano-grains were also found in this layer, which are bounded by the twin lamellas. At the deeper subsurface layer of ~200 μm, larger sizes of the two features found in the above layers were discovered. Figs. 4.11 (e, f) show the dominant one; nano-grains with the average size of a few tens of nanometers were found. Twins microstructure was another main feature at this depth; however, broadened spacing of around hundreds of nanometers was discovered, which is shown in Figs. 4.11 (g, h). At the center-layer of the matrix

(~400 μm), the grain size was further increased to around ~1 μm, and dislocation cell walls and a large number of laminae were found, as shown in Figs. 4.11 (i, j). It is worth noting that nano-twins and nano-grains coexist along the sample up to ~200 μm subsurface layer. For comparison, the TEM foil from the surface of the 400-ball treated sample was prepared. Dense nano-twins were found, as shown in Figs. 4.12 (a, b).

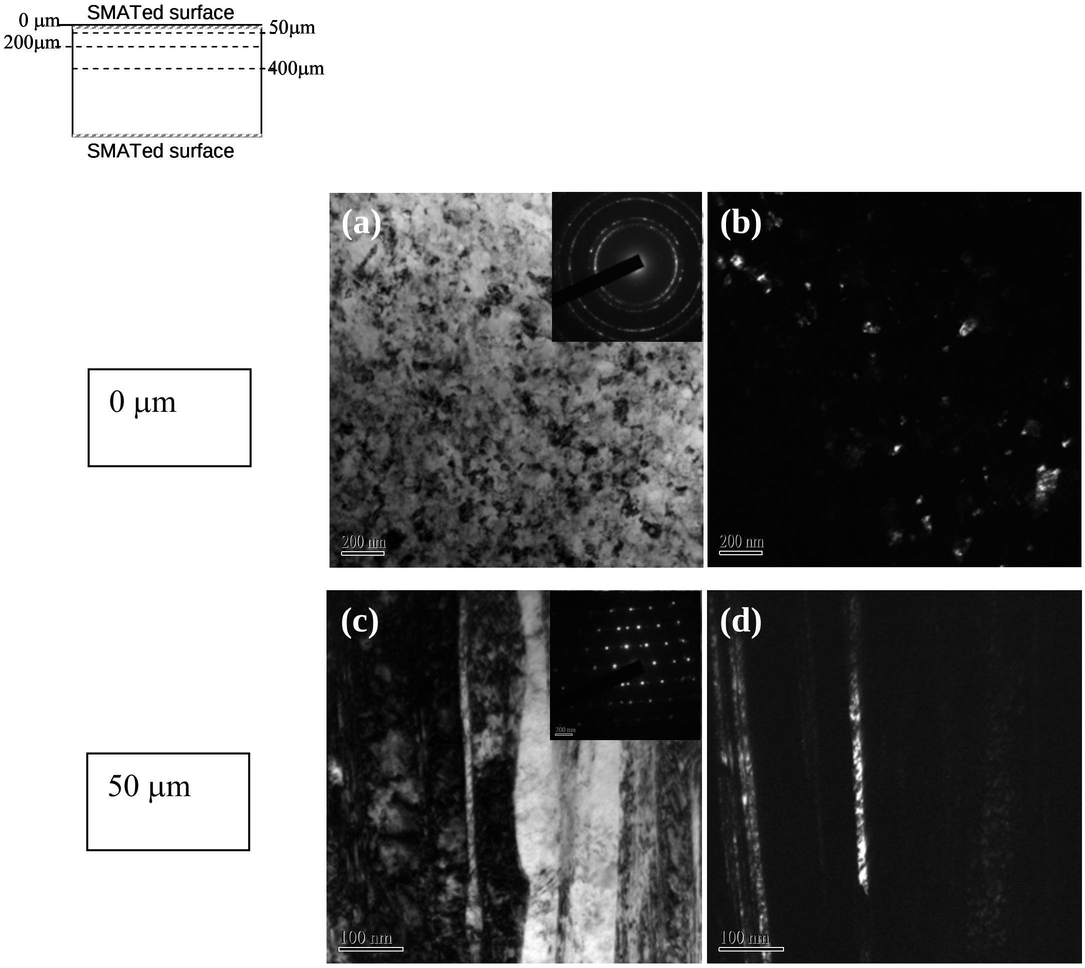

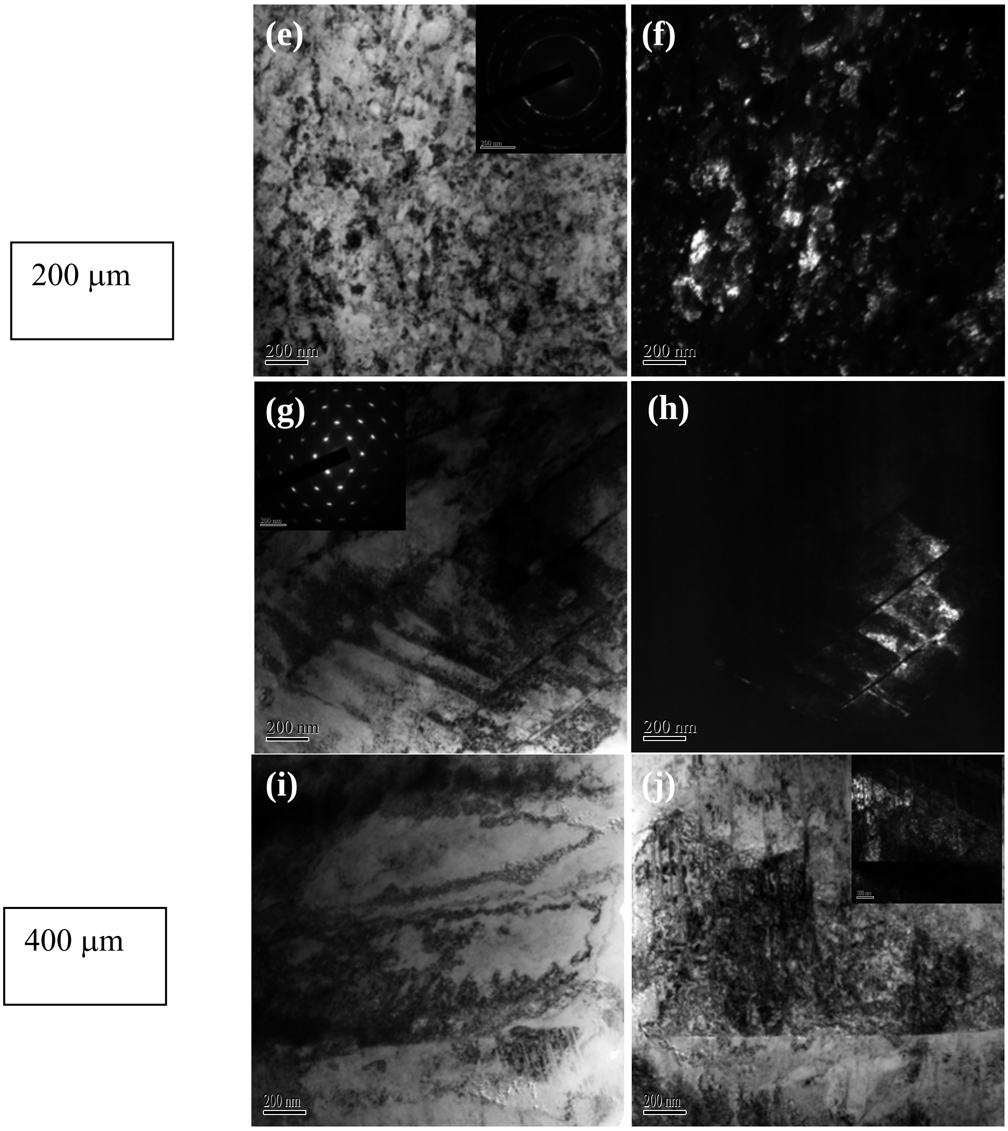

FIG. 4.11. TEM micrograph showing the microstructure of different layers of the 100-ball treated sample: (a, b) bright field (BF) with the inset of the SAED patterns, and dark field (DF) of the surface layer (0 μm): nano-grains with the average size of a few nm; (c, d) BF and with the inset of the SAED patterns, and DF of the subsurface layer (~50 μm): nano-twins with minimum spacing less than 10 nm; (e, h) BF and with the inset of the SAED patterns, and DF of the nano-grains of a few tens of nm in average size and the nano-twins with spacing of around ~200 nm at the subsurface layer (~200 μm); (i, j) BF of the grains with dislocation cell walls, and BF with the inset of DF of a grain with a large number of laminae at the depth of ~400 μm.

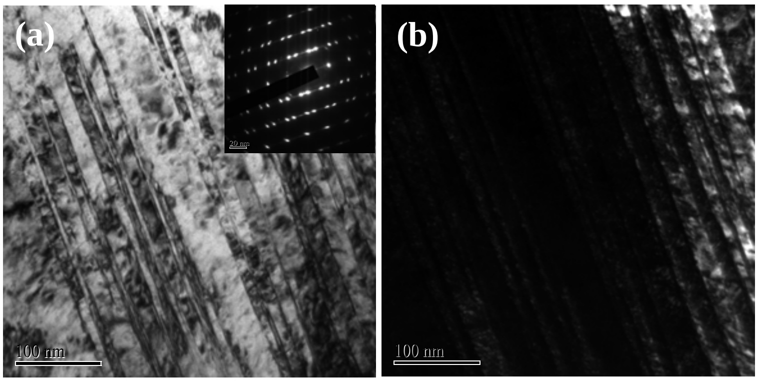

FIG. 4.12. TEM micrograph showing the microstructure of the surface layer: (a) BF with the inset of the SAED patterns; (b) DF of 400-ball treated samples, which contain dense nano-twins of a few tens of nm spacing.

It is hard to confirm the detailed forming process of the nano-grains and nano-twins in the SMAT process. However, the distinction between Fig. 4.11 and Fig. 4.12 is apparently due to the large difference of the nominal impact velocities. For the higher velocity impact, which pertains to the 100-ball case, the surface layer must be more significantly strained with a higher strain-rate. This renders the formation of extremely refined grains, which might be the consequences of subdivision of deformation twins and dislocation grids, as was described by Zhang et al. [84] in application of a low frequency SMAT process to AISI 304 stainless steel. If Zhang's explanation of the forming process of nano-grains is applied, the abundance of nano-twins in the surface of 400-ball treated material can be regarded as the precursor of the surface microstructure of the 100-ball case. Alternatively speaking, after the same period (10 minutes) of treatment, the subsurface layer (depth ≈ 50 μm) of the 100-ball treated sample may experience a similar strain/strain-rate history as the surface layer of the 400-ball treated sample. As a matter of fact, it is noted that after a longer treatment time (e.g. 12 minutes), the

400-ball treated sample can also achieve the same mechanical performance as the 100-ball-10-minute sample.

4.3 Theoretical Analysis

4.3.1 Theoretical estimate of strain-rate

The enhancement of the mechanical properties comes with the existence and the high density of the twins microstructure [51]. Being the driving force of the twinning induced plasticity [58], strain-rate [58, 146-148] has also been regarded as a vital key in refining the grain size. In the early attempt of SMAT [4, 79], the gradient variation of the strain and strain-rate has been generally regarded as the significant factor for the gradient grain size distribution from a few nanometers (in the top surface layer) to several micrometers (in the subsurface layer) of the sample. In a later study [60], Wang et al. further specified the main role of strain-rate to obtain the key features of the structure in the nanometer-regime which favors the mechanical properties in Copper. In the SMAT process, the velocity of the balls determines the strain-rate in the treated sample.

The theoretical model for the ball-plate dynamic indentation refers to Johnson's blunt indentation model [149]. This model, as shown in Fig. 4.13, based on Hill's elastoplastic cavity expansion model [150], assumes that the stress-strain field underneath the ball indenter exhibits hemispherical symmetry and the further movement of the ball indenter is accommodated by the instant expansion of the core of radius a.

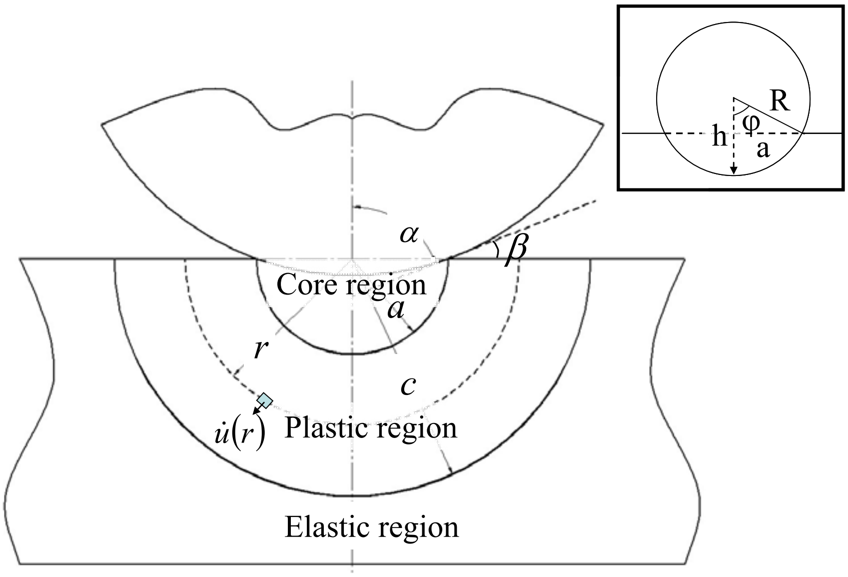

FIG. 4.13. The Cavity Expansion Model (Johnson [149]) illustrates the ball making an indent on the sample surface and results in three regions with specific materials' response from the sample itself.

The solution renders the relation between the load *P* and depth *h*, can be expressed as

$$P_{r=a} = Y_R \left\{ \frac{2}{3} + 2\ln(\frac{c}{a}) + 0.19 \right\} \cdot \pi a^2 , \tag{4.1}$$

where $\frac{c}{a}$ is found to be $(\frac{E^* \tan\beta}{Y_R})^{\frac{1}{3}}$ and *c* is the boundary radius of the plastically deformed region. E^* is the reduced Young's Modulus, which incorporates the Young's Moduli and Poisson ratios of the sample (E, ν) and the ball (E_b, ν_b) as $\frac{1}{E^*} = \frac{1-\nu^2}{E} + \frac{1-{\nu_b}^2}{E_b}$ to account for the elastic deformation of the ball where $E = 200$ GPa. Y_R is the representative stress and is taken as $300(1 + 4.92\,\varepsilon_R^{0.72})$ for our case, which is obtained from the true stress-strain curve (Fig. 4.10) of as-received 304 stainless steel after curve fitting. According to Johnson and Tabor [151], ε_R is the representative strain which changes with the angle, β (Fig. 4.13), of the ball indented at the edge of the treated sample during the ball's penetration, and is approximately equal to 0.2tanβ. tanβ herein is similar to sinβ and can be expressed in terms of the radius, a, of the core region, which varies with respect to the penetration of the depth h, which is equal to $a/R = \sqrt{R^2 - (R-h)^2}/R$.

Note that the kinetic energy of the ball is absorbed by the elastoplastic deformation of the material; the velocity of the ball changes with the indentation depth h, that is

$$v(h) = \dot{h} = \sqrt{\frac{2}{m}\left(\frac{1}{2}m{v_0}^2 - \int_0^h P dh\right)}, \tag{4.2}$$

where v_0 is the initial impact velocity of the ball and m = 0.1124 g is the mass of the ball. The relationship of the force P and the velocity of the ball is then found.

In Johnson's model [149], the compressibility of the core is neglected. This conservation of volume gives

$$2\pi a^2 du(a) = \pi a^2 dh. \tag{4.3}$$

According to Hill [150], the change rate of the radial displacement $u(r)$ in the plastic zone, $a \le r \le c$, with respective to c is

$$\frac{du(r)}{dc} = \frac{Y}{E}\left\{3(1-\nu)(c^2/r^2) - 2(1-2\nu)(r/c)\right\}. \tag{4.4}$$

Assuming incompressibility of the material, i.e. ν = 0.5, eq. (4.4) becomes

$$\frac{du(r)}{dc} = \frac{Y}{E}\left(\frac{3}{2}\right)\left(\frac{c^2}{r^2}\right), \tag{4.5}$$

which leads to

$$\dot{u}(r) = \frac{du(r)}{dt} = \frac{Y}{E}\left(\frac{3}{2}\right)\left(\frac{c^2}{r^2}\right)\left(\frac{dc}{dt}\right), \tag{4.6}$$

hence the relation between the change rate of the radial displacement with respect to time and the change rate of the boundary of the plastic region with respect to time, d*c*/d*t*, (hereafter, denoted by, $\dot{c}$) is obtained.

Noting that the displacement of the core boundary should accommodate the further indentation of the ball with respective to time, eq. (4.3) is modified to give $2\pi a^2 \dot{u}(a) = \pi a^2 \dot{h}$, $\dot{c} = dc/dt$ can be related to $\dot{h}$ as

$$\dot{c} = \frac{1}{3}\left(\frac{E}{Y}\right)\left(\frac{a^2}{c^2}\right)\dot{h}. \tag{4.7}$$

According to Hill's solution [150], the radial *(r)*, longitude *(θ)* and latitude *(ϕ)* plastic strain-rates are respectively given by

$$\dot{\varepsilon}_r(r) = \frac{\partial \dot{u}(r)}{\partial r} = -\frac{a^2}{r^3}\dot{h}, \tag{4.8a}$$

$$\dot{\varepsilon}_\theta(r) = \dot{\varepsilon}_\phi(r) = \frac{d\dot{u}(r)}{r} = \frac{1}{2}\frac{a^2}{r^3}\dot{h}. \tag{4.8b}$$

The equivalent plastic strain-rate is then

$$\dot{\varepsilon}_e(r) = \frac{2}{3}\left|\dot{\varepsilon}_r(r) - \dot{\varepsilon}_\theta(r)\right| = \frac{a^2}{r^3}\dot{h}, \tag{4.8}$$

and the average plastic strain-rate over the straining period is obtained as

$$\bar{\dot{\varepsilon}}(r) = \frac{1}{t}\int_0^t \dot{\varepsilon}_e(r)dt. \tag{4.9}$$

By numerical computation of the strain history, one is able to obtain the average strain-rate. Table 4.2 lists the average strain-rate at different depths. It is shown that the strain-rate is in the order of 10^4 for 10 m/s impact. If the initial velocity is reduced to 3 m/s, the corresponding strain-rate is also reduced by 2/3 at the surface and almost an order at the subsurface layer.

Table 4.2. The plastic strain-rates (s^{-1}) at different depths of the materials treated with 3 mm ball.

Impact velocity	Depth, r (μm)					
	15	50	100	200	300	400
10 m/s	34.2×10^4	10×10^4	5.0×10^4	2.4×10^4	1.0×10^4	4.4×10^3
3 m/s	10.1×10^4	3.0×10^4	1.5×10^4	3.5×10^3	1.0×10^3	4.4×10^2

4.3.2 Simulation results

Finite element simulation can be performed to verify the above estimate of strain-rates at different depths. As strain-rate is the main focus in this study, the effect of local heating, which is mainly on the grain refinement, is then not considered. In the simulation, the bearing steel ball was assumed to be rigid and the initial velocity is 10 m/s. The model was assumed to be axisymmetric. The 6-node quadric triangular element was adopted with the minimum element size of 0.005 mm in the contact region. The impact process was simulated by ABAQUS EXPLICT.

As strain-rate plays the main role in obtaining twins in nanometer regime, plastic strains, on the other hand, determines the depth that this key feature can present. Thus the simulations of both strain-rate and plastic strains are performed. Fig. 4.14(a) shows the contour map of the plastic strains of the 304 stainless steel plate, and Fig. 4.14(b) shows the plastic strain distributions along the center line after impact. The plastic strain within ~200 μm is maintained at a very high magnitude. It is noted that the plastic strain at the subsurface depth of ~200 μm is quite close to that of the surface layer, and the maximum plastic strain occurs at the depth of ~70 – 80 μm rather than the surface layer. Beyond 200 μm, the plastic strain decreases drastically with increase of depth. It is also worth noting that the plastic strains accumulate with the number of impacts. And as the number of impacts increase, the maximum plastic strains occurs closer to the surface layer instead, and begins the drastic decrement at the shallower subsurface layer as shown in Fig. 4.14(c). In the real SMAT process, the number of impacts is much higher and the accumulated strains can then be expected to be higher.

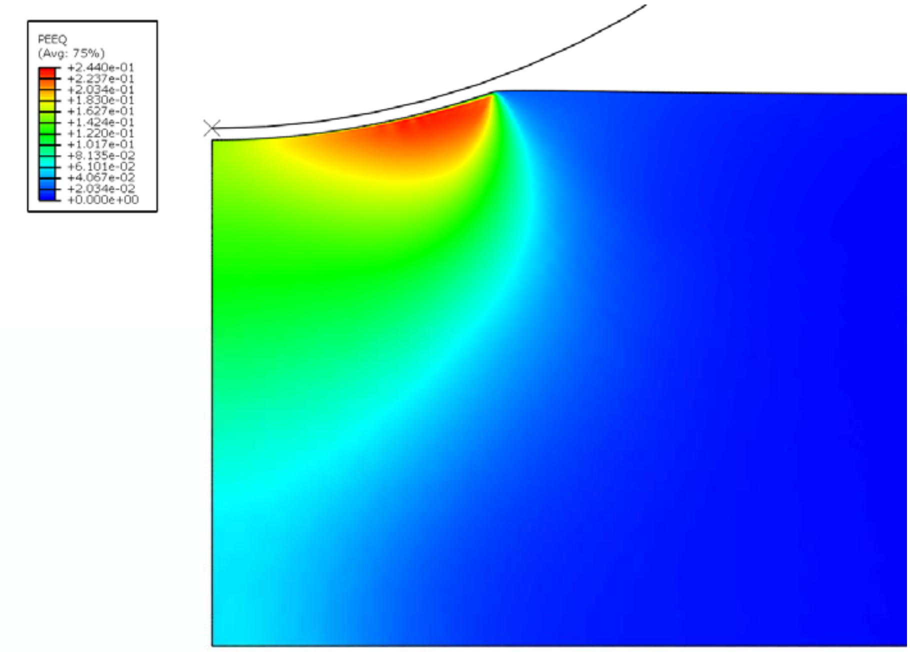

(a)

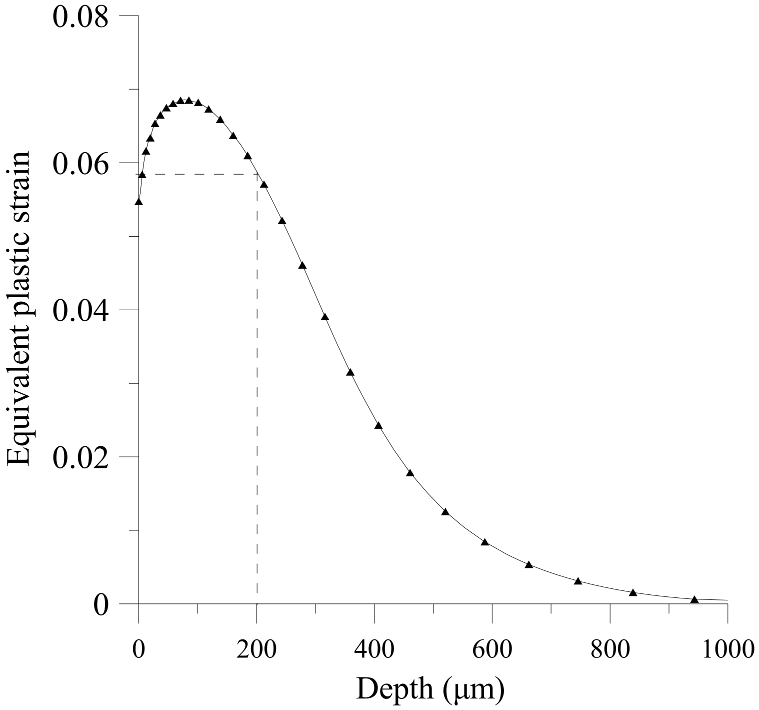

(b)

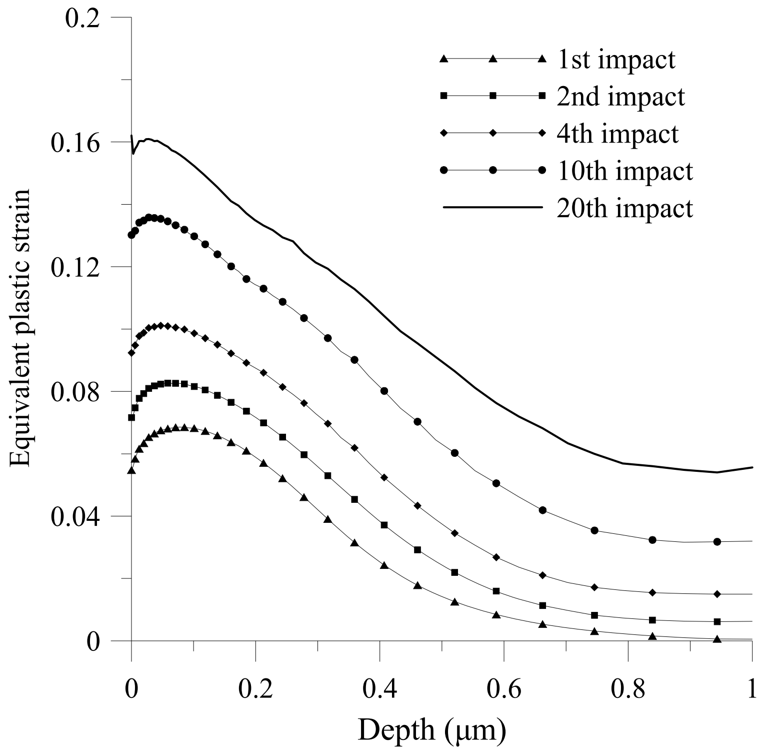

(c)

FIG. 4.14. The distribution of equivalent plastic strain in the 304 SS subjected to impact by a 3 mm rigid ball with an initial velocity of 10 m/s. (a) the contour map; (b) the distribution along the central axis after a single impact; (c) after multiple impacts.

Figs. 4.15(a-d) show the plastic strain-rate at different depths of the sample in a period of time. For comparison, Fig. 4.16 shows the variation of strain-rate with time at different depths as well as the estimated average strain-rate (by the horizontal dashed lines) from Table 4.2. The length of the horizontal lines refer to the duration of straining at the particular depth *r* from the above analytical model by noting that as the material is included in the core region (i.e. $a \geq r$), the deformation ceased. Fig. 4.16 shows that the estimated strain-rate from the analytical model indicates strain-rate level well at different depths. Especially for the subsurface layers with depths between 50 and 200 μm, the estimated strain-rate is about 80~90% of the maximum strain-rate.

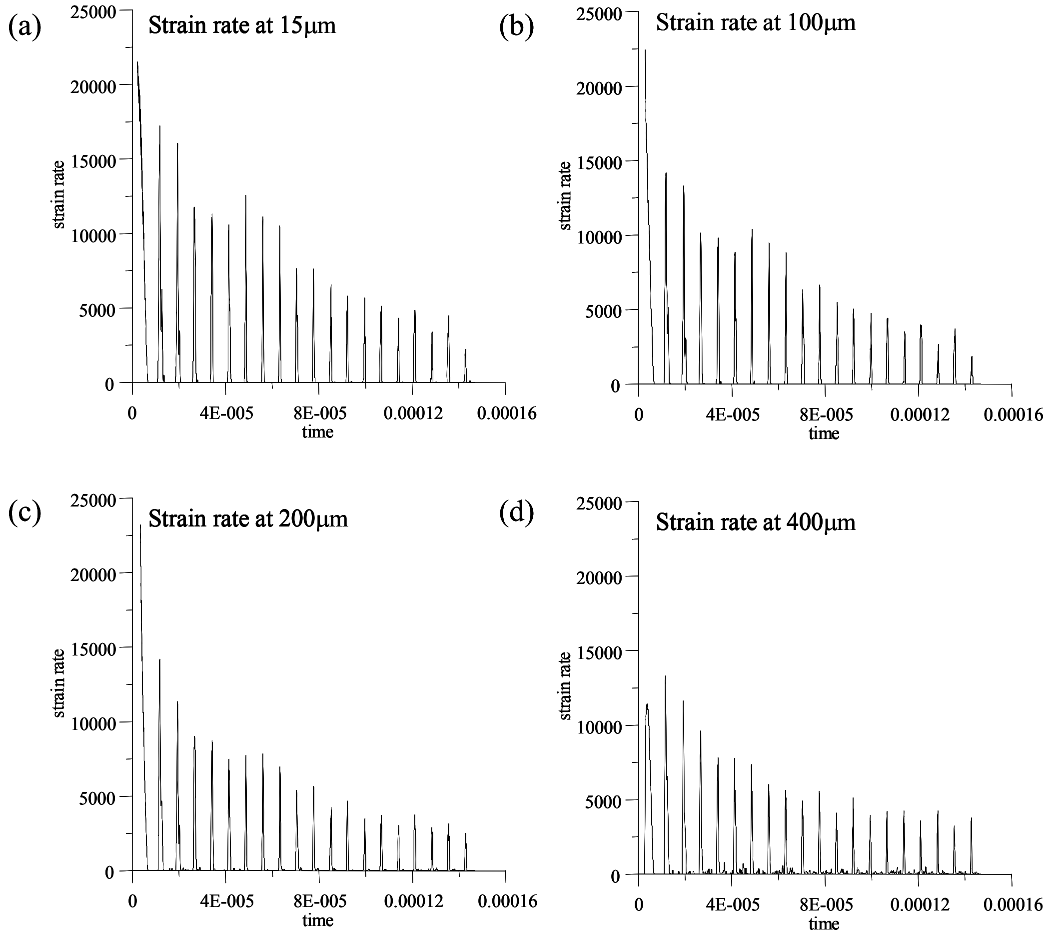

FIG. 4.15. (a-d) Strain-rate at the particular depth at different time.

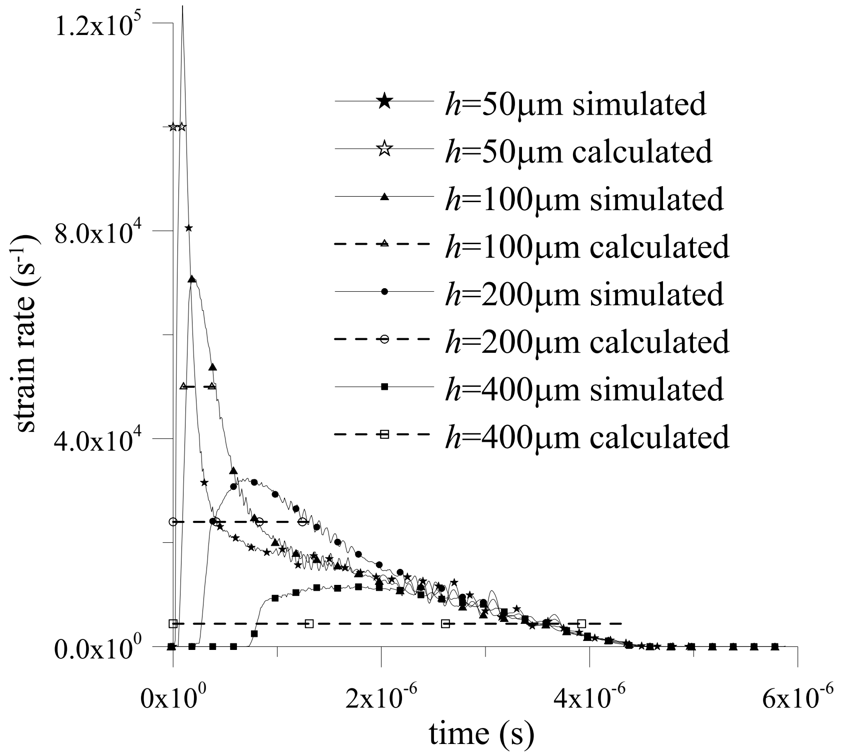

FIG. 4.16. Comparison of the strain-rate obtained by theoretical calculation and numerical simulation.

From the simulation, the rebound velocity ratio of the ball can also be obtained, as shown in Fig. 4.17, which can be the supplementary explanation to the observation in the previous part. The ratio of rebounding velocity to the impinging velocity increases as the number of impacts increases, and gradually tends to 1 at the 80th impact. It renders the fact in the actual SMAT process that as the number of impacts approaches infinity, the rebound velocity of the ball is quite close to its impinging velocity. This may be due to the treated materials being hardened as the number of impacts increases. And this is the evidence of the hardening effect of the treated materials on the velocity of the ball as mentioned previously: the harder the treated materials, the higher the rebounding velocity.

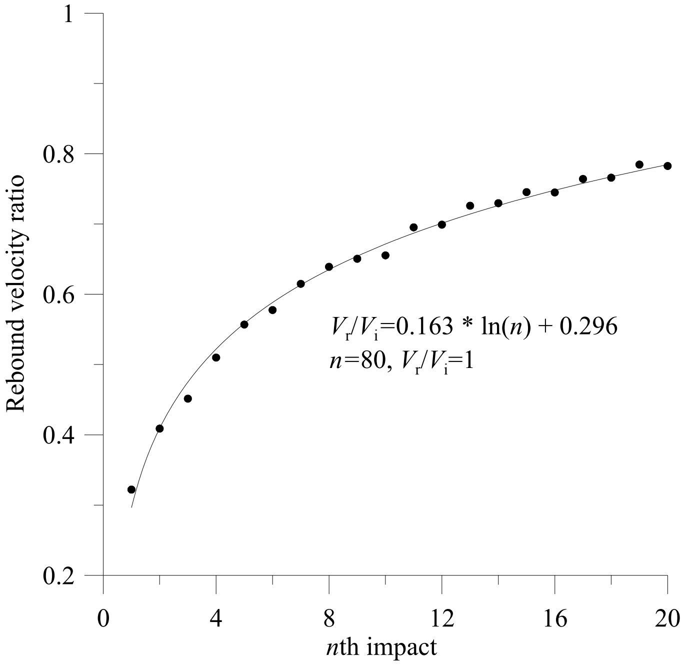

FIG. 4.17. Rebounding velocity ratio tends to 1 after multiple impacts.

4.3.3 Implications

From the above calculations, in connection with the microstructures from the TEM observations (Fig. 4.11, 4.12), one can infer that the formation of nanoscale-spaced deformation twins in the AISI 304 stainless steel is related to the high strain-rates in the present treatment process [58, 146, 147]. The above calculation indicates that the requirement of the strain-rate to form nano-twins would at least be in the order of 10^4 s^{-1} for the AISI 304 stainless steel.

This may explain why the samples treated with high velocity balls in SMAT (100-ball case) have the twins microstructure along the thickness direction up to the depth of ~200 μm with high density at the layer close to the surface where the strains is higher.

4.4 Concluding Remarks

In the present work, we attempted to study the impact velocity of SMAT process and henceforth the strain-rate estimation and impact process simulation. A high speed camera was used to observe the motion of a ball in the treatment chamber and measure its velocity. The ceiling impact velocity of a single 3 mm ball was about 10 m/s. Density and size of the ball, power of the ultrasonic generator, the mechanical properties (mainly, hardness) of the sample, as well as the number of balls, were the parameters that affect the ball velocity in SMAT.

The nominal impact velocities of multiple-ball cases were also investigated. As the number of balls increases, the corresponding nominal impact velocity of the balls decreases as more kinetic energy is dissipated or allocated to the horizontal motion due to more collisions between balls. The treatment efficiency (eff), represented by the resulting tensile strength after the same duration of treatment correlates well to total kinetic energy evaluated from the ball number and the corresponding nominal velocity. Higher total kinetic energy results in higher treatment efficiency. In the present case, 100-ball treatment seems the optimal choice, as it rendered the highest yield strength (~850 MPa) after 10-minutes of treatment.

Nano-twins were found under TEM in both 100-ball and 400-ball treated samples, which was the favorable ultrastructure in the recent technology trend to enhance the performance of metallic materials. The difference was the depths at which they were found. For the 400-ball treated sample, dense nano-twins were found in the surface layer. While, for the 100-ball treated sample, nano-grains were found in the surface layer and dense nano-twins with minimum spacing less than 10 nm were found in the subsurface (depth $\approx$ 50 μm) layer instead. It is plausible that the subsurface layer (depth ≈ 50 μm) of the 100-ball treated sample may experience similar strain/strain-rate history as the surface layer of the 400-ball treated sample.

Utilizing the ball velocity obtained in the observation, Johnson's Blunt Indentation Model was adopted to estimate the strain-rate at different depths of the treated AISI 304 stainless steel plate. The estimated average strain-rate for the impinging of a 3 mm ball with 10 m/s velocity, can be as high as $\sim 10^4\ s^{-1}$ even at the depth of 300 μm. This result agreed well with the simulation. Associating this result with the microstructures obtained from TEM observations, we believe $10^4\ s^{-1}$ is the least requirement of the strain-rate for the formation of twins with nanoscale spacing for the AISI 304 stainless steel.

Chapter 5: ELECTRODEPOSITION PROCESS DEVELOPMENT

The electrodeposition (ED) process has been developed since the 17th century; recently, it has been widely adopted in nanotechnology [8, 115, 119, 120]. It is one of the promising synthesis methods to produce NS materials in bulk form [119]. In 1994, Erb et al. [120] showed that materials with nano-scale grain size, as small as 11 nm, can be obtained using the ED process with pulsed current (**pc**). In 2004, Lu et al. [93] further demonstrated that NS materials with a promising structure, nano-twins, which are able to achieve high strength and retain desirable ductility, were also obtained by the pulsed ED process in strictly controlled conditions. Pulsed ED is proposed for fabricating NS materials since it has a significant effect on inhibiting grain growth while promoting grain nucleation [119, 120]. However, it is necessary to precisely control the conditions in the process of pulsed ED. As an alternative, the direct current type (**dc)** is easy to be manipulated. Limited work has been reported on the relationships among **dc**, grain size and duration. The focus of previous works mainly fell on the effect of additives and thin films of thickness less than 200 μm [121, 152-155]. Ibañez et al. [121] have reported that both **dc** and **pc** methods produce Cu films with nano grains of similar size with a thickness of a few micrometers. Does there exist a limit for the thickness of electrodeposits with nano-grains produced by **dc** methods? It prompts us to contemplate the probability of adopting **dc** for producing NS materials since it has the advantage of easy manipulation.

In industrial applications, free-standing electrodeposits are extensively used. In order to facilitate the removal of the substrate from the subsequently electroplated samples and allow the complex shape, resin or wax is commonly adopted as substrate. However, the effect of non-metallic substrates on the production of NS materials in the ED process is not yet fully investigated [125, 156, 157].

It is known that the structure and properties of the electrodeposits are strongly sensitive to the operating conditions, such as composition of the bath, pH value, current type used, current density, temperature and substrate, etc [121, 125]. All these parameters are found to be inter-affected [124]. Hence, the missing piece of knowledge in the relationships among non-metallic substrates, current type, current densities, microstructure and crystallographic textures, and mechanical properties prompted us to look further into their influences in the ED process and also further into the availability of the resultant electrodeposits on producing materials with nano-grains and / nano-twins. This work will systematically study the influences of deposition parameters on the microstructure and tensile properties of the electrodeposited Cu. The microstructures of the electrodeposited Cu are characterized by means of TEM, FIB, EBSD and SEM observations and XRD analysis. The tensile properties of the resultant deposits are examined.

It is known that by employing the proper conditions, one can tailor the electrodeposited materials with the desired structure and properties for different applications. This work will also examine the availability of obtaining bulk NS materials with desirable ductility in production-scale conditions through understanding the relationships among operation parameters, microstructure and properties.

5.1 Experiment

5.1.1 Setup and procedure

The ED setup was designed in the small mass production scale; details have been introduced in Chapter 3. The ED process was carried out at the ambient temperature of 24°C and pH value of 1. The detailed chemical composition of the electrolyte bath used in this study is listed in Table 3.1, which is in accordance with the well-established industrial applications. Four copper bars with 99.99% purity were used as the soluble anode without any additives in the solutions. The cathode/deposition substrate was a rectangular wax block of (30 × 30 × 120 mm^3) coated with silver conducting paint. The distance between the anode and cathode was 20 cm. The electrolyte was continuously mechanically stirred during the ED process.

The thickness of the Cu films ranged from ~30 μm to 1.1 mm according to the increase in duration or current density. The as-deposited Cu films with thickness smaller than 100 μm were directly peeled off from the substrates for structural examination. Those with thickness larger than 100 μm were separated from the substrate by the de-waxing process and cut into a dog-bone shape with the electro-discharge-machining (EDM) technique for both structural examination and property measurements.

The morphology of the cross-section of the sample of 1 mm thickness was examined by SEM (JEOL JSM-6490), EBSD (JEOL 6500F) and FIB (FEI Quanta 200 3D) to provide insight into grain growth in **dc** conditions. The sample for SEM and EBSD was first polished with silicon carbide paper and diamond cloth, and then it was etched in a mixed solution of Nitric acid and ethanol (details are listed in Table 3.2).

The morphologies at the solution side (the side making contact with the electrolyte solution), substrate side (the side attached to the substrate) and different depths (~270 and ~700 μm of the 1 mm thick sample) of Cu films obtained from different duration were examined by TEM (JEOL JEM-2010). Hence, the grain size and twins thickness were statistically estimated. The samples for TEM observations were first grinded to ~40 μm leaving the observed side or depth untouched and then they were ion-milled.

XRD measurements were performed on both solution and substrate sides of the Cu films of different thickness obtained from different duration with Bruker D8 Discover employing Ni filtered Cu Kα radiation.

Tensile property tests were performed at ambient conditions on MTS RT-50 (50 kN) Axial Static Testing Machine at the strain-rate of 2×10^{-3} s^{-1}. The extensometer (MTS 632 24F-50) was used to measure the extension of the large samples with gauge length and width of 25 ± 0.1 and 6 ± 0.1 mm, respectively. For small samples with gauge dimension of 3×1 mm^2, the strains were obtained from the displacement of the stroke of the tensile machine.

5.1.2 Preliminary study

5.1.2.1 Effect of current type

As addressed in Chapter 2, different current types can be used for electroplating. **dc** is commonly used for its uniform deposition rate, high efficiency and easy manipulation. Meanwhile, rectangular **pc** is widely adopted to produce NS materials [93, 116, 118-120] owing to its promotion of grain nucleation and inhibition of growth.

The effect of current types on these plating conditions was compared in terms of tensile properties. The current density was kept at 1.5 A/dm^2, which is calculated by the ratio of set current to the total surface area of the substrate of the cathode, and is commonly used in the industrial application of this scale. In order to produce electrodeposits with a thickness of around 0.5 mm, the total deposition time for both types of current was around 48 hours. Five sets of samples were produced by **pc** with different combinations of on-time, t_{on}, and off-time, t_{off}, as summarized in Table 5.1. One extra set of samples was obtained from **dc**. The average current density, I_a, defined as the current density of the sample during the whole pulse cycle, can be obtained by $I_p(t_{on}) / (t_{on} + t_{off})$, where $(t_{on}) / (t_{on} + t_{off})$ is the duty cycle. It is noted that the average current density was extremely low for all the **pc**-obtained samples in this study, especially for 'Sample 1' with a relatively long off-time. This low average current density resulted in low surface concentration of deposited metal ions at the anode and consequently, low deposition rate [158].

Table 5.1. On- and off- time combinations of the pulsed ED process in this study.

sample number	peak current density, I_p (A/dm^2)	on-time, t_{on} (ms)	off-time, t_{off} (ms)	duty cycle	average current density, I_a (A/dm^2)
1	1.5	0.2	2.0	0.091	0.136
2	1.5	0.1	0.3	0.250	0.375
3	1.5	0.3	0.9	0.250	0.375
4	1.5	0.3	0.5	0.375	0.563
5	1.5	0.3	0.4	0.439	0.643
6	1.5	-	-	-	-

The tensile test samples had the gauge dimension of (25 × 6) mm^2. At least five samples for each parameter were tested. The engineering yield stress-strain and ultimate stress-strain results are shown in Figs. 5.1 (a) and (b), respectively. Almost all the samples had yield strengths ranging from ~200 to 265 MPa, except 'Sample 1'. This sample was produced by the lowest average current density with the longest off-time, and had exceptionally low yield strength (~175 MPa). Samples obtained by **dc** had the highest yield strength (~265 MPa) and relatively high ductility (~25%). Samples ('Sample 2' and 'Sample 3') with the same duty cycle (25%) had similar yield strengths (~243 and 256 MPa, respectively) and ductility (18% and 16%, respectively); 'Sample 3' that had a longer off-time in the synthesis process had a higher ultimate tensile strength (404 MPa) but lower ductility as well. In general, both 'Sample 2' and 'Sample 3' had comparatively low ductility.

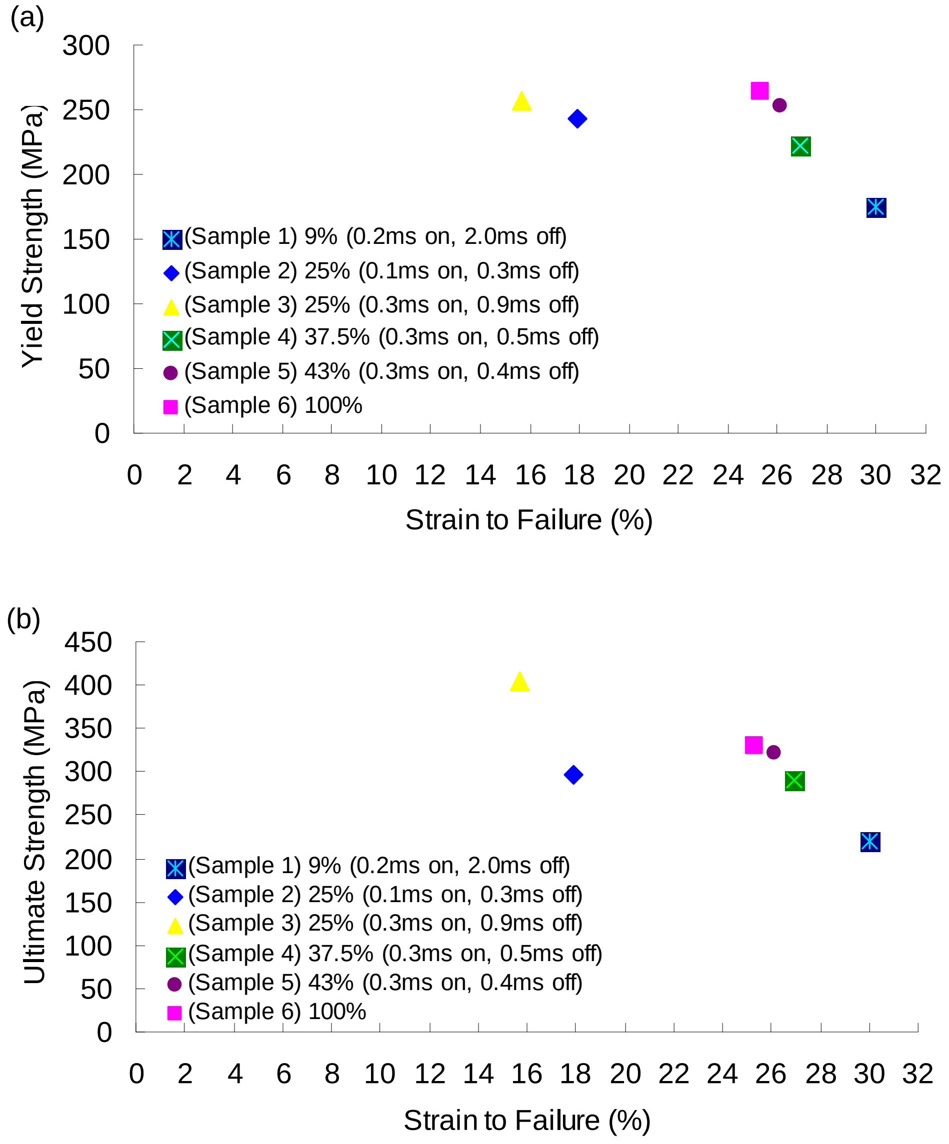

FIG. 5.1. The engineering tensile properties of the electrodeposited Cu obtained from different current types and different time settings: (a) yield stress-strain; (b) ultimate stress-strain.

The SEM image of the fracture surface of ‘Sample 2’ illustrates that large voids existed in a rather porous matrix, which is shown in Fig. 5.2 (a). This may explain the relatively low ductility. Meanwhile, the SEM image of the fracture surface of ‘Sample 6’ shows the comparatively ductile fracture characteristics, which is presented in Fig. 5.2 (b). Small voids having sizes less than 1 μm were observed.

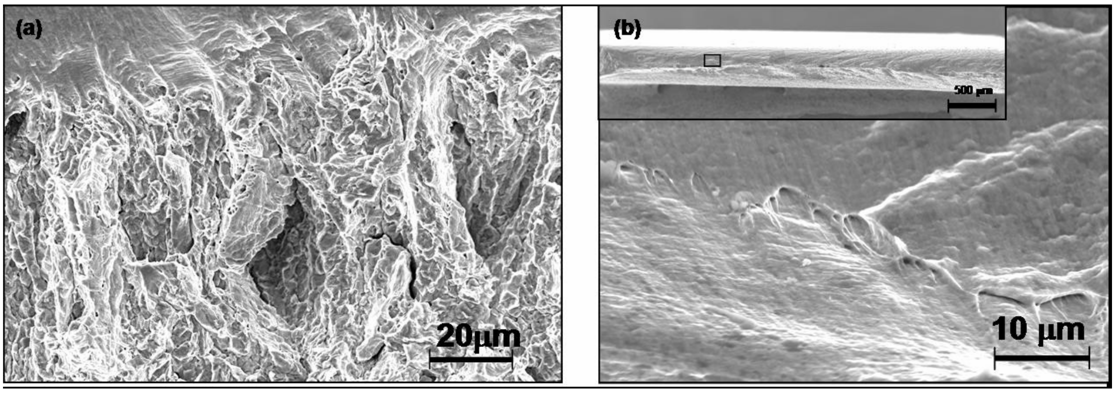

FIG. 5.2. Fractographic features: (a) electrodeposited Cu obtained by **pc** with t_{on} = 0.1 ms, t_{off} = 0.3 ms; (b) electrodeposited Cu obtained by **dc**.

In these ED process conditions, Cu films obtained from **pc** did not have markedly higher yield strength than those from **dc** as literatures have stated [116]. It is believed that the low current density is the main reason since it results in a low nucleation rate [127]; consequently, grains are harder to be refined. Another plausible reason is that the relatively long distance between the anode and the cathode reduces the concentration of Cu^{2+} ions in the vicinity of the cathode which may also result in the low nucleation rate.

5.1.2.2 Effect of current density

Current density is considered to be an important parameter to control the size of grains. According to classical theories on electrochemical phase formation and growth, high current density facilitates the production of fine grains [116, 121, 127] by promoting the nucleation rate. The effect of current density will be examined in this section. In the batch of samples, the current type used was **dc** and the deposition time was 24 hours. The highest current density to be tested was restrained by the limitation of the electronics part of this ED equipment. The current density ranging from 1 to 12 A/dm^2 was examined. The increase of current density resulted in the increase of the film thickness, as shown in Fig. 5.3 (a). The deposition rate was obtained by dividing the film thickness by the time used. The relation of current density and the deposition rate is shown in Fig. 5.3 (b). The deposition rate increased with increase of current density. However, the degree of increment decreased when the current density exceeded 8 A/dm^2.

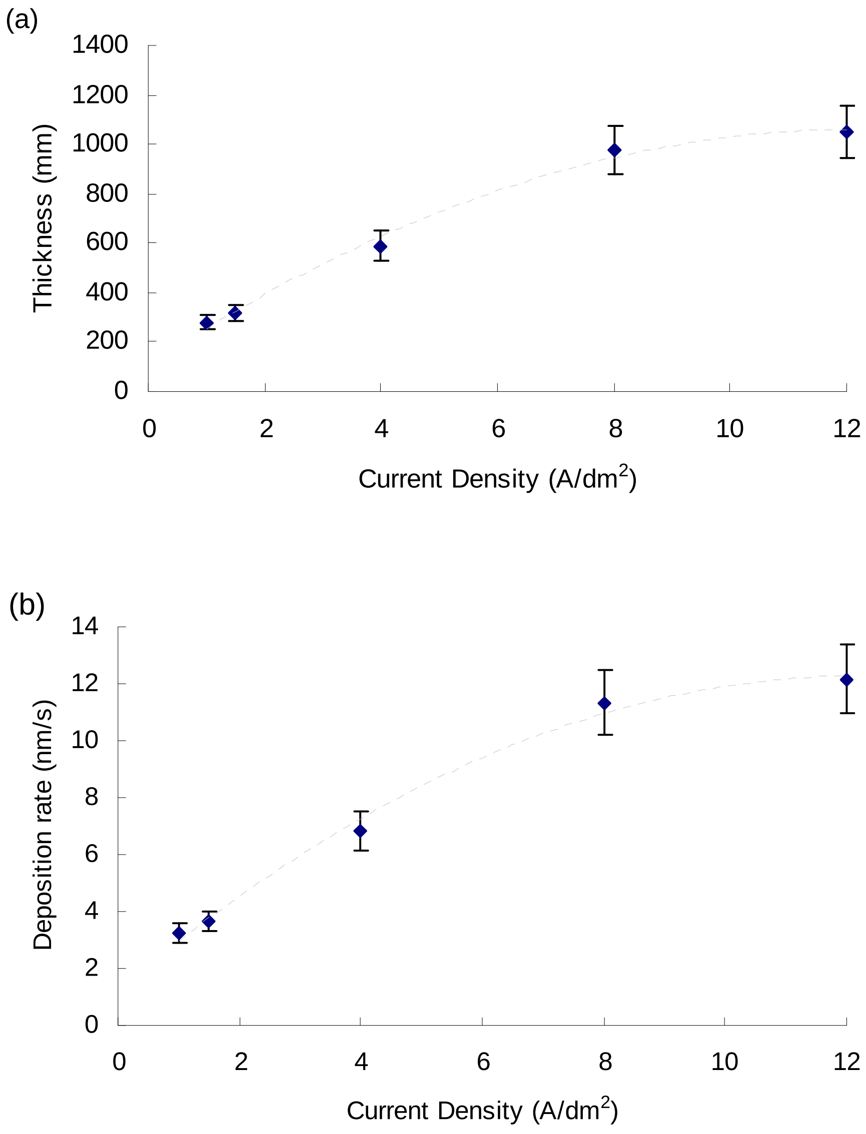

FIG. 5.3. Relation of current density and (a) the thickness of the Cu film; (b) the deposition rate.

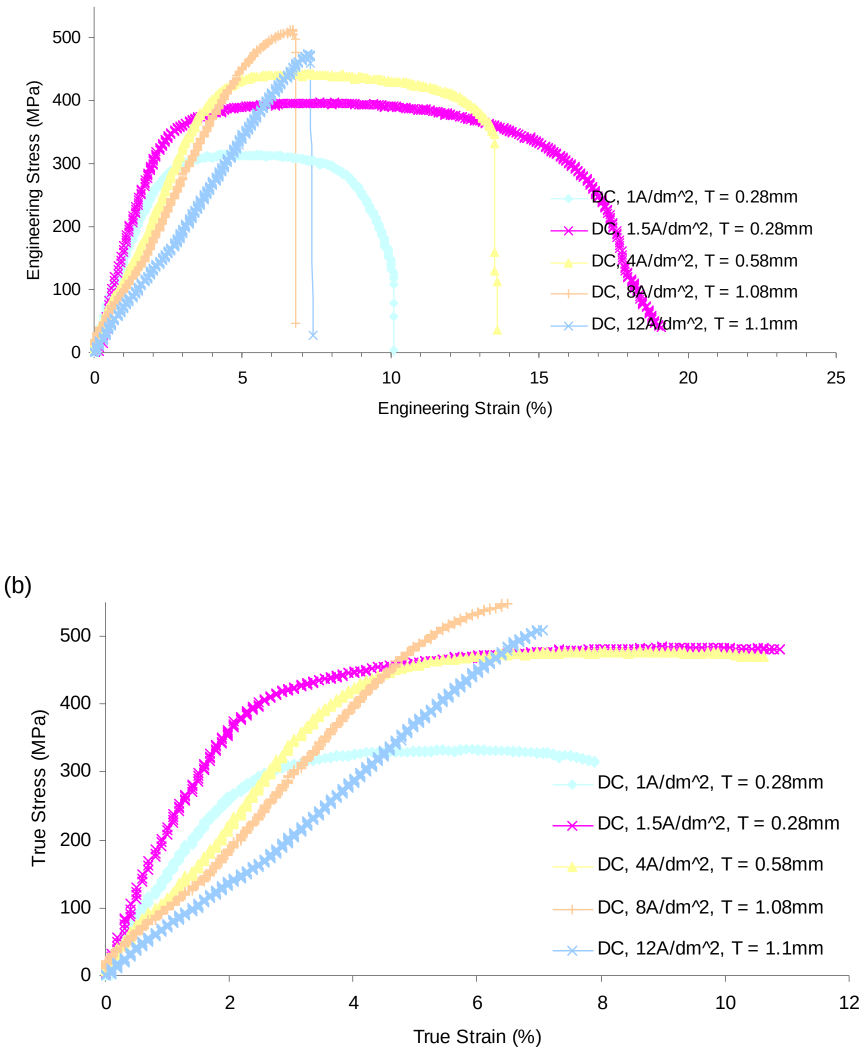

FIG. 5.4. The tensile test properties of the electrodeposited Cu obtained by current density ranging from 1 to 12 A/dm^2: (a) engineering stress-strain curve; (b) true stress-strain curve.

Both ex-situ and in-situ tensile property tests were performed. The samples had the gauge dimension of 3 × 1 mm^2. Fig. 5.4 presents the engineering stress-strain curve and the true stress-strain curve, respectively. Both the yield strength and the ultimate strength increased when the current density increased from 1 to 8 A/dm^2. They dropped when the current density reached 12 A/dm^2. Fig. 5.5 plots the summary of the ultimate strength and the strain to failure against the current density. The electrodeposited Cu films produced by current density of 1.5 A/dm^2 had the highest ductility; those undergoing the current density of 8 A/dm^2 had the highest strength.

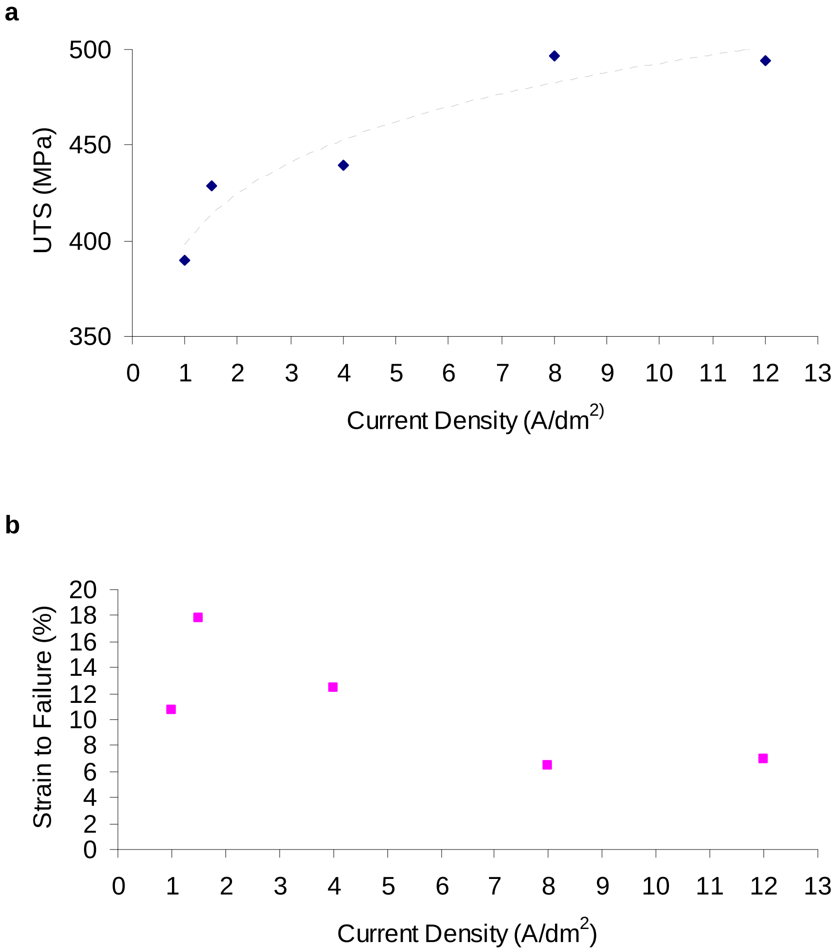

FIG. 5.5. Summary of the (a) ultimate strength; (b) strain to failure against the current density.

The porous matrix formed in these conditions is the possible reason for the fall in strength at 12 A/dm^2, the low ductility at the relatively high current density and the large variation of Young's Modulus among the samples with relatively low value.

Figs. 5.6(a-e) show the fractographs of samples obtained at current densities of 1, 1.5, 4, 8 and 12 A/dm^2, respectively.

Different rupture mechanisms have been shown for samples produced by different current densities. Necking, although in limited scale, was still observed in samples produced by current densities lower than 4 A/dm^2. Fig. 5.6(a) illustrates two rupture characteristics: dimples and void coalescence occurred through the shearing of voids. Both of them caused the failure of the sample produced by a current density of 1 A/dm^2. A few occasional voids sized around 5 - 10 μm were found, which are believed to weaken the structure and hence result in the loss of the strength and ductility. Fig. 5.6(b) shows the failure of plastic shear localizations in the sample produced by the current density of 1.5 A/dm^2. It is found that the void sizes in this condition were relatively small compared with the tested samples in other conditions, and hence higher ductility was obtained. Fig. 5.6(c) shows an even smaller degree of necking of the in-situ tensile test sample produced by the current density of 4 A/dm^2. A rather porous matrix was observed compared with the previous discussed samples, which limited the ductility. This is also true for the samples produced by current densities higher than 4 A/dm^2. The seriousness of the porosity and the size of the voids worsen the ductility of the samples produced by high current densities, i.e. 8 and 12 A/dm^2, and caused their total loss of plasticity. This resulted in their fracture in a brittle fashion, as shown in Figs. 5.6 (d) and (e). This is the reason for the rather high current density enhancing nucleation of new grains with less aid in their further growth. However, the long distance of the cathode and anode may make it hard to maintain sufficient supply of metal ions in the electrolyte to achieve a high deposition rate at these levels of current density. Therefore, the high concentration of

Cu^{2+} ions in the vicinity of the cathode cannot be sustained. This leads to the formation of a porous structure.

Considering the power limitation and the scale of the machine in this system, the current density of 1.5 A/dm^2 is a relatively optimum condition for producing Cu film with desirable strength and ductility.

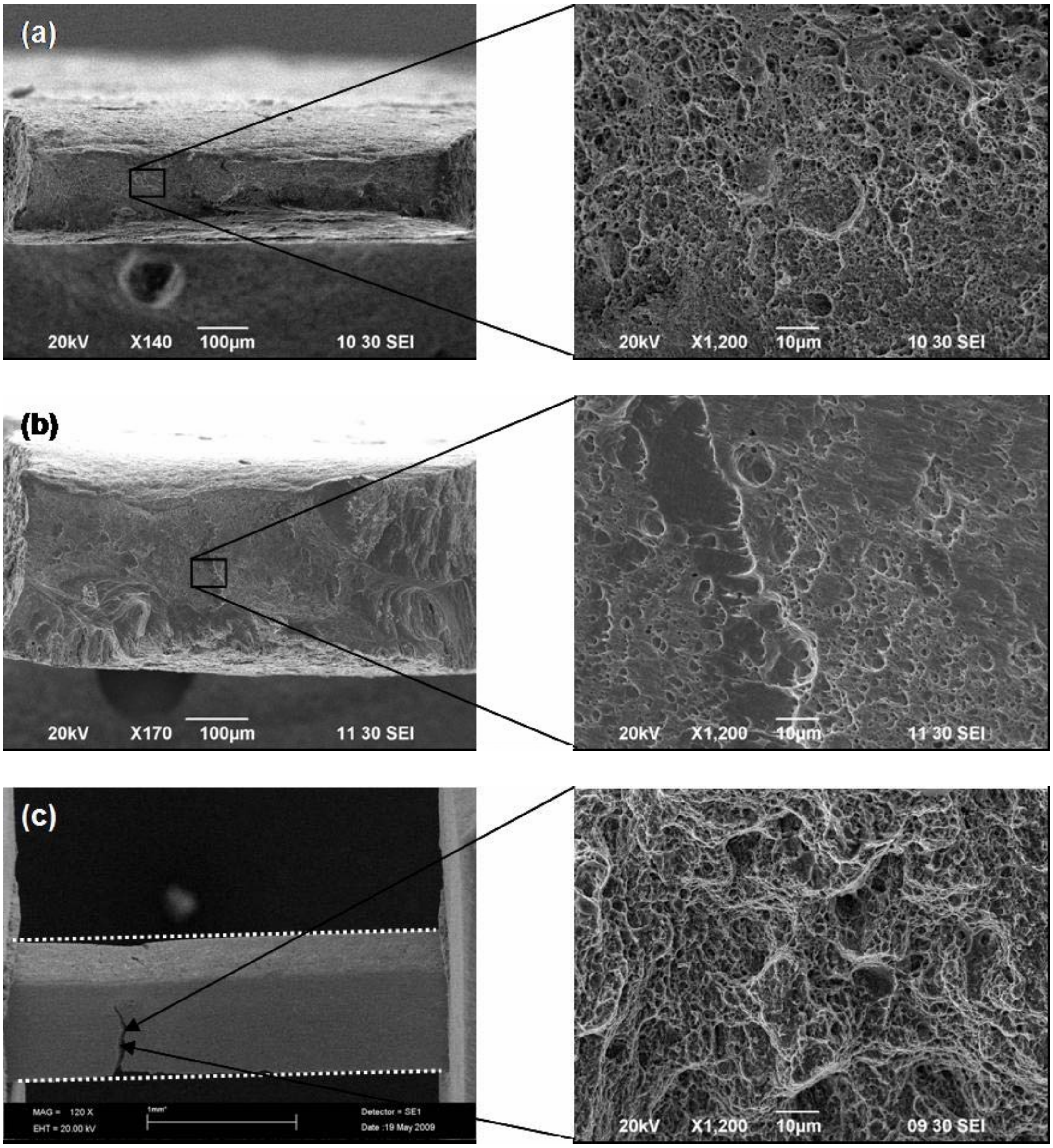

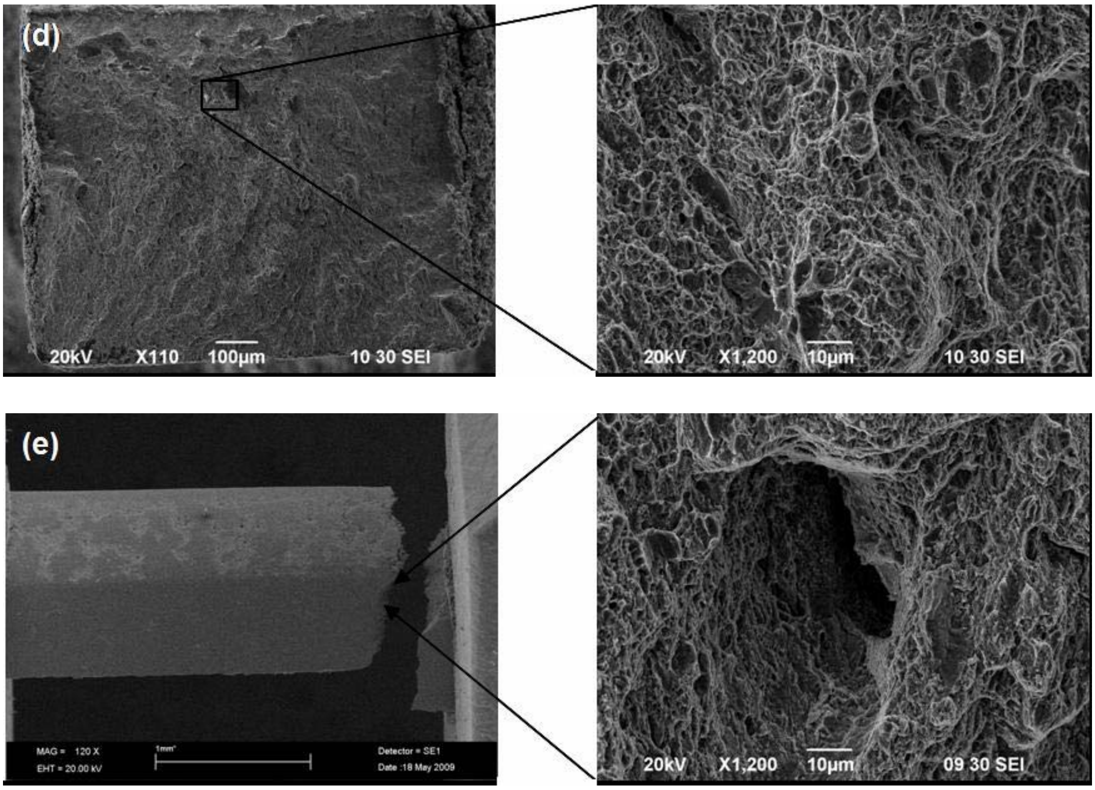

FIG. 5.6. Samples obtained at different current densities: (a) 1 A/dm^2; (b) 1.5 A/dm^2; (c) 4 A/dm^2; (d) 8 A/dm^2; and (e)12 A/dm^2.

5.1.2.3 Effect of process duration

In the conditions of the **dc** type, low current density and additive-free solution, it is known that the grains of electrodeposited Cu film always grow with its thickness and result in a soft structure [124]. However, limited studies reported on the relationship among the grain size, deposition rate and duration for the electrodeposits with thickness larger than 100 μm [124, 125] in these conditions. In this section and the following, the focus is directed to reveal this relationship.

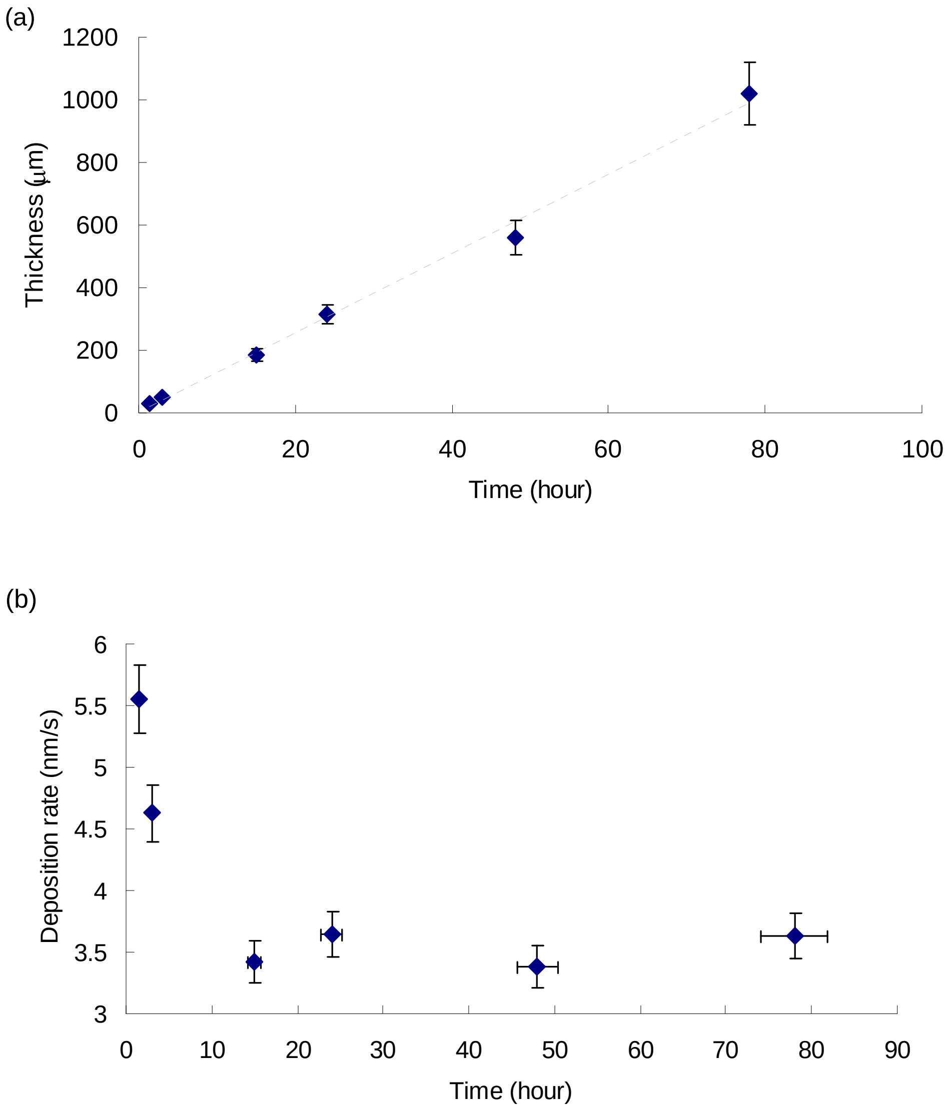

FIG. 5.7. (a) The relation of thickness and duration of the ED process; (b) relation of deposition rate and duration of the ED process of the electrodeposited Cu film.

In this batch of samples, the current type used was **dc** and the current density was kept at 1.5 A/dm^2. The deposition time ranging from 1.5 to 78 hours was taken to obtain Cu film of thickness ranging from ~30 μm to 1.1 mm. The relation of the deposition time and the thickness of the Cu film is presented in Fig. 5.7(a). This figure shows an approximate linear relation. When the deposition rate was plotted against the duration, however, it is clear that the deposition rate was high in the beginning couple of hours and dropped drastically as time passed, as shown in Fig. 5.7(b). After 15 hours, the deposition rate became steady. It is believed that the substrate played a crucial role in the first few hours by providing sufficient nucleate sites for the grains to form and by deciding the growing orientation with their own textures [125]. This may also explain why the microstructures with a thickness of a few tens of micrometers of electrodeposits are always fine grains of a size less than 1 μm [124, 125].

Tensile property tests were then carried out on the dog-bone shaped samples with a gauge dimension of 3 × 1 mm^2. The sample thickness was in the range of 0.16 to 1.02 mm. The samples were deposited for 15 to 78 hours correspondingly. The tensile property tests were not carried out on thin films with thickness of 30 and 50 μm due to equipment limitations. The measured engineering and true stress-strain curves are plotted in Figs. 5.8 (a) and (b), respectively. Both the yield and the ultimate tensile strengths decreased with the increase of the sample thickness (deposition duration); meanwhile the ductility increased with the sample thickness (deposition duration). The slope of increment in strength and decrement in ductility for samples with thickness exceeding 0.52 mm (deposition duration exceeding 48 hours) were small compared to the other samples. It is interesting to find that there were two kinds of plasticity manner among these true stress-strain curves of these electrodeposits, which are believed to reveal the plastic deformation mechanism. When the thickness of the deposits was 0.35 mm or smaller, i.e. the deposition time was 24 hours or less, the plastic deformation at a constant flow stress was observed following the linear dependence of stress and strain in the elastic deformation. It implies a near-perfect elastoplasticity behavior [159]. In the small grains of ductile materials, the dislocation activity was reduced and plastic deformation was assured by diffusional grain-boundary sliding [160]. This seemed different for the samples with thickness equal to or larger than 0.5 mm. A relative classical conventional work hardening manner was observed in the true stress-strain curve for these samples. This was caused by the continuous multiplication of dislocations owing to their comparatively large grains.

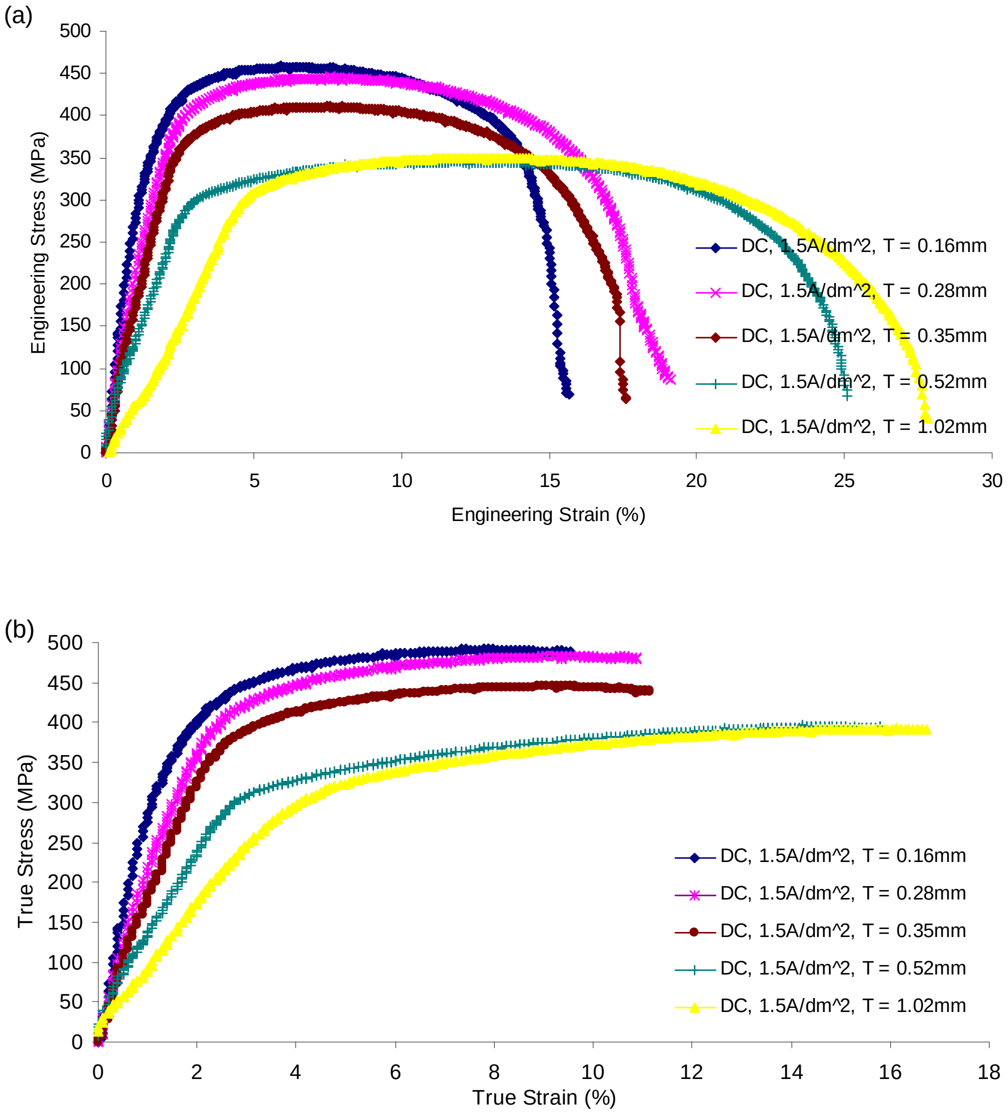

FIG. 5.8. Tensile test properties of the electrodeposited Cu of thickness ranging from 0.16 to 1.02 mm: (a) engineering stress-strain curve; (b) true stress-strain curve.

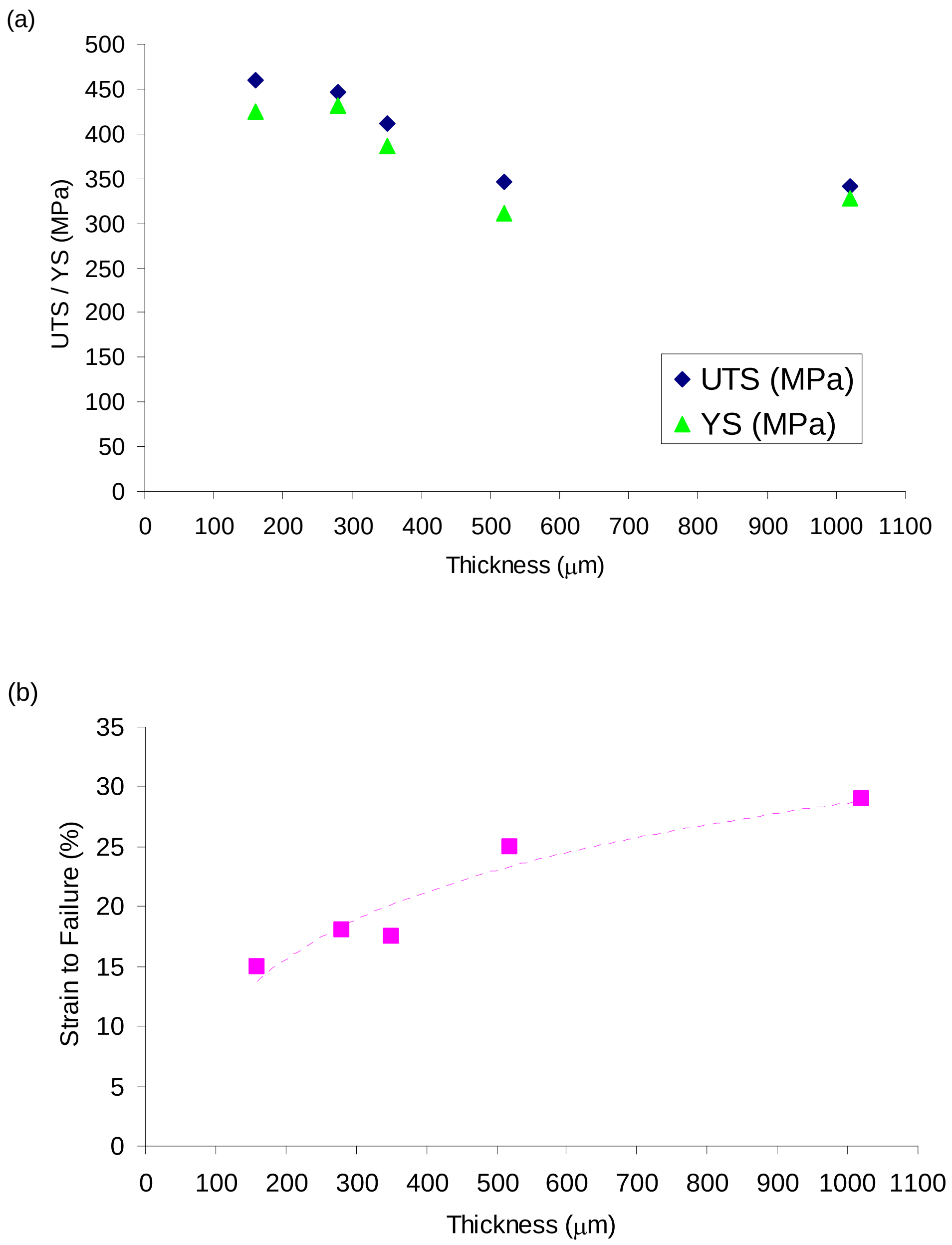

FIG. 5.9. Effect of the thickness of the electrodeposits on: (a) UTS and YS; (b) strain to failure.

A summary of the tensile properties of deposited Cu with different thickness is presented in Fig. 5.9. It is believed that the columnar structure played a significant role in enhancing the ductility while weakening the strength when the deposition time exceeded 24 hours and thickness of the Cu film was over 0.35 mm. This will be further discussed in the next section.

5.2 Results and Discussion

Mechanical properties, microstructures and textures are strongly related to each other. After the preliminary study, some idea of the effect of the current type, current density and deposition duration in terms of tensile properties was obtained. Using the **dc** type and current density of 1.5 A/dm^2, the electrodeposited Cu film with comparatively high ductility can be fabricated when the deposition duration is long enough. In this section, the samples are produced by the ED process with these conditions and the focus is directed to the evolution of microstructures and textures with the deposition duration. Different time durations, 1.5 to 78 hours, are adopted to obtain the specimens of different thicknesses in the same batch.

Then the mechanism of grain size / thickness effect on mechanical properties is discussed. The Hall-Petch relation and strain hardening exponent of NS Cu are examined based on the results in this project and compared with those in previous works.

5.2.1 Microstructure characterization

5.2.1.1 Microstructure evolution

The microstructures of the cross-sectional sample obtained by the ED process with deposition time duration of 78 hours and thickness of 1 mm were firstly examined by means of BSE imaging of SEM, FIB and EBSD. The transverse microstructures at different depths, i.e. substrate side, 270 μm, 700 μm and solution side, were analyzed by TEM.

5.2.1.1.1 Overview-cross-section

The BSE images of SEM in Fig. 5.10 show that there were three regions containing two types of grains along the cross-section of the 1 mm thick electrodeposited Cu film. At the first ~20 to 30 µm of the substrate side, a transition layer with an equiaxed grain structure was observed. Beyond this layer, columnar grain structures, similar to those of the other electrodeposited metals [161-164], were revealed. In between the columnar structures, some small grains were found. At about ~20 to 30 µm near the solution side, the grains were refined to equiax of sizes less than 500 nm again.

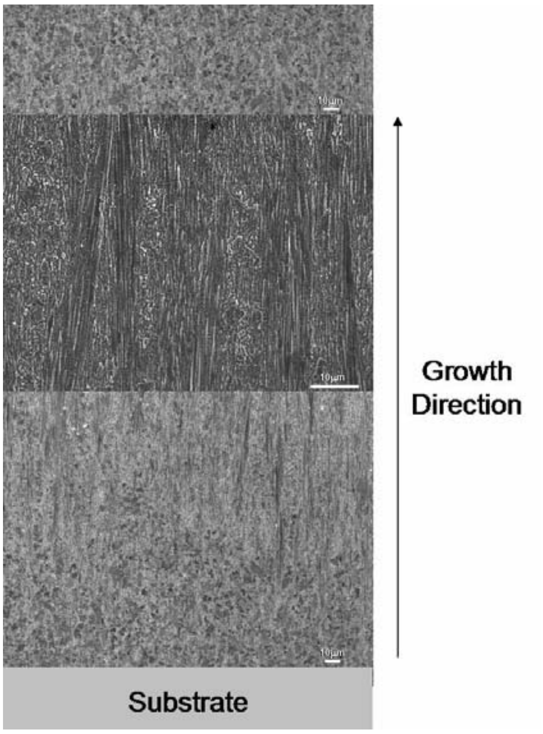

FIG. 5.10. Cross-sectional SEM images of the electrodeposited Cu film along the growing direction.

This observation agreed well with FIB cross-sectioning analysis as shown in Fig. 5.11. Fig. 5.11 (c) shows a transition layer with an equiaxed grain structure near the surface that was originally attached to the silver paint 'seed layer' during the electroplating. This figure also shows the existence of the columnar grains. It is noticed in Fig. 5.11 (b) that some of the columnar grains were 'cut' by a few straight bands about ~100 nm wide. Similar band structures, traversing the columnar grains, were also observed in the 0.5-3 μm thick electrodeposited copper thin films, which are attributed to the twinning of the individual grains during the electrodeposition [161]. Twinning in our samples will be further discussed in the next sub-section.

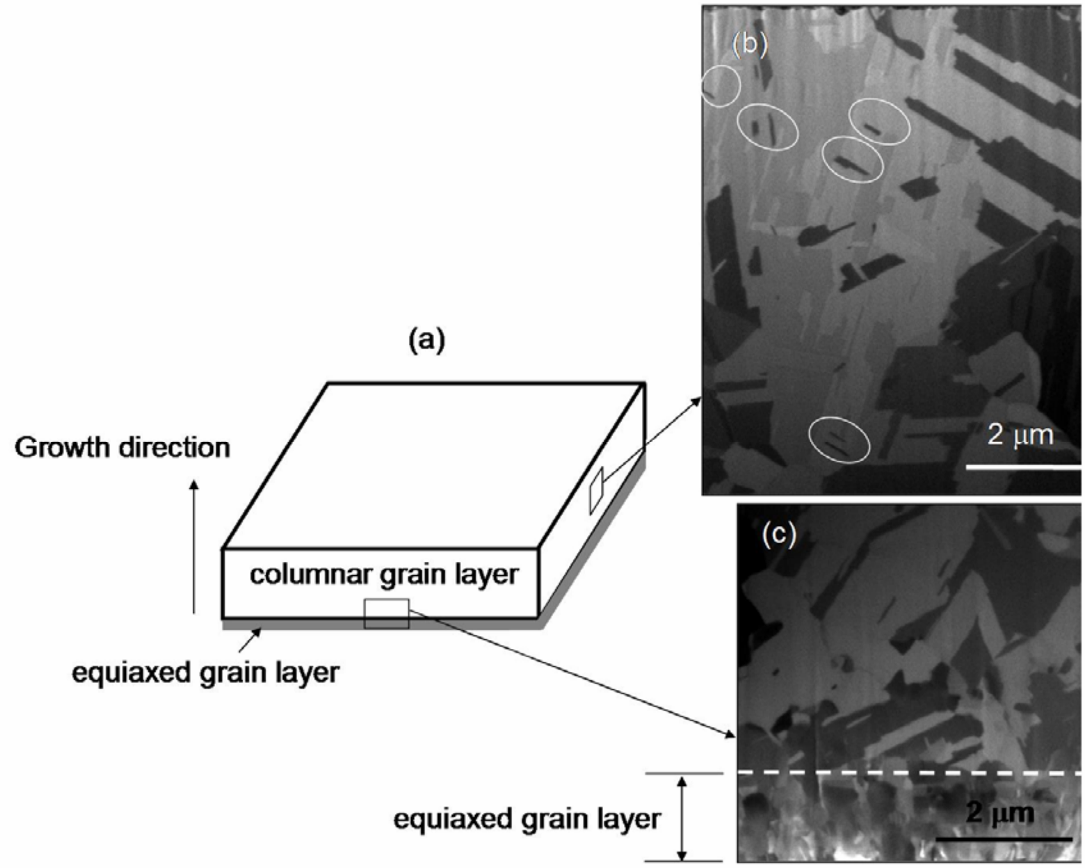

FIG. 5.11. (a) The schematic of the grain structure of the electroplated copper thin foil; (b) the columnar grain structure with the growth twins (as circled), and (c) the equiaxed grain structure.

The structure and the orientation are also presented by EBSD images in Fig. 5.12. This figure shows the columnar structure of the cross-sectional sample with the fine grains on the top layer. This is the same as the observations by other methods discussed before. An out-of-plane <111> and <110> texture in the thickness direction is displayed in Fig .5.12. In the columnar grain structure, the average width of the columnar grains slightly increased with increase of distance from the transition layer in a similar fashion as reported in Refs.[161, 163, 164]. Among these columnar structures, ultra-fine grains of only a few tens or hundreds of nanometers were observed as shown in Fig. 5.10.

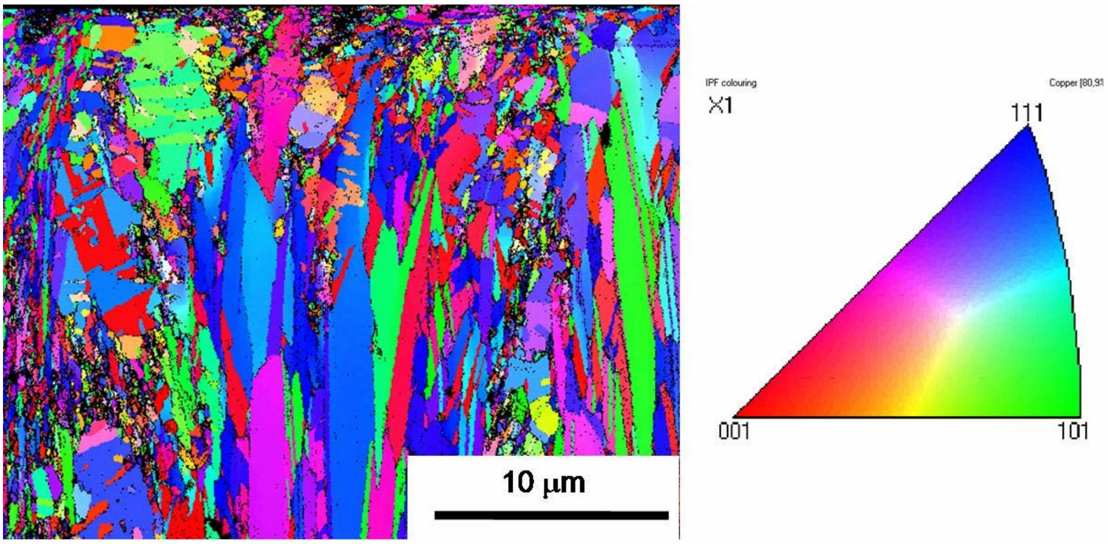

FIG. 5.12. EBSD mapping of the grain orientations of the cross-sectional view in the as-deposited copper thin foil.

From the cross-sectional analysis by means of SEM, FIB and EBSD, it is clear that the structure of an electrodeposited Cu film with a thickness of 1 mm was composed of three zones: an equiaxed transition layer with a thickness of ~20 to 30 µm; the columnar structure in the fine grain matrix with 90% thickness of the whole film; and another equiaxed layer with a thickness of ~20 to 30 µm at the solution side. The equiaxed transition layer is probably induced by the comparatively high deposition rate in the first few hours with the effect of the substrate on the texture. This is consistent with the previous studies [116, 125]. As time passed, the grains chose the preference orientation and grew as columnar structures. The last few tens of micrometers thickness of fine grains formed under the effect of current density and the electrolyte [116].

5.2.1.1.2 Overview - transverse

To reveal the growth of grains during the 78 hours, the transverse microstructures at the substrate side, the depths of 270 and 700 μm, and the solution side of the 1 mm thick sample were analyzed by TEM and are shown in Fig. 5.13.

At the beginning of the ED process, the grain started to form randomly. The grains formed at that moment were relatively small with a size of around ~40 to 320 nm, as shown in Fig. 5.13 (a). A small amount of twins with thickness ranging from ~40 to 260 nm were also observed, as shown in Fig. 5.13 (b).

At the depth of 270 μm, i.e. after deposition for ~24 hours, the grains started to grow with an average size of ~200 nm, as shown in Fig. 5.13 (c). The amount of twins was reduced and the sub-grains were usually found within the twins-embedded grains (as the one with the white arrow pointed), as observed in Fig. 5.13 (d). It can be surmised that the growth of the grains with preferred orientation can finally replace the twin structure by migration of the dislocations and hence develop the sub-grains.

As deposition time further increased, the columnar structures developed with the ultra-fine grains embedded in-between, whose cross-sectional view along the thickness has been shown previously in Figs. 5.10 and 5.12. Figs. 5.13 (e-f) show the transverse view of the grains with sizes of a few tens of nanometers. These grains were surrounded by a bundle of ultra-fine grains of sizes of a few hundreds of nanometers which are believed to be the composition of the columnar grains.

At the solution side of the Cu film where the ED process was about to finish, the size of the grains further increased. This is quite different from the results obtained in SEM and EBSD images as aforementioned. It is probable that the first few tens of micrometers of the Cu film were polished during the preparation for the TEM samples. Moreover, it is clear that there was a large amount of twins with thickness ranging from ~40 to 440 nm. Some of them singularly existed in the grains, as shown in Fig. 5.13 (g); some of them existed as a bundle filling the entire grain with rather wide thickness, as shown in Fig. 5.13 (h). It is believed that the increasing formation of the twins structures results from the strong surface energy originated from the electrolyte.

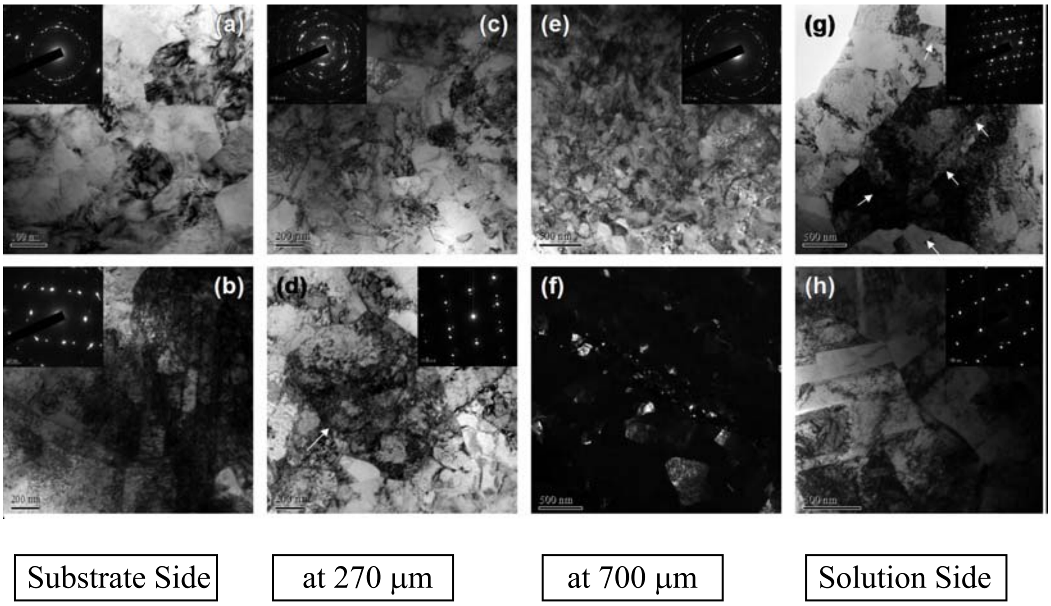

FIG. 5.13. Transverse TEM images at different depths of electrodeposited Cu of 1 mm thickness: (a) substrate side; (b) the depth of 270 μm; (c) the depth of 700 μm; (d) the solution side.

The grain size distributions of these samples are summarized in Figs. 5.14 (a-d), and the twins thickness distribution at the solution side is plotted in Fig. 5.14

(e). A clear trace of the deposition time of the ED process on grain size increment is demonstrated in Fig. 5.15, which agrees well with the observations in the preliminary studies. The comparatively small average grain size at the beginning can be attributed to the relatively high deposition rate at that moment. Meanwhile, the overall grain sizes of electrodeposited Cu with 1 mm thickness were rather large and their distribution range was wide, resulting in the bimodal structure and the ductile characteristics for the sample.

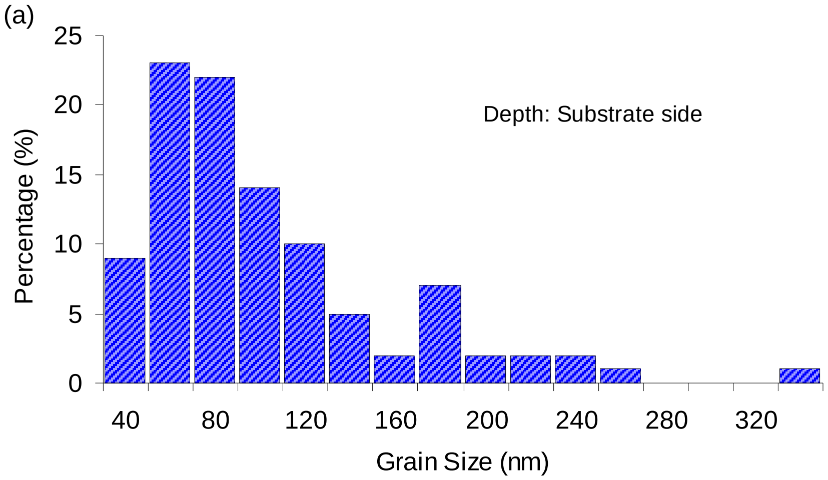

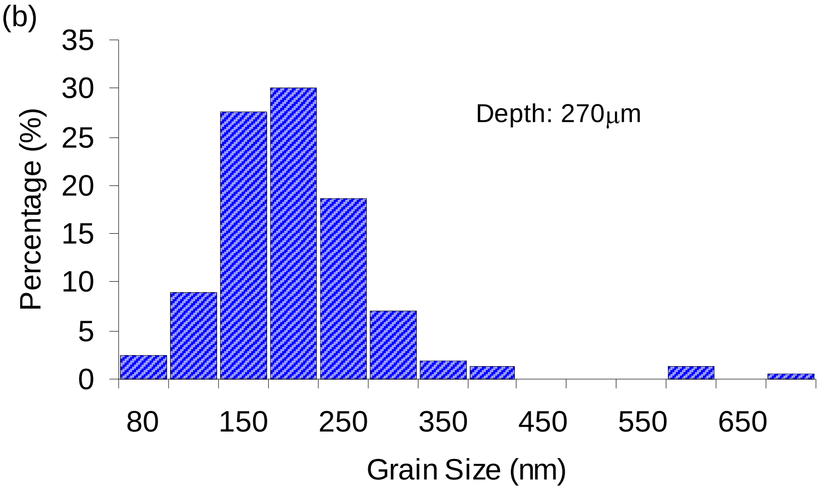

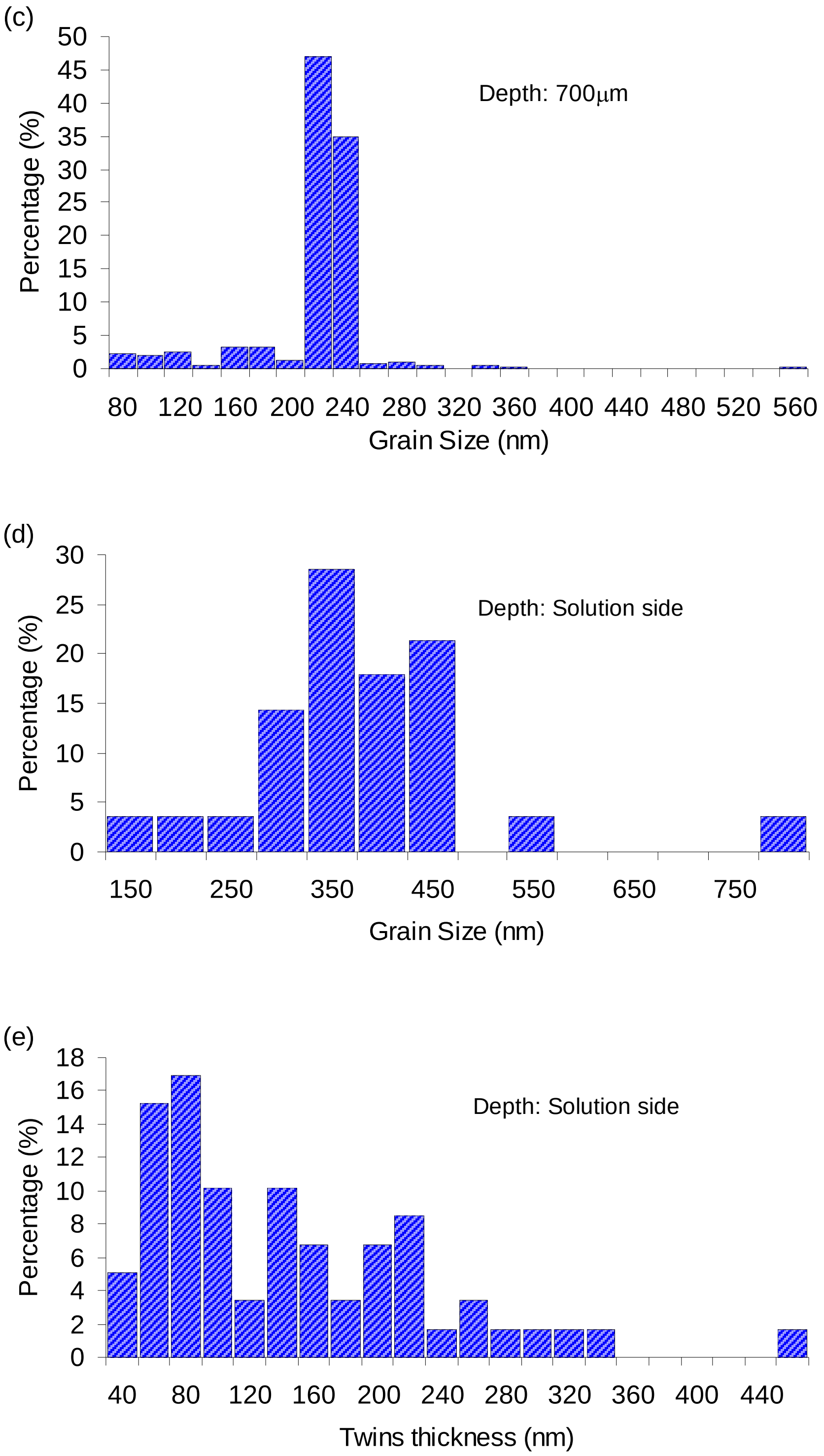

FIG. 5.14. Grain size and twins thickness distribution of the transverse Cu film of 1 mm thickness at different depths: (a) the substrate side; (b) 270 μm; (c) 700 μm; (d, e) the solution side.

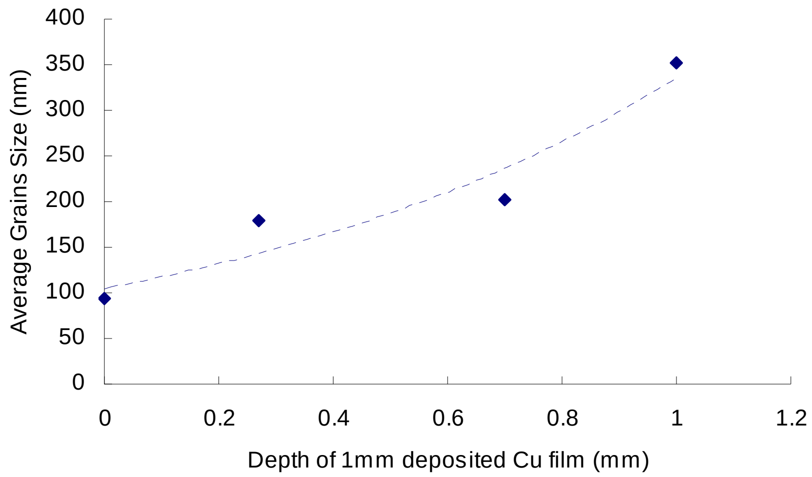

FIG. 5.15. Growth of grain size along the thickness direction of the 1 mm deposited Cu film.

5.2.1.1.3 *Grain size and twins thickness distribution*

As shown in section 5.2.1.1.2, the electrolyte and the deposition duration have great influences on the microstructures of the electrodeposits. In this section, the microstructures at the solution sides of transverse samples obtained in different deposition durations, i.e. 1.5, 3, 15 and 48 hours, were also examined by TEM. The obtained images are shown in Figs. 5.16 (a-j). The transverse TEM images of the sample with the deposition duration of 78 hours are also displayed in Figs. 5.16 (k-l) for comparison.

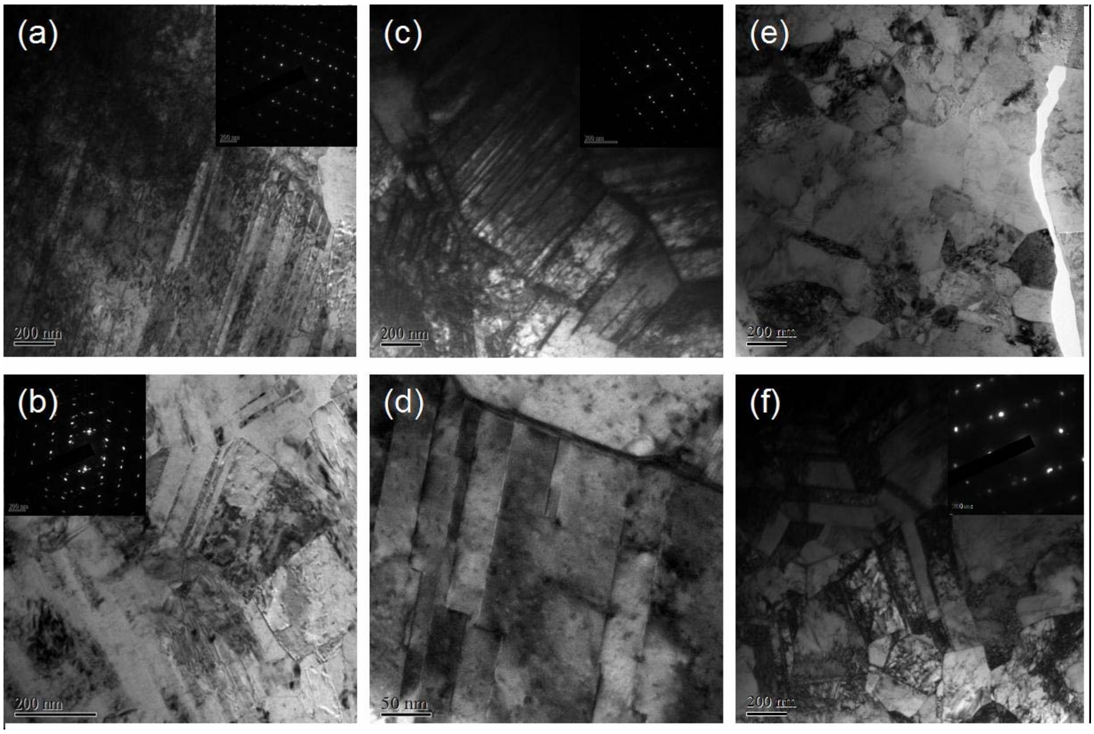

1.5 hours 3 hours 15 hours

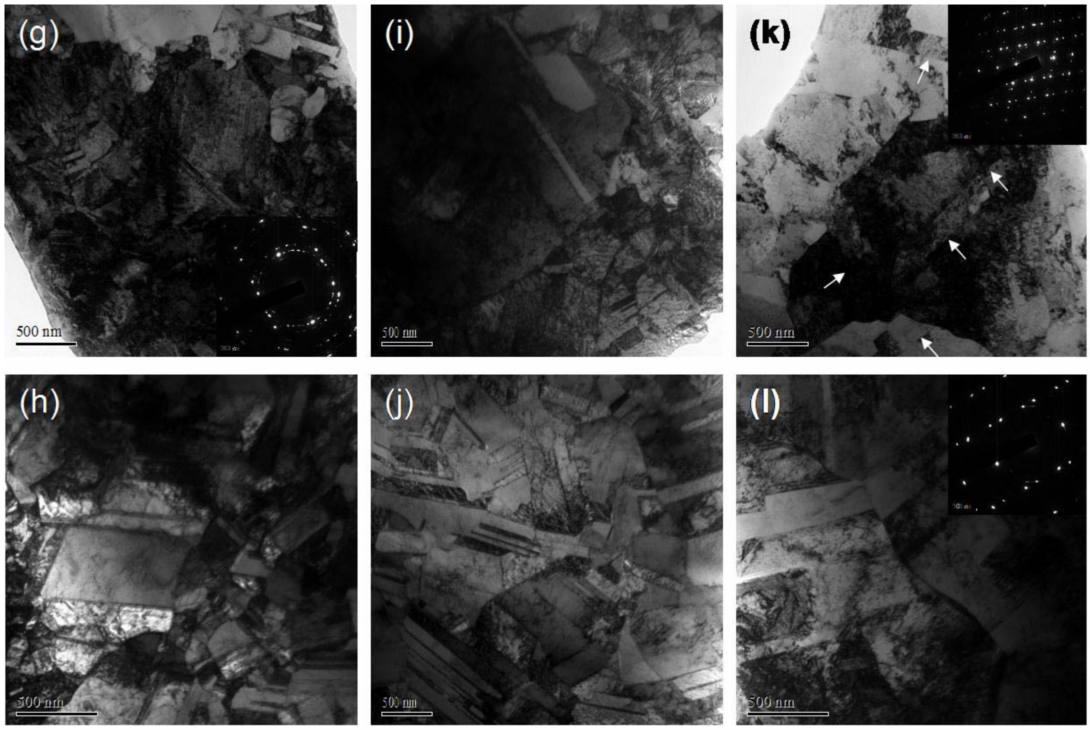

24 hours 48 hours 78 hours

FIG. 5.16. Transverse TEM images of electrodeposited Cu film obtained by different deposition times: (a-b) 1.5 hours; (c-d) 3 hours; (e-f) 15 hours; (g-h) 24 hours; (i-j) 48 hours; (k-l) 78 hours.

After deposition for 1.5 hours, the thickness of the Cu film was ~30 μm. A large number of twins with thickness in the range of ~20 to 240 nm were discovered in this sample (Figs. 5.16 (a-b)). The lengths of the twins were about several hundred nanometers. The grain sizes were small and in the range of ~40 to 320 nm, with an average size of 80 nm. However, the grain boundaries were quite vague.

As the deposition time increased to 3 hours, grains with clear boundaries then developed with increasing numbers of narrow twins inside, as shown in Figs. 5.16 (c-d). Cu film produced with this deposition time was covered with over 95% twins and had the average twins thickness of 68 nm and grain size of 80 nm. Similar to the sample obtained by a deposition of 1.5 hours, the lengths of the twins were several hundred nanometers.

When the deposition time increased to 15 hours and Cu film had the thickness of 160 μm, the number of small grains without containing a twins structure increased. However, there was still almost a 90% twins matrix. Unlike the previous two cases, the twins matrix was embedded in small grains with rather large thickness. The lengths of the twins were comparatively short, as shown in Figs. 5.16 (e-f). The Cu film obtained under this condition had the average grain size of 107 nm and twins thickness of 79 nm. The Cu film with the thickness of 280 μm, as shown in Figs. 5.16 (g-h), had a similar structure as the one which was 160 μm thick, except for the distribution of the grain sizes. The distribution was in the range of ~20 to 320 nm and was comparatively wide.

When the deposition time increased to 48 hours and the thickness of the Cu film was 530 μm, the grain sizes further increased and narrow twins emerged in some of them, as shown in Figs. 5.16 (i-j). The amount of twins was less than that in the samples discussed previously. As for the length of twins, it increased with the grain size. In the current Cu film, the average grain size was 200 nm and the average thickness of twins was 94 nm. The distributions of the grain size and the twins thickness were both wide. For samples obtained with the deposition duration of 78 hours, the average grain size was 350 nm and the thickness of twins was 133 nm. The distribution of the grain size and the twins thickness of Cu film with different thickness are summarized in Fig. 5.17.

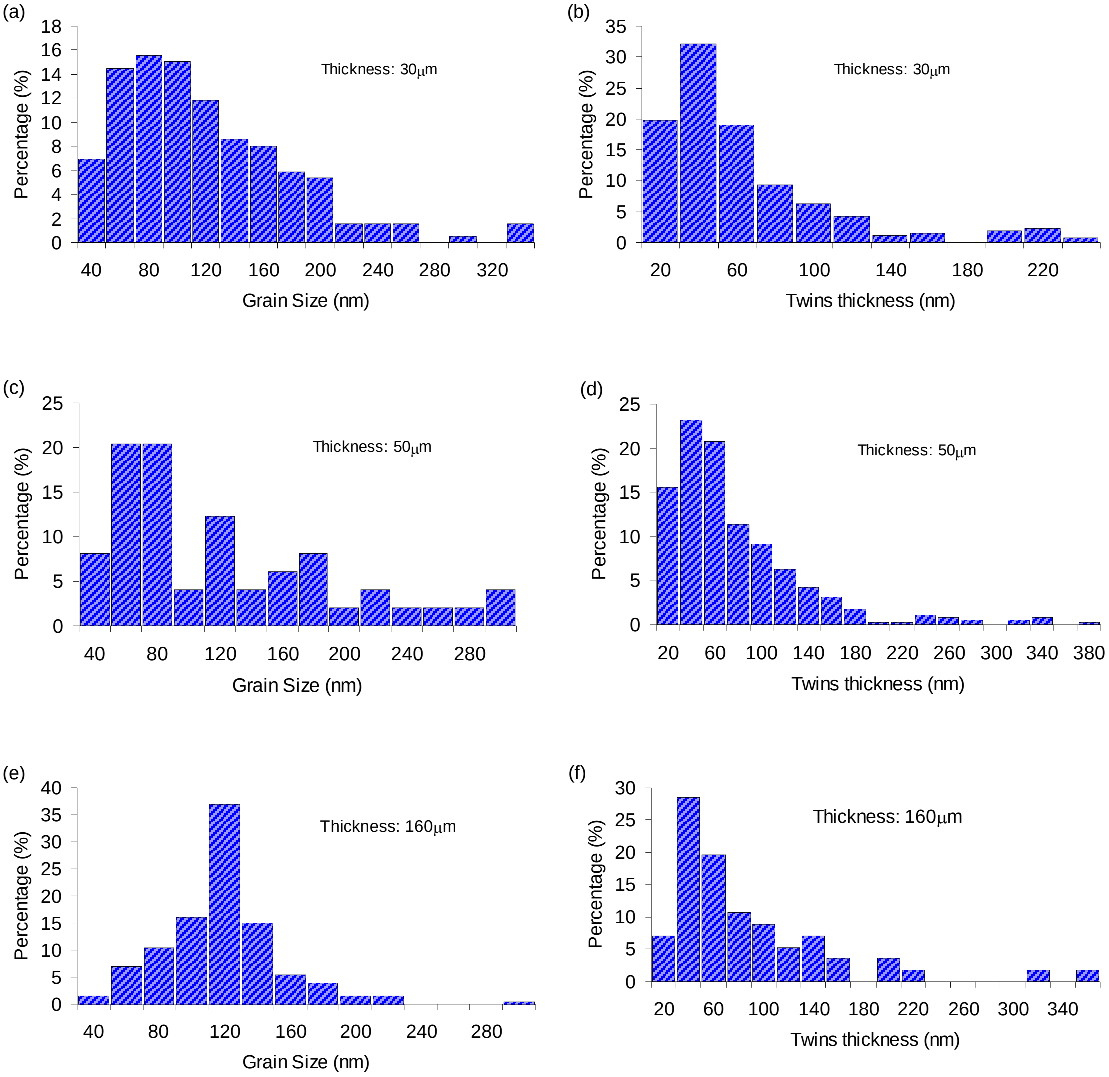

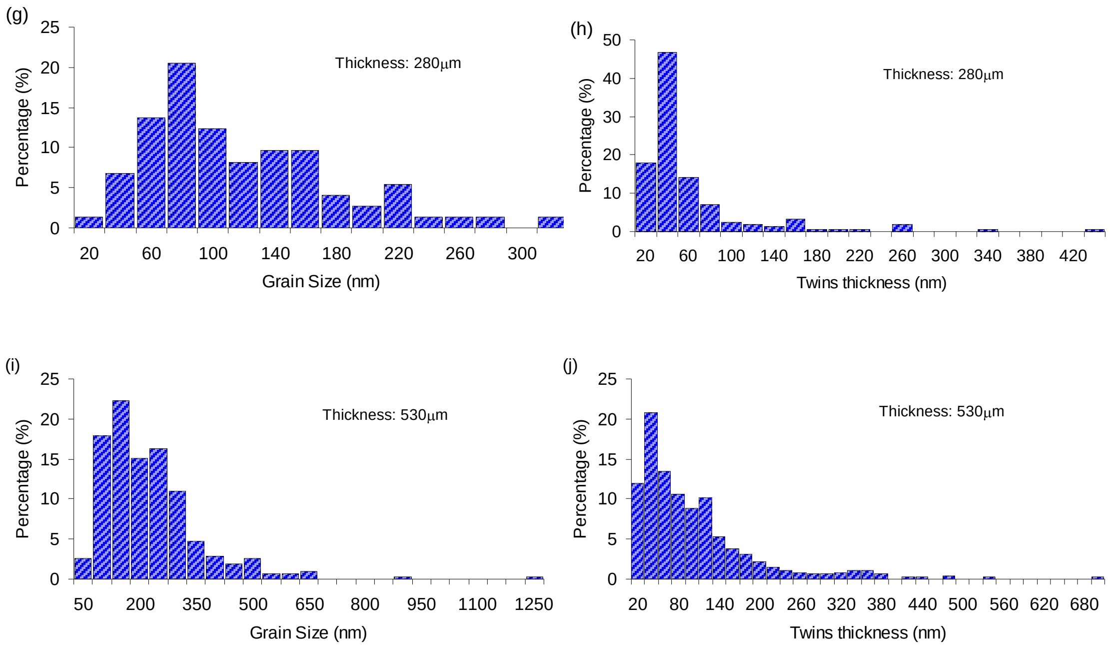

FIG. 5.17. Distribution of the grain size and the twins thickness of samples obtained by different deposition times: (a-b) 1.5 hours; (c-d) 3 hours; (e-f) 15 hours; (g-h) 24 hours; (i-j) 48 hours.

Generally, as the deposition time increased, the grain size increased and the amount of twins decreased. Following this change, the thickness of twins increased and the range of the thickness distribution became wide. The effect of deposition time on the average grain size and the average twins thickness is plotted in Fig. 5.18. It can be seen that the rate of the increase of the grain size and the twins thickness increased with deposition time. As expected, the grains started to grow with special crystallographic orientations after several tens of hours, and hence the columnar structure formed and grew at a higher rate.

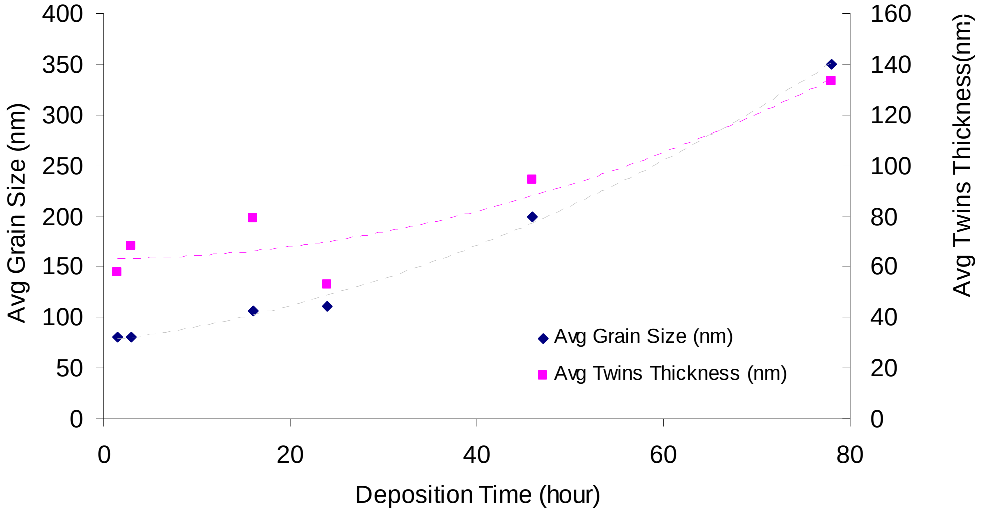

FIG. 5.18. Effect of the deposition time on the average grain size and the average twins thickness.

5.2.1.2 *Texture characterization*

The textures of the electrodeposited Cu films obtained from different deposition duration, i.e. 15, 24, 48 and 78 hours, were analyzed with XRD. Figs. 5.19 and 5.20 demonstrate that both the electrolyte and the deposition duration impacted on the textures. After the substrate was coated with silver paint, some silver element was left on the substrate side of the sample. This silver paint consequently resulted in {111}, {100}, {110} and {311} out-of-plane silver-corresponding textures which coexisted with the original Cu-related textures: {111}, {100}, {110} and {311}. The initial layer of Cu deposited on Ag was observed to inherit {111} and {110} out-of-plane texture of the Ag layer.

Meanwhile, the solution side of the Cu film which was obtained by a deposition duration of 15 hours had only the {111}, {100}, {110} and {311} out-of-plane textures of Cu elements with a very strong {110} out-of-plane texture.

The texture intensity of the solution side was stronger than that of the substrate side, as observed from Fig. 5.19.

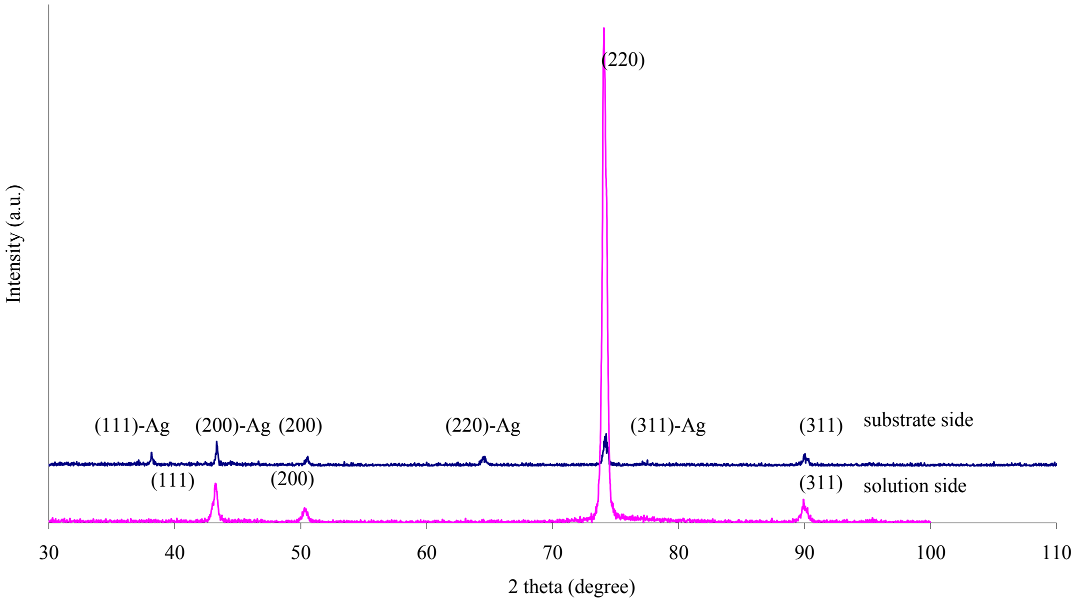

FIG. 5.19. XRD patterns of the substrate and solution sides of the electrodeposited Cu film.

For all of the deposited films obtained from different deposition time, the types of textures were the same. However, the texture intensity decreased as the deposition time increased. When the deposition time increased to 78 hours, the strong out-of-plane texture changed from {110} to {111}, as shown in Fig. 5.20. The probable reason for this phenomenon is that the substrate effect on the texture decreased as the deposition duration and the thickness of the sample increased. Consequently, the effect of the solution or current density took place when the deposits grew farther away from the substrate. Contrary to the intensity of the strong texture in the samples obtained with short deposition time, the intensity of {111} on sample deposited for 78 hours did not have such large differences compared to the textures of the other samples.

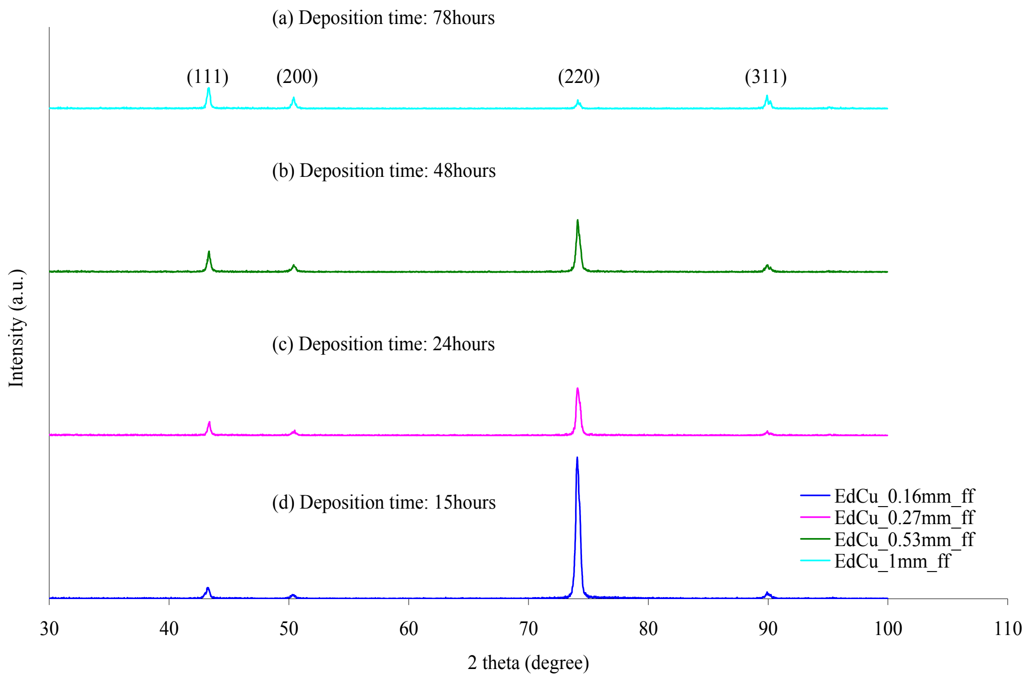

FIG. 5.20. XRD patterns of the solution sides of the electrodeposited Cu film obtained with different deposition times: (a) 78 hours; (b) 48 hours; (c) 24 hours; (d) 15 hours.

As mentioned before, the columnar structures grew with the deposition time. Fig. 5.21 demonstrates the orientation map taken by EBSD for the sample deposited for 78 hours. The cross-section along the thickness direction containing the columnar structure embedded with equiaxed grains is shown in Fig. 5.21 (a). The corresponding transverse view at the 0.6 mm depth is displayed in Fig. 5.21 (b). It can be seen that the columnar structures are composed of small grains with similar texture, <220> // ND; the equiaxed grains in-between were rather random, but still had a preferential texture, <102> // ND. Combined with the results obtained from XRD, it seemed that the strong out-of-plane texture, {110}, of the samples deposited for 15 to 48 hours was the implication of columnar structure. Therefore, the columnar structure intended to grow in a particular direction, <220> // ND, under the effect of the substrate.

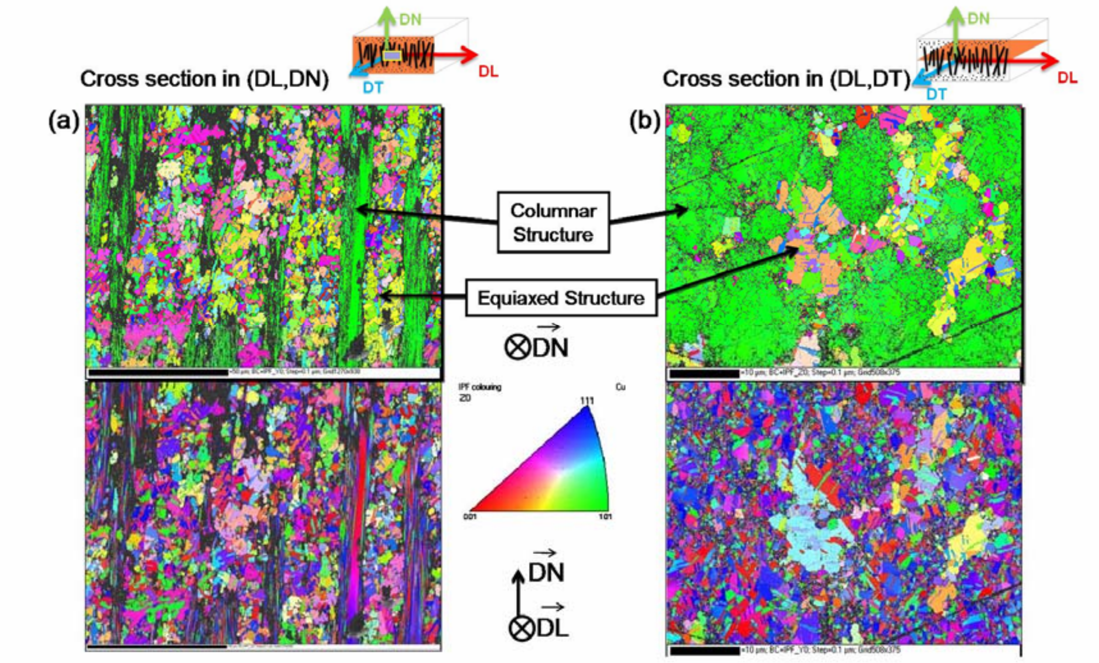

FIG. 5.21. EBSD images of the sample deposited for 78 hours: (a) cross-sectional view along the thickness direction showing the columnar and equiaxed structure; (b) transverse view at the depth of 0.6 mm away from the substrate showing the columnar structures have a similar texture, <220> // ND, and equiaxed structures with the texture of <102> // ND.

5.2.1.3 *Fracture mechanism*

In the observations from the previous parts, the measured 0.2% offset yield strength and ductility exhibited a thickness-dependent behavior. The increase of the thickness (also in terms of deposition time previously) of the specimens led to the reduction of the yield strength (YS) and the improvement of the ductility when the deposition time was less than 48 hours and the thickness was smaller than ~0.5 mm, as shown in Fig. 5.22. When the thickness of the samples is large enough, their YS changed slowly but their ductility was further promoted with increase of thickness. The thickness-dependent behavior has been discussed in view of grain size distribution. In this section, it will be further discussed from the perspective of fracture mechanism.

Beforehand, a standard mechanical analysis by applying the classical theory of J2 plasticity was performed to compare the necking strains of electrodeposits of different thickness in both plane stress ($\overline{\sigma} = \sigma_{11}$, $\overline{\varepsilon} = \varepsilon_{11}$) and plane strain ($\overline{\sigma} = \frac{\sqrt{3}}{2}\sigma_{11}, \overline{\varepsilon} = \frac{2}{\sqrt{3}}\varepsilon_{11}$) conditions in order to manifest if the plane stress and the plane strain play roles in the difference of the necking and fracture behaviour between the thinner and the thicker samples. The results show that the difference of the necking strains under these two extreme conditions was less than 10% for all the electrodeposits with various thicknesses. This indicates that the thickness effect may be the more dominant explanation for the different fracture behavior among electrodeposits of different thickness.

In line with the variation in ductility, the angle of the fracture plane with respect to the loading axis, together with the necking morphologies, also showed a dependence on the grain size and thickness, as shown by the insets of Fig. 5.22. At the thickness of 0.5 mm or smaller, i.e. the average grain size of ~200 nm or smaller obtained from a deposition duration of 48 hours or shorter, the fracture angles were about ~45° with limited material necking in the width direction. In contrast, when the fracture angle changed to ~90° at a thickness of 1.0 mm, i.e. the average grain size of ~350 nm obtained from the deposition duration of 78 hours, necking was appreciable in the width direction.

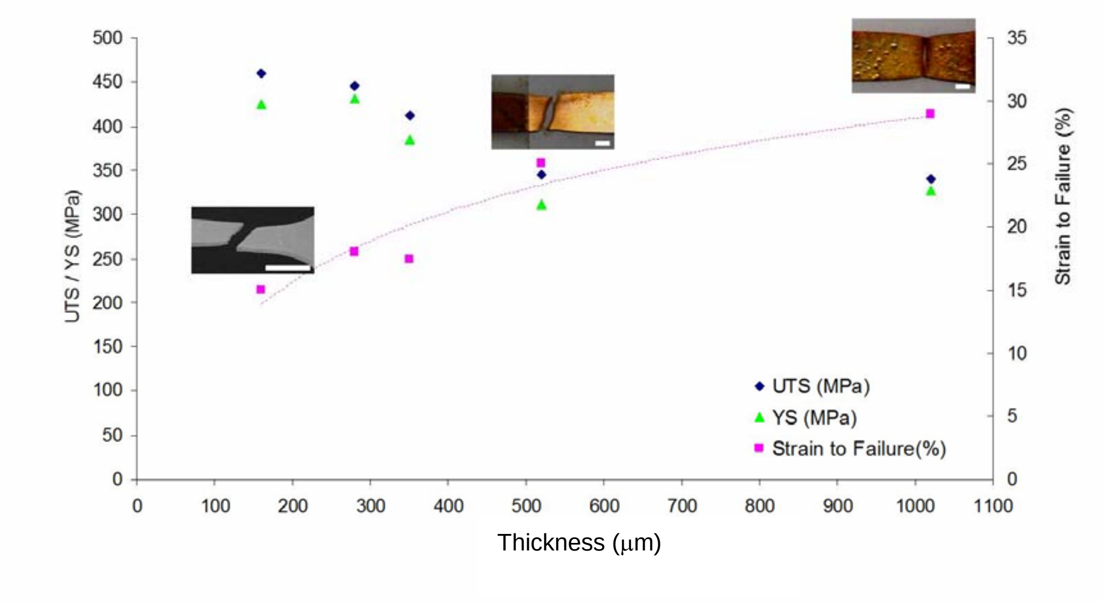

FIG. 5.22. Variation of the measured yield strength, ultimate tensile strength and ductility with the specimen's thickness (the insets display the angle of the fracture plane at different specimen thickness and the embedded length scales, as indicated by the white line segments, corresponding to 1 mm).

In order to observe the fracture mechanism, *in-situ* SEM tensile experiments were performed on three sets of samples with thickness of 0.5, 0.7 and 1.0 mm, respectively. These three sets of thickness are chosen with the purpose of revealing the role of columnar structure in the thickness effect in the thicker thin film. Two sets of fixtures were adopted in these experiments, with which the deformation and failure processes in the copper thin foils could be imaged either in the mode of 'top view' or 'side view' by the SEM.

In Refs [161, 164-166], the plastic deformation process in an electrodeposited metallic thin film was postulated to occur in a sequential manner. The materials with the largest columnar grains first yielded, thus triggering a domino type of yielding process in the columnar grain structure. In the present tensile experiments, this was manifested by the asymmetrical necking in the thickness direction, as shown in Fig. 5.23. Numbers at the left top corner state the occurring sequence. Conforming to the previous postulation, the plastic flow initially occurred in the coarse-grain regions and then propagated towards the fine-grain regions. It should be emphasized that the trend of the asymmetrical necking in the thickness direction was observed to be irrespective of the specimen's thickness. However, the extent of necking was found to display a thickness-dependent behavior in accordance with the measured ductility. Based on the experimental findings, it is believed that the thickness effect on the yield strength was caused by the grain size distribution in the columnar grain structure.

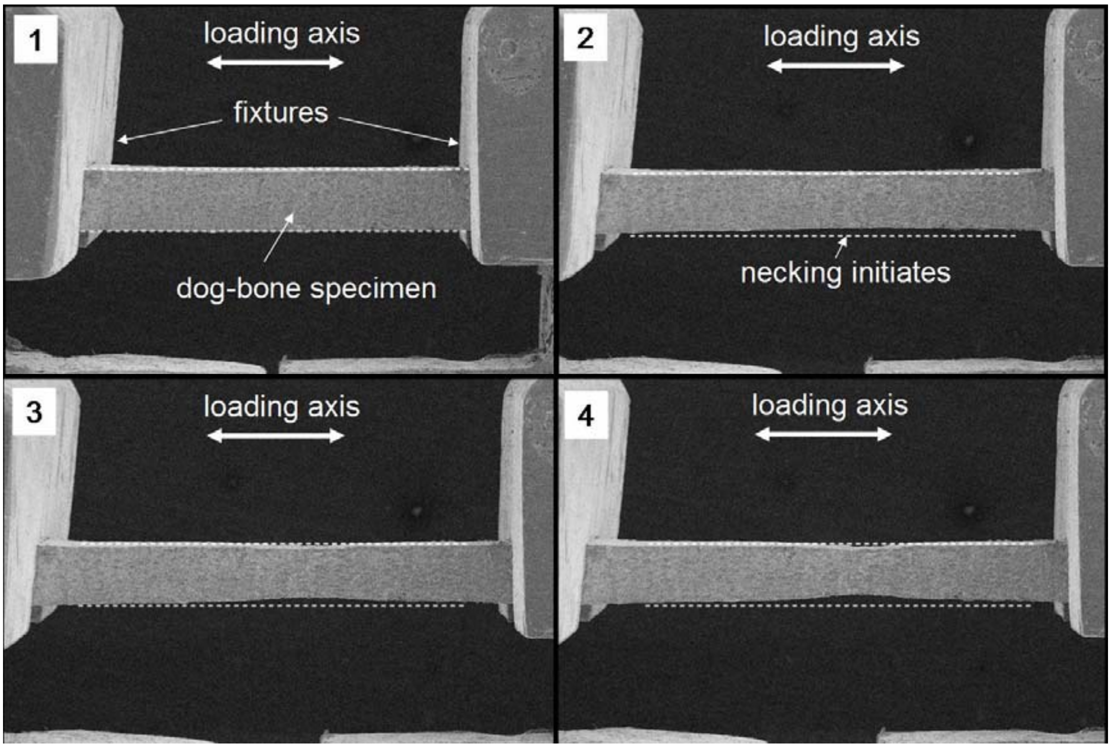

FIG. 5.23. The side view of the deformation sequence in a ~0.7 mm thick copper thin-foil showing the asymmetrical necking morphologies in the thickness direction (note that the dashed lines mark the positions of the two edges on the side surface of the undeformed dog-bone specimen).

For the ~1 mm thick dog-bone specimens, the in-plane plastic deformation occurred in a homogeneous manner prior to necking. When the necking developed to stage 3, both edges of the specimen's top surface curved inward symmetrically (Fig. 5.24). The symmetrical necking behavior is consistent with the in-plane random orientations of grains as revealed by EBSD (Fig. 5.12(a)). The curvature of the necking region increased progressively with the plastic deformation but it was saturated when stage 4 was reached, at which the surface of the necking region was significantly roughened.

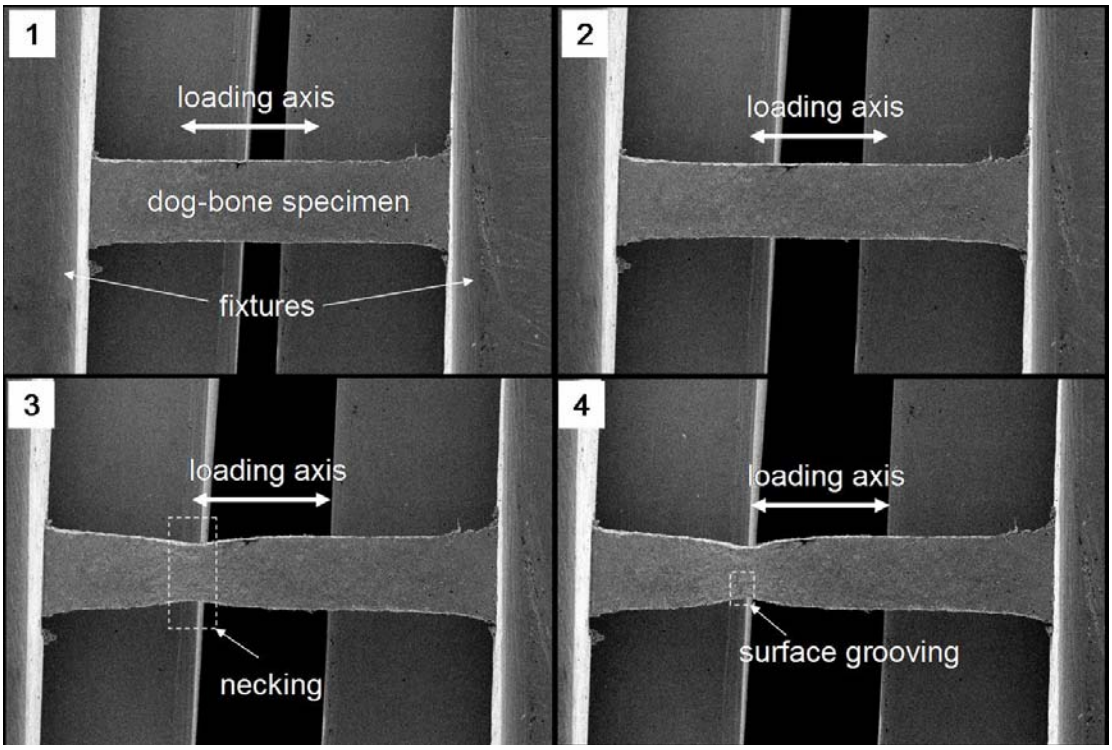

FIG. 5.24. Top view of the deformation sequence in a ~1 mm thick copper thin foil.

Fig. 5.25(a) shows the SEM image of the roughened surface at a higher magnification. Surface grooves became visible around the roots of the curved edges. In stage 3, the surface grooves evolved into an inclined shear plane and the lateral necking ceased to develop. The stretching of the dog-bone specimen was then accommodated by the sliding of materials along the inclined shear plane, as shown in Fig. 5.25(b). With the further plastic deformation, cavities developed and emerged on the shear plane, and then formed a center crack in the dog-bone specimen, as displayed in Fig. 5.25(c). The mode I propagation of the center crack towards the two edges of the dog-bone specimen finally led to the fracture with an apparent fracture angle of about ~90° with respect to the loading axis, as shown in Fig. 5.25(d).

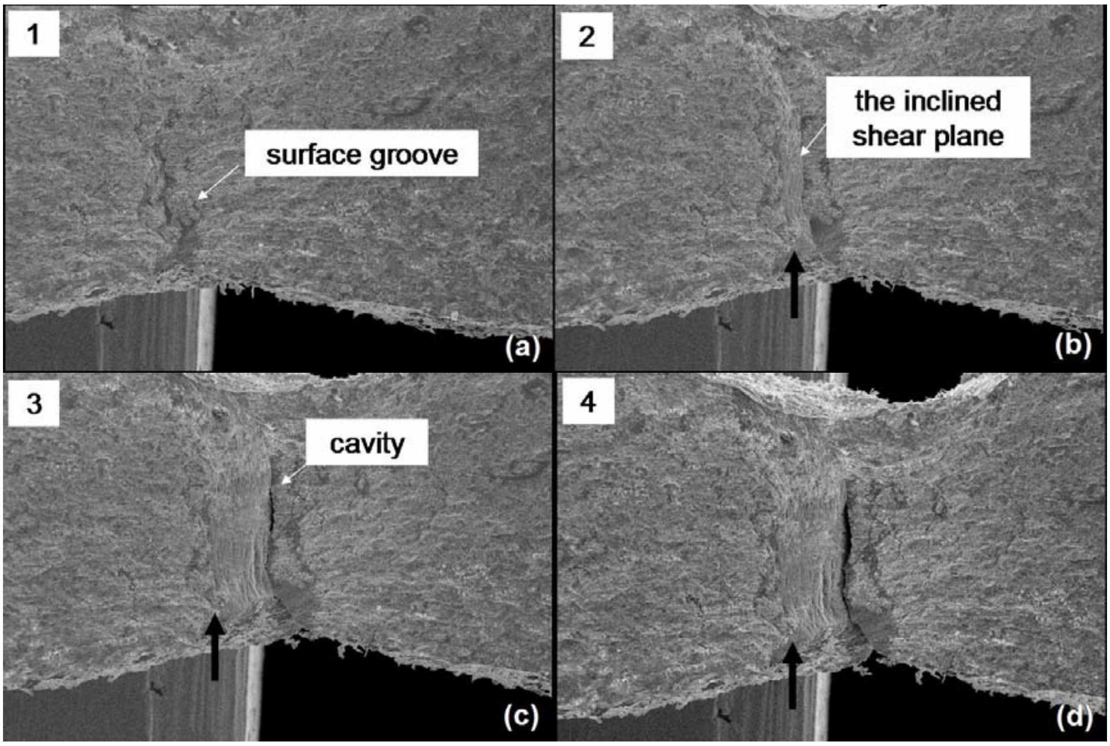

FIG. 5.25. (a-d): The failure process of the ~1 mm thick dog-bone specimen (the arrows indicate the transition of position from the specimen's top surface to the inclined shear plane).

In sharp contrast, the 0.5 mm thick copper thin foil displayed a 45°-oriented fracture in the in-situ SEM tensile experiment as shown in Figs. 5.26(a–d). Similar to the previous case, necking was initiated from a geometrical imperfection along the edge of the specimen's top surface, as shown in Fig. 5.26(b). However, at stage 3, an inclined edge crack, having an angle of about ~45° with respect to the loading axis, was nucleated in the necking area (Fig. 5.26(c)). Final fracture then occurred due to the mode II crack growth (Fig. 5.26(d)).

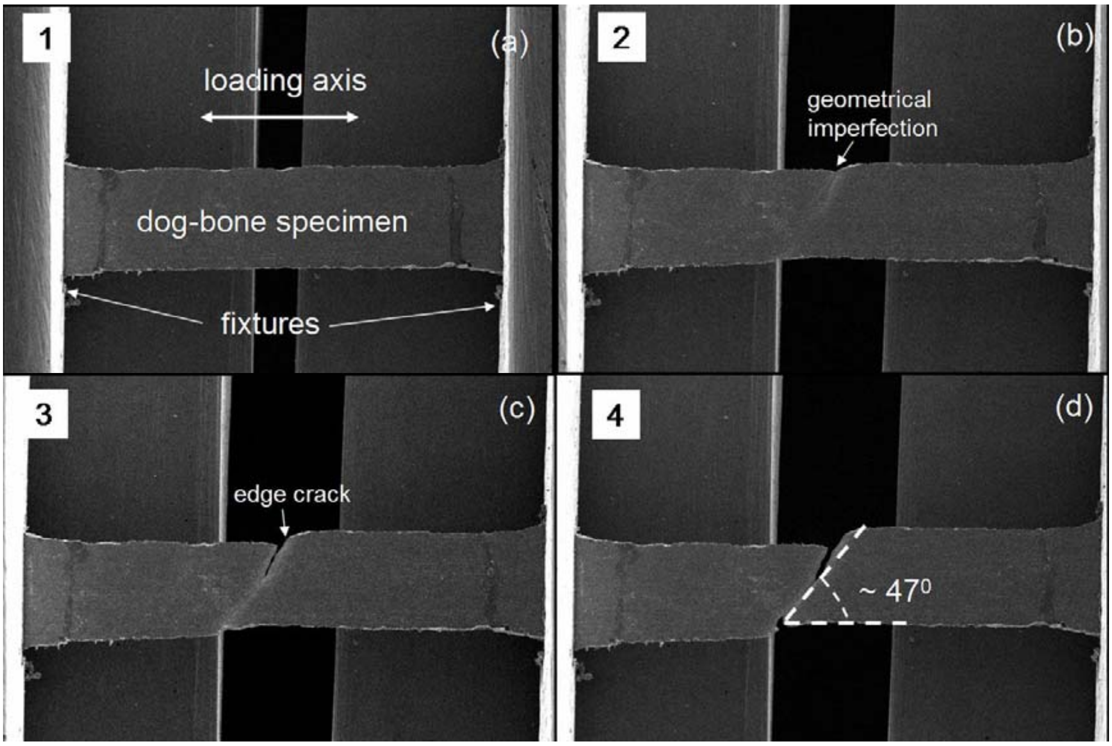

FIG. 5.26. (a-d): Top views of the deformation and failure processes in a ~0.5 mm thick copper thin foil.

Fractographic analysis of the above two fracture modes indicated two different microscopic failure processes. For the 1.0 mm thick dog-bone Cu thin foil, voids of the ellipsoidal shape were visible on the fractured cross-section (Figs. 5.27(a) and (b)). Due to the high width-to-thickness ratio, the void growth was apparently biased towards the width direction and the subsequent void coalescence took place through the necking and breakage of the inter-void ligaments. In contrast, no appreciable void growth was observed on the fractured cross-section of the 0.5 mm thick dog-bone Cu thin foil (Figs. 5.28(a-c)). Void coalescence occurred through the shearing of voids in the inclined plane (Fig. 5.28(a)).

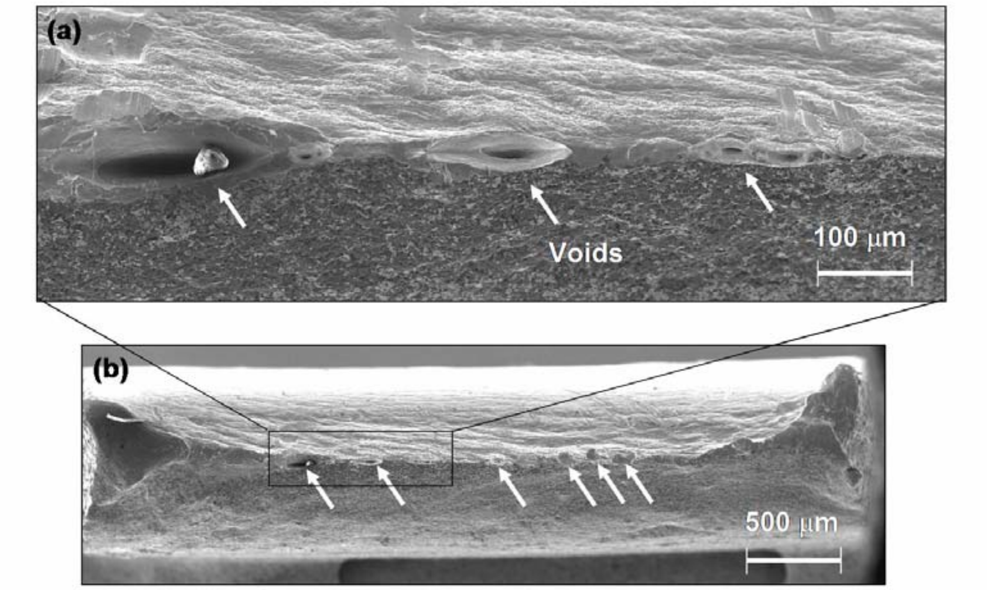

FIG. 5.27. (a-b): The fractographic features on the cross-section of a broken 1.0 mm thick Cu thin foil.

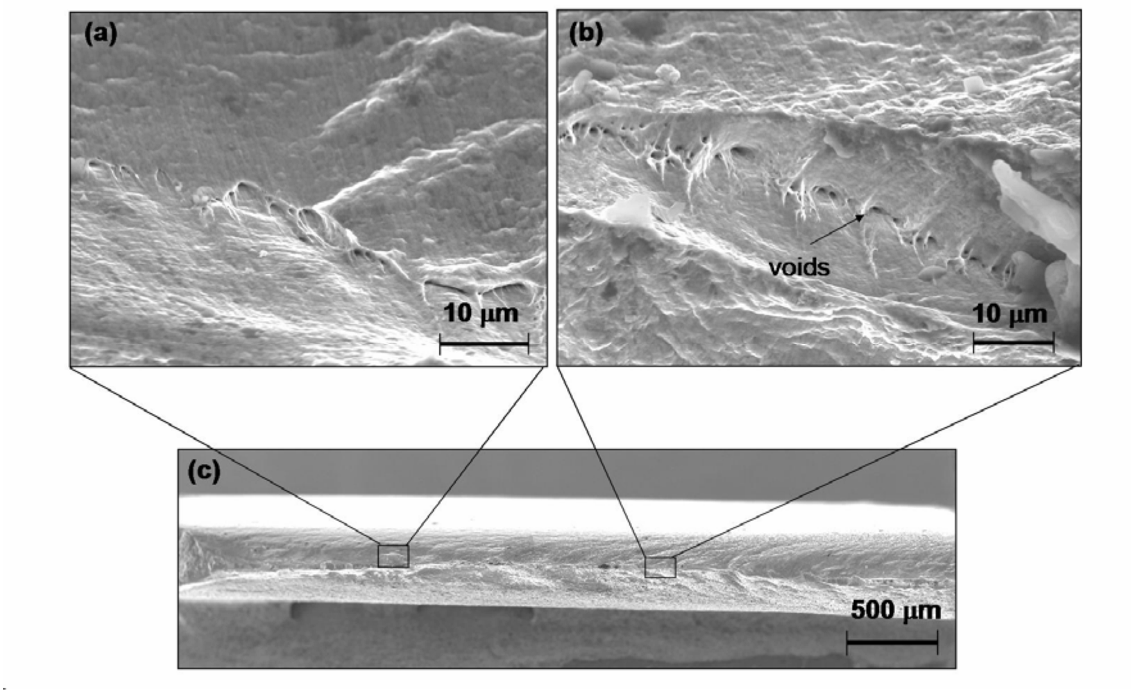

FIG. 5.28. (a-c): The fractographic features on the cross-section of a broken 0.5 mm thick Cu thin foil.

Similar fracture mode transition was reported in the fracture of the notched 2024 aluminum alloy thin sheets [167]. In the proximity of the notch root with high stress triaxiality, the voids grew and coalesced through the internal necking of the inter-void ligaments. However, as the stress triaxiality decreased with increase of distance from the notch root, the void growth was restricted due to the low hydrostatic stress and the void coalescence was triggered by the shearing of the inter-void ligaments. The above mechanisms were also investigated and confirmed by the numerical simulations using the finite element method (FEM) [168].

In our experiments, besides the grain size effect caused by deposition time, the stress triaxiality in the thin-foil specimen after necking was also related to the original specimen's geometry. At a given specimen's gauge width, increasing the gauge thickness promoted the degree of necking in the width direction and vice versa (Figs. 5.25 and 5.26), thus resulting in the different stress triaxiality in the center of the necked region. For thick thin foils, the high stress triaxility favored the internal necking mechanism for void growth and coalescence, giving rise to a 90°-oriented fracture plane; for thin ones, the low stress triaxility favored the void-shearing mechanism and resulted in a 45°-oriented fracture plane, as illustrated in Fig. 5.29.

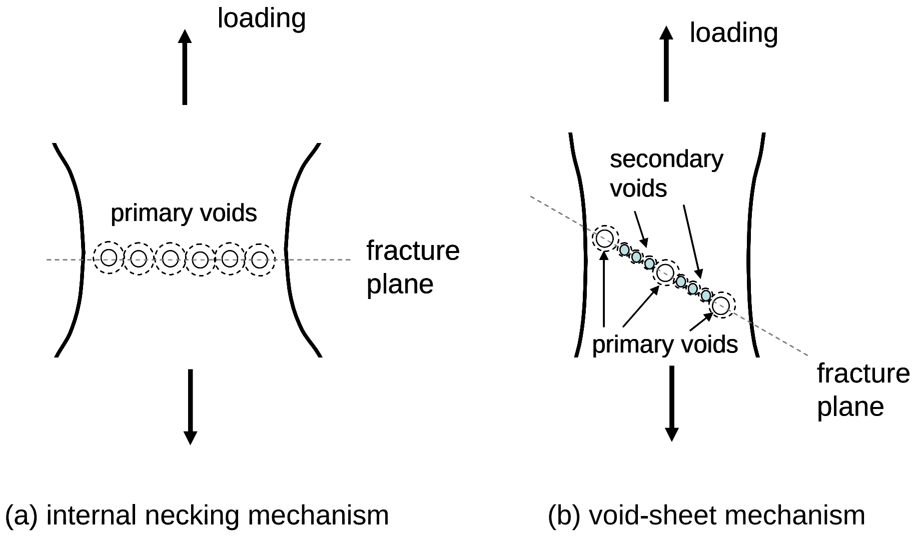

FIG. 5.29. Schematic illustrations: (a) internal necking mechanism; (b) void-sheet mechanism for the thicker thin film (~1 mm) and thinner film (~0.5 mm) respectively.

5.2.2 Hall-Petch relation

The effects of the average grain size on the ultimate tensile strength (UTS), yield strength (YS), strain to failure are plotted in Fig. 5.30. As observed from this figure, increasing grain size resulted in the reduction of both the ultimate tensile and the yield strength, while improving the ductility.

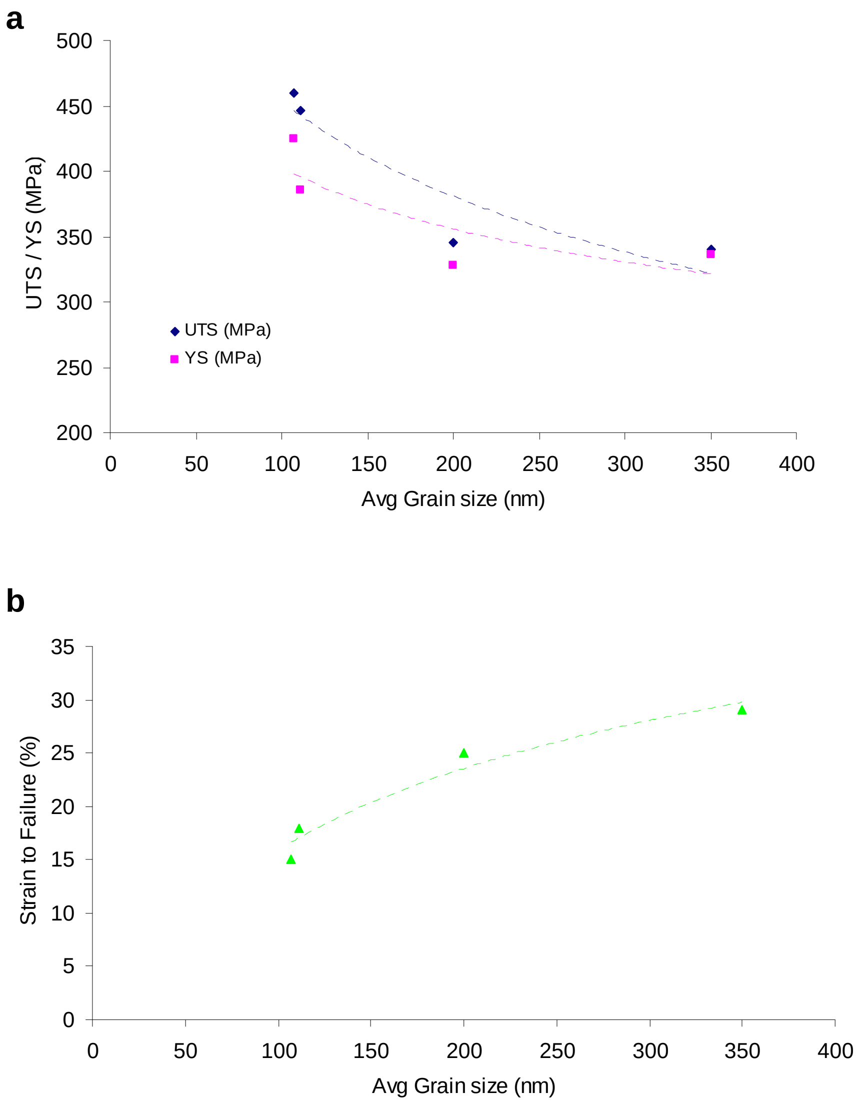

FIG. 5.30. Effect of the average grain size on: (a) the ultimate tensile strength and yield strength; (b) strain to failure.

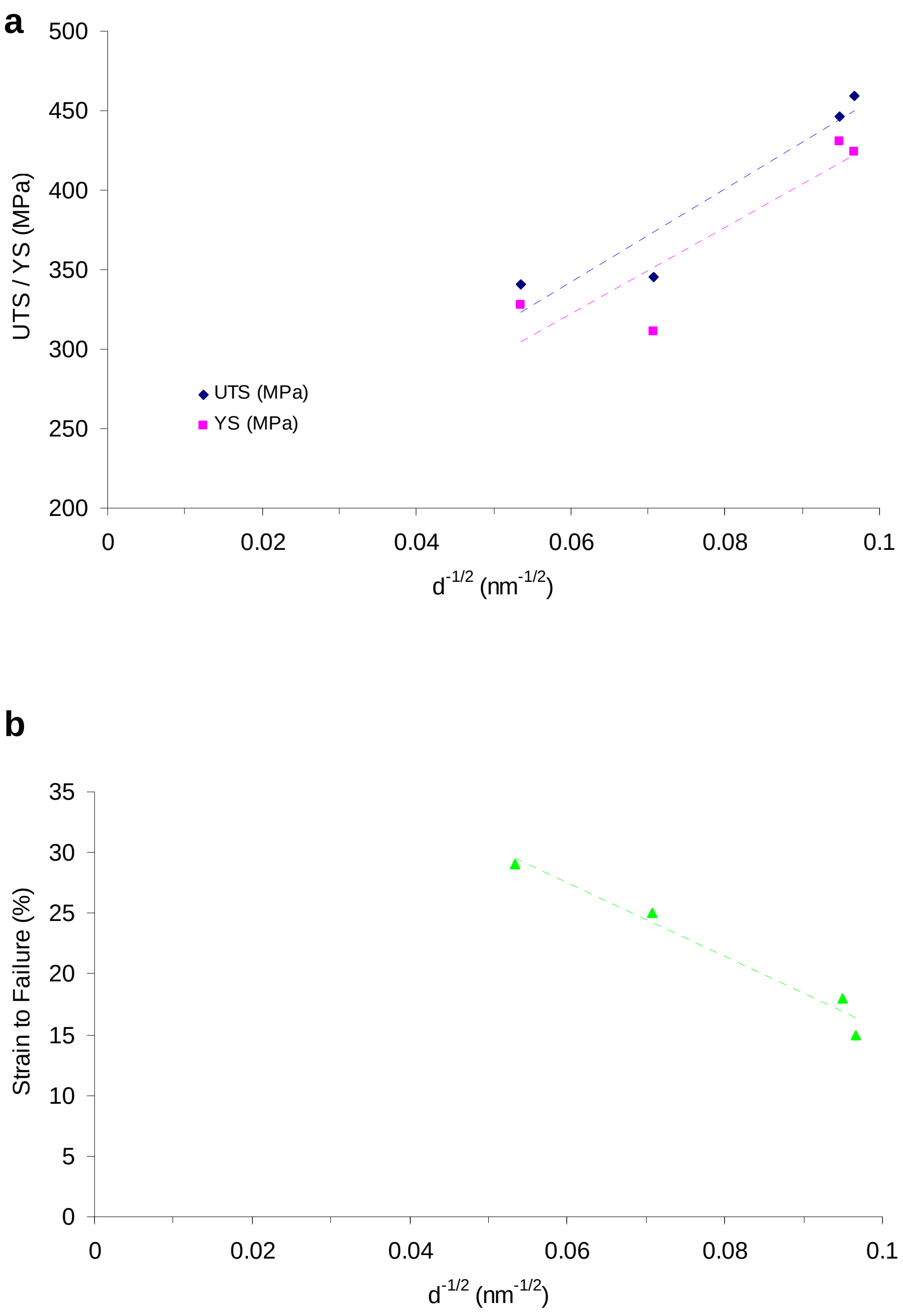

FIG. 5.31. Effect of the inverse of the square root of the grain size on: (a) UTS and YS; (b) strain to failure.

To compare to the conventional Hall-Petch relation and the similar relations developed in previous works, the variations of UTS, YS, and strain with respect to the inverse of the square root of the grain size were examined and are plotted in Fig. 5.31. The relation of YS and the grain size was found to be

$\sigma_{YS} = 2717.2d^{-1/2} + 159.11$ in the current case. This variation trend deviated from the conventional Hall-Petch relation of Cu and those in previous works, as shown in Fig. 5.32. The test samples in previous literatures usually reported a high yield strength and small grain sizes. However, it should be noted that most of these samples had thickness no larger than ~100 μm. Compared with the values of k (~3478.5 MPa) and σ_0 (~25.5 MPa) for Cu in conventional Hall-Petch relation [169], our experimental results were small. The gradient structure of Cu deposits is responsible for this difference. The grain size considered here was the average value; grains with larger size existing in the Cu film might yield first and hence lower the yield stress. Nevertheless, the deviation of our results from the other literatures was still small.

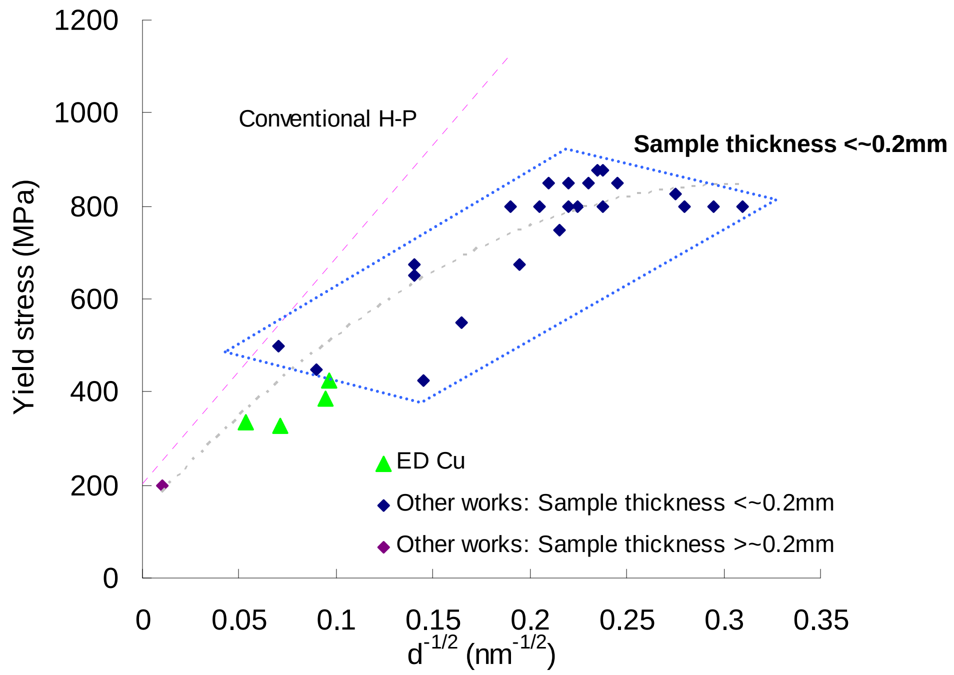

FIG. 5.32. Comparison of the relationship between YS and the grain size of Cu.

5.2.3 Strain hardening exponent

The flow curve of many metals in the region of uniform plastic deformation can be expressed by a simple power curve relation as

$$\sigma = K\varepsilon^{n}, \tag{4.10}$$

where n is the strain-hardening exponent; and K the strengthening coefficient. n is the linear slope of the straight line resulting from a log-log plot of true stress-strain up to maximum load; K is the true stress at $\varepsilon = 1$ [170]. The strain hardening coefficient is one of the indications of the material's characteristic which lies between 0 and 1. A value of 0 means that a material is a perfectly plastic solid; a value of 1 represents a 100% elastic solid.

The strain hardening exponents, n, of electrodeposited Cu film of different thickness in our studies ranged from 0.09 to 0.16 (usually coarse-grained Cu has the n value of 0.35), which are plotted in Fig. 5.33. It can be seen that the smaller the grain size, the smaller the strain hardening exponent. This tendency is consistent with that in reference [51]. Meanwhile, the n value in this study was comparatively small, especially those determined from the thin Cu film with thickness less than 0.5 mm and grain size smaller than ~200 nm. Usually this is attributed to the lack of plasticity for NS materials with smaller grain size since the n value decreases with grain size. However, the extremely small n values are believed to be induced by the near-perfect elastoplastic behavior [159]. As mentioned before, the electrodeposits with thickness less than ~0.5 mm exhibited a small degree or absence of necking before failure. However, the electrodeposits still sustained certain ductility to around 10%. The probable reason is that the grain size presented here was the average grain size, and the effect of the twins structure was not taken into account. Moreover, it is believed that both twins and grain boundaries played significant roles in providing room for the dislocations and hence enhancing the overall ductility. In such case, Fig. 5.33 presents the combined effect of nano-twins and gradient grain size on strain-hardening exponent.

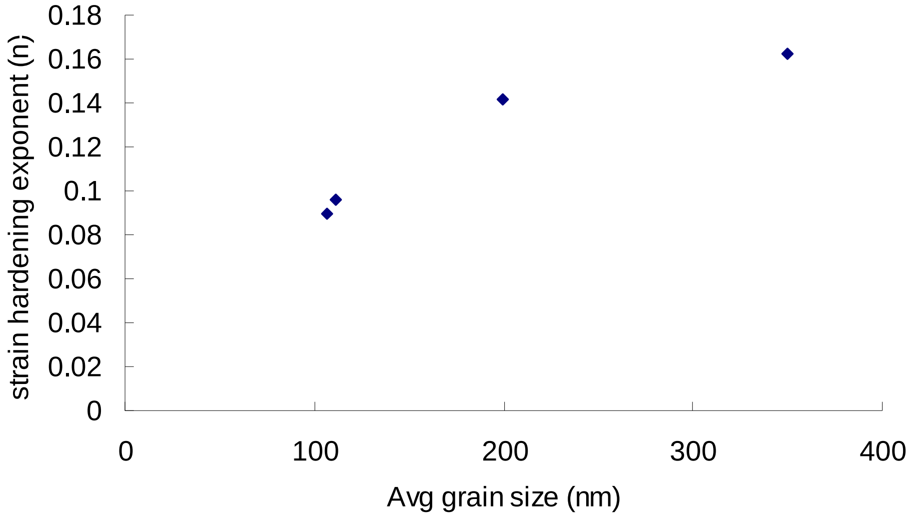

FIG. 5.33. Relation of strain hardening exponent, *n*, and average grain size of the electrodeposited Cu film in this study.

5.3 Concluding Remarks

Pulsed-current type (**pc**) was usually adopted to produce NS materials for its facilitation of the nucleation and inhibition of grain growth in other studies. However, it is necessary to precisely control the on-time and off-time, and also the distance between the anode and cathode (which was seldom addressed by other studies). On the contrary, direct current type (**dc**) was easy to be manipulated. Irrespective of its simplicity, **dc** was rarely used for the production of NS materials because of its allowance of grain growth. In this chapter, the grain growth rate in **dc** type and the effects of other parameters on the deposits were studied. The microstructure, texture and tensile properties of the electrodeposits were also examined.

The electrodeposition (ED) process of Cu conducted in an acidic bath with electrolyte of Cu_2SO_4 on a small mass production scale was studied. Silver paint coated wax was used as the substrate in this study since it can be easily removed after the ED process and is widely applied in industrial applications. The current density of 1.5 A/dm^2 was adopted.

First of all, the effect of current type was studied. The rather porous structures were obtained by **pc** type with different on-time and off-time combinations. This was induced by the rather low current density and the comparatively long distance between anode and cathode. The porous structure obtained in this project was found to have a comparatively high strength, as well as the common low ductility. Deposits produced by the **dc** type had both high strength and high ductility compared with those produced by **pc** since less porous structures were produced.

The effect of current density was also elucidated. Generally, increasing the current density resulted in increased tensile strength of the deposits. The strength reached its maximum when the current density was 8 A/dm^2. Further increasing the current density decreased the tensile strength. On the other hand, the ductility reached its maximum at a current density of 1.5 A/dm^2. At high current densities, the structure of the deposits became extremely porous, which led to the reduction of ductility and in the extreme case, the lack of plasticity.

As the deposition duration increased, the deposition rate drastically decreased. This resulted in grain growth. Hence, the thinner the deposits, the higher the strength and the lower the ductility. Thick deposits had relatively low strength but high ductility. This can be attributed to the increase of the grain size and twins thickness with deposition duration. Meanwhile, the grain size and the twins thickness of all samples with the thickness discussed (from ~30 μm to ~1 mm) were in nano-scale or ultra-fine regime. As the thickness of the Cu film grew, the gradient structure of the deposits allowed the sample to have a rather ductile characteristic.

For the samples with the same thickness, grains and twins with nano-scale thickness can be usually found at the substrate and the solution side. In between the ultra-fine grain layers at the substrate and solution sides, columnar structures were observed with the direction of <220>//ND and nano-grains were embedded in the columnar structures with the direction of <102>//ND. It is noted that the texture of the deposits also varied with deposition time. Strong-textured deposits were obtained with short deposition duration. Deposits obtained with deposition time of 48 hours or less had {110} out of plane texture which coincided with the direction of the columnar structure. This coincidence suggests that under the effect of the substrate, the columnar structures were promoted in the specimens with short deposition time. As the duration increased, the effect of the substrate decreased while that of the solution and the current density became dominant.

Besides the texture, the fracture mechanisms also varied with deposition duration / specimens thickness. The thin specimens (<~0.5 mm) exhibited the void sheet mechanism displaying a 45°-oriented fracture; thick specimens (~1 mm) demonstrated internal necking mechanism showing a 90°-oriented fracture.

The Hall-Petch relation and the strain hardening exponent for the Cu films in the current study were found to slightly deviate from the ones in previous works. The deviation is believed to be caused by the bimodal structure and the coexistence of nano-grains and nano-twins in the current films.

Chapter 6: STUDY OF SMATED ELECTRODEPOSITS

As analyzed in Chapter 5, when proper operation conditions are adopted, NS materials produced by the ED process can be tailored to obtain desirable structures and mechanical properties. There are two approaches that affect the mechanical properties, i.e. the change of grain size and thickness of twins. In the ED process, both of them can be achieved by adjusting the current type, current density and deposition duration.

For electrodeposited Cu film, the yield strength increases with decrease of thickness of twins. When the thickness is reduced to 15 nm, the yield strength reaches its maximum with the strain remaining less than 10% [51]. With further decreasing the thickness of twins, the yield strength decreases and ductility increases [51]. Therefore, to acquire desirable mechanical properties, the thickness of twins has to be carefully controlled. This can be implemented by using strict conditions, for example, pulsed current (**pc**) type with short on-time and long off-time, high current density, specific pH value, oxygen and hydrogen level. However, for thick electrodeposits, the proper conditions to obtain twin-structure become very complicated. The maximum thickness of the electrodeposits with twin structures reported in previous works was around 200 μm [51]. To produce twin structure in thick samples, simple and reliable approaches need to be developed.

On the other hand, the improvement of the yield strength can also be realized through the reduction of the grain size. In the ED process, **pc** is usually adopted.

Thus obtained electrodeposits, however, are often brittle even though the grain size is reduced. As an alternative, the direct current (**dc**) type was also found to be able to produce electrodeposits with similar grain size as the **pc** type does when the thickness is confined below a few tens of nanometers [121]. This can be demonstrated by the experimental results in Chapter 5, where the electrodeposits having nano-grains and nano-twins were produced by **dc** type. Besides this, the experimental results in Chapter 5 also proved that the electrodeposited Cu film with a large thickness, i.e. 1 mm, can still have ultra-fine grains and ultra-fine twins. Nevertheless, long deposition duration for thick electrodeposits increased the grain size and developed columnar structures. The formed gradient structure lowered the tensile strength, but, retained the ductility. As expected, the ED process shows its availability in producing NS materials with large thickness.

As the failure of materials is very often triggered from the surface (fatigue, fretting, corrosion, wear, etc.), the optimization of the surface microstructure and properties is often an effective approach to enhance the global behavior and service lifetime of materials. SMAT recently emerged as a powerful technique to create nanostructures at the top surface and harden the material over a depth of several tens of micrometers. Under the impact of the balls at sufficiently high velocity, twins structures can be obtained and the mechanical properties are then improved. However, this technique usually induces a rather low ductility. As aforementioned in Chapter 4, SMAT has been successfully applied to many materials, especially coarse-grained materials. Knowledge about its application on electrodeposits *per se* having ultra-fined grain matrix is still discrepant.

Utilizing the features of ED and SMAT, this chapter will apply SMAT on electrodeposits to produce NS materials with large thickness. NS materials are required to sustain desirable strength and ductility for further applications. The microstructure, mechanism, texture and tensile properties of SMATed electrodeposits will be examined thoroughly.

6.1 Experiment

Deposited Cu films of thickness of ~1 mm were obtained using the ED process with an electrolyte of $CuSO_4$ solution employing direct current (**dc**). The current density was 1.5 A/dm^2. The choice of these conditions is to obtain the ductile characteristics of electrodeposits. After removal of the wax substrate, the rectangular electrodeposited Cu blocks were EDMed to 4 plates for SMAT.

Three durations of SMAT, 1, 4 and 10 minutes, were applied to the electrodeposited Cu plates of 1 mm thickness, respectively. For the electrodeposited Cu plates of 0.16 mm thickness, a 2-minute duration was used. The SMAT conditions were the same as described in Chapter 4. The balls used for treatment were made of bearing steel, being 3 mm in diameter. The effect of SMAT on substrate side, solution side and both sides of deposits of 1 mm thickness was studied in terms of tensile properties. After SMAT, samples were subjected to EDM in a dog-bone shape according to the ASTM E8M-04 standard, whose gauge dimension was $(25 \times 6)\ mm^2$. Thus the samples can withstand the impact force of SMAT which is too large for the small ones used in Chapter 5.

The microstructural evolution and texture of the SMATed Cu samples were then characterized by TEM and EBSD, respectively.

6.2 Mechanical Properties and Microstructure Characterization

6.2.1 Mechanical properties

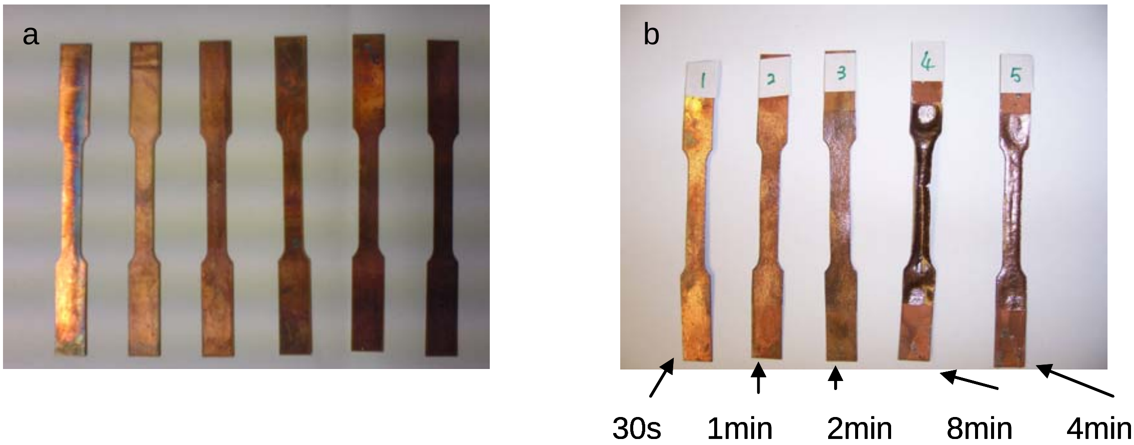

FIG. 6.1. Photographs of electrodeposited Cu film of 0.28 mm thickness: (a) before subjected to SMAT; and (b) after SMATed for 30 seconds, 1 minute, 2 minutes, 8 minutes and 4 minutes.

In the preliminary study, SMAT with different durations were applied to the electrodeposits of different thickness. The results suggest that the Cu film with small thickness deformed severely under long-duration SMAT. If the thickness of the Cu film was less than 0.3 mm, 2-minute treatment was the limit for not causing over-severe deformation on the Cu film. Fig. 6.1 shows the electrodeposited Cu films before and after SMAT. After SMAT for 4 minutes or more, the films deformed severely as shown in Fig. 6.1 (b).

Fig. 6.2 (a) and (b) show the engineering and true stress-strain curve of the electrodeposited Cu film of 160 μm thickness with and without SMAT for 2 minutes. As expected, both the yield and ultimate tensile strengths were enhanced after SMAT for 2 minutes on both sides of the samples. The yield strength was enhanced by ~20%, but the strain to failure was reduced by ~7%. It is known that SMAT enhanced the yield strength by creating high-density dislocations in the top layer of the treated materials [60]. In such a way, however, the ductility was reduced due to the limitation of the dislocations in the small grains. On the other hand, the Young's Modulus or toughness was also enhanced with the benefit from the reduction of the porosity by the strong impact force of SMAT. This became significant in this sample because of its original small thickness. The true stress-strain curve of the SMATed samples also showed the near-perfect elastoplastic manner [159] which implied that the grain size was small and the SMATed samples had the same plastic deformation behavior as the non-SMATed ones as discussed in Chapter 5. The effect of the grain size will be further verified in the next section.

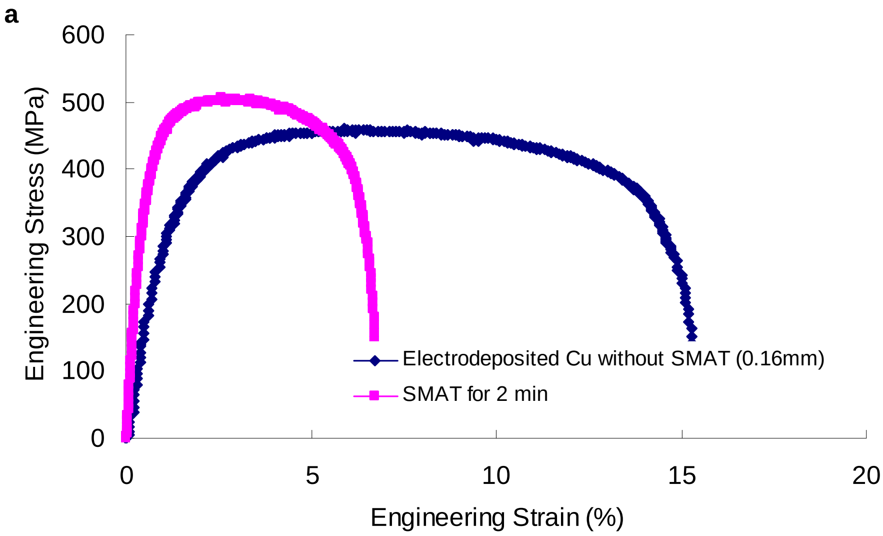

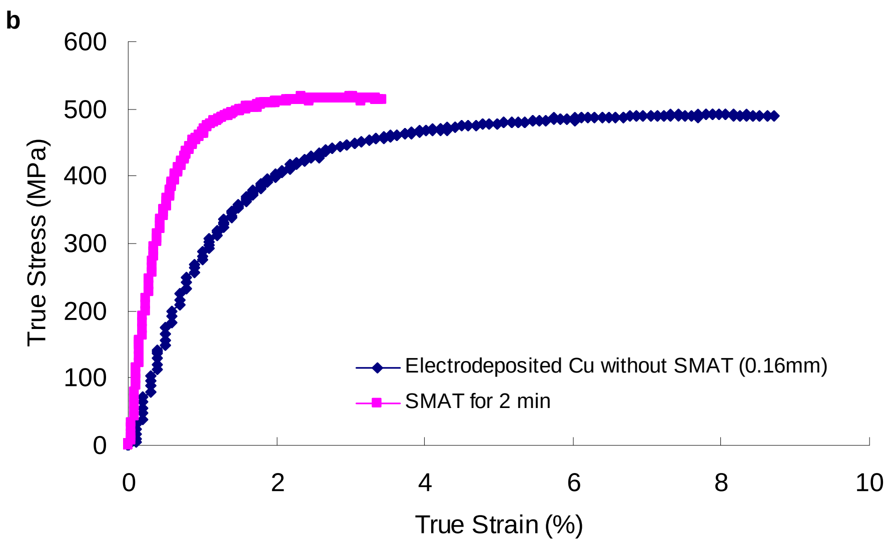

FIG. 6.2. Tensile test properties of electrodeposited Cu film of 160 μm with and without SMAT for 2 minutes: (a) engineering stress-strain curve; (b) true stress-strain curve.

Although the sample size seemed not to influence the properties of the thin specimens, it did have an effect on the thick ones, such as the example shown in Fig.6.3, corresponding to a specimen of 1 mm. The yield strength of the non-SMATed sample of large size was slightly reduced while the ductility was greatly increased compared with the results obtained in Chapter 5 for small-sized samples (Fig. 5.8). It is plausible that the large gauge width provided sufficient room for the necking and crack propagation to proceed after yielding, and hence resulted in a high ductility. The large-sized thick samples also preserved the normal Young's Modulus of the coarse-grained Cu.

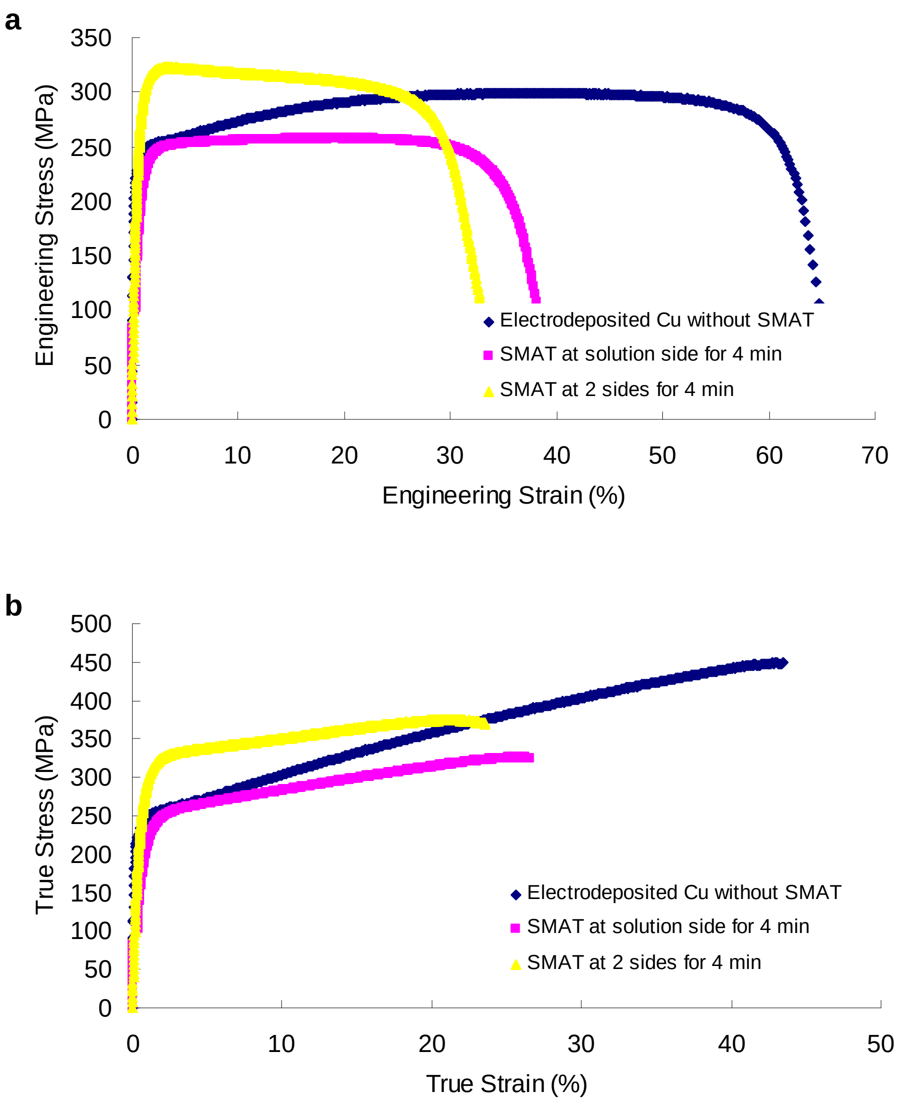

FIG. 6.3. Tensile test properties of electrodeposited Cu film of 1 mm thickness with and without SMAT for 4 minutes: (a) engineering stress-strain curve; (b) true stress-strain curve.

Fig. 6.3 shows the engineering and true stress-strain curves of the electrodeposited Cu film of 1 mm thickness with and without SMAT for 4 minutes. SMAT was applied to the solution side, substrate side and both sides of the 1 mm thickness Cu electrodeposits. The application of SMAT on only the solution or the substrate side resulted in similar tensile test properties. For simplification, only the sample with SMAT on the solution side was employed for comparison. The final results are shown in Fig. 6.3. As observed, the sample with only one SMATed face had similar yield strength as the non-SMATed one of the same thickness. The ineffectiveness of SMAT on the yield strength was due to the unbalanced residual stress caused by SMAT on only one face. The bending of the sample had the tendency towards the SMATed side. This resulted in the yielding occurring first at the non-SMATed side, and consequently lowered the strength. The effect of SMAT also led to a remarkable reduction in ductility.

On the contrary, samples with SMAT on both sides significantly increased in yield strength by ~30% but the ductility was reduced by half. The reason was similar to the case of the SMATed Cu film of 160 μm thickness. However, it should be noted that the plasticity regions of all samples in the true stress-strain curves (Fig. 6.3 (b)) had a positive slope which is different from that of the thin samples. This positive slope implied that the plastic deformation mechanism was the continuous multiplication of dislocations pertaining to the dislocation density. The ultimate tensile strength of the non-SMATed samples in the true stress-strain curve was found to be higher than that of the SMATed ones. This low ultimate tensile strength of SMATed samples is believed to be caused by the limitation of dislocation activities from work-hardening during the SMAT process.

To evaluate the duration effect of the SMAT process, 1-minute, 4-minute and 10-minute SMAT were applied on both sides of the Cu electrodeposits of 1 mm thickness, respectively. The corresponding engineering and true stress-strain curves are plotted in Fig. 6.4. It can be seen that the yield strength of the SMATed deposits increased with the treatment duration, but the ductility was reduced. The 1-minute and 4-minute SMATed Cu films had very similar yield strength and ductility, although these two properties still followed the global variation tendency with respect to the duration. Furthermore, Cu electrodeposits after SMAT for 10 minutes had significant enhancement in yield strength by 30%. However, the reduction of the ductility was still remarkable. It was interesting to point out in Fig. 6.4(b) that the 10-minute SMATed Cu had different plastic deformation manner from the 1- and 4-minute SMATed ones. The latter two kinds of samples followed the conventional plastic deformation. In contrast, the plastic deformation at a constant flow stress was observed for the 10-minute SMATed sample. This implied that the grains were small. The small grains can reduce the dislocation activity and make the sample sustain the plastic deformation by diffusional grain-boundary sliding [160].

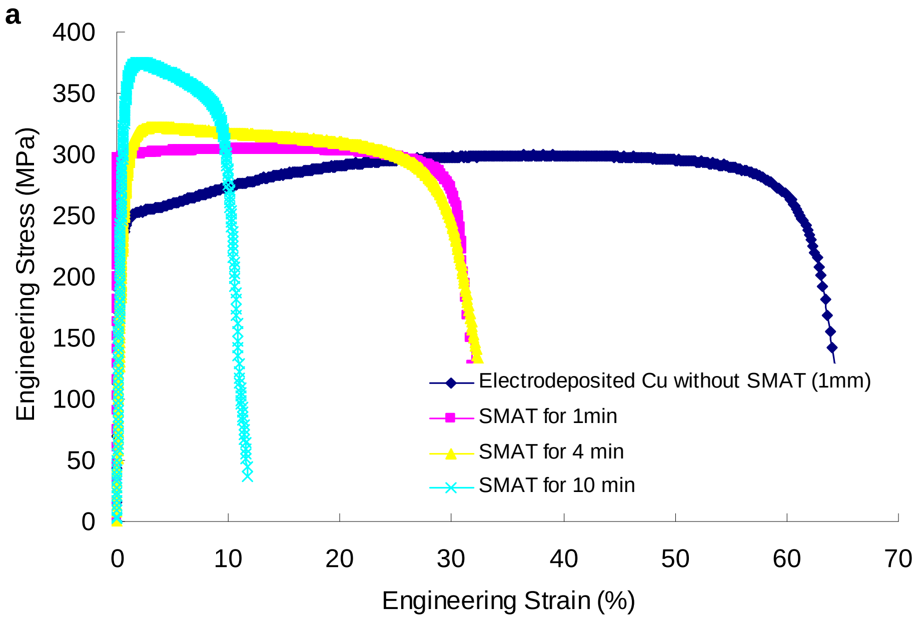

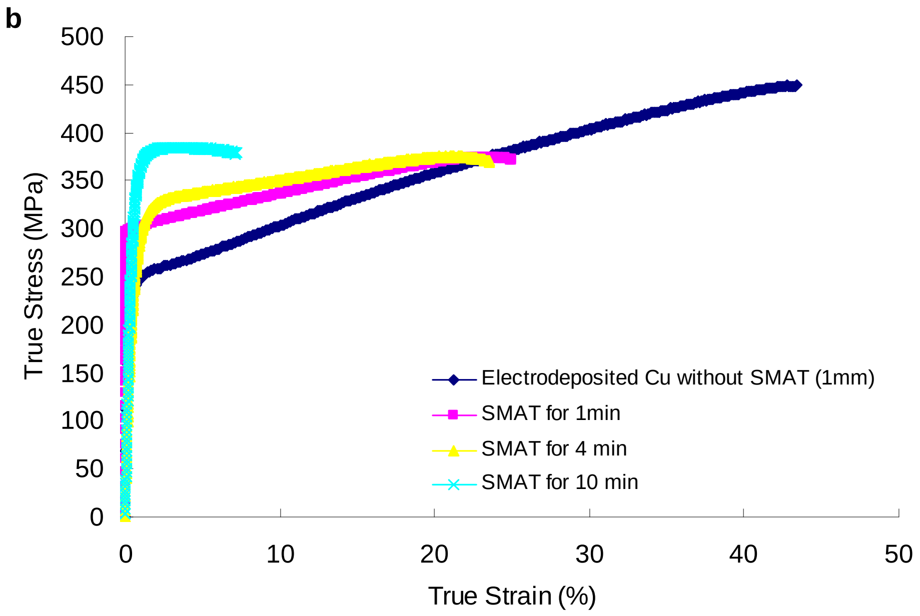

FIG. 6.4. Tensile test properties of Cu electrodeposits with and without SMAT for 1, 4 and 10 minutes: (a) engineering stress-strain curve; (b) true stress-strain curve.

6.2.2 Microstructure evolution

The microstructures of the topmost surface of the Cu electrodeposits with a thickness of 160 μm after being subjected to SMAT for 2 minutes were first evolved. The thickness of the Cu electrodeposits then increased to 1 mm and the SMAT durations of 4 and 10 minutes were adopted for these thick samples. It has been reported that two different grain refinement mechanisms can be detected for SMATed Cu (in that study, coarse-grained Cu was used): formation and evolution of dislocation cells (DCs), and mechanical twinning. The former one is a process analogous to that observed in deformed coarse grains [60] and is dominant in the deformation layer (>~25 μm depth); in the top layer (<~25 μm depth), mechanical twinning played an important role in the grain refinement. Hence, the microstructures at the depth of ~30 μm of the Cu electrodeposits after SMAT for 10 minutes were also examined.

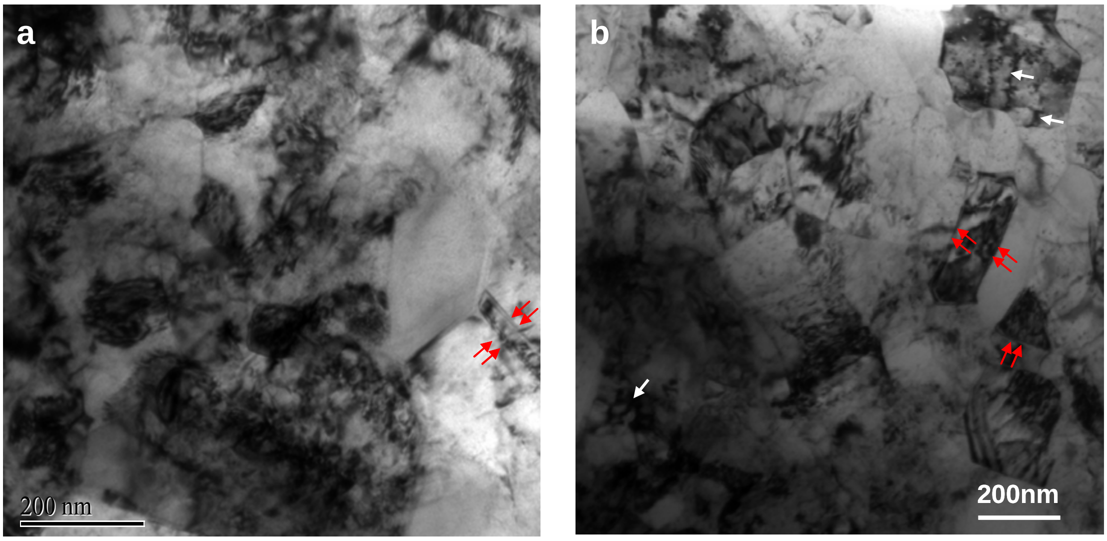

FIG. 6.5. Typical cross-sectional bright-field TEM images at the topmost surface of the 2-minute SMATed Cu electrodeposits with 160 μm thickness with white arrow and red arrows pointing at the newly formed grain boundaries and apparent original twins lamella structures, respectively.

Fig. 6.5 shows the typical cross-sectional bright-field TEM images at the topmost surface of the 2-minute SMATed Cu electrodeposits with 160 μm thickness. Different from the non-SMATed deposits, only a small amount of twins structures (<~5% volume fraction) were observed in this figure; meanwhile, dislocation cells (DCs) and sub-grains (indicated by white arrows) were formed inside the original grains instead. Because of the inhomogeneity of the plastic deformation, some grains had DCs and sub-grains while some had just a few dislocations inside. The original twins lamella structures, indicated by red arrows, were also discovered, some of which had sub-grains formed inside. The short SMAT duration was insufficient for the homogeneous transformation of all the grains into smaller ones, hence resulting in the rather small degree of improvement of yield strength. The missing of a large amount of nano-twins is believed to be responsible for the reduction of ductility. Based on the TEM observations, the grain size distribution of the current Cu electrodeposits was obtained and is compared with that of the non-SMATed ones in Fig. 6.6. As observed, the grain sizes in the current sample ranged from 40 to 240 nm and were slightly small compared to the non-SMATed ones.

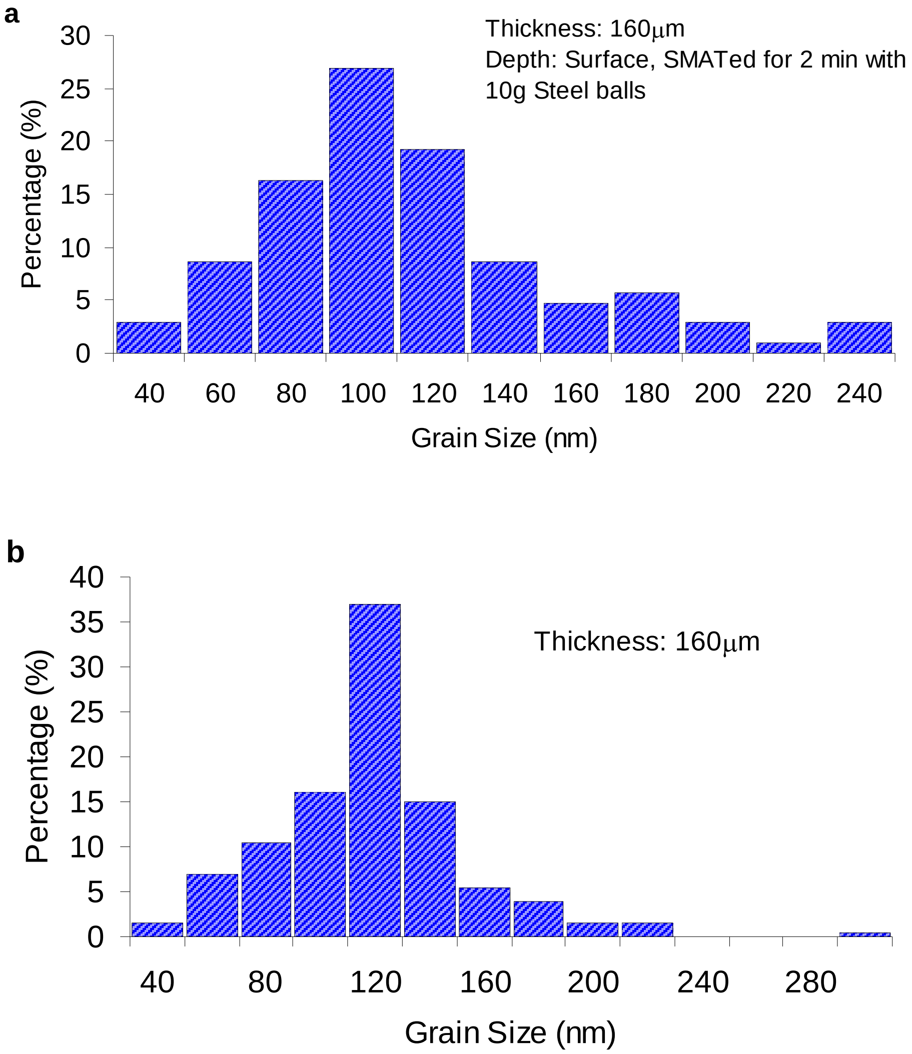

FIG. 6.6. Grain size distribution of the topmost surface of the cross-sectional Cu film of 160 μm thickness: (a) SMATed for 2 minutes; (b) non-SMATed.

It has been reported that longer duration of SMAT results in the further refinement of grains and consequently a high yield strength [80]. However, the SMAT duration has to be considered according to the thickness of the specimen since severe deformation can occur. In the following study, the Cu electrodeposits were 1 mm thick, with a comparatively high ductility and low strength. It, therefore, can be subjected to SMAT for long durations. Fig. 6.7 shows typical cross-sectional TEM images of the top surface layer of the 4-minute SMATed Cu electrodeposits of 1 mm thickness. It can be observed that DCs and sub-grains were formed inside some of the original grains. Some sub-grains had dense dislocations and some had clear DC walls (indicated by the white arrows in Figs. 6.7 (b) and (c)). Dislocation bands, marked by red arrows in Fig. 6.7(c), were also found, which were believed to be formed by high density dislocations [171] and seemed to be the former status of equiaxed sub-grains [171]. One can surmise that further increasing the strain will promote the grain refinement further.

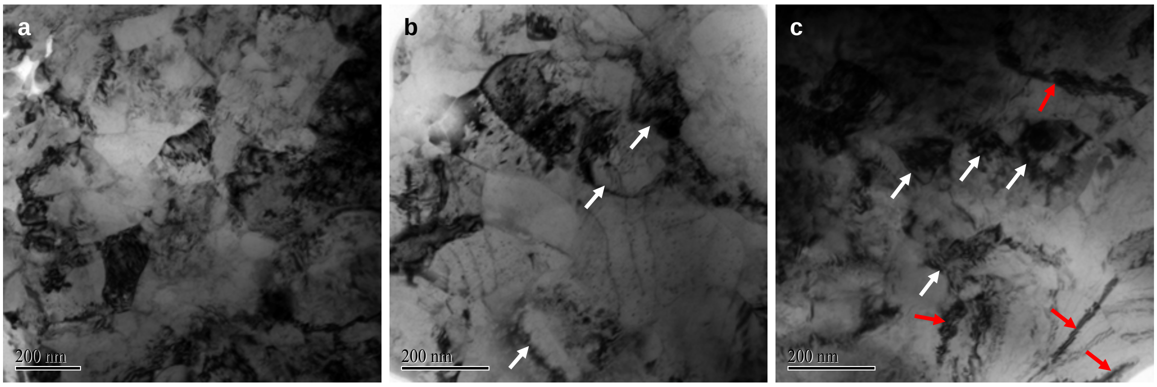

FIG. 6.7. Typical cross-sectional TEM images of top surface layer of 4-minutes SMATed Cu electrodeposits of 1 mm thickness.

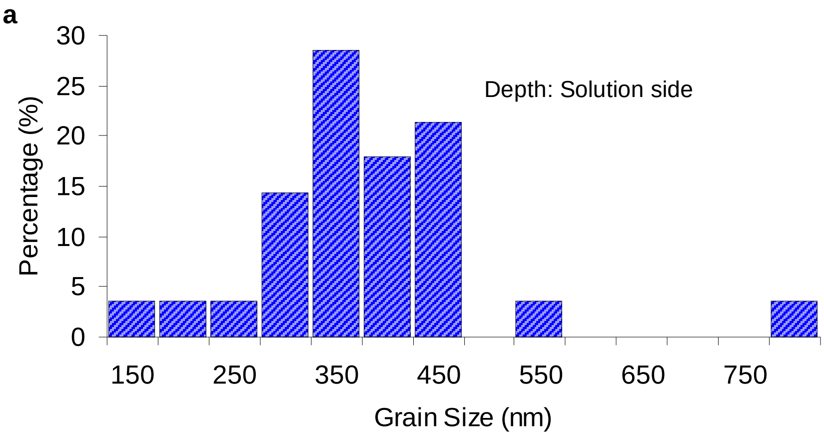

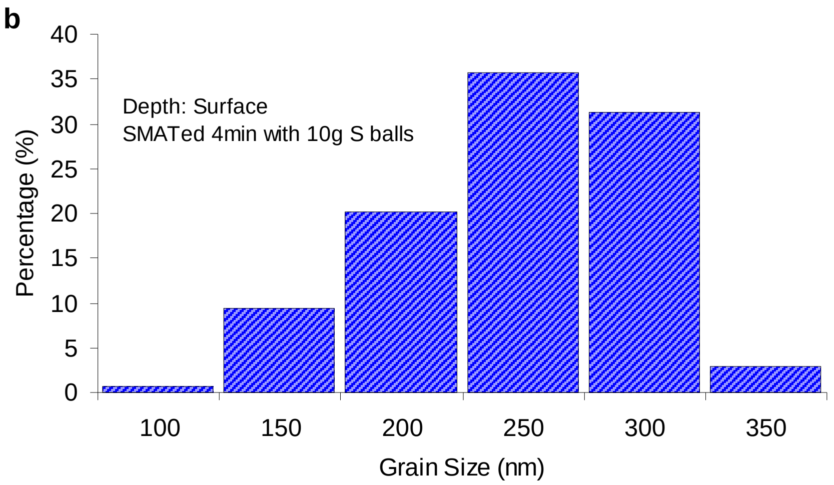

FIG. 6.8. Grain size distribution of the surface layer of 1 mm thick Cu electrodeposits: (a) non-SMATed; (b) SMATed for 4 minutes.

The Cu electrodeposits after being subjected to SMAT for 4 minutes had grain sizes ranging from 100 to 350 nm with an average size of ~250 nm, as shown in Fig. 6.8. Compared to the non-SMATed ones (Fig. 6.8(a)), the grain size of Cu was refined, though the twins structures were rarely discovered.

After increasing the SMAT duration to 10 minutes, grains were further refined and a small amount of twins were found. Fig. 6.9 shows the TEM images of the top surface of the 10-minute SMATed Cu electrodeposits. DCs and sub-grains with clear DC walls, as indicated by white single arrows, were observed. Some sub-grains with dense dislocations were formed in the possible pre-existing twins. The high density of dislocations was still found in the sub-grains and some were in the form of dislocation bands, as marked by white double arrows. Multiple twins with thickness of around ~40 - 50 nm were occasionally discovered within grains, as indicated by the red arrow. It was apparent that these kinds of small nano-twins with lengths of about 200 nm or less were caused by the high strain-rate during SMAT [60]. With further increasing of the strain-rate and the plastic strain, the amount of twins will probably increase with decrease of thickness [60].

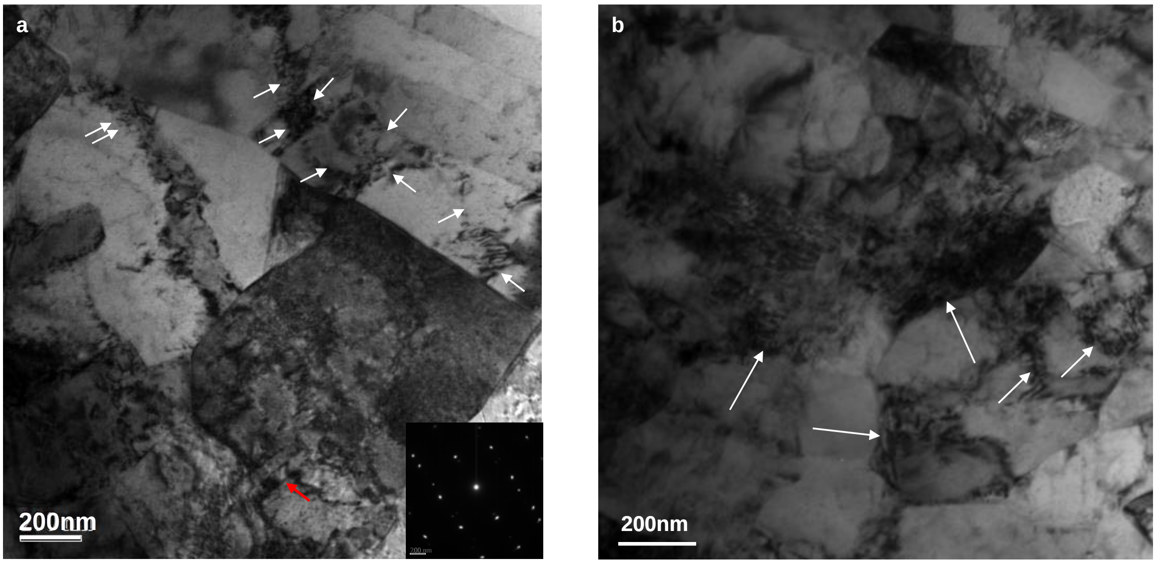

FIG. 6.9. Typical TEM images showing the microstructures of the top surface of the 10-minute SMATed electrodeposits.

Fig. 6.10 shows the distribution of the grain size and twins thickness of the 10-minute SMATed electrodeposits. The grain sizes ranged from ~100 - 450 nm with an average size of ~204 nm, as plotted in Fig. 6.10 (a). They were smaller than those of the non-SMATed and the 4-minute SMATed samples. This allows the current sample to have a higher tensile strength. A small number of nano-twins were also observed in the 10-minute SMATed electrodeposits. The thickness of the twins was larger than those of the non-SMATed ones, as presented in Fig. 6.10 (b). However, it is hard to determine if these nano-twins are the existing growth twins or the mechanical twins formed by SMAT. Meanwhile, sub-grains were always found inside those twins.

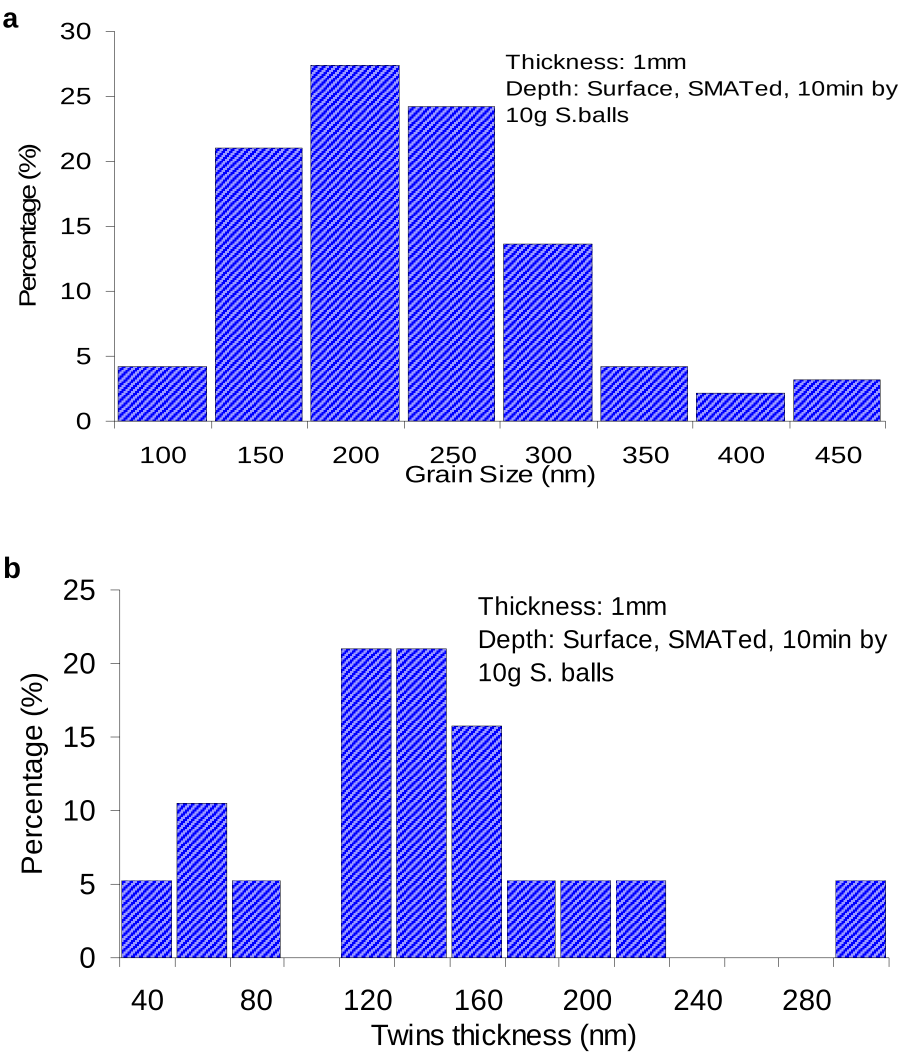

FIG. 6.10. Microstructures of the surface layer of 1 mm thick Cu electrodeposits with SMAT for 10 minutes: (a) grain size distribution; (b) twins thickness distribution.

As the depth increased to ~30 μm, a high density of dislocations was found, and many of them were in the form of the dislocations band, as shown in Fig. 6.11. Some DCs with thin cell walls were also observed. A very small amount of twins were discovered inside the dislocations-filled grains.

In general, SMAT induced a large number of dislocations in the grains which size was originally in the ultra-fine regime. Increasing the strain-rate and the plastic strains resulted in DCs and dislocation bands. When the strains further increased, sub-grains with clear DC walls or grain boundaries were formed inside the original grains and growth twins. Hence, grains were refined. If sufficient strain-rate and strains were applied, twins with a few tens of nanometers thick were formed among grains.

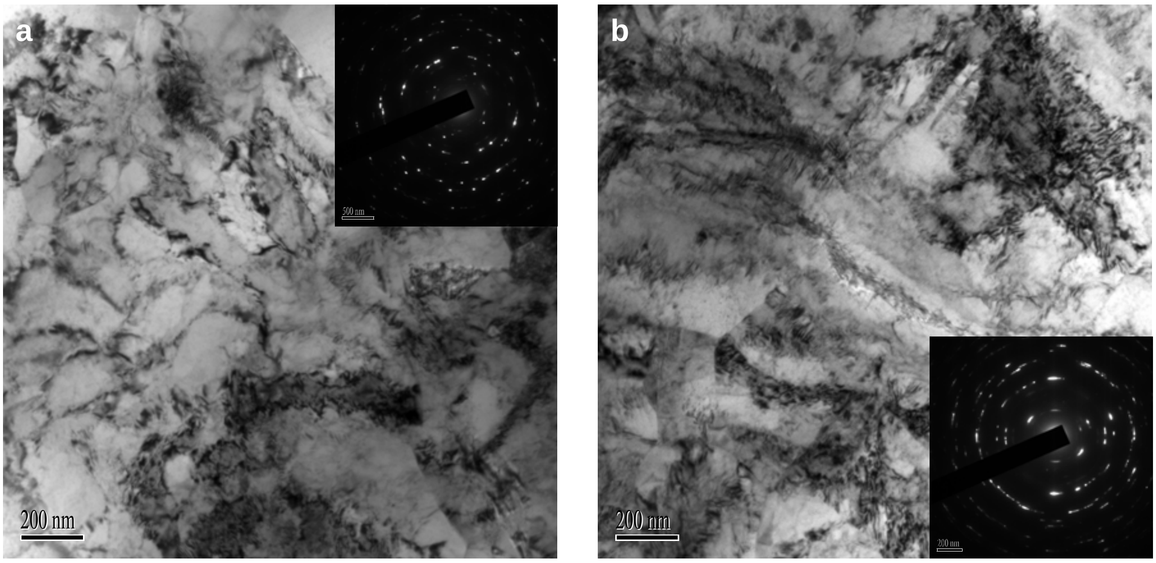

FIG. 6.11. Typical TEM images showing the microstructures of layers at the depth of ~30 μm of the 10-minute SMATed electrodeposits.

6.3 Discussion

As discussed in section 6.2, SMAT can significantly enhance the mechanical properties of the treated materials and influence the microstructures which can be observed from the TEM observations. In this section, the special effect of SMAT on textures of the electrodeposits will be investigated. The Hall-Petch relation and the tensile properties of the electrodeposited Cu in this study are examined and compared with those in previous works.

6.3.1 Texture characterization

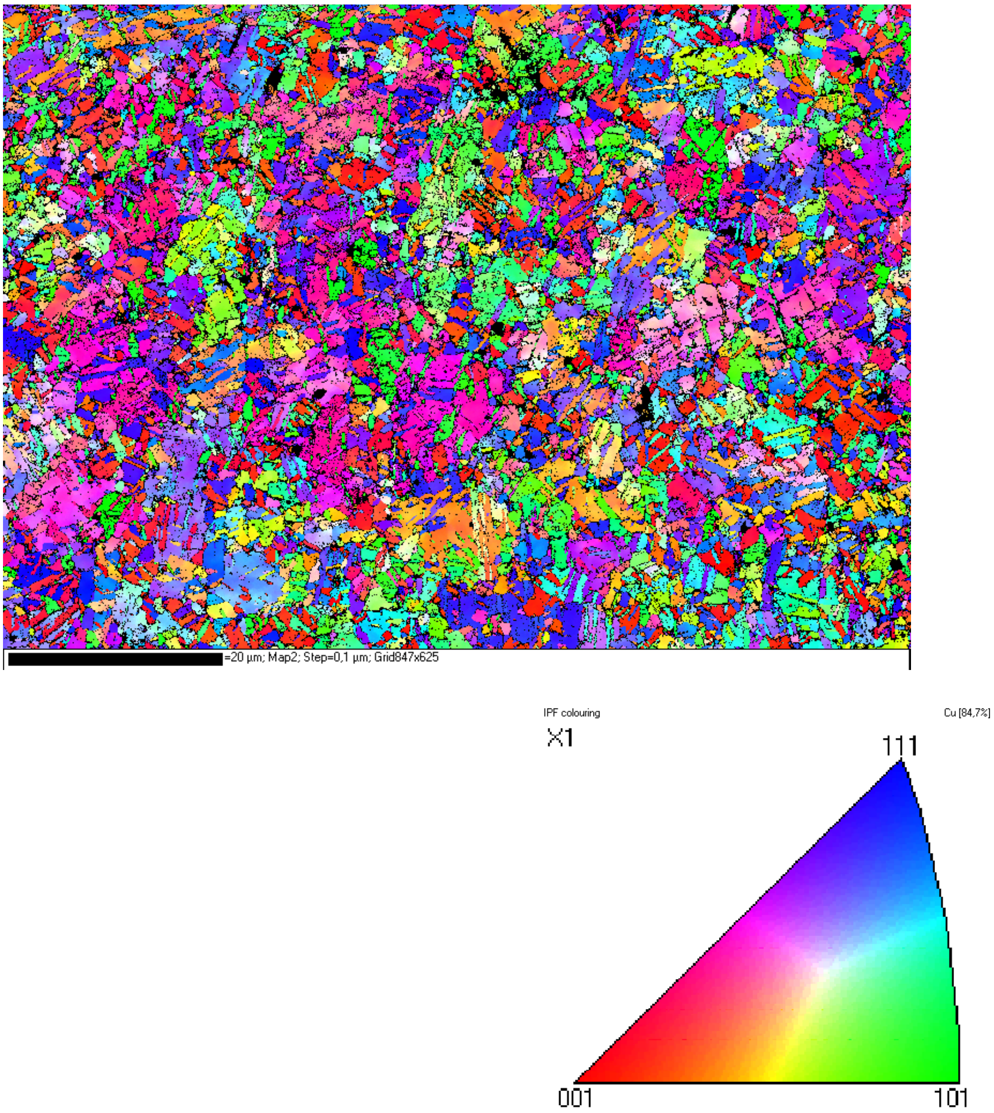

FIG. 6.12. The EBSD mapping of the grain orientations in the top view of the 4-minute SMATed electrodeposits.

The SMATed electrodeposits not only demonstrated the refined grains, but also maintained a random grain orientation. Fig. 6.12 shows the EBSD mapping of the grain orientations of the top view of the 4-minute SMATed electrodeposits. This figure provides an overview of a larger area composed of nano-grains with the size of a few tens of nanometers, and ultra-fine grains with the size of a few hundreds of nanometers to a few micro-meters with twins inside.

Fig. 6.13 displays the pole figures of the Cu electrodeposits before and after SMAT for 4 minutes. It shows that the overall texture was rather weak and the comparatively strong texture was <102>//ND and <220>//ND. After SMAT, though the texture was still fairly weak, new components are created. The crystallographic texture is modified from <102> // ND and <220>//ND towards <111> and <200> // ND.

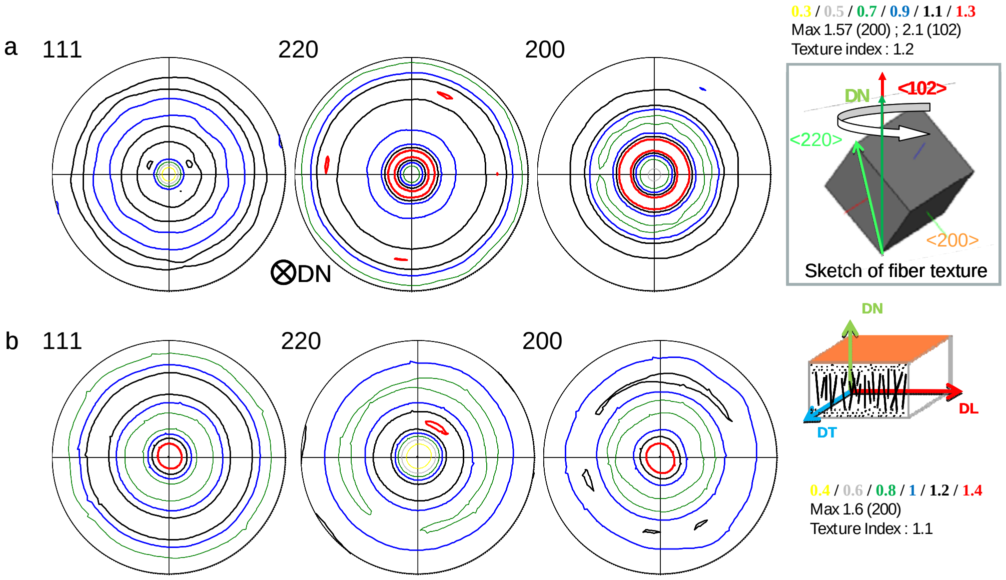

FIG. 6.13. Pole figures of the top surface of the electrodeposits, (a) non-SMATed; and (b) SMATed for 4 minutes.

The results of EBSD mapping and the pole figures are consistent with the XRD analysis in Fig. 5.20. For the electrodeposits obtained by short deposition duration, they showed strong texture in the growing direction of the columnar structures. However, as the electrodeposited Cu deposited for 78 hours and the thickness was about 1 mm, the sharpness of the texture decreased. This agrees well with the overview of the random grain orientation that the EBSD mapping displayed. Pole figures were a comparatively sensitive tool and hence it detected the relatively strong texture of the sample even though the intensity was weak.

The difference of texture before and after SMAT prompted us to contemplate the possibility of employing SMAT for the electrodeposits in the early stage of the ED process to diminish the strength of the texture in order to retard the growth of columnar structures. This may need to be further proved by more experiments in the future.

6.3.2 Hall-Petch relation

As addressed in Chapter 5, the samples in previous works had small size and thin thickness compared to those in this study. The size effect of the NS materials has been reported in many literatures [172], showing the necessity for considering this effect. Therefore, using the data from large-sized samples, this section will re-examine the variations of UTS, YS and strain to failure with respect to the inverse of the square root of the grain size. The corresponding results are plotted in Fig. 6.14. As observed, UTS and YS increased with decrease of grain size, following the general trend. The current relations for UTS and YS were determined to be $\sigma_{UTS} = 3666.5d^{-1/2} + 112.89$ and $\sigma_{YS} = 3433.6d^{-1/2} + 108.11$, respectively. Thus the obtained *k* value was similar to that of the conventional Hall- Petch relation as shown in Fig. 6.15 and was large compared with that in section 5.2.2. It is plausible that the original rather porous structure of the electrodeposits was improved by the strong impact force during the SMAT treatment and hence the results obtained in this chapter were comparatively close to the theoretical values.

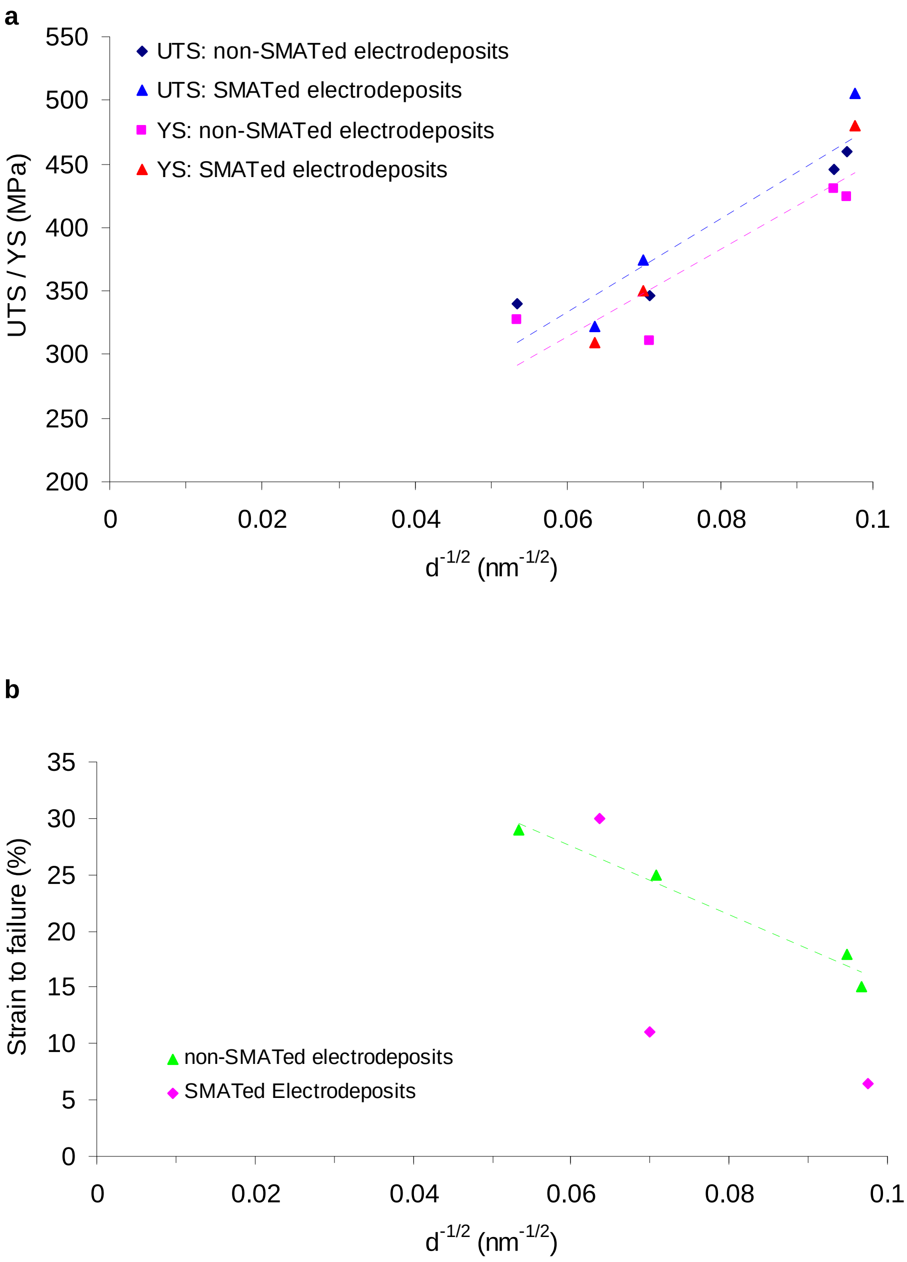

FIG. 6.14. Effect of the inverse of the square root of the grain size on: (a) UTS and YS; (b) strain to failure.

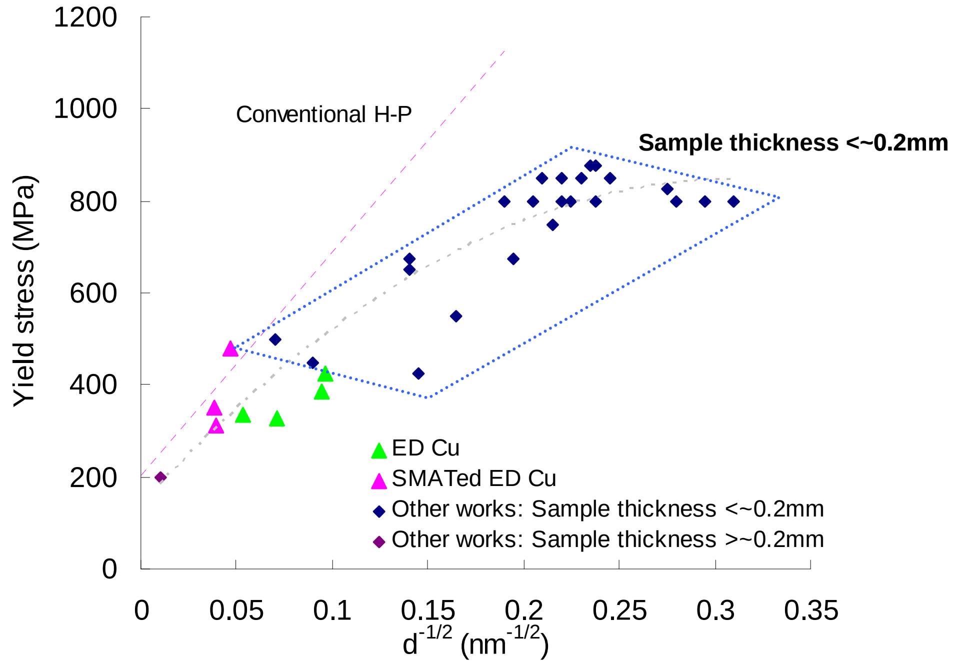

FIG. 6.15. Comparisons of the results in this study and that from other literatures and the conventional Hall-Petch relation of Cu.

Besides the yield strength, the ductility of the materials obtained in this study was of the great concern. Fig. 6.16 shows the comparison of the tensile properties of the NS or ultra-fine grained Cu produced by SMAT and/or ED, which were denoted by red color, and that of those produced by other synthesis methods. The materials fabricated in this work have a large variety of tensile properties owing to the different process parameters adopted during the treatment. Also, it is worth to note that the samples obtained in this study are comparatively large in size, unlike those from other literatures as stated in section 2.5.

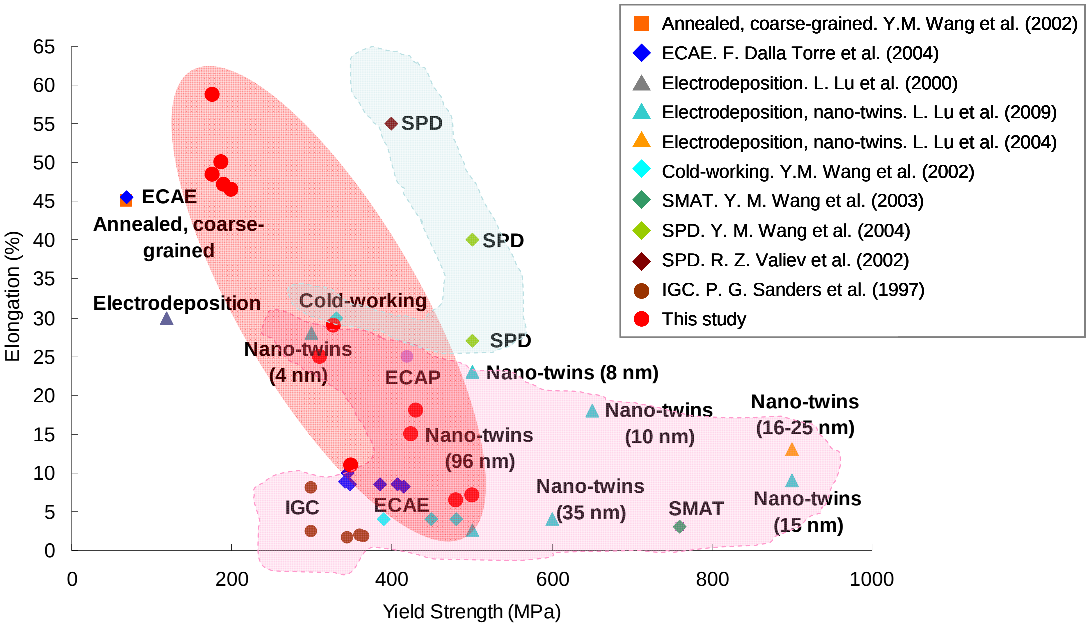

FIG. 6.16. Comparisons of the tensile property results in this study and that from other literatures [29, 33, 34, 51, 53, 65, 93, 142, 143].

6.4 Concluding Remarks

SMAT was applied to the electrodeposited Cu of thickness of 0.16 and 1 mm. Experimental results showed that SMAT duration cannot exceed 2 minutes for thin samples; otherwise, the deformation becomes very severe. As expected, SMAT significantly enhances the tensile strength and the Young’s modulus since the grain size is refined and the porosity formed during the ED process is reduced. However, the loss of ductility is still a shortcoming.

The effect of SMAT on a rather thick sample, i.e. the sample with 1 mm thickness, was explicit. When the SMAT duration was 10 minutes, the yield strength was enhanced by 30%. By increasing the SMAT duration, the yield strength can be further enhanced. Although there was still loss in ductility, a certain amount was retained owing to the ductile characteristics of the electrodeposits *per se*. The 10-minute SMATed Cu was found to have a different plastic deformation manner from the 1- and 4-minute SMATed ones. The latter two kinds of samples followed the conventional plastic deformation. In contrast, the plastic deformation at a constant flow stress was observed for the 10-minute SMATed sample. This implied that the grains were small. The small grains can reduce the dislocation activity and make the sample sustain the plastic deformation by diffusional grain-boundary sliding.

Through the TEM observations, the mechanism of the grain refinement for SMAT was obtained. A large number of dislocations were induced by SMAT to the grains which size was originally in the ultra-fine regime. Increasing strain-rate and plastic strains resulted in the formation of the DCs and the dislocation bands. When the strains further increased, the sub-grains with clear DC walls or grain boundaries were formed inside the original grains and the growth twins. Following this process, grains were refined. If sufficient strain-rate and strains were applied, twins of a few tens of nanometers thick were formed among the grains.

In general, the texture of the electrodeposited Cu of 1 mm thickness was rather weak and the grain orientation was rather random. A comparatively strong texture of <102>//ND and <220> //ND was observed by the pole figures though the overall intensity was still relatively weak. After SMAT, a rather random grain orientation was still observed. However, the intensity of the texture was slightly enhanced. The crystallographic texture was modified from <102> // ND and <220>//ND towards <111> and <200> // ND.

Compared with the *k* value in the Hall-Petch relation obtained in section 5.2.2, those resulting from the SMATed samples were comparatively close to the theoretical values from the conventional Hall-Petch relation. This is the reason that the porosity created in the ED process was reduced by the high impact force of SMAT.

The encouraging results demonstrated that the ED process can produce NS materials with sufficient thickness and high ductility, while SMAT technology can further improve the strength of the electrodeposits with desirable ductility retained. The effect of SMAT on the crystalline texture prompted us to contemplate the possibility of employing SMAT for the electrodeposits in the early stage of the ED process to diminish the strength of the texture in order to retard the growth of columnar structures. This may need to be further proved by more experiments in the future.

Chapter 7: CONCLUDING REMARKS AND SUGGESTIONS FOR FUTURE WORK

7.1 Concluding Remarks

Most NS materials produced by recently developed synthesis methods have ultra-high strength, but low ductility. This restricts their applications in industry. In addition, the current fabrication methods of NS materials often have limitations on the size and the shape of materials, which also confines the development of producing NS materials for practical implementation. The electrodeposition (ED) process is one of the methods to produce NS materials with fewer restrictions. The publication of Lu et al. in Science [51] have demonstrated that a large amount of nano-twins with controlled thickness can be produced by the ED process with strictly controlled conditions. However, the sample size was still small. This kind of small-sized sample was also extensively used in other works. Limited researches have shown the practicality of this method in maintaining the superior properties of NS materials with a thickness larger than ~200 μm. SMAT is another method capable of producing NS materials in bulk form. However, low ductility is always the drawback for treated materials if improper operating conditions are chosen. Nevertheless, the relation of the operation parameters and the microstructures obtained is still not fully understood. In this project, through the thorough acknowledgement of SMAT technology and the ED process, the effect of the process parameters and the properties of the produced NS materials were discussed, and the practicality of combining these two technologies to produce bulk NS materials with good strength and desirable ductility was demonstrated. The extended possibility to produce NS materials in free shape was shown via using wax as a substrate in the ED process. Materials with nano-grains and nano-twins having thickness larger than 1 mm were demonstrated.

In the study of the SMAT process, the relationship among the ball velocity, the attained strain-rate and the microstructures of the treated materials was systematically investigated. The number of balls was found to greatly affect the nominal impact velocities of the balls in the treatment chamber, as well as the total kinetic energy transferred to the sample *per se* and the treatment efficiency in terms of the tensile properties of treated samples. As the number of balls increased, the corresponding nominal impact velocity of the balls decreased since more kinetic energy was dissipated or allocated to the horizontal motion due to more collisions between balls. The treatment efficiency correlates well with the total kinetic energy evaluated from the ball number and the corresponding nominal velocity. Higher total kinetic energy resulted in higher treatment efficiency. Using the measured ball velocity, the strain-rate at different depths of the treated samples was approximately predicted. Numerical analysis using FEM verified the predicted strain-rate. The strains level at different depths was also simulated by FEM. By associating strain-rate and strains with the microstructures obtained from TEM observations, the least requirement of the strain-rate for the formation of twins with nanoscale spacing for the materials was obtained. By treating the AISI 304 under optimum conditions for obtaining more nano-twins, the possibility to obtain NS materials with high strength and high ductility was demonstrated.

In the study of the ED process, the feasibility of employing direct current (**dc**) to produce NS Cu with large thickness was examined. Considering the easy shaping of wax, it was used as the substrate throughout this project. Electrodeposits with a thickness ranging from ~160 μm to 1 mm with ultra-fine grains and nano-twins were obtained. SEM observations and results of tensile property tests showed that the pulse-current (**pc**) can result in a porous structure when producing NS materials of Cu. The porous structure enhanced the strength of the electrodeposits but lowered their ductility. When **dc** was adopted, the use of high current density might also cause the formation of porosity in the microstructure thereby weaken the tensile properties of the electrodeposits. Direct current and low current density, i.e. 1.5 A/dm^2, were found to be the proper conditions to produce NS materials with a less porous structure with high strength and desirable ductility. The deposition duration can greatly affect the growth of the columnar structure and the grains, and hence the tensile properties. The consistent results obtained from EBSD and XRD analysis suggested that under the effect of the substrate, the columnar structures were promoted in the specimens with short deposition time. As the duration increased, the effect of the substrate decreased while that of the solution and current density became dominant. Experimental results showed that the fracture mechanism was also affected by the deposition duration.

The Hall-Petch relation and strain hardening exponent for the Cu films in the present study were found to have a little deviation from ones in previous works. The bimodal structure and the coexistence of nano-grains and nano-twins in current films were the reason for the difference. In this study, the electrodeposition process was proved to be a practical method to produce NS materials in bulk form. Direct current was confirmed to be capable of producing electrodeposits with nano-grains and nano-twins.

After combining SMAT and ED technologies, the materials obtained the tensile strength close to that from the conventional Hall-Petch relation and retained ductility with a desirable level. Experimental findings showed that employing SMAT on the electrodeposited Cu further reduced the grain size and enhanced its tensile strength. Through the TEM observations, the grain refinement mechanism for SMATed ultra-fine grained electrodeposited Cu was revealed. Furthermore, the EBSD analysis showed that the effect of SMAT on the texture of the deposits was remarkable. As a rule of thumb, the combination of SMAT and the ED process can enhance the strength, retain the desirable ductility and is capable of processing NS materials on a large scale. These advantages allow this combined approach to be one of the potential ways to produce NS materials in bulk form for industrial applications.

7.2 Suggestions for Future Work

Since the very first attempt of producing NS materials on the laboratory scale which has shown the superior mechanical properties, development of the NS fabricating processes for synthesizing NS materials in bulk form has become the world-wide challenges. This thesis explores the ideas and develops the possible way for the evolution of potential industrial-applicable bulk NS materials by SMAT and ED process. Experimental results provided by this study showed the availability of production of SMATed electrodeposited Cu in bulk form with nanostructures, with comparatively high strength and desirable ductility; however, there is still room for improvement for the fabrication processes and worth for further study as follows:

- In this work, the motion of a single ball has been modeled and simulated. In order to further understand the real SMAT process, the behaviour of the multiple balls is worth to be considered. Also, the role of the local heating in the SMAT process is worth to be taken into account in the future study as it is one of the important factors in the process of grain refinement.
- The effect of SMAT on the crystalline texture of the electrodeposited Cu was impressive. It seemed plausible that employing SMAT may modify the texture of the electrodeposits and prohibit the growth of columnar structures. In order to have sufficient thickness and as well as retain the strength and ductility, applying SMAT to the electrodeposits before the columnar structures becoming dominant and re-electrodepositing again to reach the desired thickness may be possible. Experimental studies are required to verify this idea.
- Recent SMAT for electrodeposited Cu plate in this study was done by treating the solution side and substrate side alternatively, however, failure was always occurred at the side of the plate along the thickness direction which composed of comparatively large grains having a more ductile but weak characteristics. Treating the materials with rotational motion may be a way to further improve the performance. Extend works on this idea, both experimentally and theoretically, are in need of further investigation.
- Electrodeposition process is not only applicable to Cu and SMAT technology also shows its significant effect on different materials, the exploitation of these

two synthesis methods on different materials may provide a good opportunity to further develop NS materials in bulk form for industrial applications.

- The idea of adopting ED process to produce the base materials and SMAT process to further enhance the tensile properties may be able to apply to produce heat pipe. Heat pipe is commonly used in a large variety of applications to transfer heat. It requires high heat conductivity, certain mechanical strength to withstand the external force and good diffusivity during welding. Pure Copper is commonly used. However, a more complex geometry is required to fit the applications these days. The techniques demonstrated in this work may be a possible way to meet this requirement, nevertheless further study is required.

BIBLIOGRAPHY

[1] Feynman, R. P., *There's Plenty of Room at the Bottom.* Engineering and Science, 1960. **23**: p. 22-36.

[2] Gleiter, H., *Structure and Properties of Microcrystalline Materials*, in *Proceedings of the Ninth International Vacuum Congress and Fifth International Conference on Solid Surfaces*, d.S.J. L., Editor. 1983, Asociacion Espanola de Vacio y sus Aplicaciones, Spain: Madrid, Spain. p. 397-401.

[3] Gleiter, H., *Nanocrystalline Materials.* Progress in Materials Science, 1989. **33**(4): p. 223-315.

[4] Lu, K. and Lu, J., *Nanostructured Surface Layer on Metallic Materials Induced by Surface Mechanical Attrition Treatment.* Materials Science and Engineering: A, 2004. **375 - 377**: p. 38-45.

[5] Cahn, R. W., *Materials Science- Nanostructured Materials.* Nature, 1990. **348**: p. 389-390.

[6] Gleiter, H., *Nanostructured Materials: State of the Art and Perspectives.* Nanostructured Materials, 1995. **6**: p. 3-14.

[7] Ma, E., *Eight Routes to Improve the Tensile Ductility of Bulk Nanostructured Metals and Alloys.* JOM Journal of the Minerals, Metals and Materials Society, 2006. **58**(4): p. 49-53.

[8] Shaw, L. L., *Processing Nanostructured Materials: An Overview.* JOM Journal of the Minerals, Metals and Materials Society, 2000. **52**(12): p. 41-45.

[9] Valiev, R. Z., Islamgaliev, R. K., and Alexandrov, I. V., *Bulk Nanostructured Materials from Severe Plastic Deformation.* Progress in Materials Science, 2000. **45**(2): p. 103-189.

[10] Meyers, M. A., Mishra, A., and Benson, D. J., *Mechanical Properties of Nanocrystalline Materials.* Progress in Materials Science, 2006. **51**(4): p. 427-556.

[11] Koch, C., *Bulk Behavior of Nanostructured Materials*, in *Nanostructure Science and Technology, a Worldwide Study*, R.W. Siegel, E. Hu, M.C. Roco, and e. al., Editors. 1999. p. 93.

[12] Mehl, R. F. and Cahn, R. W., *Historical Development*, in *Physical Metallurgy.* 1983: North Holland.

[13] Siegel, R. W., *Mechanical Properties and Deformation Behavior of Materials Having Ultrafine Microstructures*, M. Nastasi, D.M. Parkin, and H. Gleiter, Editors. 1993. p. 509.

[14] Gleiter, H., *Nanostructured Materials: Basic Concepts and Microstructure.* Acta Materialia, 2000. **48**(1): p. 1-29.

[15] Hall, E. O., *The Deformation and Aging of Mild Steel: Ii Characteristics of the Lüders Deformation.* Proceedings of the Physical Society. Section B, 1951. **64**: p. 747-753.

[16] Petch, N. J., *The Cleavage Strength of Polycrystals.* Journal of the Iron and Steel Institute, 1953. **174**: p. 25-28.

[17] Chattopadhyay, P. P., Pabi, S. K., and Manna, I., *On the Inverse Hall-Petch Relationship in Nanocrystalline Materials.* Zeitschrift Fur Metallkunde, 2000. **91**(12): p. 1049-1051.

[18] Chokshi, A. H., Rosen, A., Karch, J., and Gleiter, H., *On the Validity of the Hall-Petch Relationship in Nanocrystalline Materials.* Scripta Metallurgica, 1989. **23**(10): p. 1679-1683.

[19] Fougerc, G. E., Weertman, J. R., Siegel, R. W., and Kim, S., *Grain-Size Dependent Hardening and Softening of Nanocrystalline Cu and Pd.* Scripta Metallurgica Et Materialia, 1992. **26**(12): p. 1879-1883.

[20] Giga, A., Kimoto, Y., Takigawa, Y., and Higashi, K., *Demonstration of an Inverse Hall-Petch Relationship in Electrodeposited Nanocrystalline Ni-W Alloys through Tensile Testing.* Scripta Materialia, 2006. **55**(2): p. 143-146.

[21] Lu, K. and Sui, M. L., *An Explanation to the Abnormal Hall-Petch Relation in Nanocrystalline Materials.* Scripta Metallurgica Et Materialia, 1993. **28**(12): p. 1465-1470.

[22] Koch, C. C., *Optimization of Strength and Ductility in Nanocrystalline and Ultrafine Grained Metals.* Scripta Materialia, 2003. **49**(7): p. 657-662.

[23] Weertman, J. R., *Hall-Petch Strengthening in Nanocrystalline Metals.* Materials Science and Engineering: A, 1993. **166**(1-2): p. 161-167.

[24] Han, B. Q., Lavernia, E. J., and Mohamed, F. A., *Mechanical Properties of Nanostructured Materials.* Reviews on Advanced Materials Science, 2005. **9**(1): p. 1-16.

[25] Lee, W. S. and Lam, H. F., *The Deformation Behaviour and Microstructure Evolution of High-Strength Alloy Steel at High Rate of Strain.* Journal of Materials Processing Technology, 1996. **57**(3-4): p. 233-240.

[26] Lu, K., *Nanocrystalline Metals Crystallized from Amorphous Solids:*

Nanocrystallization, Structure, and Properties. Materials Science and Engineering: R, 1996. **16**(4): p. 161-221.

[27] Mohamed, F. A. and Xun, Y. W., *Correlations between the Minimum Grain Size Produced by Milling and Material Parameters.* Materials Science and Engineering: A, 2003. **354**(1-2): p. 133-139.

[28] Roland, T., Retraint, D., Lu, K., and Lu, J., *Enhanced Mechanical Behavior of a Nanocrystallised Stainless Steel and Its Thermal Stability.* Materials Science and Engineering: A, 2007. **445**: p. 281-288.

[29] Sanders, P. G., Eastman, J. A., and Weertman, J. R., *Elastic and Tensile Behavior of Nanocrystalline Copper and Palladium.* Acta Materialia, 1997. **45**(10): p. 4019-4025.

[30] Sanders, P. G., Youngdahl, C. J., and Weertman, J. R., *The Strength of Nanocrystalline Metals with and without Flaws.* Materials Science and Engineering: A, 1997. **234**: p. 77-82.

[31] Tao, N. R., Sui, M. L., Lu, J., and Lu, K., *Surface Nanocrystallization of Iron Induced by Ultrasonic Shot Peening.* Nanostructured Materials, 1999. **11**(4): p. 433-440.

[32] Tao, N. R., Tong, W. P., Wang, Z. B., Wang, W., Sui, M. L., Lu, J., and Lu, K., *Mechanical and Wear Properties of Nanostructured Surface Layer in Iron Induced by Surface Mechanical Attrition Treatment.* Journal of Materials Science and Technology, 2003. **19**(6): p. 563-566.

[33] Valiev, R. Z., Alexandrov, I. V., Zhu, Y. T., and Lowe, T. C., *Paradox of Strength and Ductility in Metals Processed by Severe Plastic Deformation.* Journal of Materials Research, 2002. **17**(1): p. 5-8.

[34] Wang, Y. M., Wang, K., Pan, D., Lu, K., Hemker, K. J., and Ma, E., *Microsample Tensile Testing of Nanocrystalline Copper.* Scripta Materialia, 2003. **48**(12): p. 1581-1586.

[35] Youssef, K. M., Scattergood, R. O., Murty, K. L., Horton, J. A., and Koch, C. C., *Ultrahigh Strength and High Ductility of Bulk Nanocrystalline Copper.* Applied Physics Letters, 2005. **87**(9).

[36] Schiϕtz, J. and Jacobsen, K. W., *A Maximum in the Strength of Nanocrystalline Copper.* Science, 2003. **301**(5638): p. 1357-1359.

[37] Meyers, M. A. and Chawla, K. K., *Mechanical Behavior of Materials.* 2008, New York: Cambridge University Press.

[38] Ma, E., *Instabilities and Ductility of Nanocrystalline and Ultrafine-Grained Metals.* Scripta Materialia, 2003. **49**(7): p. 663-668.

[39] Wu, X., Tao, N., Hong, Y., Liu, G., Xu, B., Lu, J., and Lu, K., *Strain-Induced Grain Refinement of Cobalt During Surface Mechanical Attrition Treatment.* Acta Materialia, 2005. **53**(3): p. 681-691.

[40] Guo, J., Wang, K., and Lu, L., *Tensile Properties of Cu with Deformation Twins Induced by SMAT.* Journal of Materials Science and Technology, 2006. **22**(6): p. 789-792.

[41] Mishra, A., Richard, V., Gregori, F., Asaro, R. J., and Meyers, M. A., *Microstructural Evolution in Copper Processed by Severe Plastic Deformation.* Materials Science and Engineering: A, 2005. **410**: p. 290-298.

[42] Conrad, H., *Grain Size Dependence of the Plastic Deformation Kinetics in Cu.* Materials Science and Engineering: A, 2003. **341**(1-2): p. 216-228.

[43] Conrad, H. and Narayan, J., *Mechanisms for Grain Size Hardening and Softening in Zn.* Acta Materialia, 2002. **50**(20): p. 5067-5078.

[44] Swygenhoven, H. V., Spaczer, M., Caro, A., and Farkas, D., *Competing Plastic Deformation Mechanisms in Nanophase Metals.* Physical Review B, 1999. **60**(1): p. 22-24.

[45] Zhu, B., Asaro, R. J., Krysl, P., and Bailey, R., *Transition of Deformation Mechanisms and Its Connection to Grain Size Distribution in Nanocrystalline Metals.* Acta Materialia, 2005. **53**: p. 4825-4838.

[46] Yamakov, V., Wolf, D., Phillpot, S. R., Mukherjee, A. K., and Gleiter, H., *Dislocation Processes in the Deformation of Nanocrystalline Aluminium by Molecular-Dynamics Simulation.* Nature Materials, 2002. **1**(1): p. 45-48.

[47] Yamakov, V., Wolf, D., Phillpot, S. R., Mukherjee, A. K., and Gleiter, H., *Deformation-Mechanism Map for Nanocrystalline Metals by Molecular-Dynamics Simulation.* Nature Materials, 2003. **3**: p. 43-47.

[48] Raj, R. and Ashby, M. F., *On Grain Boundary Sliding and Diffusional Creep.* Metallurgical Transactions, 1971. **2**(4): p. 1113-1127.

[49] Liao, X. Z., Zhou, F., Lavernia, E. J., Srinivasan, S. G., Baskes, M. I., He, D. W., and Zhu, Y. T., *Deformation Mechanism in Nanocrystalline Al: Partial Dislocation Slip.* Applied Physics Letters, 2003. **83**(4): p. 632-634.

[50] Shan, Z., Stach, E. A., Wiezorek, J. M. K., Knapp, J. A., Follstaedt, D. M., and Mao, S. X., *Grain Boundary–Mediated Plasticity in Nanocrystalline Nickel.* Science, 2004. **305**: p. 654-657.

[51] Lu, L., Chen, X., Huang, X., and Lu, K., *Revealing the Maximum Strength in Nanotwinned Copper.* Science, 2009. **323**: p. 607-610.

[52] Wang, Y. M. and Ma, E., *Temperature and Strain-Rate Effects on the Strength and Ductility of Nanostructured Copper.* Applied Physics Letters, 2003. **83**(15): p. 3165-3167.

[53] Wang, Y. M., Chen, M. W., Zhou, F. H., and Ma, E., *High Tensile Ductility in a Nanostructured Metal.* Nature, 2002. **419**(6910): p. 912-915.

[54] Chen, J., Lu, L., and Lu, K., *Hardness and Strain-Rate Sensitivity of*

Nanocrystalline Cu. Scripta Materialia, 2006. **54**(11): p. 1913-1918.

[55] Gray, G. T., Lowe, T. C., Cady, C. M., Valiev, R. Z., and Aleksandrov, I. V., *Influence of Strain-Rate and Temperature on the Mechanical Response of Ultrafine-Grained Cu, Ni, and Al-4Cu-0.5Zr.* Nanostructured Materials, 1997. **9**(1-8): p. 477-480.

[56] Lu, L., Li, S. X., and Lu, K., *An Abnormal Strain-Rate Effect on Tensile Behavior in Nanocrystalline Copper.* Scripta Materialia, 2001. **45**(10): p. 1163-1169.

[57] Lu, L., Schwaiger, R., Shan, Z. W., Dao, M., Lu, K., and Suresh, S., *Nano-Sized Twins Induce High Rate Sensitivity of Flow Stress in Pure Copper.* Acta Materialia, 2005. **53**(7): p. 2169-2179.

[58] Meyers M.A., Vohringer O., and V.A., L., *The Onset of Twinning in Metals: A Constitutive Description.* Acta Materialia, 2001. **49**: p. 4025-4039.

[59] Schwaiger, R., Moser, B., Dao, M., Chollacoop, N., and Suresh, S., *Some Critical Experiments on the Strain-Rate Sensitivity of Nanocrystalline Nickel* Acta Materialia, 2003. **51**(17): p. 5159-5172.

[60] Wang, K., Tao, N. R., Liu, G., Lu, J., and Lu, K., *Plastic Strain-Induced Grain Refinement at the Nanometer Scale in Copper.* Acta Materialia, 2006. **54**(19): p. 5281-5291.

[61] Wang, Y. M. and Ma, E., *Strain Hardening, Strain-Rate Sensitivity, and Ductility of Nanostructured Metals.* Materials Science and Engineering: A, 2004. **375-77**: p. 46-52.

[62] Shen, Y. F., Lu, L., Dao, M., and Suresh, S., *Strain-Rate Sensitivity of Cu with Nanoscale Twins.* Scripta Materialia, 2006. **55**(4): p. 319-322.

[63] Dao, M., Lu, L., Shen, Y. F., and Suresh, S., *Strength, Strain-Rate Sensitivity and Ductility of Copper with Nanoscale Twins.* Acta Materialia, 2006. **54**(20): p. 5421-5432.

[64] Dao, M., Lu, L., Asaro, R. J., De Hosson, J. T. M., and Ma, E., *Toward a Quantitative Understanding of Mechanical Behavior of Nanocrystalline Metals.* Acta Materialia, 2007. **55**(12): p. 4041-4065.

[65] Wang, Y. M. and Ma, E., *Three Strategies to Achieve Uniform Tensile Deformation in a Nanostructured Metal.* Acta Materialia, 2004. **52**(6): p. 1699-1709.

[66] Malow, T. R., Koch, C. C., Miraglia, P. Q., and Murty, K. L., *Compressive Mechanical Behavior of Nanocrystalline Fe Investigated with an Automated Ball Indentation Technique.* Materials Science and Engineering: A, 1998. **252**(1): p. 36-43.

[67] Wei, Q., Cheng, S., Ramesh, K. T., and Ma, E., *Effect of Nanocrystalline and Ultrafine Grain Sizes on the Strain-Rate Sensitivity and Activation Volume:*

Fcc Versus Bcc Metals. Materials Science and Engineering: A, 2004. **381**(1-2): p. 71-79.

[68] Elmustafa, A. A., Tambwe, M. F., and Stone, D. S., *Activation Volume Analysis of Plastic Deformation in Fcc Materials Using Nanoindentation.* Surface Engineering 2002-Synthesis, Characterization and Applications, 2003. **750**.

[69] Hart, E. W., *Theory of the Tensile Test* Acta Metallurgica, 1967. **15**(2): p. 351-355.

[70] Oleszak, D. and Shingu, P. H., *Nanocrystalline Metals Prepared by Low Energy Ball Milling.* Journal of Applied Physics, 1996. **79**(6): p. 2975-2980.

[71] Eckert, J., Holzer, J. C., Krill, C. E., and Johnson, W. L., *Investigation of Nanometer-Sized Fcc Metals Prepared by Ball Milling.* Materials Science Forum, 1992. **88-90**: p. 505-512.

[72] Eckert, J., Holzer, J. C., Krill, C. E., and Johnson, W. L., eds. *Synthesis and Characterization of Ball-Milled Nanocrystalline Fcc Metals*. Structure and Properties of Interfaces in Materials, ed. W.T. Clark, Dahmen, U. and Briant, C. L. . Vol. 238. 1992, Materials Research Society Symposium Proceedings: Pittsburgh, PA. 739.

[73] Eckert, J., Holzer, J. C., Krill, C. E., and Johnson, W. L., *Structural and Thermodynamic Properties of Nanocrystalline Fcc Metals Prepared by Mechanical Attrition.* Journal of Materials Research, 1992. **7**(7): p. 1751-1761.

[74] Shen, T. D. and Koch, C. C., *Formation, Solid Solution Hardening and Softening of Nanocrystalline Solid Solutions Prepared by Mechanical Attrition.* Acta Materialia, 1996. **44**(2): p. 753-761.

[75] Huang, J. Y., Wu, Y. K., and Ye, H. Q., *Deformation Structures in Ball Milled Copper.* Acta Materialia, 1996. **44**(3): p. 1211-1221.

[76] Guo, F. A., Trannoy, N., and Lu, J., *Microstructural Analysis by Scanning Thermal Microscopy of a Nanocrystalline Fe Surface Induced by Ultrasonic Shot Peening.* Superlattics and Microstructures, 2004. **35**: p. 445-453.

[77] Guo, F. A., Zhu, K. Y., Trannoy, N., and Lu, J., *Examination of Thermal Properties by Scanning Thermal Microscopy in Ultrafine-Grained Pure Titanium Surface Layer Produced by Surface Mechanical Attrition Treatment.* Thermochimica Acta, 2004. **419**: p. 239-246.

[78] Liu, G., Lu, J., and Lu, K., *Surface Nanocrystallization of 316l Stainless Steel Induced by Ultrasonic Shot Peening.* Materials Science and Engineering: A, 2000. **286**: p. 91-95.

[79] Lu, K. and Lu, J., *Surface Nanocrystallization (Snc) of Metallic Materials-Presentation of the Concept Behind a New Approach.* Journal of Materials Science and Technology, 1999. **15**(3): p. 193-197.

[80] Tao, N. R., Wang, Z. B., Tong, W. P., Sui, M. L., Lu, J., and Lu, K., *An Investigation of Surface Nanocrystallization Mechanism in Fe Induced by Surface Mechanical Attrition Treatment.* Acta Materialia, 2002. **50**(18): p. 4603-4616.

[81] Tao, N. R., Wu, X. L., Sui, M. L., Lu, J., and Lu, K., *Grain Refinement at the Nanoscale Via Mechanical Twinning and Dislocation Interaction in a Nickel-Based Alloy.* Journal of Materials Research, 2004. **19**(6): p. 1623-1629.

[82] Tao, N. R., Zhang, H. W., Lu, J., and Lu, K., *Development of Nanostructures in Metallic Materials with Low Stacking Fault Energies During Surface Mechanical Attrition Treatment (SMAT).* Materials Transactions, 2003. **44**(10): p. 1919-1925.

[83] Wu, X., Tao, N., Hong, Y., Xu, B., Lu, J., and Lu, K., *Microstructure and Evolution of Mechanically-Induced Ultrafine Grain in Surface Layer of Al-Alloy Subjected to USSP.* Acta Materialia, 2002. **50**(8): p. 2075-2084.

[84] Zhang, H. W., Hei, Z. K., Liu, G., Lu, J., and Lu, K., *Formation of Nanostructured Surface Layer on Aisi 304 Stainless Steel by Means of Surface Mechanical Attrition Treatment.* Acta Materialia, 2003. **51**(7): p. 1871-1881.

[85] Zhu, K. Y., Vassel, A., Brisset, F., Lu, K., and Lu, J., *Nanostructure Formation Mechanism of A-Titanium Using SMAT.* Acta Materialia, 2004. **52**(14): p. 4101-4110.

[86] Ma, E., Wang, Y. M., Lu, Q. H., Sui, M. L., Lu, L., and Lu, K., *Strain Hardening and Large Tensile Elongation in Ultrahigh-Strength Nano-Twinned Copper.* Applied Physics Letters, 2004. **85**(21): p. 4932-4934.

[87] Shen, Y. F., Lu, L., Lu, Q. H., Jin, Z. H., and Lu, K., *Tensile Properties of Copper with Nano-Scale Twins.* Scripta Materialia, 2005. **52**: p. 989-994.

[88] Han, W. Z., Wu, S. D., Li, S. X., and Zhang, Z. F., *Origin of Deformation Twinning from Grain Boundary in Copper.* Applied Physics Letters, 2008. **92**(22).

[89] Liao, X. Z., Zhao, Y. H., Srinivasan, S. G., Zhu, Y. T., Valiev, R. Z., and Gunderov, D. V., *Deformation Twinning in Nanocrystalline Copper at Room Temperature and Low Strain-Rate.* Applied Physics Letters, 2004. **84**(4): p. 592-594.

[90] Chen, M. W., Ma, E., Hemker, K. J., Sheng, H. W., Wang, Y. M., and Cheng, X. M., *Deformation Twinning in Nanocrystalline Aluminum.* Science, 2003. **300**: p. 1275-1277.

[91] Liao, X. Z., Zhao, Y. H., Zhu, Y. T., Valiev, R. Z., and Gunderov, D. V., *Grain-Size Effect on the Deformation Mechanisms of Nanostructured Copper Processed by High-Pressure Torsion.* Journal of Applied Physics, 2004. **96**(1): p. 636-640.

[92] Zhu, Y. T., Liao, X. Z., and Wu, X. L., *Deformation Twinning in Bulk Nanocrystalline Metals: Experimental Observations.* JOM Journal of the Minerals, Metals and Materials Society, 2008. **60**(9): p. 60-64.

[93] Lu, L., Shen, Y. F., Chen, X. H., Qian, L. H., and Lu, K., *Ultrahigh Strength and High Electrical Conductivity in Copper.* Science, 2004. **304**: p. 422-426.

[94] Mahajan, S., Pande, C. S., Imam, M. A., and Rath, B. B., *Formation of Annealing Twins in F.C.C. Crystals.* Acta Materialia, 1997. **45**(6): p. 2633-2638.

[95] Andrade, U. R., Meyers, M. A., Vecchio, K. S., and Chokshi, A. H., *Dynamic Recrystallization in High-Strain, High-Strain-Rate Plastic Deformation of Copper.* Acta metallurgica et Materialia, 1994. **42**(9): p. 3183-3195.

[96] Lu, K., Lu, L., and Suresh, S., *Strengthening Materials by Engineering Coherent Internal Boundaries at the Nanoscale.* Science, 2009. **324**(5925): p. 349-352.

[97] Krstic, V., Erb, U., and Palumbo, G., *Effect of Porosity on Young Modulus of Nanocrystalline Materials.* Scripta Metallurgica et Materialia, 1993. **29**(11): p. 1501-1504.

[98] Wong, L., Ostrander, D., Erb, U., Palumbo, G., and Aust, K. T. *Mechanical Properties of Nanocrystalline Ni-P Alloys*. in *Nanophases and Nanocrystalline Structures*. 1993. San Diego, California; United States.

[99] Birringer, R., Gleiter, H., Klein, H. P., and Marquardt, P., *Nanocrystalline Materials an Approach to a Novel Solid Structure with Gas-Like Disorder.* Physics Letters A, 1984. **102**(8): p. 365-369.

[100] Gleiter, H. and Marquardt, P., *Nanocrystalline Structures - an Approach to New Materials?* Zeitschrift Fur Metallkunde, 1984. **75**(4): p. 263-267.

[101] Nieman, G. W., Weertman, J. R., and Siegel, R. W., *Mechanical Behavior of Nanocrystalline Cu and Pd.* Journal of Materials Research, 1991. **6**(5): p. 1012-1027.

[102] Suryanarayana, C., *Mechanical Alloying and Milling.* Progress in Materials Science, 2001. **46**(1-2): p. 1-184.

[103] Suryanarayana, C., Ivanov, E., and Boldyrev, V. V., *The Science and Technology of Mechanical Alloying.* Materials Science and Engineering: A, 2001. **304-306**: p. 151-158.

[104] Fecht, H. J., Hellstern, E., Fu, Z., and Johnson, W. L., *Nanocrystalline Metals Prepared by High-Energy Ball Milling* Metallurgical and Materials Transactions A, 1990. **21**(9): p. 2333-2337.

[105] Valiev, R., *Nanostructuring of Metals by Severe Plastic Deformation for Advanced Properties.* Nature Materials, 2004. **3**(8): p. 511-516.

[106] Segal, V. M., Reznikov, V. I., Drobyshevskii, A. E., and Kopylov, V. I., *Plastic Working of Metals by Simple Shear.* Russian Metallurgy, 1981(1): p. 99-105.

[107] Valiev, R. Z., Krasilnikov, N. A., and Tsenev, N. K., *Plastic Deformation of Alloys with Submicron-Grained Structure.* Materials Science and Engineering: A, 1991. **137**: p. 35-40.

[108] Valiev, R. Z., *Structure and Mechanical-Properties of Submicrometer-Grained Materials Produced by Severe Plastic-Deformation.* Mechanical Properties and Deformation Behavior of Materials Having Ultra-Fine Microstructures, 1993. **233**.

[109] Valiev, R. Z., Korznikov, A. V., and Mulyukov, R. R., *Structure and Properties of Ultrafine-Grained Materials Produced by Severe Plastic Deformation.* Materials Science and Engineering: A, 1993. **168**(2): p. 141-148.

[110] Alexandrov, I. V. and Valiev, R. Z., *Nanostructures from Severe Plastic Deformation and Mechanisms of Large-Strain Work Hardening.* Nanostructured Materials, 1999. **12**(5-8): p. 709-712.

[111] Saito, Y., Utsunomiya, H., Tsuji, N., and Sakai, T., *Novel Ultra-High Straining Process for Bulk Materials—Development of the Accumulative Roll-Bonding (ARB) Process.* Acta Materialia, 1999. **47**(2): p. 579-583.

[112] Valiev, R. Z. and Alexandrov, I. V., *Nanostructured Materials from Severe Plastic Deformation.* Nanostructured Materials, 1999. **12**(1-4): p. 35-40.

[113] Zhilyaev, A. P., Nurislamova, G. V., Kim, B. K., Baro, M. D., Szpunar, J. A., and Langdon, T. G., *Experimental Parameters Influencing Grain Refinement and Microstructural Evolution During High-Pressure Torsion.* Acta Materialia, 2003. **51**(3): p. 753-765.

[114] Valiev, R. Z., Estrin, Y., Horita, Z., Langdon, T. G., Zehetbauer, M. J., and Zhu, Y. T., *Producing Bulk Ultrafine-Grained Materials by Severe Plastic Deformation.* JOM Journal of the Minerals, Metals and Materials Society, 2006. **58**(4): p. 33-39.

[115] Clark, D., Wood, D., and Erb, U., *Industrial Applications of Electrodeposited Nanocrystals.* Nanostructured Materials, 1997. **9**(1-8): p. 755-758.

[116] Cui, B. Z., Han, K., Xin, Y., Waryoba, D. R., and Mbaruku, A. L., *Highly Textured and Twinned Cu Films Fabricated by Pulsed Electrodeposition.* Acta Materialia, 2007. **55**: p. 4429-4438.

[117] Dini, J. W., *Electrodeposition: The Materials Science of Coatings and Substrates*. Materials Science and Process Technology Series, ed. R.F. Bunshah and G.E. McGuire. 1993, United States of America: Noyes Publications.

[118] Elsherik, A. M. and Erb, U., *Synthesis of Bulk Nanocrystalline Nickel by*

Pulsed Electrodeposition. Journal of Materials Science, 1995. **30**(22): p. 5743-5749.

[119] Erb, U., *Electrodeposited Nanocrystals - Synthesis, Structure, Properties and Future Applications.* Canadian Metallurgical Quarterly, 1995. **34**(3): p. 275-280.

[120] Erb, U. and El-Sherik, A. M., *Nanocrystalline Metals and Process of Producing the Same*, U.S.P.a.T. Office, Editor. 1994, Queen' University at Kingston, Canada.

[121] Iban˜ez, A. and Fata´s, E., *Mechanical and Structural Properties of Electrodeposited Copper and Their Relation with the Electrodeposition Parameters.* Surface & Coatings Technology, 2005. **191**: p. 7-16.

[122] Kanani, N., *Electroplating- Basic Principles, Processes and Practice*. 2004, Oxford, U.K.: Elsevier Advanced Technology. 353.

[123] Ludwig, H., *Electroplating and Electroless Plating of Copper & Its Alloys*, ed. N. Kanani. 2003: Finishing Publications Ltd & ASM International. 304.

[124] Pantleon, K., Jensen, J. A. D., and Somers, M. A. J., *Interpretation of Quantitative Crystallographic Texture in Copper Electrodeposits on Amorphous Substrates.* Journal of The Electrochemical Society, 2004. **151**(1): p. C45-C51.

[125] Rasmussen, A. A., Jensen, J. A. D., Horsewell, A., and Somers, M. A. J., *Microstructure in Electrodeposited Copper Layers; the Role of the Substrate.* Electrochimica Acta, 2001. **47**: p. 67-74.

[126] Schlesinger, M., *Electroplating*, in *Electrochemistry Encyclopedia*. 2002.

[127] Qu, N. S., Zhu, D., Chan, K. C., and Lei, W. N., *Pulse Electrodeposition of Nanocrystalline Nickel Using Ultra Narrow Pulse Width and High Peak Current Density.* Surface and Coatings Technology, 2003. **168**(2-3): p. 123-128.

[128] Tao, N. R., Wang, Z. B., Tong, W. P., Sui, M. L., Lu, J., and Lu, K., *An Investigation of Surface Nanocrystallization Mechanism in Fe Induced by Surface Mechanical Attrition Treatment.* Acta Materialia, 2002. **50**(18): p. 4603-4616.

[129] Zhu, K. Y., Vassel, A., Brisset, F., Lu, K., and Lu, J., *Nanostructure Formation Mechanism of A-Titanium Using SMAT.* Acta Materialia, 2004. **52**(14): p. 4101-4110.

[130] Wang, K., Tao, N. R., Liu, G., Lu, J., and Lu, K., *Plastic Strain-Induced Grain Refinement at the Nanometer Scale in Copper.* Acta Materialia, 2006. **54**(19): p. 5281-5291.

[131] Wu, X., Tao, N., Hong, Y., Liu, G., Xu, B., Lu, J., and Lu, K., *Strain-Induced Grain Refinement of Cobalt During Surface Mechanical Attrition Treatment.*

Acta Materialia, 2005. **53**(3): p. 681-691.

[132] Wu, X., Tao, N., Hong, Y., Xu, B., Lu, J., and Lu, K., *Microstructure and Evolution of Mechanically-Induced Ultrafine Grain in Surface Layer of Al-Alloy Subjected to USSP.* Acta Materialia, 2002. **50**(8): p. 2075-2084.

[133] Zhang, H. W., Hei, Z. K., Liu, G., Lu, J., and Lu, K., *Formation of Nanostructured Surface Layer on AISI 304 Stainless Steel by Means of Surface Mechanical Attrition Treatment.* Acta Materialia, 2003. **51**(7): p. 1871-1881.

[134] Sun, H. Q., Shi, Y., Zhang, M., and Lu, K., *Plastic Strain-Induced Grain Refinement in the Nanometer Scale in a Mg Alloy.* Acta Materialia, 2007. **55**: p. 975-982.

[135] Lu, J. and Lu, K., *Surface Nanocrystallization (SNC) of Materials and Its Effect on Mechanical Behavior*, in *Comprehensive Structural Integrity*, I. Milne, R.O. Ritchie, and B.L. Karihaloo, Editors. 2003, Elsevier Science: New York. p. 495 - 528.

[136] Wang, Z. B., Tao, N. R., Li, S., Wang, W., Liu, G., Lu, J., and Lu, K., *Effect of Surface Nanocrystallization on Friction and Wear Properties in Low Carbon Steel.* Materials Science and Engineering: A, 2003. **352**: p. 144-149.

[137] Zhang, Y. S., Han, Z., and Lu, K., *Fretting Wear Behavior of Nanocrystalline Surface Layer of Copper under Dry Condition.* Wear, 2008. **265**(3-4): p. 396-401.

[138] Chen, X. H., Lu, J., Lu, L., and Lu, K., *Tensile Properties of a Nanocrystalline 316L Austenitic Stainless Steel.* Scripta Materialia, 2005. **52**(10): p. 1039-1044.

[139] Roland, T., Retraint, D., Lu, K., and Lu, J., *Fatigue Life Improvement through Surface Nanostructuring of Stainless Steel by Means of Surface Mechanical Attrition Treatment.* Scripta Materialia, 2006. **54**(11): p. 1949-1954.

[140] Tong, W. P., Han, Z., Wang, L. M., Lu, J., and Lu, K., *Low-Temperature Nitriding of 38CrMoAl Steel with a Nanostructured Surface Layer Induced by Surface Mechanical Attrition Treatment.* Surface and Coatings Technology, 2008. **202**(20): p. 4957-4963.

[141] Tong, W. P., Tao, N. R., Wang, Z. B., Lu, J., and Lu, K., *Nitriding Iron at Lower Temperatures.* Science, 2003. **299**(5607): p. 686-688.

[142] Torre, F. D., Lapovok, R., Sandlin, J., Thomson, P. F., Davies, C. H. J., and Pereloma, E. V., *Microstructures and Properties of Copper Processed by Equal Channel Angular Extrusion for 1–16 Passes.* Acta Materialia, 2004. **52**(16): p. 4819-4832.

[143] Lu, L., Wang, L. B., Ding, B. Z., and Lu, K., *High-Tensile Ductility in Nanocrystalline Copper.* Journal of Materials Research 2000. **15**(2): p. 270-273.

[144] Lee, W. S. and Lin, C. F., *Impact Properties and Microstructure Evolution of 304L Stainless Steel.* Materials Science and Engineering: A, 2001. **308**(1-2): p. 124-135.

[145] Lee, W. S. and Lin, C. F., *High-Temperature Deformation Behaviour of Ti6Al4V Alloy Evaluated by High Strain-Rate Compression Tests.* Journal of Materials Processing Technology, 1998. **75**(1): p. 127-136.

[146] Meyers, M. A., Chen, Y. J., Marquis, F. D. S., and Kim, D. S., *High-Strain, High-Strain-Rate Behavior of Tantalum.* Metallurgical and Materials Transactions A, 1995. **26**(10): p. 2493-2501.

[147] Chichili, D. R., Ramesh, K. T., and Hemker, K. J., *The High-Strain-Rate Response of Alpha-Titanium: Experiments, Deformation Mechanisms and Modeling* Acta Materialia, 1998. **46**(3): p. 1025-1043.

[148] Molinari, A. and Ravichandran, G., *Constitutive Modeling of High-Strain-Rate Deformation in Metals Based on the Evolution of an Effective Microstructural Length.* Mechanics of Materials, 2005. **37**(7): p. 737-752.

[149] Johnson, K. L., *Contact Mechanics*. 1985, Cambridge: Cambridge University Press.

[150] Hill, R., *The Mathematical Theory of Plasticity*. 1950, New York: Oxford University Press Inc. 354.

[151] Tabor, D., *The Hardness of Metals*. 1951, New York, United States: Oxford University Press Inc. 173.

[152] Bonou, L., Eyraud, M., Denoyel, R., and Massiani, Y., *Influence of Additives on Cu Electrodeposition Mechanisms in Acid Solution: Direct Current Study Supported by Non-Electrochemical Measurements.* Electrochimica Acta, 2002. **47**(26): p. 4139-4148.

[153] Schuh, C. A., Nieh, T. G., and Yamasaki, T., *Hall-Petch Breakdown Manifested in Abrasive Wear Resistance of Nanocrystalline Nickel.* Scripta Materialia, 2002. **46**(10): p. 735-740.

[154] Tao, S. and Li, D. Y., *Tribological, Mechanical and Electrochemical Properties of Nanocrystalline Copper Deposits Produced by Pulse Electrodeposition.* Nanotechnology, 2006. **17**(1): p. 65-78.

[155] Mishra, R., Basu, B., and Balasubramaniam, R., *Effect of Grain Size on the Tribological Behavior of Nanocrystalline Nickel.* Materials Science and Engineering: A, 2004. **373**(1-2): p. 370-373.

[156] Hepel, M., Chen, Y. M., and Stephenson, R., *Effect of the Composition of Polypyrrole Substrate on the Electrodeposition of Copper and Nickel.* Journal of the Electrochemical Society, 1996. **143**(2): p. 498-505.

[157] Kozlov, V. M. and Bicelli, L. P., *Texture Formation of Electrodeposited Fcc*

Metals. Materials Chemistry and Physics, 2003. **77**(1): p. 289-293.

[158] Choi, K. H., Kim, H. S., and Lee, T. H., *Electrode Fabrication for Proton Exchange Membrane Fuel Cells by Pulse Electrodeposition.* Journal of Power Sources, 1998. **75**(2): p. 230-235.

[159] Champion, Y., Langlois, C., Guerin-Mailly, S., Langlois, P., Bonnentien, J. L., and Hy¨tch, M. J., *Near-Perfect Elastoplasticity in Pure Nanocrystalline Copper.* Science, 2003. **300**(5617): p. 310-311.

[160] Mukherjee, A. K., *An Examination of the Constitutive Equation for Elevated Temperature Plasticity.* Materials Science and Engineering: A, 2002. **322**(1-2): p. 1-22.

[161] Xiang, Y., Tsui, T. Y., and Vlassak, J. J., *The Mechanical Properties of Freestanding Electroplated Cu Thin Films.* Journal of Materials Research, 2006. **21**(6): p. 1607-1618.

[162] Xiang, Y. and Vlassak, J. J., *Bauschinger and Size Effects in Thin-Film Plasticity.* Acta Materialia, 2006. **54**(20): p. 5449-5460.

[163] Yang, Y., Yao, N., Imasogie, B., and Soboyejo, W. O., *Nano-Scale and Submicron Fatigue Crack Growth in Nickel Microbeams.* Acta Materialia, 2007. **55**(13): p. 4305-4315.

[164] Yang, Y., Yao, N., Soboyejo, W. O., and Tarquinio, C., *Deformation and Fracture in Micro-Tensile Tests of Electrodeposited Freestanding Nickel Thin Films.* Scripta Materialia, 2008. **58**(12): p. 1062-1065.

[165] Espinosa, H. D., Berbenni, S., Panico, M., and Schwarz, K. W., *An Interpretation of Size-Scale Plasticity in Geometrically Confined Systems.* Proceedings of the National Academy of Sciences of the United States of America, 2005. **102**(47): p. 16933-16938.

[166] Bažant, Z. P., Guo, Z., Espinosa, H. D., Zhu, Y., and Peng, B., *Epitaxially Influenced Boundary Layer Model for Size Effect in Thin Metallic Films.* Journal of Applied Physics, 2005. **97**(7): p. 073506-1-073506-13.

[167] Bron, F., Besson, J., and Pineau, A., *Ductile Rupture in Thin Sheets of Two Grades of 2024 Aluminum Alloy.* Materials Science and Engineering: A, 2004. **380**(1-2): p. 356-364.

[168] Bandstra, J. P. and Koss, D. A., *Modeling the Ductile Fracture Process of Void Coalescence by Void-Sheet Formation.* Materials Science and Engineering: A, 2001. **319-321**: p. 490-495.

[169] Cheng, S., Ma, E., Wang, Y. M., Kecskes, L. J., Youssef, K. M., Koch, C. C., Trociewitz, U. P., and Han, K., *Tensile Properties of in Situ Consolidated Nanocrystalline Cu.* Acta Materialia, 2005. **53**(5): p. 1521-1533.

[170] Moosbrugger, C., *Representation of Stress-Strain Behavior*, in *Atlas of Stress-Strain Curves*, H.E. Boyer, Editor. 1990, Metals Park, Ohio: ASM

International, 1990, ©1987. p. 630.

[171] Wen, M., Liu, G., Gu, J. F., Guan, W. M., and Lu, J., *Dislocation Evolution in Titanium During Surface Severe Plastic Deformation.* Applied Surface Science, 2009. **255**(12): p. 6097-6102.

[172] Simons, G., Weippert, C., Dual, J., and Villain, J., *Size Effects in Tensile Testing of Thin Cold Rolled and Annealed Cu Foils.* Materials Science and Engineering: A, 2006. **416**(1-2): p. 290-299.